

Thesis

The Modification of Thin Film Surface Structure via Low Temperature Atmospheric Pressure CVD Post Process Treatment

Author: Michael Thomson

**Material & Physics Research Centre
School of Computing Science and Engineering
University of Salford
Greater Manchester
M5 4WT
United Kingdom**

Acknowledgement

I would like to thank everyone who helped me throughout the years. It has not been an easy journey, many people believed I would never achieve anything academic. I found a great ally in stubbornness and persistence in the face of adversity.

I would not be here today without the help and support of some very important people. Vitally I would like to thank are my parents. My Mum and Dad have given me endless support, bolstering me and a swift kick in the right direction when needed. Helen has been with me through my triumphs and defeats for the last three years. Her care and attention has kept me on track through the years, making my life better. Three important people I would to thank are Mr Starling, Mrs Kenningham and Dr Pilkington. Rarely do you meet such characters who have a great impact on the direction of your life. Without your wise words and encouragement I would not be who I am.

Thanks to everyone in the CVD Group for your friendship, support and guidance.

Thanks to everyone at Salford University for this great opportunity and decade of memories.

“Make Yourself”

Abstract

In photovoltaic thin film cells, a transparent conducting oxide (TCO) layer is required to transport current. The most common TCOs used are F:SnO₂ (fluorine doped tin oxide), ZnO (zinc oxide) and ITO (indium doped tin oxide). ZnO is normally deposited in a vacuum based process, sputtering or low pressure chemical vapour deposition (LPCVD). Atmospheric pressure chemical vapour deposition (APCVD) is an attractive alternative for ZnO deposition. A critical parameter for TCOs in photovoltaic thin films is the surface morphology which defines the optical scattering properties. The ability to control the spectral sensitivity and degree of scattering are both important process parameters for high performance cells. This thesis investigates APCVD for film growth of ZnO plus dopants (fluorine and aluminium), and the effects of atmospheric pressure plasma etching of ZnO and F:SnO₂.

ZnO was deposited in multiple system geometries all based on thermal activated CVD. The oxidant source purity is shown to be critical for stable growth at higher temperatures required for dopant incorporation. A fundamental problem was encountered with fluorine doping, whereby the films would crack beyond a critical thickness. A solution was found with the development of a F:SnO₂ and F:ZnO composite stack. Photovoltaic testing of this hybrid TCO was encouraging, showing the potential benefit of the composite structure.

Modification of the surface morphology was achieved by atmospheric pressure plasma, based on a dielectric barrier discharge configuration. This novel system enables the etching of TCO films without the introduction of hazardous wet chemistry. In this thesis the effects of etching regime and feedgas composition are studied and an etching mechanism is proposed. Isolation of the etching environment enabled investigation into the feed gas mixture, demonstrating which were critical for etching. Both materials showed a dependence on the feed gas mixture for etching, with F:SnO₂ requiring HCl and O₂ and H₂O for ZnO.

Contents

Abstract.....	1
1 - Introduction	6
1.1 Prologue.....	6
1.2 Motivation	10
1.3 Aims and Objectives.....	16
2 - Theory & Background	18
2.1 Transparent Conducting Oxides	18
2.2 Properties of Thin Films	24
2.3 Electrical Properties of TCOs.....	29
2.3 Optical Properties of TCOs	32
2.4 Solar Cell Design.....	37
2.4.1 Thin-Film Solar Cells <i>c-Si</i> & <i>pc-Si</i> (Crystalline & Polycrystalline)	37
2.4.2 Thin Film Amorphous and Nano Silicon Solar Cells.....	38
2.4.3 Material and Properties.....	38
2.4.4 Amorphous Silicon Solar Cells and Configurations (<i>a-Si:H</i>)	41
2.4.5 Multiple-Junction and Tandem Solar Cells	45
2.5 Photovoltaic Performance Assessment.....	47
3 - Thin Film Deposition Techniques & Processes	53
3.1 Fundamentals of Chemical Vapour Deposition.....	55
3.2 Mass Transport	61
3.3 Nucleation and Film Growth	65
3.4 Chemical Vapour Deposition Activation Methods	69
3.4.1 Thermal Activation.....	69
3.4.2 Plasma Enhanced Activation	70
3.4.3 Photo Assisted Activation	71
3.4.4 Combustion Activation.....	71
4 - Plasma General	73
4.1 Introduction	73
4.2 Fundamentals of Plasmas	73
4.2.1 Plasma Generation.....	73

4.2.2 Chemistry of Plasma and Origin of Species	75
4.3 Plasma Classification.....	77
4.3.1 LTE Plasmas.....	77
4.3.2 Non-LTE Plasmas.....	78
4.4 Atmospheric Pressure Plasmas.....	79
5 - Etching Methods.....	87
5.1 Chemical Etching and Photolithography.....	87
5.2 Resist Masking	88
5.3 Reactive Ion Etching and Deep Reactive Ion Etching	90
5.4 Surface Activation and Etching via Plasma's	92
5.5 Microelectronics Plasma Etching	92
5.5.1 Microelectronics Plasma Etching Process Overview	95
5.5.2 Benefits and Drawbacks of Microelectronic Plasma Etching	97
5.6 Four Basic Low Pressure Etching Processes.....	98
5.8 Chlorine as an Etchant Source.....	102
6 - Analytical Techniques	103
6.1 Atomic Force Microscopy (AFM).....	103
6.2 Scanning Electron Microscope (SEM).....	108
6.3 Four Point Probe and Hall Effect Measurement.....	114
6.3.1 Four Point Probe.....	114
6.3.2 Mobility Measurements.....	117
6.3.3 Hall Effect involving van der Pauw Structures	118
6.3.4 Hall Measurements	120
6.3.5 The Van Der Pauw Technique.....	122
6.4 Optical Measurements	124
6.5 X-Ray Diffraction (XRD).....	131
7 -Experimental Investigation.....	136
7.1 CVD System.....	136
7.1.1 Precursor Delivery.....	136
7.1.2 Nozzle Coater	137
7.1.3 Tube Coater	138
7.1.4 Dual Flow System	139

7.2 Zinc Oxide Growth – First phase	141
7.2.1 Initial Stages	141
7.2.2 Alternative Oxygen Source for ZnO Growth	145
7.3 Fluorine Doping of ZnO	152
7.3.1 Initial Stages	152
7.4 Aluminium Doping of ZnO	154
7.4.1 Initial Stages	154
7.5 Plasma Etching System	156
7.6 Plasma System Modification	165
7.7 Plasma Etching of F: SnO ₂	171
7.7.1 Etching of F: SnO ₂	171
7.7.2 Activated Chemical Etching of F: SnO ₂	173
7.7.3 Initial Indications of the Plasma Mechanism F:SnO ₂	183
7.8 Plasma Etching of Zinc Oxide.....	185
7.8.1 Initial Investigation.....	185
7.8.2 Plasma Etching of ZnO in a Nitrogen Environment.....	189
7.8.3 Open Atmospheric Etching vs. Nitrogen Atmosphere	192
7.8.4 Nitrogen Atmosphere with Plasma Feedgas of Nitrogen and Oxygen.....	194
7.8.5 Nitrogen Atmosphere with Plasma Feedgas of Air	196
7.8.6 Nitrogen Atmosphere with Plasma Feedgas of Nitrogen, Oxygen and H ₂ O.....	199
7.8.7 Plasma Etching of ZnO – Regulated H ₂ O Etching.....	203
7.9 Zinc Oxide Growth – Second phase	209
7.9.1 Fluorine Doped Zinc Oxide	209
7.9.2 F:ZnO Passes Series	217
7.9.3 F:ZnO Reduced Passes with Slow Transition Speed.....	221
7.9.4 Film Cracking Monitoring.....	224
7.9.5 F:ZnO Dopant Series	226
7.9.6 F:ZnO Oxidant Introduction Series	229
7.9.7 F:ZnO Growth Current Status	237
7.10 Seeding Layer for Fluorine Zinc Oxide Growth	239
7.10.1 Initial Investigation.....	239
7.10.3 500/500 Series F:SnO ₂ /F:ZnO.....	248

7.11 Photovoltaic Testing Round Two	252
8 - Discussion.....	265
9 - Conclusion	271
10- Bibliography	276
11 – Appendix.....	309
11.1 Published Papers.....	309

1 - Introduction

1.1 Prologue

Science and engineering research has for centuries been propelled by the desire to understand and manipulate our surroundings. Mankind has constantly invented tools to aid our species survival ranging from spears for hunting animals, to modern day laboratory equipment that help develop cures for diseases. Currently we stand on the verge of a very challenging time as natural resources are diminishing and the necessity for creating alternative fuel sources is imminent ^{(1) (2) (3)}. Considerable progress within the field of renewable energy systems have been documented with advances in electric vehicles ^{(4) (5)}, photovoltaic technologies ^{(6) (7) (8)}, hydro-electrical energy ^{(2) (9) (10)}, wind energy farms ^{(2) (11) (12)} and renovation of the nuclear industry ^{(13) (14) (15)}.

In recent history a global industrial revolution occurred, consuming immense quantities of resources ^{(2) (13)}. Sustained expansion relied on accessible and efficient fuel, principally coal supplies ^{(2) (16)}. Currently these non-renewable sources comprise 80% of the world's fuel sources, and it is predicted that energy usage will at least double before 2030 ⁽¹⁶⁾. Traditional energy sources deliver our immediate power requirements; however these natural resources are in decline and produce harmful pollutant materials that damage our environment ^{(17) (18)}. Global warming was first raised as an issue in 1980's ⁽¹⁹⁾, studies have revealed that CO₂ levels have increased by 31% in the last 200 years ⁽¹⁸⁾. Changes to civilization have directly impacted on global temperature, with an average surface temperature increase by 0.4-0.8°C ⁽¹⁸⁾. Modern societies demand for instant electrical power requires highly efficient energy supplies ⁽¹⁶⁾. Efficiency and cleanliness of a power source are two critical factors that dictate the feasibility production ⁽²⁾. Current generations of renewable energy systems suffer low efficiency, stunting their extensive implementation ^{(13) (16) (20)}.

Concerns regarding energy production have been highlighted by the media and even dictated parliamentary policies ^{(2) (3) (13) (16) (17)}. We are constantly threatened by energy shortages and global warming ⁽¹⁷⁾. Pollution attributed to dirty processing of waste products the main protagonist whilst excessive usage of non-renewable energy sources propels us towards an energy drought ^{(2) (17)}. Energy is a vital component of modern life and new safe, clean, renewable cost effective alternatives need to be developed for the future. An increasing global population which exceeded 7 billion ⁽²¹⁾ in 2011 and is predicted to exceed 8 billion by

2050⁽²²⁾ with an ageing population⁽²¹⁾ will require a staggering 30TW to sustain economic growth⁽²⁾⁽²³⁾.

Two factors have driven the requirement for development and implementation of sustainable energy. Depletion of traditional energy sources, coal, oil, natural gas and their adverse impact on the environment. Rapid industrial development in countries such as China, India, South Africa and the Russian Federation using readily available non-renewable coal supplies are estimated by 2020 to contribute to half of global CO₂ emissions⁽³⁾⁽¹⁸⁾. From 2005 – 2012 China aimed to build 532 additional coal fired power stations causing significant increases in CO₂ emissions⁽³⁾. Fossil fuels remain dominant in energy generation accounting for 80% in total⁽¹⁸⁾. Despite a rise in oil production, its share of the market has fallen, coal and natural gas volumes have increased since 1990⁽³⁾⁽¹⁸⁾.

Renewable energy sources saw less than a quarter of the expansion of world coal production. Increasing between 1990 - 2001 less than 20% from 2002 – 2003 and under 20% from 2005 – 2006⁽³⁾. Currently renewable sources supplying approximately 14% of the total world demand, which include biomass, hydropower, geothermal, solar, wind and marine engines⁽¹⁸⁾. Considerable changes are required to reduce dependence on non-renewable energy sources and help reduce the impact on environment.

Reducing energy expenditure has intensified government campaigns and policies to help reduce energy consumption are being promoted, free energy saving light bulbs, with incentives for low energy users⁽¹³⁾⁽²⁴⁾⁽²⁵⁾. Industry has paralleled these concerned by manufacturing where possible products with energy efficient components responsibly sourced⁽²⁾⁽³⁾. Energy rating systems are universally apparent to gauge energy efficiency of merchandise resulting in energy conscious households⁽²⁶⁾⁽²⁷⁾⁽²⁸⁾. Recycling and the reduction of waste are now an integral part of manufacturing⁽²⁹⁾. Car manufactures are now producing fuel efficient, low emission vehicles exempt from road tax presenting affordable solutions to the customer⁽³⁰⁾.

Hybrid vehicles (mainly electrical/petrol hybrid) have been adopted into the domestic market place⁽³¹⁾⁽³²⁾. However these vehicles suffer from constraints due to the battery storage size. Additionally battery fabrication requires large quantities of energy, greatly reducing the efficiency of manufacturing. Current research collaboration between the Imperial College London and Volvo has put forth a 3.4 million euro project to investigate storage of electrical

energy in the body work of vehicles. Using a special composition of carbon and glass fibre, kinetic energy is able to be stored in the material and power the vehicle. A further benefit of this construction is the lighter weight over traditional body panels if devices in the vehicle are constructed of the same material, they can become self-powered meaning an overall improvement in efficiency⁽³³⁾.

Scientific research is constantly moving forward in trying to understanding our surroundings and pushing forward the capabilities of our existing technology. Solar power is an excellent renewable energy source; and with the application of solar cells we are able to utilize this energy⁽¹³⁾⁽³⁴⁾. Traditionally capturing of solar energy was achieved using single crystalline silicon based cells⁽⁷⁾⁽³⁵⁾, which still yield the highest efficiency conversion. However this cell construction suffers limitation's from cell size, manufacturing costs and flexibility of the final product⁽³⁵⁾. Consequently the demand for lower cost solutions has encouraged the research and development into thin film technology⁽¹³⁾⁽¹⁶⁾⁽³⁶⁾⁽³⁷⁾⁽³⁸⁾.

Thin film cells offer technical benefits over the traditional solar cell construction, predominately through low material consumption and a wide variety of coating techniques capable of producing the films layers⁽⁷⁾⁽³⁶⁾⁽³⁹⁾⁽⁴⁰⁾. Employment of chemical vapour deposition (CVD) techniques allows deposition of film coatings over large volume areas⁽⁴¹⁾. This has the potential to reduce manufacturing costs and expands the energy capturing surface through a physically larger cell size⁽³⁵⁾. To combat the lower efficiency of the thin film based cells, research has currently focused into material compositions and more complex arrangement of film layers⁽¹⁾⁽⁶⁾⁽⁷⁾⁽³⁵⁾⁽²³⁾⁽³⁴⁾. Tin oxide is one of the conventional transparent conducting oxide (TCO) core materials with various dopant species added for conductivity with a dominant use in cadmium telluride (CdTE) cells⁽²⁰⁾⁽⁴²⁾⁽⁴³⁾. Significant interest in Zinc Oxide has developed due to recent advances in the material and has seen wide adoption in CIGS (copper indium gallium selenide) and tandem cells.⁽⁴⁴⁾⁽⁴⁵⁾⁽⁴⁶⁾. It can offer beneficial properties over traditional materials with greater light scattering performance and significantly reduce the cost of the material compared to Indium⁽⁴⁷⁾⁽⁴⁵⁾⁽⁴⁸⁾. A challenge encountered with zinc oxide production is adding a dopant material into the film for the desired properties. Several techniques including magnetron sputtering⁽⁴⁹⁾, reactive magnetron sputtering⁽⁵⁰⁾⁽⁵¹⁾, spray pyrolysis⁽⁵²⁾⁽⁵³⁾, sol-gel⁽⁵⁴⁾⁽⁵⁵⁾, pulsed laser deposition⁽⁵⁶⁾⁽⁵⁷⁾, molecular beam epitaxy⁽⁵⁸⁾ and chemical vapour deposition⁽⁵⁹⁾⁽⁶⁰⁾⁽⁶¹⁾ are used to deposit zinc oxide including multiple dopants.

Photovoltaics are into their fiftieth year of research and significant developments have been made in these years. Movement from the novel aspect of solar cell research has slowly become dominated by the economic state. Increasing pressure is being applied to research and industry to produce cost effective and cheaper devices ^{(7) (23)}. One solution for reducing manufacturing costs is the implementation of cheaper production systems.

This can be achieved by using an online (glass coatings deposited on glass production line e.g. non batch processed) atmospheric pressure coating system that does not require costly vacuum equipment and maintenance ⁽⁶²⁾. An additional benefit of applying atmospheric conditions to the processing parameters is the high throughput rate, as a large number of units can be produced in contrast to that of reduced pressure fabrication ^{(62) (41)}.

1.2 Motivation

Thin film technologies have the ability to become widely accepted in this generation of solar cell products; however work is needed to improve and refine manufacturing processes^{(63) (35) (23) (64) (34)}. Production issues have led the research to improve the overall efficiency of the final products. Two main routes of exploration revolve around advancing the growth techniques and surface modification of the transparent conducting oxide layer (TCO)^{(20) (63) (64) (46) (65) (66) (67)}. A key aspect of this research is to involve effective methods that are adaptable to current processes (retro-fitting) being readily implemented into industrial applications. Furthermore with regards to post growth treatment, to develop a process that does not involve hazardous wet chemistry or expensive specialist equipment. Essentially the driving force behind this body of research is to enhance the current field of knowledge with respect to APCVD growth and atmospheric pressure etching techniques specifically for TCO's.

Solar power is a relatively new method of producing electrical energy and the technology has now demonstrated the potential to become a significant contributor to global energy needs^{(2) (13) (35) (34)}. A theoretical calculation of solar cell energy conversion of light assumes a maximum potential of 41% at peak solar saturation (Shockley-Queisser limit of single cell junction of approximately concentrated 1,000 suns), whilst current generation of cells on average achieve 6 - 12% for thin film devices^{(35) (34)}. In 2011 peak solar cell efficiencies were recorded above 43% for triple junction cells⁽⁶⁸⁾, and record efficiency for flexible substrate CIGS cells of 20.4% in 2013⁽⁶⁹⁾. Amorphous silicon cells have reached a peak efficiency of 13.4% as demonstrated by LG electronics⁽⁶⁸⁾. Recent developments in black silicon improve overall cell performance through improved hydrogen passivation, increase spectral response efficiency from 95% -98% and reduce reflection⁽⁷⁰⁾. Figure 1 shows the progression of efficiencies achieved by each type of photovoltaic device over the last 40 years.

Innovative steps are required to harvest the remaining incident photons, bridging the gap between practical and theoretical efficiencies. Several generations of cells have been produced over 40 years of development. The first generation of cells were expensive due to research, manufacturing and installation costs, which is expected of a new product⁽²³⁾. Second generation implemented polycrystalline thin film silicon cells over crystalline silicon wafer cells, were cheaper to fabricate. Thin films based technologies suffered low efficiencies

through design bottlenecks and required improvement to achieve their theoretical potential^{(23) (34)}. Third generation devices are the current focus and aim to produce high performance at a relatively low cost to replace existing energy sources and secure the future energy demands⁽²³⁾. This generation is looking towards advanced designs and materials with the scope of involving organics, 3D cell structuring, wide band cells and multi-junction structures. Research is currently focusing on several factors for developing this third generation of photovoltaics^{(7) (23) (71)};

- a) Improve conversion efficiency
- b) Improve spectral response
- c) Effectively use thinner substrates (reduce required thickness of silicon in cells)
- d) Reducing effective costs for both primary and secondary power generation

Contemporary structures of cells are fabricated upon crystalline silicon and multiple junctions to achieve these high rates of efficiency but are difficult to manufacture and expensive^{(7) (35)}⁽²³⁾. Aspirations to attain the theoretically predicted maximum efficiency will require greater process control. This would involve cell construction with reduced defects, improved light scatter and electrical properties^{(39) (46) (66)}. Fundamentally these goals can be achieved; it is a matter of consistent research with an intelligent thought process. Advanced growth and post treatment of thin film layers is a proposed simple method of refining process control, and tuning a material to desired properties^{(36) (67)}. Exploration into further understanding the scientific principles involved in these areas motivated this investigation. Its primary focus was to develop a surface modification technique in conjunction with doped zinc oxide growth for enhancing solar cell performance.

Many changes have occurred within the field of photovoltaics. Numerous technical achievements resulted in peak efficiencies being surpassed (CdTe hit 18.7%⁽⁷²⁾, multi-junctions 37.8%⁽⁷³⁾, flexible thin film 20.4%⁽⁷⁴⁾, organic 12%⁽⁷⁵⁾, concentrator cell 44%⁽⁷⁶⁾), but this has not been without threat⁽⁷⁷⁾. The photovoltaic market is struggling, with many companies leaving the industry and budget cuts hindering research⁽⁷⁸⁾. Cheaply manufactured cells have flooded the market, resulting in severe price reduction⁽⁷⁹⁾. Competition from around the world has been forced to shrink budgetary margins to meet the price demand; a consequence is that research funding and capital investment have been scaled back. Cheap production has been enabled by government subsidies in China, enabling cheaper

manufacturing that western countries cannot compete against⁽⁸⁰⁾⁽⁸¹⁾. The worsening Chinese environment has forced the government to bail out companies to maintain jobs and dominate world production despite market impact. Currently discussions are being held to resolve market flooding into Europe⁽⁸²⁾. Installation of high efficiency cells is limited to the commercial sector, with the average consumer purchasing cheap lower efficiency units⁽⁸³⁾. Political movements have reduced feed in incentives to consumers, further impacting the purchasing decision⁽⁸⁴⁾. In 2011 a peak uptake in PV modules was seen due to the diminishing government incentives⁽⁸⁴⁾⁽⁸⁵⁾.

It has been expressed that many companies will have to fail to allow the market place to recover and stabilize production to consumer demand⁽⁸⁶⁾. For example, in 2011 China had rapid growth of PV companies from government schemes with upwards of 500 companies in Beijing alone⁽⁸⁶⁾. The excessive number of manufacturers producing units has rapidly lowered the costs over 60% of panels from \$4 per watt to 78 cents per watts in eight years⁽⁸⁶⁾. Manufacturers have managed to reduce prices as demand for materials increased. However the lack of profit margin and abundance of competition means new processes and tools are not affordable. Novel techniques and commercialization of advanced technologies have yet to be implemented due to funding issues despite the efficiency benefits⁽⁸⁶⁾. Without the technology advancements it will be difficult for photovoltaics to overtake traditional non-renewable sources.

With the global photovoltaic market growth declining, a handful of core companies and research departments remain strong. This will hopefully benefit the consumer as research and products become more focused. Budgetary confinements have forced research to develop cheap processes to enhance the existing technology⁽⁸³⁾. Research innovations are focusing on improving current technology in contrast to simply increasing manufacturing, which is currently hindering the PV market. Modification of the light interaction elements are currently being investigated⁽⁸⁷⁾⁽⁸⁸⁾⁽⁸⁹⁾. Introduction of black silicon as the absorber material will increase the spectral absorption and reduce reflection improving overall efficiency⁽⁹⁰⁾⁽⁹¹⁾⁽⁹²⁾⁽⁹³⁾. Adoption of black silicon promises to instantly improve cell performance, with gains of 2-3% when implemented against traditional silicon. In addition to enhanced light absorption, nanowires have seen recent development that enable “light soaking” to improve efficiencies solar cell efficiencies by 25%⁽⁹⁴⁾⁽⁹⁵⁾. The TCO layer is operated as the electrical contacts and critically as a light scattering medium. Tailoring of TCO structure to emphasize

the optical properties has shown to increase cell efficiency⁽⁸⁷⁾. Commercially and in research this is traditionally achieved by wet chemical etching^{(96) (97)}. With these developments enhancing light absorption/interaction, applications of higher performing anti-reflective layers externally and internally intend increase light transmission^{(98) (99) (100)}. Increasing overall light input and uptake will enhance cell technology. Third generation of solar cells concentrates on process development instead of new material generation. Implementation of nanoscale components to control the energy band gap intends to improve energy generation. This includes the development of nanotubes (CNT), quantum dots (QDs) and hot carrier (HC) solar cell devices^{(23) (83)}. An alternative concern to cell performance is the storage elements^{(101) (102) (103)}. Traditional battery materials have shown to be a very inefficient method of storage⁽¹⁰¹⁾, with schemes being implemented to improve storage facilities^{(104) (105)}. Reducing generated energy loss and enabling storage of excess energy for drought periods will help secure photovoltaics as a viable energy alternative⁽¹⁰⁶⁾.

Beyond scientific innovation targeting solely efficiency, photovoltaics require production methods that are reliable and cost effective^{(23) (107)}. Amorphous silicon cells utilizing thin film technology would need to be developed onto float glass technologies to produce efficiency/cost effective units. Progressing high efficiency single crystalline cells needs simpler and cheaper manufacturing methods⁽²³⁾. Stable production methods will ultimately define the processes that will continue to be researched. Bosetti et al⁽¹⁰⁷⁾ describe the main barriers for the each cell technology as shown in Table 1.

Technology	Barriers
Crystalline-Silicon	Efficiency, materials
Thin-Film	Efficiency, Stability, Toxicity, Lifetime
Concentrating PV	Stability, Complexity, Very High Costs
Organic PV	Efficiency, Stability, Lifetime
Third Generation PC	Efficiency, Proof of Concept
Concentrated Solar Power	Heat Storage, Lifetime, Material

Table 1 - Technical Barriers for Cell Technology⁽¹⁰⁷⁾

With respects to this body of research several groups have led TCO development. Zinc oxide growth is dominated by physical deposition and LPCVD processes⁽¹⁰⁸⁾. EPFL research group deposit boron doped zinc oxide materials via LPCVD^{(88) (109)}. This is utilized as the standard TCO material for their novel micromorph cells⁽¹¹⁰⁾. EPFL have led the research into optimum

structural properties for the ZnO TCO layer^{(87) (96) (109)}. As described by Nicolay^{(96) (109)}, pyramidal structures offer the optimum light scattering abilities and electrical characteristics, whilst allowing for reduced defect processing. Structural layer interfacing has been a core focus, aiming to reduce morphological deposition induced defects. Fleischer⁽⁸⁷⁾ & Escarre⁽⁸⁸⁾ describe the requirement to advance the anti-reflective properties between material boundaries to enhance performance.

In 1991, Gordon⁽⁵⁹⁾, documented the first research into fluorine doped zinc oxide via chemical vapour deposition. Since then little research has been conducted in the field using CVD techniques. Recently Bhachu et al⁽⁶⁰⁾ documented fluorine doped zinc oxide films produced by aerosol assisted chemical vapour deposition. This work shows the viability of using atmospheric pressure processes to achieve fluorine doping of zinc oxide. Sputtered processes have struggled to achieve high crystallinity resulting in a number of grain boundaries and interfaces that are problematic. Poor crystallinity due to deposition at low temperatures results in susceptibility to plasma erosion through development. The aerosol assisted process produces films that are comparable to commercial available SnO₂ and In₂O₃ products, however the process is long, taking 90 minutes for deposition.

Optimization of surface morphology is typically achieved through post deposition treatment. Hupkes et al⁽⁹⁷⁾ proposed a model based on experimental data to describe the effects of wet chemical etching of sputter deposited ZnO. This paper describes the techniques used to tailor a desired morphology and the process conditions that affect the etching regime. Multiple groups have been using diluted HCl to obtain the desired surface morphologies over the last two decades^{(66) (111) (97)}. EPFL standard boron doped zinc oxide morphology is modified using wet chemical processing to define the crater width and height^{(96) (112)}. Recent advancements reported by the EPFL show that wide shallow craters offer the best balance between optical performance and post processing into cell construction^{(96) (109)}.

Wet chemical techniques dominate TCO etching. As the design rule shrunk with micro-electronics, the necessity to diverge from crude wet etching to nanoscale control from plasma etching was required. Plasma etching offers the ability to define the etching regime in a clean and safe environment. This technique is not confined to the photovoltaic TCO, and may be applied to an array of materials. Critically as research identifies the correct etchant specie/s per material, it will become a versatile etching system.

Best Research-Cell Efficiencies

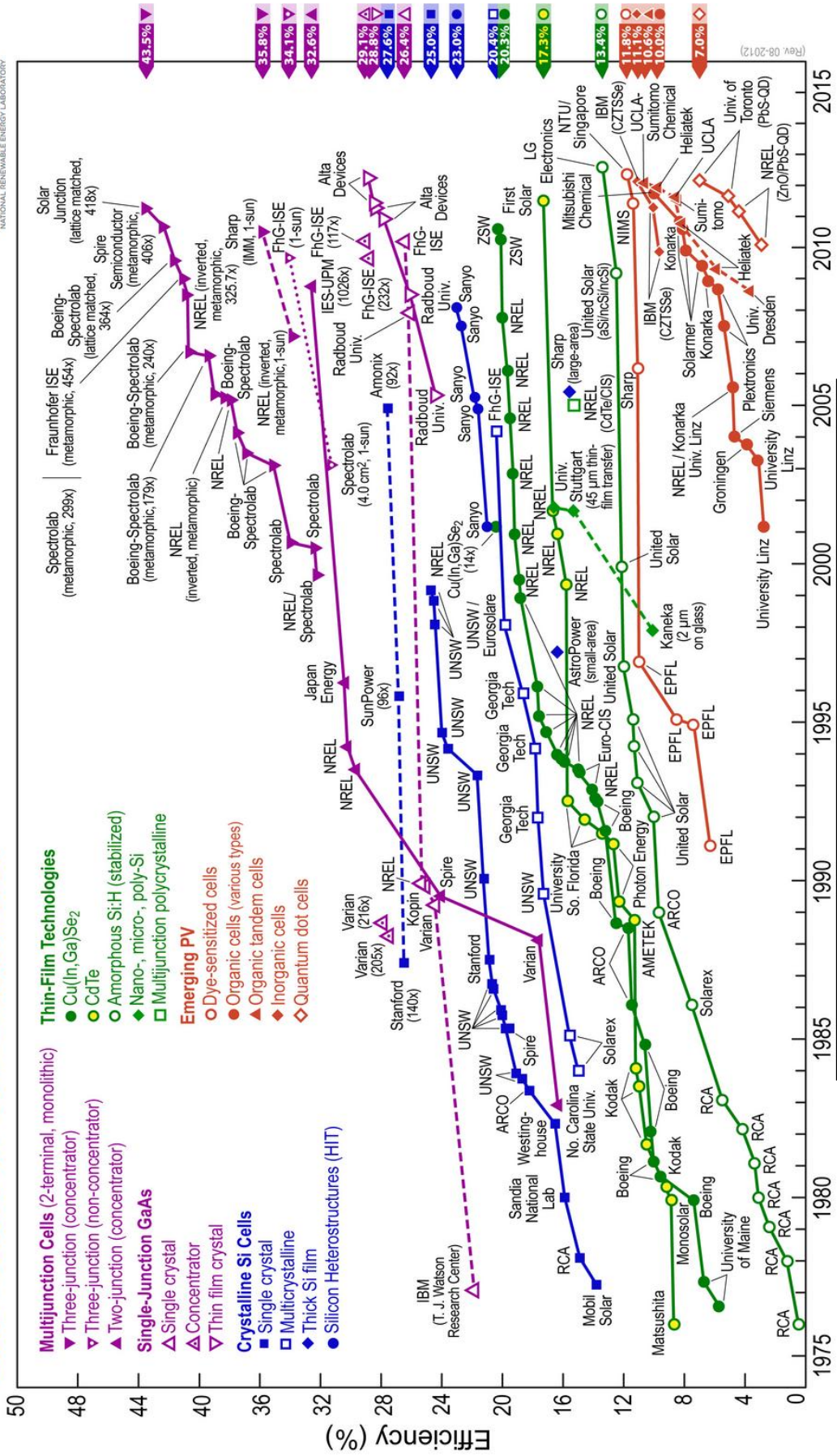


Figure 1 - Best Research Solar Cell Efficiencies ⁽⁷⁸⁾

(Rev. 08-2012)

1.3 Aims and Objectives

The primary focus of this research was the production and characterisation of TCO films and this was broken down into two subsections; film growth and post modification. From the beginning it was clear these were the two main areas of investigation, complementing each other as developments were made. Consideration of these allowed the following aims and objectives to be set.

ZnO Growth

- A.1. Low temperature ZnO deposition - primary investigation into the conditions required for effective ZnO growth.
- A.2. ZnO growth rate, structure and oxidant sources. Investigation of the influence of temperature and oxidant source on the resultant structure and the growth rate.
- A.3. CVD routes to influence the growth rate and control the ZnO structure.
- A.4. Optimization of ZnO growth for dopant introduction.
- A.5. Investigate of the influence the dopant source on the resultant film properties.
- A.6. Successfully incorporate fluorine and aluminium into ZnO. Production of optically transparent and conductive films for use as TCOs.
- A.7. Observation of multiple oxidants and doping sources, investigating their influence on the resultant growth parameters and film properties.
- A.8. Determine a suitable coating geometry for optimized deposition.
- A.9. Introduce grown TCO film into a photovoltaic structure. Improve the growth process to enable high efficiency PV cells.
- A.10. Develop a viable process for ZnO growth suitable for scalability onto large area substrates.

Plasma Etching

- B.1. Report the initial investigation into the novel atmospheric plasma etching system, observing the structural, optical and electrical properties of the etched films.
- B.2. Investigate the parameters required for etching F:SnO₂.
- B.3. Investigate the parameters required for etching ZnO.
- B.4. Investigate the discharge properties and experienced etching.
- B.5. Investigate the feed-gas mixture and experienced etching.
- B.6. Structure control through manipulation of the process conditions. Determine if specific etching conditions result in a specific etching regime.
- B.7. Development of the atmospheric plasma etching system, ensuring safe operation and effective etching.
- B.8. Implementation of modified TCOs into photovoltaic devices. Investigate if the etching process improves TCO performance.
- B.9. Characterisation of the plasma and species generated.

2 - Theory & Background

2.1 Transparent Conducting Oxides

Semiconducting oxides (SnO_2 , ZnO , In_2O_3 , etc.) have been thoroughly researched leading to a diverse array of applications^{(47) (42) (44) (114) (39) (40) (115) (116)}. Most notably they have been implemented into transparent electrodes^{(114) (117)}, lasers and sensors^{(118) (119)}. These oxide materials are important due to their combination of low electrical resistance in conjunction with high optical transparency in the visible range of the electromagnetic spectrum⁽¹²⁰⁾. Many pieces of apparatus benefit from this special ability as they are able to produce an electrical contact without prohibiting inbound photons from either entering or escaping the optically active region of the device⁽¹²¹⁾. Furthermore TCO's are highly reflective in the infrared region, which is responsible for the employment of certain TCO's for energy conservation materials^{(115) (116)}. High conductivity is sought, which many of the TCO's possess due to intrinsic defects i.e. oxygen deficiencies⁽⁴³⁾. For the purposes of this work we are predominately interested in SnO_2 and ZnO ⁽⁸⁷⁾, as these are the two materials that we will be developing for enhanced TCO products.

Tin oxide (SnO_2) is one of the most studied of these metal oxides, displaying n-type semiconducting properties⁽¹¹⁷⁾. SnO_2 exhibits a direct band gap of E_g of $\sim 3.6\text{eV}$ ⁽¹¹⁷⁾⁽¹²²⁾. With the presence of oxidizing and reducing agents, it is known to have dramatic effects on the electronic properties of the material surface^{(123) (124)}.

Undoped SnO_2 contains a carrier density of approximately 10^{20}cm^{-3} which is similar to semi-metals demonstrating between 10^{17}cm^{-3} and 10^{20}cm^{-3} ⁽¹²⁵⁾. As a consequence of its properties, it is commonly implemented into transparent electrical technology such as display devices⁽¹²⁶⁾ and photovoltaics⁽¹²⁵⁾. Theories have been suggested to de-convolute the simultaneous nature of optical transparency and electrical conductivity, but no clear definition currently exists⁽¹²⁷⁾. It has been generally considered that the existence of shallow donor levels close to the conduction band from concentrations of oxygen vacancies, gives rise to the TCO⁽¹²⁸⁾. Optical transparency exists across the band gap for visible light however far infra-red is absorbed through Drude-like interaction⁽¹²⁷⁾. Non-stoichiometry is critical for the conductivity of undoped SnO_2 with implemented intrinsic oxygen defect^{(129) (130)}. Stoichiometric samples however exhibit high resistance⁽¹³¹⁾.

An aspect that makes SnO₂ very special is that it contains dual valency, preferably accepting an oxidation state of 2+ or 4+, which assists the variation of the surface oxygen composition (43). It is noted that this variance in surface composition is a general mechanism involved with metal oxides. Critically this permits the tailoring for many unique chemical properties for a diverse array of intended applications⁽⁴³⁾. Rarely is tin oxide used in its pure form it is mostly modified by impurity dopants alongside other additives. Fluorine doping is the most common type of dopant, which has seen wide commercial success in amorphous silicon (a-Si) solar cells⁽⁴⁴⁾ and low emissivity windows⁽¹³²⁾. Fluorine has preference as a dopant material due to its high transparency and conductivity⁽¹³³⁾. Manipulation of these impurities allows control of the material properties for specific applications⁽¹²⁷⁾⁽¹³⁴⁾.

Zinc Oxide (ZnO) has had a long standing history of being used in cosmetic products, lubricants, ointments etc. The first application of ZnO for its semiconducting properties was found in the 1920's "build your own radio sets"⁽¹³⁵⁾. Its use was to convert incoming radio signals from AC to DC. In 1957 the New Jersey Zinc Company published a booklet entitled "Zinc Oxide Rediscovered" in an attempt to promote ZnO materials properties. At this time research was focused on developing varistors, surface acoustic wave devices and transparent conductive films that did not require single crystal phases⁽¹³⁵⁾. Single crystalline growth of ZnO was achieved through the developments of epitaxial systems. These films were developed for the original intention of gallium nitride (GaN) epitaxy, which is another wide, direct bandgap semiconductor used for optoelectronic devices. ZnO was researched as a suitable substrate for GaN devices, leading to the first Zinc Oxide Workshop in 1999⁽¹³⁵⁾. Look et al⁽¹³⁶⁾ in 2002 first published p-type ZnO homoepitaxial film growth by molecular beam epitaxy (MBE), which lead towards achieving p-n junctions for light emitting devices (LED).

ZnO⁽¹³⁷⁾ is a semiconductor that belongs to the classification of TCO materials. It possesses a direct band structure exhibiting wide gap energy of $\sim 3.37\text{eV}$ ⁽³⁶⁾ and large excitation binding energy of $\sim 60\text{meV}$ ⁽¹³⁸⁾. Its large binding energy allows excitonic absorption and recombination at room temperature, making this material very attractive⁽¹³⁹⁾. Significant interest has been generated in zinc oxide primarily due to its abundance, non-toxic, high chemical resistance, thermal stability, good film adhesion for variety of substrates, lower deposition temperatures and is relatively inexpensive⁽⁴⁶⁾⁽¹⁴⁰⁾. F:SnO₂ has predominately being used for commercial production as a transparent contact for photovoltaic applications.

Another distinct advantage of zinc oxide is its stability in a hydrogen atmosphere, which is required in certain solar cell fabrication processes (silane plasma discharge which is used for a-Si: H thin film solar cells) ^{(45) (141)}. Dopants can be introduced into zinc oxide films, producing materials of high electrical conductivity whilst retaining optical transparency. Notably for TCO applications common dopants are aluminium ⁽¹⁴¹⁾, boron ⁽⁶¹⁾, indium ⁽¹⁴²⁾ and gallium ⁽¹¹¹⁾. Research with fluorine ⁽⁵⁹⁾ has provided little success for commercial applications ⁽¹⁴³⁾. Appropriate dopant selection can tailor the electrical and optical properties for specific applications.

Zinc oxide is a promising material for optoelectronics ^{(144) (145)}, gas/chemical sensors ^{(146) (147)}, data storage ⁽¹⁴⁸⁾, solid state lighting ⁽¹⁴⁹⁾ sources and photovoltaics ⁽¹⁵⁰⁾. It also exhibits unique piezoelectric/electro-optic properties, with the prospective for applications in ultra violet photonic and transparent electronics ⁽¹⁵¹⁾. The major scattering mechanisms that typically govern the electron transport in III-V semiconductors remain true for zinc oxide ⁽¹³⁸⁾. Electron mobility for undoped zinc oxide exhibits grain boundary scattering limitations, whilst doped films encounter intra-grain scattering dominance ^{(45) (152)}.

The morphology of zinc oxide is dependent on deposition type and process conditions, however in its crystalline form can be found in three morphologies, hexagonal wurtzite, cubic rocksalt and cubic zincblende. Wurtzite is commonly produced for transparent conducting oxide applications ^{(153) (154)}. Development of process control is used to manipulate the morphology of the film which can be adjusted preferentially for its application ^{(153) (155)}. As the movement towards the more abundant zinc oxide is prevalent, manufacturing methods need to be able to satisfy demands by improving yields from production and the efficiency of products.

Hu and Gordon ⁽¹¹¹⁾ initially reported fluorine doped zinc oxide (F:ZnO) by atmospheric pressure chemical vapour deposition (APCVD) in 1991. Documented in this paper is F:ZnO with a sheet resistance of $5 \Omega/\square$, ~90% transmission and absorption of ~3% in the visible range. Film roughness was controlled by the deposition temperature and water introduction. The temperature was varied between 350°C to 470°C, with roughness increasing with temperature. The films show a high crystallinity with a preferred orientation of (002). Amorphous solar cells produced from the F:ZnO TCOs showed quantum efficiencies of up to 90%. Critically what was shown by these results was the feasibility of producing a high

efficiency TCO product and the effective fluorine doping of ZnO from APCVD. Following this research little studies have been performed on the combinations of F:ZnO and APCVD.

Fujimura et al ⁽¹⁵³⁾ in 1993 demonstrated the controlled growth of ZnO through the manipulation of the sputtering gas composition during radio frequency magnetron sputtering. Application of this deposition technique enabled the manipulation of the preferred structure from (0001) to (11 $\bar{2}$ 0). Films grown with this preferred orientation exhibited a higher carrier concentration due to an excess of Zn atoms. The proposed growth mechanism was applied effectively to produce epitaxial films.

Haga et al ⁽¹⁵⁶⁾ reported in 2001 doped zinc oxide films using aluminium (Al) and gallium (Ga) deposited via APCVD. These film possessed high conductivity with a lowest resistivity value achieved by Ga doping of $2 \times 10^{-3} \Omega\text{cm}$. A preferred orientation of (002) was shown for Al/Ga doping, with peak intensities reaching a maximum with improved crystallinity. Reduction of this high crystallinity was suggested to increase the resistivity of the films from a decrease in carrier mobility. The best performance film Ga:ZnO, deposited at a temperature of 425°C. Importantly this paper compliments the earlier work of Hu et al ⁽¹¹¹⁾ with approximate deposition temperatures, growth conditions and film properties. Both papers report a preferred (002) with APCVD despite dopant precursor selection. Critically both works show the ability to deposit doped ZnO via APCVD.

Altamirano-Juárez et al ⁽¹⁵⁷⁾ demonstrated in 2004 the deposition of F:ZnO and Al:ZnO deposition using a sol-gel technique. These films exhibited transmission greater than 90% with resistivities between $8.6 \times 10^{-3} \Omega\text{cm}$ to $5.6 \times 10^{-3} \Omega\text{cm}$ in darkness and illumination respectively. Introduction of combined dopants further reduced the resistivity of the films and was achieved with high transmission. F:ZnO and Al:ZnO demonstrated a (002) crystal peak, however with a combination of dopants this peak was reduced with the (100) and (101) peaks prevailing. The durability of the films was assessed for a year and remained stable, although continued durability has not been determined. This paper established the criteria for combined dopant introduction with great success. Sol-gel techniques appeared comparable to APCVD deposition in terms of film properties; however the long term durability has not been determined.

Further Al:ZnO deposition was shown in 2005 by Yoo et al ⁽¹⁵⁰⁾ via RF magnetron sputtering. These films had promising properties for a TCO with a resistivity of $1.9 \times 10^{-4} \Omega\text{cm}$ and

high transmittance, greater than 80% in the visible region. XRD analysis revealed the typical (002) preferred orientation for these films with no other peaks being represented. Surface roughness was shown to increase with argon pressure at the expense of reduced growth rate. To achieve highly textured films, wet chemical post etch regime was applied using dilute hydrochloric acid (HCl). The applied etching regime resulted in a maximum of 70% spectral haze indicating the high scattering properties of the films. AFM analysis confirmed the textured surface of the films, but showed signs of sharp peak features and pitted valleys that introduced problems through further processing. This surface structure would enhance the scattering properties of the film at the expense of electrical defects in a full solar cell construction. The films produced by this technique showed properties comparable to indium doped tin oxide (ITO), however the deposition time was 120mins with completion times extending over several hours.

Bailat et al ⁽¹⁵⁸⁾ demonstrated in 2006 an optimized low pressure chemical vapour deposition (LPCVD) process for ZnO deposition for implementation into microcrystalline solar cells. This achieved cell efficiencies close to 10% through optimization of the ZnO layer. Optimization targeted an increase surface roughness with a decrease the free carriers, which resulted in an increase in current density (I_{sc}) but significantly reduced the fill factor (FF) and open-circuit voltage (V_{oc}). To avoid these decreases, application of a new surface treatment was applied to the ZnO layer. This transformed the V-shaped valleys of the ZnO layer into U-shaped valleys reducing the small sized pyramids and asperities. Resulting from this was a jump in cell efficiency from 3.3% to 9.9% through additional optimization. A balance was found during the post processing of these films to achieve high V_{oc} and FF without reducing the I_{sc} . The treatment time for this process was between 60 to 140 minutes, with immediate improvement shown after 20 minutes of treatment. Critically what was shown by this newly modified ZnO layer was the reduction of cracks and voids that emanate from the V-shape valleys leading to electrical defects. These improvements highlighted a new surface structure to be pursued for enhanced TCO properties in solar cell fabrication.

From 2008 to 2011 several developments were made with zinc oxide from a variety of growth techniques. Calnan et al ⁽¹⁴¹⁾ demonstrated a high deposition rate Al:ZnO via reactive mid-frequency sputtering with yielding rates of 40-115 nm/min, with post HCl etching resulting in μ c-Si:H solar cell efficiency of 8.4%. In 2009 Rozati et al ⁽¹⁵⁹⁾ reported the effects of solution age for F:ZnO spray pyrolysis prepared films. Improvements in film crystallinity,

conductivity and optical properties could be controlled by application of an aged solution. Fay et al ⁽⁶¹⁾ in 2010 demonstrated the effective doping ZnO with boron via LPCVD. Heavily doped boron doped films showed a greater resistance to humidity testing, where by exposure of moisture increased the resistivity of the doped films. Boron doping was shown to offer an alternative dopant source for ZnO films for effective implementation as a TCO layer. Bugnon et al ⁽¹⁰⁸⁾ in 2011 introduced ZnO layers as an intermediate reflector for tandem micromorph solar cells. This utilized the ZnO optimized processed developed at École polytechnique fédérale de Lausanne (EPFL) as shown by Bailat et al ⁽¹⁵⁸⁾. Application of the ZnO layer as an intermediate reflector led to a relative increase in cell performance of 7% compared to a cell without this layer. Issues with shunt resistances and low light yield were encountered with further optimization required.

Zinc oxide films prepared by LPCVD have shown to have a preferred orientation parallel to the substrate plane of $(11\bar{2}0)$. In 2011 Nicolay et al ⁽¹⁰⁹⁾ developed a method for controlling the growth mode of ZnO, resulting in a film developing with a (002) preferred orientation deposited via LPCVD. Introduction of crystal orientations in the axis reported to improve light scattering at larger angles than the state-of-the-art TCOs developed by EPFL. These novel ZnO films were produced by manipulation of the growth conditions and resulted in a comparable FF and V_{oc} to the standard plasma etched ZnO film. The novel films produced a high top cell performance from a layer as low as 250nm thick. Prior to cell construction a $75 \Omega/\square$ was shown for the novel films which is higher than normally required for TCO films, however it did not affect the FF or V_{oc} . It was proposed that the exposure to H_2 plasma during cell construction reduced the resistivity of these films leading to improved cell properties. A consequence of using this novel TCO construction was a decreased current density which was attributed to reflection $\lambda > 650\text{nm}$ due to the intermediate reflector. Further optimization of the micromorph cell was required to suit the new TCO structure. Application of the new structure was proposed to reduce the a-Si:H layer thickness, increasing the resultant stable efficiency. Consideration of the proposed benefits of this structure and the developing TCO requirements, APCVD produced ZnO offered an alternative attractive to LPCVD for TCO production.

2.2 Properties of Thin Films

A transparent conducting oxide (TCOs) is a semiconductor material that is optically transparent to visible light and is critically defined by the band gap energy^{(20) (36) (42) (64) (44) (114) (39) (40) (46) (115)}. These materials exhibit an energy band gap between three to four electron volts which often absorbs in the infra-red region whilst permitting the transmission of visible light. A smaller band gap tends to enhance the conductivity whilst an increased band gap seeks to achieve higher transparency^{(20) (36) (42) (44) (114) (39) (40) (46)}. Conductivity performance of these materials is described by the resistivity, governed by the charge transport properties as; electron effective mass, carrier concentration (quantity of electrons/holes) and charge carrier mobility (flow of electrons/holes)⁽³⁶⁾. Film conductivity can be improved by increasing carrier concentration/mobility through various techniques. Recent focus has been on developing low carrier concentration with high mobility, for improved optical performance^{(64) (39)}. More effective optical transparency range necessitates a large band gap to avoid absorption, which subsequently may reduce the semiconducting properties^{(20) (36)}. Dopant materials may be introduced from various elements to enrich conductivity of the film whilst retaining the beneficial optical properties proffered by the large band gap^{(42) (40)}. Two basic conditions exist that generally defines metal oxide TCO^{(114) (160)};

1. The oxide must have band gap energy above 3.1eV , allow wavelengths of $\geq 400\text{nm}$ with 80% transmission through the film.
2. The metal oxide must be susceptible to degenerate doping (with increasing doping the material begins to act more like a metal than a semiconductor) so that carrier densities of $10^{20} - 10^{21}\text{cm}^{-3}$ can be achieved.

Transparent contacts are required for almost all photovoltaic devices, predominately comprising of transparent conducting oxide. Several key challenges still remain for TCO research and implementation, which will ultimately improve photovoltaic device performance. Transparent contacts are critical for device performance, lifetime and a critical component of nearly all photovoltaic technologies. Optimization of transparent contacts for PV requires high conductivity in correspondence with high transparency. The focus of this research employs a plasma etching technology to optimize the light handling of the TCO. This must be critically achieved without affecting the electrical properties of the film. Growth

techniques in conjunction with post modification enable fine tuning of this layer. Tuning high mobility contacts without excessive carrier concentration is essential for low free carrier absorption⁽³⁹⁾. Application of low cost TCO products is required (raw material and processing) as it contributes to a significant cost of the final photovoltaic device. Production of cheaper devices will aid the uptake in the mass market place. Generation of process stable contacts (thermally and humidity stable material) is required for cell processing and through lifetime operation⁽¹¹⁹⁾. Tailoring the interfacial chemistry and surface topology is required for optimum contact between subsequent deposited layers and increased contact stability.

Edwards et al showed in Figure 2 the relation between electron mobility and densities for a range of materials (metals, semi-metals and semi-conductors) involving a variety of transparent conducting oxide materials⁽⁴²⁾. Observation of the relative positions of these materials shows that they lay between metals and semi-conductors, exposing the unique properties demonstrated by these materials. Explanation of these properties is expressed by the Drude model which describes how a local current density responds to a time-dependant electric field⁽²⁰⁾⁽⁴²⁾⁽³⁹⁾. Drude concludes that an electromagnetic skin depth is developed for the material at a given wavelength of incident radiation. For TCO materials it is found for incident visible light that the skin depth increases in correspondence with the carrier mobility however an increase in carrier density causes a decrease in skin depth⁽²⁰⁾⁽⁴²⁾⁽³⁹⁾.

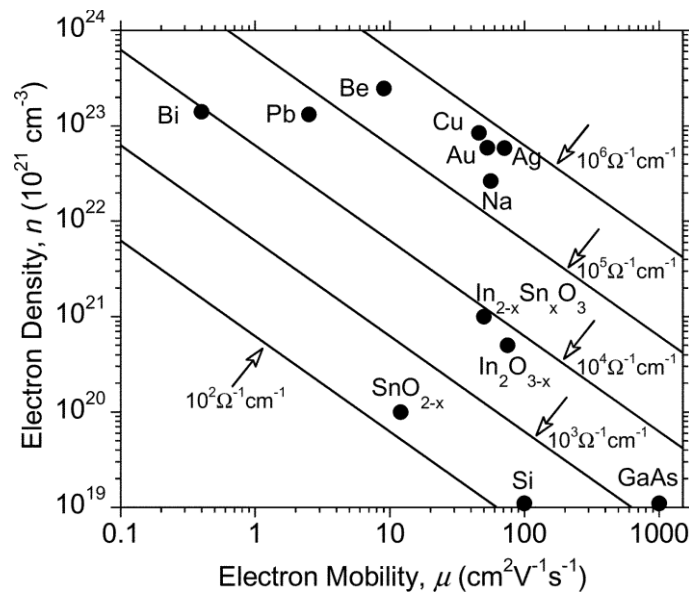


Figure 2 - Comparative electron properties of metals, semi-metals and semi-conductors (42)

Transparent conducting materials have a specific and well defined range of transparency, typically encompassing the visible light from wavelengths $0.4 < \lambda < 0.7\mu\text{m}$ ^{(20) (36) (64)}. The metallic properties of the material causes infra-red light to suffer reflectance and at sufficiently short wavelengths ultra-violet light becomes absorbed within excitations across the energy gap^{(20) (36)}. Introduction of dopants into these materials enable their use as current collectors in solar cell manufacturing^{(161) (143) (162)}.

Transparent conducting oxides (TCO's) contain a metallic & oxygen component. Part *A* can be used to describe the metal (or multiple combinations of metals), and part *B* denotes the non-metal oxygen component. Combination of these materials forms a compound semiconductor A_xB_y with varying optoelectronic properties dependant on composition. Addition of dopant species can be implemented to influence the optoelectronic characteristics. Dopant (*D*) may be a metal, metalloid or non-metal, resulting a material $A_xB_y:D$ ⁽¹⁶³⁾.

Extensive research has been focusing on the discovery of new transparent conducting oxide materials with their relevant dopant compounds^{(42) (23) (39) (40) (163)}. Table 2 is a list of the current TCO materials and associated dopants. Despite a wide scope of materials available for thin film TCO applications, the primary employed materials are four elements; Indium, Tin, Zinc and Cadmium^{(42) (114)}. Due to the hazardous nature of cadmium it is not commonly used. Current Indium prices make it a difficult option for photovoltaic applications despite wide adoption in the display market^{(35) (34)}. Zinc and Tin offer more cost effective solutions for thin film applications and subsequently are under increasing investigation to improve fabrication processes to boost final cell performance^{(64) (44) (38) (87)}.

Material	Dopant or compound
SnO ₂	Sb, F, As, Nb, Ta
In ₂ O ₃	Sn, Ge, Mo, F, Ti, Zr, Hf, Nb, Ta, W, Te
ZnO	Al, Ga, B, In, Y, Sc, F, V, Si, Ge, Ti, Zr, Hf
CdO	In, Sn
ZnO-SnO ₂	Zn ₂ SnO ₄ , ZnSnO ₃
ZnO-In ₂ O ₃	Zn ₂ In ₂ O ₅ , Zn ₃ In ₂ O ₆
In ₂ O ₃ -SnO ₂	In ₄ Sn ₃ O ₁₂
CdO-SnO ₂	Cd ₂ SnO ₄ , CdSnO ₃
CdO-In ₂ O ₃	CdIn ₂ O ₄
MgIn ₂ O ₄	
GaInO ₃ , (Ga, In) ₂ O ₃	Sn, Ge
CdSb ₂ O ₆	Y
ZnO-In ₂ O ₃ -SnO ₂	Zn ₂ In ₂ O ₅ -In ₄ Sn ₃ O ₁₂
CdO-In ₂ O ₃ -SnO ₂	CdIn ₂ O ₄ -Cd ₂ SnO ₄
ZnO-CdO-In ₂ O ₃ -SnO ₂	

Table 2 - Compiled list of TCO's suitable for thin film devices with their corresponding dopant options⁽¹¹⁴⁾

Previously TCO coatings have been produced using spray techniques, pulsed laser deposition and physical vapour deposition^{(36) (40) (67) (119) (164)}. These techniques produce successful film coatings however they are hindered by batch process requirements⁽⁴¹⁾. Scaling coating processes from research to industry requires high throughput mass production capability. Chemical vapour deposition offers the ability to produce such materials on large scale continuous processes^{(41) (165)}. TCOs are employed in a wide array of application from thin film voltaics, flat-panel displays, architectural windows, smart windows and polymer-based electronics^{(166) (167)}. These technologies combine to give a significant market value that encompasses a wide range of products which proves the commercial importance of TCO merchandise^{(42) (166) (167)}. Semiconductor SnO₂ (tin oxide) has been extensively employed into low-E glass for energy conservation due to its durability and excellent optical/electrical properties⁽¹¹⁶⁾. The TCO layer is a vital component of solar cell construction, enabling higher attainable efficiencies of fully constructed cells^{(2) (7) (13) (20) (35) (36) (23) (64) (44)}.

There are several key properties which allow us to characterise TCO films performance. Conductivity and optical transparency are not mutually exclusive properties of TCO's. They require careful manipulation of film parameters to be tailored towards the intended application. Optimization for photovoltaics requires the TCO layer to exhibit high visible transparency and conductivity through increased mobility over carrier concentration^{(36) (42) (39) (46) (65)}.

Exaggeration of one property can counteract the performance in other areas. For example, a film with very high roughness with sharp peak features could improve optical performance; however this may introduce shunt resistance into the film and lower the conductivity of the film through defects^{(20) (63) (42) (44) (114) (39)}. Equally the introduction of excessive dopants to improve conductivity causes an increase in optical absorption due to an increase in carrier concentration^{(36) (44) (38) (39)}.

Several parameters are utilized to describe the relative performance of a TCO material. These are the conductivity (σ), sheet resistance (R_s), free carrier mobility (μ), free carrier density (N) and the imaginary or lossy part of the refractive index termed the extinction coefficient (κ) that is proportional to the absorption coefficient (α) through the wavelength (λ)⁽¹⁶⁸⁾.

$$I = I_0 \exp(-\alpha d) \quad (2.1)$$

$$\alpha = 4\pi\kappa/\lambda \quad (2.2)$$

I_0 – Incident light

I – Transmitted light

d – Material thickness

κ - Extinction coefficient

α - Absorption coefficient

λ - Wavelength

In equation (2.1) I_0 is the incident light intensity upon a material of thickness d , where I is defined as the transmitted intensity through the material ⁽¹⁶⁸⁾. Interpretation of this equation with respects to thin film samples requires consideration of optical scattering and reflection losses at the interfaces. A quantitative measure of a performance for a TCO is described by the ratio of electrical conductivity to the optical absorption coefficient;

$$\frac{\sigma}{\alpha} = 1[R_s \ln(T + R)]^{-1} \quad (2.3)$$

T – Total transmitted light

R – Total reflection of light

Total transmittance T , reflectance R and sheet resistance R_s are the calculated from the physical measured properties of the material ⁽¹⁶⁸⁾. The ratio of equation (2.3) is used to assess the relative performance of various TCO materials and is wavelength dependent. The material properties are all parameters of processing conditions which are determined by the microstructure and defect chemistry of the material ⁽¹⁶⁸⁾. Materials exhibiting high optical scatter due to the presence of polycrystalline grain structure will have diminished transmission and higher resistivity due to a decrease in carrier mobility arising from scattering of charge carriers at grain boundaries ⁽¹⁶⁸⁾. Assessment of equation (2.3) gives a good qualitative estimate of TCO performance for material exhibiting similar microstructure.

Conductivity and optical properties are the main characteristics of TCO's, which are influenced by surface energy, mobility, grain size, light scattering and roughness of the film^{(20) (36) (119) (87)}. Resultant TCO performance for photovoltaics requires a careful balance of conductivity and optical transparency^{(160) (87) (160)}.

2.3 Electrical Properties of TCOs

Transparent conducting oxides are semiconducting oxide exhibiting a wide band gap (E_g). Fundamentally this should be $\geq 3eV$ which defines the low energy/high wavelength limit of optical transparency, enabling transmission of the visible spectrum^{(45) (143) (117)}. Films can be deposited with resistivities in the region of 1 to $5 \times 10^{-4} \Omega\text{cm}$ ⁽⁴⁵⁾, carrier concentration of approximately 10^{20}cm^{-3} ⁽¹¹⁴⁾ and mobility around $30 \text{cm}^2/V_s$ to $60 \text{cm}^2/V_s$ ⁽³⁶⁾. Conductivity is achieved by introducing dopants, oxygen vacancies or by extrinsic dopants, into the grown film which act as free charge carriers^{(114) (39) (45) (46)}. Majority of TCO materials are natively n-type semiconductors⁽³⁶⁾, but recent work intends to produce p-type materials⁽¹⁶⁵⁾. Degenerate n-type semiconductors generally accept intrinsic doping by native donors such as oxygen vacancies and/or interstitial metal atoms⁽¹⁶⁰⁾. Extrinsic doping can be achieved by donor impurities as shown in Table 2. N-type thin film TCO's electrical conductivity depends on the electron density in the conduction band and their mobility.

Sheet resistance is the main characteristic to consider for TCO devices, where properties are specified per application^{(36) (160)}. Typically for photovoltaics a sheet resistance of 10-15 ohm $/\text{cm}^{-2}$ ^{(46) (169) (170) (171) (160)} is utilized, which strikes a balance between electrical and optical performance of the TCO layer. If sheet resistance is lowered by introducing higher levels of charge carrying species (increased doping levels) the conductivity of the film is improved at the expense of greater light absorption (which is wavelength dependant) from the mobile species^{(39) (169) (170) (171)}. Production of high mobility films with reduced carrier concentration has been researched to prevent the adverse effects on optical transparency whilst retaining high conductivity^{(39) (65) (67) (170)}. Mobility is calculated from equation (2. 4) and (2. 5)^{(39) (172) (168)}.

$$\sigma = \mu n e \quad (2.4)$$

$$\mu = \frac{e\tau}{m^*} \quad (2.5)$$

σ - Conductivity

μ - Electron mobility

n - Number density

e - Electron charge

τ - Mean time between collisions

m^* - Effective electron mass

Mean time between collisions and the density follow an inverse relationship resulting in a limited magnitude of the electron mobility. As the density increases the time between collisions is reduced, with a reduction in density increasing time between collisions. A consequence of the wide energy band ($E_g \geq 3\text{eV}$) is that the conduction band cannot be thermally populated at room temperature ($kT \sim 0.03 \text{ eV}$, k is Boltzmann's constant), demonstrating that stoichiometric crystalline TCOs are good insulators^{(42) (173)}. Validation of TCO mechanics encouraged several proposed models for the electron mobility. Electron population of the conduction band was shown to be in conjunction with electronic structure studies, verifying that mobility is proportional to the magnitude of the band gap^{(173) (174)}.

Intrinsic materials have an electron density attributed to the inadvertent introduction of donor centres^{(43) (114) (39)}. These centres are typically recognized as metallic interstitials or oxygen vacancies producing shallow donor or impurity states situated close to the conduction band^{(43) (114) (39)}. The host conduction band may be populated with an excess of donor electrons, being thermally ionized at room temperature⁽⁴³⁾. Experimental determination of the predominant donor type has currently been inconclusive^{(173) (175)}.

Population of the conduction band depends on extrinsic dopants, inadvertently in some cases^{(42) (43) (114) (39)}. Zinc oxide (ZnO) is postulated to contain carrier electrons due to an H^+ donor state from interstitial hydrogen⁽¹⁷⁶⁾. Tin oxides (SnO_2) important factor is portrayed by the

Tin (Sn) in populating the conduction band in addition to the oxygen (O) vacancies^{(20) (114)}. This was verified by the work conducted by Kilic and Zunger⁽¹²⁷⁾. They demonstrated that Sn interstitials and O vacancies dominate the defect structure of SnO₂ due to Sn multi-valence nature. This clarifies SnO₂ nature as a non-stoichiometry material with its corresponding shallow donor levels as an intrinsic n-type semiconductor. Released electrons due to the imposed defects are not compensated for, as the acceptor-like intrinsic defects involving Sn voids and O interstitials do not form spontaneously. These released electrons do not encounter a direct optical transition in the visible range as a consequence of the large gap between the Fermi level and unoccupied first energy level states. Thus giving rise to the SnO₂ characteristics exhibiting a carrier density with minor effects upon its transparency^{(43) (127)}.

Conductivity of TCO's are inherently limited for two main reasons, density and mobility which may not be increased independently at relatively high carrier concentrations^{(42) (43) (39) (40)}. Carrier transport is limited with rising electron density as a consequence of ionized impurity scattering from Coulomb interactions between electrons and ionized donor centres^{(42) (43) (39) (40) (45)}. This source of scattering is inherent with doped materials^{(177) (160) (178)}. Additionally for metal oxides with excessive free carrier, some absorption of the incident radiation by interaction with the electron gas takes place around the characteristic electron plasma frequency^{(160) (168) (179)}. As carrier densities exceed $2 \times 10^{21} \text{cm}^{-3}$, the TCO exhibits a plasma frequency that shifts from absorbing infrared wavelength to visible light, reducing visible wavelength transparency^{(160) (179)}. Following the requirements of transparency in the visible region and the fundamental scattering mechanism an absolute limit for the resistivity of $4 \times 10^{-5} \Omega \text{cm}$ is established^{(177) (160) (178)}. Practically this resistivity limit is not attainable due to additional scattering mechanism from neutral impurities, grain boundaries or other forms of structural disorder which are material dependant^{(160) (180)}. Carrier mobility is hindered by excessive dopant, resulting in a conductivity plateau and optical absorption at the near infra-red edge.

First to document these findings were Bellingham et al⁽¹⁷⁷⁾, expressing the relationship between mobility and resistivity of TCO's (ITO, SnO₂, and ZnO), showing that they are limited by ionized impurity scattering, involving carrier concentrations in excess of 10^{20}cm^{-3} ^{(114) (181)}. Ellmer^{(45) (182)} demonstrated for ZnO that resistivity and mobility were independent of the deposition method and limited respectively to approximately $2 \times 10^{-4} \Omega \cdot \text{cm}$ and $50 \text{cm}^2/\text{Vs}$. ITO experiences a maximum carrier concentration of

approximately $1.5 \times 10^{21} \text{ cm}^{-3}$ incorporating the same conductivity and mobility limitations⁽⁴⁵⁾.

This phenomenon is a universal characteristic within all semiconductors^{(183) (184)}. Scattering by the ionized dopants atoms homogeneously distributed in the semiconductor is one of possible effects for reducing mobility. Recently developed TCO materials, including doped and undoped binary, ternary and quaternary compounds experience these limitations and only in exceptional circumstances have certain samples produced a resistivity $\leq 1 \times 10^{-4} \Omega \cdot \text{cm}$ ^{(42) (43) (39) (40) (45)}. High dopant concentrations could lead to clustering of the dopant ions⁽¹⁸⁵⁾, significantly increasing the scattering rates. This may lead to non-parabolicity in the conduction band, which has to be taken into account in degenerately doped semiconductors containing filled conduction bands⁽¹⁸⁶⁾.

2.3 Optical Properties of TCOs

Effective control of incident light through the TCO layers is critical for high performance photovoltaics^{(36) (114) (39) (40) (45) (46)}. To attain high efficiencies the TCO layer must exhibit high transmission whilst amplifying interaction in the device region without losses^{(160) (114)}. Absorption by interaction, reflection between surfaces, reflection out of the cell and inefficient capturing of specific wavelengths is responsible for efficiency reduction^{(36) (114) (39) (40) (45) (46)}.

Improving light capturing through enhanced TCO scattering whilst retaining high transmission is an important factor for TCO research.^{(36) (38) (46)}. Amorphous silicon solar cells a:Si requires TCOs with large pyramidal structures for increasing scatter performance⁽⁹⁶⁾. Optimization through post treatment processes seek to develop this formation^{(38) (187) (61)}. An issue arising from creating these larger rougher structures is the formation of sharp peaks and troughs^{(87) (112) (158)}. These facets become problematic when subsequent device layers are deposited^{(114) (112) (158)}. Voids can emanate from the sharp peak, evolving into cracks and film defects^{(188) (96) (112) (158)}. Troughs may produce pin holes and incite stresses/cracks into subsequent layers^{(96) (112) (158)}. These defects ultimately result in shunt resistances lowering the performance of the device^{(37) (39)}. Grain size also affects the light scatter and the

transitional ability of the mobile species within the film structure ^{(20) (36) (114)}. Therefore this property directly affects both optical properties and conductivity.

The important optical properties of TCO's are;

- Transmission, T
- Reflection, R
- Absorption, A
- Refraction Index, n
- Extinction Coefficient, k
- Band Gap, E_g
- Geometry

Transmission, reflection and absorption are intrinsic properties of the film dependant on the chemical composition ⁽¹⁷³⁾. They are determined by the resultant four properties refractive index, extinction coefficient, band gap and geometry ^{(189) (190)}. Geometry is an extrinsic property which encompasses the physical attributes of the film, including thickness, uniformity and surface roughness.

Ideally for TCO applications we seek to maximise the electron mobility without increasing the carrier concentration that affects transmission. Effective TCO films require a very low absorption coefficient within the ultra violet, visible and near infra-red regions (UV-VIS-NIR) ^{(20) (36) (114) (39)}. This is attained by effective tailoring of film structure to reduce impurities and promote reduction in grain boundaries. Transmission in the near ultra-violet is limited by the band gap as photons possessing energy greater than the band gap are absorbed ⁽¹⁷³⁾. The secondary transmission edge is encountered around the near infra-red region which as a consequence of reflection at the plasma frequency which can vary with carrier concentration ^{(160) (168) (179)}. Operation of a wide band gap TCO would promote a larger transmission window in the UV-VIS-NIR to effectively reduce absorption; however such a material is not available. Reflection and interference contribute to the optical losses in the material, meaning that 100% transmission of the desired range is not a possibility ⁽¹⁷³⁾.

A negative correlation exists between the carrier density and the relative position of the infra-red absorption edge, however a positive correlation between carrier density and the ultra-

violet absorption edge, as the band gap increases with large carrier densities ⁽¹⁷³⁾. This is known as the Moss Burstein Effect ^{(173) (191)}.

Lewis ⁽¹²⁶⁾ described the nature of dopant materials with respects to Indium doped tin oxide (ITO). Maximization of tin (Sn) incorporation with optimal oxygen substoichiometry is critical for effective TCO applications. Oxygen stoichiometry plays a vital role in minimizing the film resistivity, by both doubly charged oxygen vacancy donating two free electrons. Indium Oxide in its crystalline form with doubly charged vacancies generates an impurity band that overlaps conduction band. This is the formation of a degenerate semiconductor. Compositional impurities from excess charged defects from Sn on an indium or doubly charged oxygen vacancy, decreases the electron mobility through impurity scattering. ITO transparency region is derived from the bandgap (E_g) in the ultra-violet ^{(164) (189) (192)}, up to the infra-red end by the plasma absorption frequency ^{(189) (119)}. Degenerate oxide formation increases the carrier concentration that causes a widening of the E_g as described by the Burstein-Moss effect ⁽¹⁹¹⁾. Plasma absorption frequency also depends on the carrier concentration and effective mass of the carrier ⁽¹²²⁾, which limits the infra-red transparency window. This degenerate band structure ⁽¹⁹³⁾ configuration generates a plasma absorption edge in the infra-red.

The visible range transparency of TCO is affected by the native material optical properties and the substrate employed. Commonly glass substrates have a refractive index around ~ 1.6 and fused silica has a refractive index approximately ~ 1.45 ⁽¹⁷³⁾. Extinction coefficient describes the absorption rate of light in a medium, which for a silica substrate is typically less 10^{-7} meaning any light absorption would occur in the film if $\kappa_{film} > \kappa_{substrate}$ ⁽¹⁷³⁾. Interference bands may be experienced as the film thickness develops beyond 100nm, developing minimum and maximum transmission with thickness and wavelength variation. In terms of TCO development we find a transmission maximum that is equal to the transmission of the substrate as the deposited material is responsible for absorption ⁽¹⁴²⁾. Transmission maximum for substrates in air would be 90% for glass and 95% for fused silica, where by the minimum transmission is determined equation (2. 6) ⁽¹⁷³⁾.

$$T_{min} = \frac{4n^2n_{sub}}{(1 + n^2)(n^2 + n_{sub}^2)} \quad (2.6)$$

T_{min} – Transmission Minimum

n – Refractive Index

Refractive index for most TCO materials resides in the visible range between $n = 1.8 - 2.8$ which gives a minimum transmission within the range of $T_{min} = 0.5 - 0.8$. Minimum transmission may be approximated from equation (2.7)⁽¹⁷³⁾.

$$T_{min} = 0.051n^2 - 0.545n + 1.654 \quad (2.7)$$

In the visible spectrum the refractive index decreases with increasing wavelength and the transmission minimum increases. As the extinction coefficient becomes significant enough to affect the transmission ($T_{maximum} < T_{Substrate}$), the transmission minimum with decrease accordingly.

As the film thickness decreases the transmission will increase, unfortunately the sheet resistance will increase. Combination of the optical and electrical properties of the thin solid film gives us an expression for the proportion of the flux absorbed in a film as shown in equation (2.8).

$$A \cong 1 - e^{\frac{-\alpha}{\sigma R}} \quad (2.8)$$

In Figure 3a the fraction of absorbed power at $\lambda = 400nm$ and $\kappa \sim 0.02$ is represented as a function of the conductivity for multiple sheet resistances. Obtaining a high conductivity value with a corresponding low sheet resistance requires the use of thick films. Implementation of thicker films however results in a reduction in radiated power. Figure 3b demonstrates the conductivity dependence on film thickness for multiple sheet resistance values.

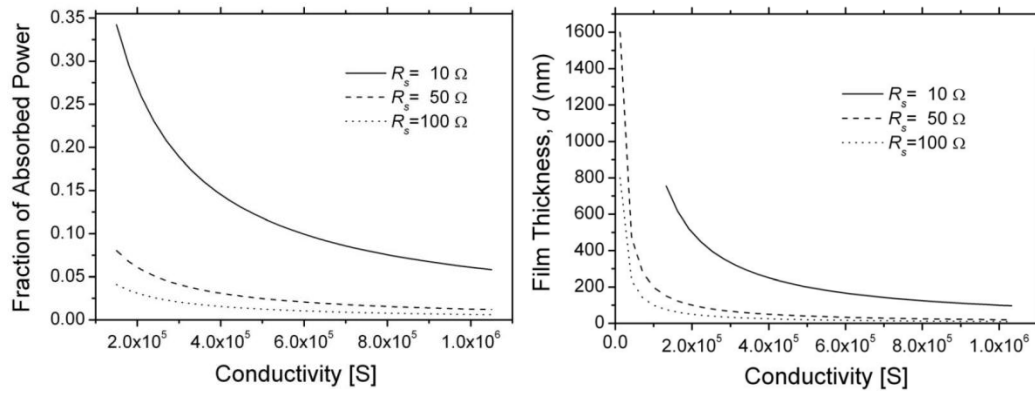


Figure 3 – a) Fraction of absorbed power as a function of TCO conductivity, b) TCO thickness as a function of conductivity⁽¹⁷³⁾

Applications of a film requiring a set conductivity but with minimal sheet resistance will naturally require an increased film thickness. Films with lower extinction coefficient and conductivity can be utilized, permitting the use of thicker films. Combination of film thickness, conductivity and extinction coefficient enables the determination of the absorption of radiative flux. Consequently when the transmission is considered, reflection and interference need to be considered⁽¹⁷³⁾. These parameters are dependent on the refractive index of the film and substrate as well as the film thickness⁽¹⁷³⁾⁽¹⁹⁴⁾.

2.4 Solar Cell Design

Many years of development have seen several designs and configurations being proposed and manufactured. Specific compositions gain advantages in different situations, enabling a diverse array of potential applications. Highest efficiency, size, cosmetics, low light level performance, stability, flexible substrates, environmental conditions etc. all have an effect on which architecture should be employed for a given requirement.

Engineering constraints of the solar cell have posed certain difficulties when designing units. Panels are composed of multiple cells separated by the current collecting tracks. Energy produced in the cells must be effectively collected whilst maintaining a maximum solar active area. These tracks are reduced in size to increase the active solar region of the cell. Optimization must be attained so the neighbouring active region does not short circuit the track. Design of the active solar region must be configured to operate cohesively for maximum efficiency in full solar cell arrays^{(34) (195)}.

For the purposes of this research we are interested in the application of thin film solar cells predominately amorphous based technologies.

2.4.1 Thin-Film Solar Cells *c-Si* & *pc-Si* (Crystalline & Polycrystalline)

Thin-film silicon solar cells have distinct advantages over traditional wafer based crystalline cells⁽³⁴⁾.

1. Silicon thickness can be significantly reduced (to at least 50 μm or even lower⁽¹⁹⁵⁾)
2. Deposition on to low-cost substrates
3. Deposited on to module sized substrates (large area substrates) and in integrally interconnected structures.

Silicon has been exploited in the microelectronic industry for many decades, and recently *pc-Si* (polycrystalline) been fabricated with acceptable efficiencies. Direct deposition of silicon on to glass followed by solid phase crystallization process produced mini module efficiencies with 8%. This technology was developed by Basore and called Crystalline Silicon on Glass (CSG)⁽³⁴⁾. Continuous *poly-Si* films deposited on glass utilized an aluminium induced crystallization technique (Ebil)⁽¹⁹⁶⁾. Yamamoto produced a cell of 10.7% efficiency with a

2 μ m thick cell. The poly-Si films exhibit an average grain size of 10-15 μ m, showing a grain size to thickness ratio of greater than 20.

	Wafers		Thin Film	
Device	<i>c-Si</i>	<i>pc-Si</i>	<i>c-Si</i>	<i>pc-Si</i>
Efficiency (%)	24.7	19.8	8.2	13.7

Table 3 - Best Silicon Solar Cell Efficiencies to Date⁽³⁴⁾

2.4.2 Thin Film Amorphous and Nano Silicon Solar Cells

Amorphous silicon thin film cells typically contain a small percentage of hydrogen for dangling bond passivation to improve material integrity⁽³⁴⁾. These films are commonly fabricated by plasma enhanced chemical vapour deposition (PECVD). Current collection of these cells is optimized through thin *p* & *n* layers and reduced intrinsic intermediate layer. The *p-i-n* structure is able to absorb incident light, however the intrinsic layer suffer light induced degradation. Under illumination of visible light the *Si-H* bonds begin to breakdown, reducing the stabilized efficiency. Controlling this defect may be achieved through reducing the intrinsic layer thickness and operation of multiple junctions⁽¹⁹⁷⁾. Currently the best initial efficiencies that have been reported are 13.7% and 9.8%, these were achieved by triple junction cells and modules respectively⁽¹⁹⁸⁾. Stabilized efficiencies for single junctions still remain low (6 – 7%), however 8 – 10% of the worldwide photovoltaic production incorporates *a-Si* technology⁽³⁴⁾.

2.4.3 Material and Properties

Stemming from the oil crisis of the 1970's R&D on photovoltaic flourished, with numerous thin film PV design concepts being drafted. Carlson and Wronski⁽¹⁹⁹⁾ in 1976 demonstrated the first *a-Si* thin film product⁽³⁴⁾. It took several years to understand the fundamentals of these materials and device properties, not until the 1980's were they introduced into consumer products. The critical problem being inherent defects of the design architecture⁽³⁴⁾. Amorphous silicon is the most studied and applied material for thin-film solar cells. Silicon has a distinct advantage for research purposes, being abundant on earth, permitting rapid development⁽³⁴⁾.

Silicon in its crystalline form has long range atomic ordering; in its amorphous state it exhibits a very short range atomic ordering. Comparatively this extends from a few centimetres in a single crystal of crystalline structure and less than 1nm in the amorphous material ⁽³⁴⁾. Amorphous silicon exhibits a disordered lattice of localised tetrahedral bonding arrangement; however it contains broken *Si-Si* bonds of random orientations ⁽³⁴⁾. These broken/unsaturated bonds are denoted as “dangling bonds”, which add to the defect density of the material. Figure 4 shows the difference in bonding and dangling bonds between crystalline and amorphous silicon. Amorphous silicon material displays a higher absorption coefficient (α) due to this disorder, and requires only a thickness of a few microns to effectively capture the solar spectrum ⁽³⁴⁾. The absorption coefficient is several times that of crystalline silicon and offers an attractive benefit. High localised defect density states are created within the energy gap that causes Fermi level pinning from the disordered structure. As a result of Fermi level pinning the material cannot be effectively doped, as free carriers are trapped by the defects ⁽³⁴⁾.

Passivation of the dangling bonds is an effective method to reduce the effects of Fermi level pinning. Hydrogen is able to penetrate the structure attaching to the available dangling bonds, reducing the density from $\sim 10^{19}$ to $\sim 10^{15} \text{ cm}^{-3}$ ⁽³⁴⁾. Doping is possible with the reduced defect density, being p-type with boron or n-type with phosphorous ⁽³⁴⁾. In n-type doping the Fermi level does not drastically alter from the donor and defect levels due to the relatively high defect density.

Amorphous silicon may be considered as an alloy of silicon with hydrogen. Hydrogen passivation causes a distortion of the bond length and bond angle, which adjusts defect distribution. This results in variation of the optical and electrical properties. Variation of the deposition conditions has shown that hydrogen diluted microcrystalline Si ($\mu\text{c-Si}$) can be obtained that has distinctly different properties ^{(200) (201) (202) (203)}.

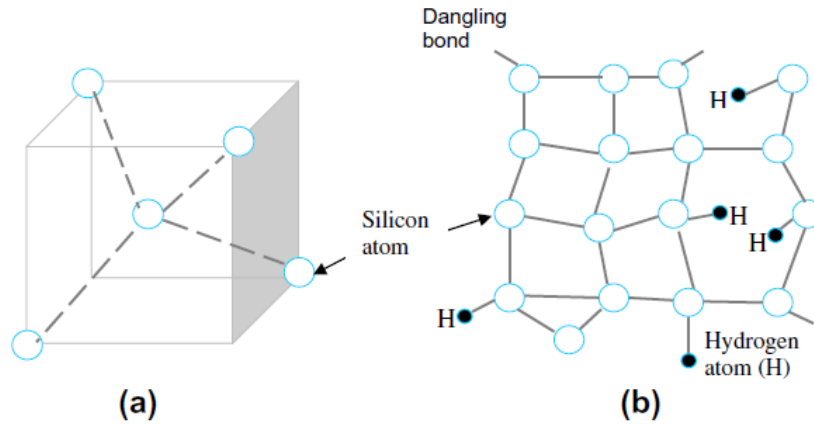


Figure 4 – (a) Tetrahedral *c-Si* Bonding (b) *a-Si* Dangling Bonds with Hydrogen Passivation⁽³⁴⁾

In Figure 5 is the comparison of absorption coefficients of several photovoltaic materials. The absorption bands plateau at low values for *a-Si:H* and $\mu c-Si$ are attributed to the presence of large density mid-gap defects and band-tail states. The absorption coefficient of monocrystalline Si wafers and microcrystalline thin-film Si initially develop equally but $\mu c-Si$ has a higher coefficient for lower wavelengths. The absorption coefficient for $\mu c-Si$ however is lower than *a-Si*, which requires thicker $\mu c-Si$ layers for effective absorption of the solar spectrum compared to *a-Si* as shown in Figure 5. A combined stack of *a-Si* and $\mu c-Si$ layers offers an attractive design for absorbing the most useful part of the spectrum in thin films. This successfully demonstrated by IMT in Neuchatel (Switzerland) followed by several groups developing *a-Si*/ $\mu c-Si$ tandem cells which are often called “micromorph”.

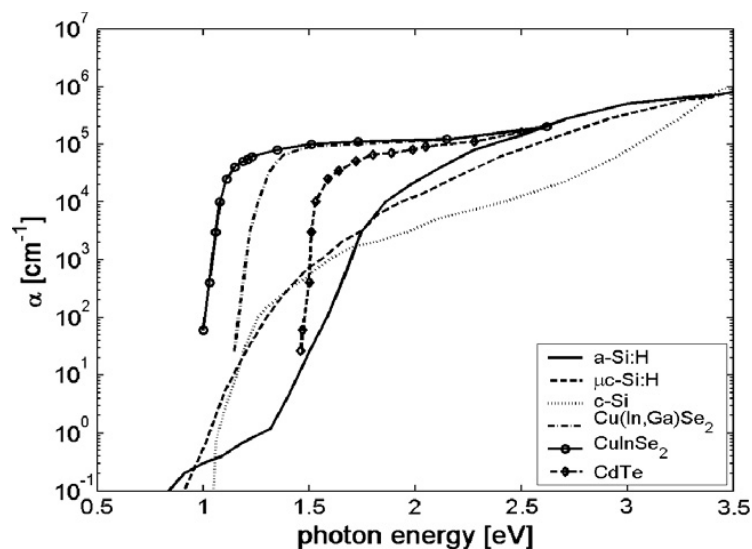


Figure 5 - Optical Absorption (α) Versus Bandgap (E_g) for Multiple Thin Film Solar Cell Materials⁽³⁴⁾.

The bandgap of *a-Si* can be tailored by adding oxygen, carbon and germanium to produce amorphous materials of wider or narrower bandgaps. Doping utilizing carbon and germanium into *a-Si:H* results in bandgaps of 2.2 - 1.1eV, but presents sub-standard electronic properties. Appropriate devices have bandgaps of 2eV (*a-Si:H*) and 1.3 eV (*a-SiGe:H*). Band gaps of multiple materials are shown in Table 4.

Material (Semiconductor/Alloy)	E_g Min (eV)	E_g Max (eV)
<i>c-Si</i>	1.1	1.1
μ c-Si:H	1	1.2
a-Si:H	1.7	1.8
a-SiC:H (20% C)	2	2.2
a-SiGe:H (60% Ge)	1.3	1.7
a-Ge:H	1.1	

Table 4 - Bandgaps of a-Si:H Alloys (Carbon and Germanium in multiple junction configurations)

2.4.4 Amorphous Silicon Solar Cells and Configurations (*a-Si:H*)

Implementation of the conventional *p-n* junction configuration suffers inherent limitations for implementation into *a-Si:H* solar cells. This is due to the larger presence of defect states from dangling bonds that remain despite hydrogen passivation. Introduction of dopants into *a-Si:H* increases the defect concentration, which consequently reduces the average lifetime of free carriers through very high recombination probabilities and low diffusion length of $\sim 0.1\mu\text{m}$ ⁽³⁴⁾. These limitations severely affect device performance and the *p-n* junction is not considered suitable.

The basic structure of an *a-Si* solar cell configuration utilizes the *p-i-n* junction, whereby the intrinsic “*i*” layer is used as the absorber layer. In Figure 6 the device shown is an amorphous single junction in a superstrate configuration, with comparable thicknesses and suggested roughness of each layer being illustrated.

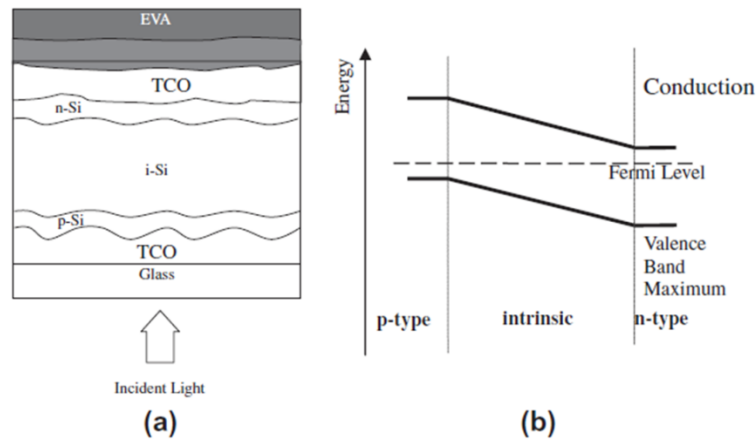


Figure 6 - Single Amorphous Solar Cell Junction ⁽³⁴⁾

This design was introduced in 1976 by Carlson and Wronski ⁽¹⁹⁹⁾, where an intrinsic layer of *a-Si:H* is confined by a *n*-type and *p*-type doped layer of *a-Si:H* or alloy. A consequence of the very short lifetime of carriers in the doped layers, results in no contribution to the photocurrent generated. The photons however are absorbed in the intrinsic layer, adding to the optical losses of the device ⁽³⁴⁾. The *p* and *n* layers develop an electric field across the intrinsic layer. The developing electric field drives photo-generated electrons and holes in the intrinsic layer in opposite directions, with the intrinsic layer effectively becoming the absorber layer ⁽³⁴⁾. Doping concentration of the *p* and *n* layers affects the generated electric field, and defines the thickness of the intrinsic layer. As the *p* and *n* layers do not contribute to the photocurrents and may cause further recombination of the generated carriers before transitioning the layer, it is critical to minimize their thickness ($\sim 10\text{-}30\text{nm}$) ⁽³⁴⁾. The intrinsic layer is limited to a thickness of $\sim 500\text{nm}$ due to charge defects that reduce the effective field ⁽³⁴⁾. Therefore if the width of the intrinsic layer exceeds the space-charge width the device layer would be inactive.

Initial results in the 1970's of the *a-Si* indicated a high potential for attaining efficiencies greater than 10% ⁽³⁴⁾. In subsequent years it was quickly discovered that attaining such efficiencies easily was difficult due to inherent defects. These materials suffered light-dependant degradation that directly affected cell performance under continuous light exposure. This effect was attributed to the Staebler - Wronski effect ⁽²⁰⁴⁾ (SWE). Performance drops were noted of 30-40% over several months, this ultimately stabilized. Cell performance would be significantly lower than 10% which is considered the base efficiency of thin film vacuum-based prepared modules ⁽³⁴⁾.

Light induced degradation was considered to be experienced due to *Si-H* bonds breakdown and increase in the density of dangling bonds through extended light exposure. At this point the device is driven into an excited or higher energy state where active defect centres lead to higher recombination of free carriers reducing efficiency⁽³⁴⁾. Depreciation of the efficiency depends on the illumination level and operation temperature of the cell. Partial recovery of efficiency is possible by reduction of dangling bonds through annealing the device.

Controlling the defect states and dangling bond passivation for effective doping of *a-Si:H* layers is crucial for amorphous solar cell design. SWE cannot be eliminated from *a-Si*, being only reduced through advanced engineering⁽³⁴⁾. Implementation of a thinner intrinsic layer may reduce the effects, but is at the expense of absorption losses. A second problem encountered with the technology is the doping of *a-Si* tends to increase defect density⁽³⁴⁾. Increased defect density increases the recombination effect reducing efficiency, where the layer is limited to ~10-30nm. The limit of each layer thickness has a direct influence on the device structure and therefore the performance stability⁽³⁴⁾.

Amorphous silicon cells have the advantage of being able to be grown in both superstrate and substrate configurations. The *p-i-n* layers are deposited in the corresponding sequence onto a transparent substrate for the superstrate configuration. With the substrate configuration the *p-i-n* layers deposited in corresponding reverse order, and may be deposited on any type of material substrate⁽³⁴⁾. In either device configuration the incident light always enters through the *p*-layer. This is due to the *p*-layer having a higher band gap than *i* and *n* layers. Additionally the mobility of holes is less than the electrons, with a thin front *p*-layer promoting hole collection (Rech and Wagner)⁽³⁴⁾⁽²⁰⁵⁾.

Normally amorphous silicon solar cells are deposited onto glass in the superstrate arrangement, whereby a TCO layer is deposited first as shown in Figure 7. The additional *p-i-n* layers are subsequently deposited onto the TCO layer, followed by a secondary TCO and metallic back reflector⁽³⁴⁾. TCO selection is essential for electrical conduction as well as light trapping in the device. Light trapping is essential for efficient performance of *a-Si* cells where device thickness is limited by several adverse factors (intrinsic layer thickness for reducing light degradation performance issues)⁽³⁴⁾.

A consequence of limiting the intrinsic layer to approximately 300nm is insufficiency to capture a large proportion of the solar spectrum. Strategies to effectively capture and utilize incident photons;

- Implementation of anti-reflection layers through refractive index grading. This allows the entire spectral wavelength in response to the cell ability range to be captured.
- Permitting multiple scattering of light in the device for increased absorption probability.

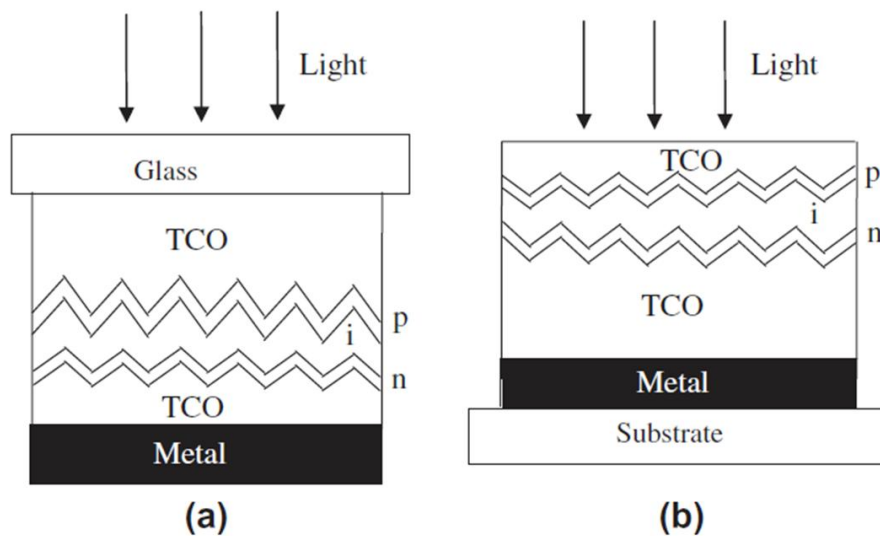


Figure 7 - Amorphous Cell Constructions - Superstrate and Substrate Respectively⁽³⁴⁾

Reflection is reduced by deposition of an anti-reflection coating on the glass to increase light transmission into the device. Further reduction is achieved by suitable surface texturing of the TCO layer with feature sizes comparable to the wavelength of light⁽³⁶⁾. Multiple light scattering is achieved through the involvement of a back reflector⁽³⁶⁾. TCOs commonly adopted are F:SnO₂, Indium doped tin oxide (ITO) and Al:ZnO. The following criteria must be adhered for high performing *a-Si:H* solar cells;

- Glass and front TCO should have high optical transmission over the whole spectral range (>80%).
- TCO with a sheet resistance of approximately 10-15 Ω/□ that is obtained through high mobility opposed to increased carrier concentration. This reduces the free-carrier absorption in the near infra-red.

- TCO layers and doped silicon layers which do not contribute to the photo-generated and collection should be deposited to minimal thickness and have very low absorption coefficients.
- TCO layers should not be degraded by chemical reduction during the subsequent *a-Si:H* deposition.
- Back reflectors exhibit very low optical absorption.

Properties of doped and intrinsic layers have been widely studied, however light trapping through various structures have resulted in recent innovations for improving cell performance⁽³⁶⁾. Device architecture has helped progress *a-Si:H* cells through implementation of multi-junctions/devices, enhancing the stability and efficiency.

2.4.5 Multiple-Junction and Tandem Solar Cells

Degeneracy of performance and stability through light exposure has severely hindered *a-Si* technology. Manipulation of device parameters to minimize these short falls has hindered potential device performance. Light induced degradation has fuelled a body of research developing new architectures to operate within the constraints of the intrinsic layer thickness. Tandem cells engage double and triple junctions executing intrinsic layer thickness of approximately 300nm to avoid the previously described *a-Si* bottlenecks⁽³⁴⁾. A consequence of this advanced design is that single junction *a-Si* are less frequently used and multiple junction solar cells have taken favour, demonstrating improved stabilized efficiency. Single junctions have a stabilized efficiency of 9.3%, whereas double and triple junctions show stabilized efficiency of 12.4% & 13% respectively⁽²⁰⁶⁾.

Currently three designs have evolved for producing multi-junction solar cells;

1. Strictly *a-Si:H* intrinsic layers
2. Combination of *a-Si* and *Ge* alloys junctions
3. Combination of *a-Si* and μc -*Si:H* (*microcrystalline amorphous silicon*)

In the first case Fuji Electric & Co (Japan) and Phototronics (Germany) have developed devices with cell efficiencies ~8.5% and modules ~5.5%^{(34) (207)}.

The second design involves *a:Si* and *Ge* alloys with different bandgap combinations to form tandem junctions. This utilizes a top cell based on 1.7eV *a-Si:H* and a bottom cell of 1.3-1.5eV *a-SiGe:H*. In this configuration United Solar (USSC) produced a triple junction cell of 13% efficiency with a stabilized efficiency of 6.5% on stainless steel ⁽³⁴⁾.

The third design utilizes a combination of *a-Si* and $\mu c-Si:H$ with bandgaps of 1.7eV and 1.1eV respectively. This configuration minimizes the light induced degradation ⁽²⁰⁸⁾ of the cell as only the a-Si is affected. Optimizing layer thickness has helped restrain the effects, with *a-Si* layer being 0.2-0.3 μm and the $\mu c-Si$ approximately 1-2 μm . This design, introduced by the IMT (Neuchatel, Switzerland) and the Kaneka Corporation (Japan), have produced large area modules of $\sim 13.2\%$ being stabilized to $\sim 10\%$ efficiency ⁽³⁴⁾. Yamamoto et al ⁽²⁰⁹⁾ demonstrated a test cell efficiency of 14.7% by exploiting an intermediate TCO reflector enabling advanced light-trapping. Spectral response of the composite bandgaps from *a-Si:H* and $\mu c-Si:H$ enables capturing of a large proportion of the solar spectrum ⁽³⁴⁾. Figure 8 shows the three design architectures of multiple junction configurations.

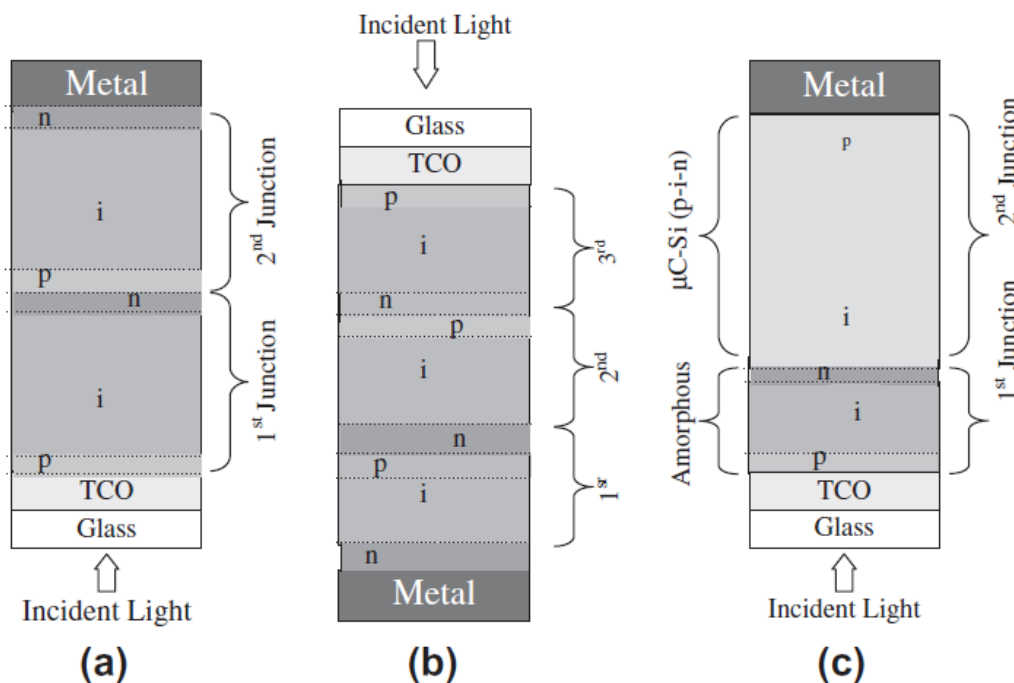


Figure 8 - Design Architecture of Multiple Junction *a:Si* Solar Cells (a) Double Junction “Superstrate” (b) Triple Junction “Substrate” (c) Micromorph “Superstrate” ⁽³⁴⁾

2.5 Photovoltaic Performance Assessment

Solar cell assessment requires the measurement of a range of values under specific conditions to enable comparisons between products and standardization of interpretation⁽²¹⁰⁾. To begin with the illumination for testing must be considered. AM is the air mass index defined as the path length which light takes through the atmosphere normalised to the shortest possible path length⁽²¹¹⁾. This value quantifies the reduction in power of the incident light through absorption effects⁽²¹²⁾. Theta (θ) is the zenith angle of the sun to the earth. AM is calculated from equation (2.9).

$$AM = \frac{1}{\cos\theta} \quad (2.9)$$

AM – Air mass index

θ – Zenith angle

The efficiency of a solar cell is sensitive to the power and incident spectrum of light, which varies throughout the position of the sun. Standardization of the spectrum was agreed upon so that comparative analysis between cell efficiencies can be conducted. AM1.5 was agreed upon for the standard spectrum of light, which gives approximately $1 \text{ kW}/\text{m}^2$ ⁽²¹²⁾.

Several important parameters are used to characterise the solar cell properties. The short-circuit current (I_{sc}), open-voltage (V_{oc}), fill factor (FF) and efficiency are all parameters determined using the IV curve (current-voltage curve)⁽²¹³⁾. The IV curve of a solar cell (Figure 9) is the superposition of the IV curve of the solar cell diode in the dark with the light generated current.

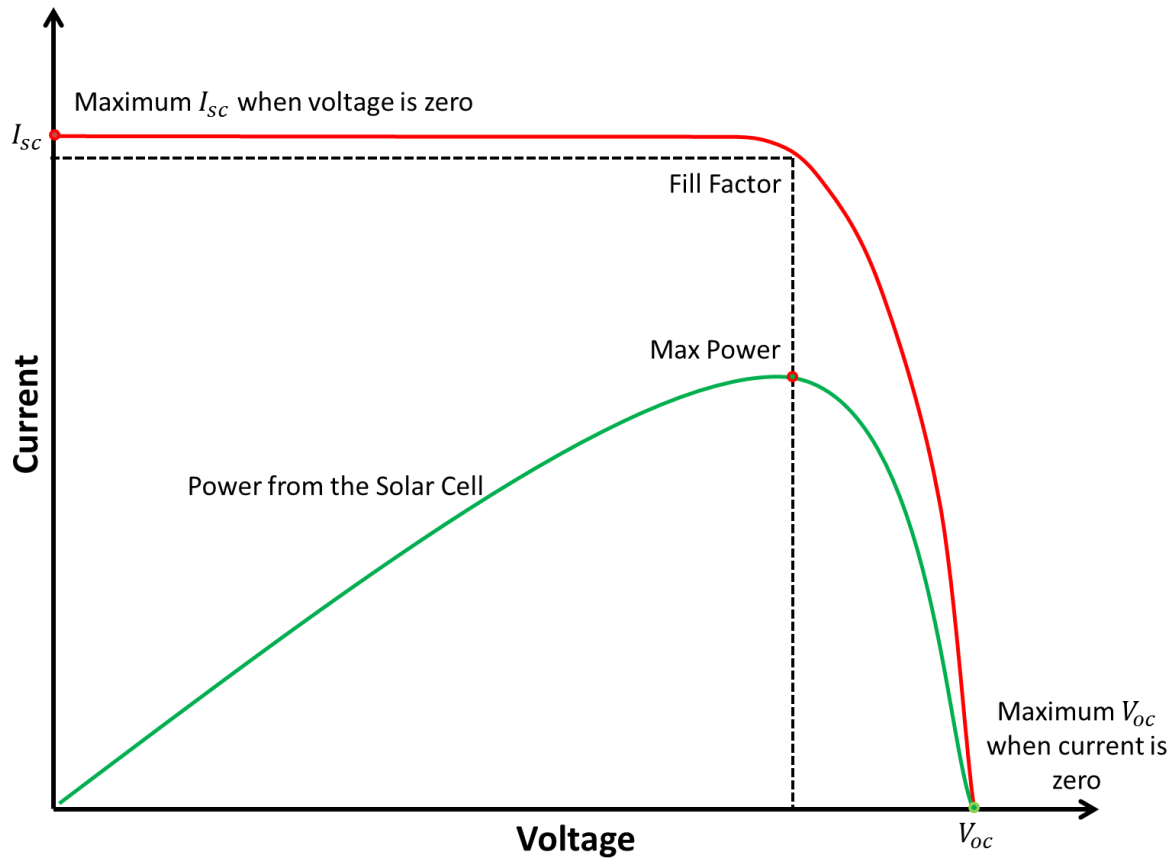


Figure 9 - IV Curve for Ideal Solar Cell ⁽²¹⁴⁾

Short-circuit current is the current through the solar cell when the voltage across the solar cell is zero (essential the cell is short-circuited) ⁽²¹²⁾. This current is due to the generation and collection of light-induced carriers. In ideal solar cells we would hope to generate a short circuit current equal to the light-induced current. Short circuit current is therefore the maximum current that may be drawn from a cell ⁽²¹²⁾.

The short-circuit current is dependent on the solar active area, and it is more common to describe the current density (J_{sc}) of the cell. The short-circuit current depends directly on the illumination intensity, and the spectrum of light (this is standardised to AM1.5) ⁽²¹⁴⁾.

Open-circuit voltage is the maximum voltage available from a solar cell which occurs when the current is zero ⁽²¹⁴⁾. This voltage corresponds to the amount of forward bias on the solar cell due to the bias of the solar cell junction with the light-induced current ^{(213) (214)}. V_{oc} is calculated from equation (2. 10) ⁽²¹²⁾.

$$V_{oc} = \frac{nkT}{q} \ln \left(\frac{I_L}{I_0} + 1 \right) \quad (2.10)$$

I_0 - Light Generated Current

I_L - Dark Saturation Current

V_{oc} depends on the saturation current and light-generated current of the cell ⁽²¹²⁾ ⁽²¹⁴⁾. Typically the short circuit current has small variations, the saturation current is critical as it can vary in orders of magnitude. Saturation current is dependent on the recombination in the device; therefore V_{oc} is a measure of the recombination in the device ⁽²¹²⁾. V_{oc} may also be determined from the carrier concentration given in equation (2.11) ⁽²¹²⁾ ⁽²¹³⁾.

$$V_{oc} = \frac{kT}{q} \ln \left[\frac{(N_A + \Delta n)\Delta n}{n_i^2} \right] \quad (2.11)$$

$\frac{kT}{q}$ – Thermal Voltage

N_A – Doping Concentration

Δn – Excess Carrier Concentration

n_i – Intrinsic Carrier Concentration

I_{sc} & V_{oc} describe the maximum current and voltage produced by a solar cell, however both these parameters are determined with no power generation from the cell. Fill factor in conjunction with I_{sc} & V_{oc} enables determination of the cells maximum power ⁽²¹⁴⁾. Therefore the fill factor is defined as the ratio of the maximum power from the solar cell and the product of I_{sc} & V_{oc} .

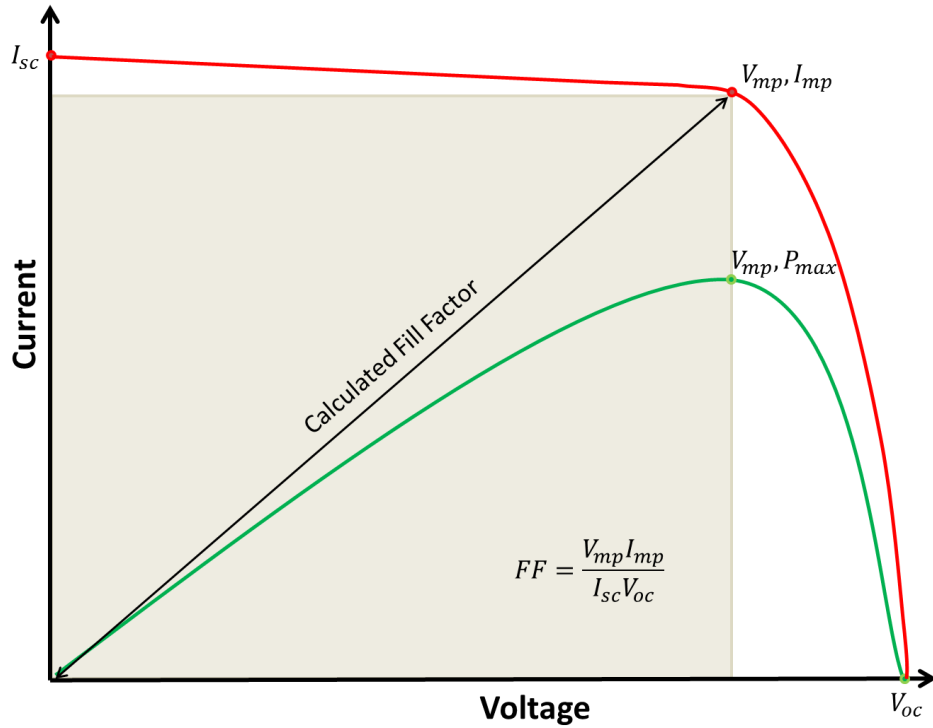


Figure 10 – Calculated Fill Factor ⁽²¹⁴⁾

Fill factor is determined by differentiating the power from the solar cell with respects to the voltage and determining where these equals to zero;

$$\frac{d(IV)}{dV} = 0 \quad (2.12)$$

This enables the determination of the maximum voltage given by equation (2.13) ^{(212) (214)}.

$$V_{MP} = V_{oc} - \frac{nkT}{q} \ln\left(\frac{V_{mp}}{nkT/q} + 1\right) \quad (2.13)$$

This equation only relates to the open voltage to the maximum voltage, implementation of this is required to find the maximum current using the fill factor. Therefore commonly the fill factor is expressed directly as given in equation (2.14) ⁽²¹⁴⁾.

$$FF = \frac{V_{oc} - \ln(V_{oc} + 0.72)}{V_{oc} + 1} \quad (2.14)$$

Where V_{oc} is defined as a normalized V_{oc} ⁽²¹²⁾ ⁽²¹⁴⁾;

$$V_{oc} = \frac{q}{nkT} V_{oc} \quad (2.15)$$

The efficiency is typically used to compare solar cell performance. It is defined as the ratio of energy output of the cell to the energy input from the sun. Efficiency is spectrum and intensity dependent and also dependent on the temperature of the cell. Terrestrial solar cells are measured using AM1.5 at 25°C, and amorphous cells go through a stabilization process to determine their stabilized efficiency. Maximum power of the cell is calculated from (2.16) and the resultant efficiency from equation (2.17) ⁽²¹²⁾.

$$P_{max} = V_{oc} I_{sc} FF \quad (2.16)$$

$$\eta = \frac{V_{oc} I_{sc} FF}{P_{in}} \quad (2.17)$$

P_{max} – Maximum Power

P_{in} – Input Power

η – Efficiency

Quantum efficiency (QE) is the ratio of number of carriers collected by the cell to the number of photons of a given energy incident on the solar cell ⁽²¹⁴⁾. The quantum efficiency is either represented as a function of wavelength or energy. If all photons of a certain wavelength are absorbed and the resulting minority carriers are collected, then the quantum efficiency for the given wavelength is unity ⁽²¹⁴⁾.

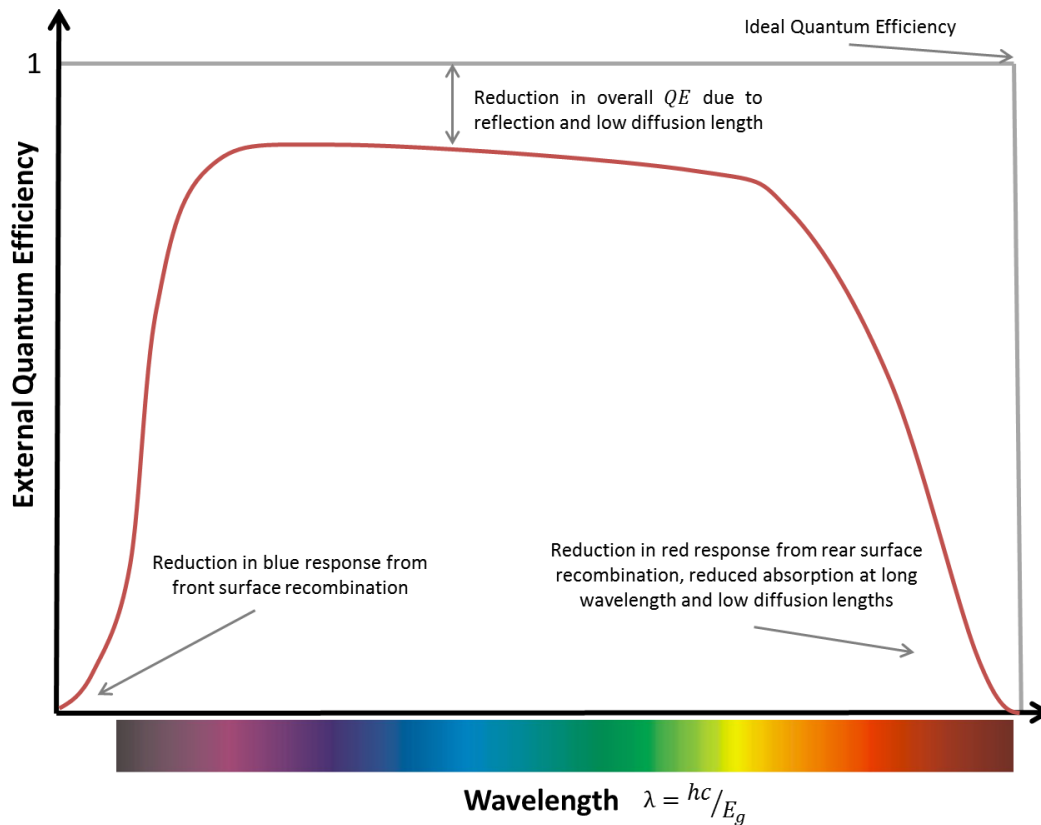


Figure 11 - External Quantum Efficiency, Ideal vs. Calculated

QE is typically reduced in most solar cells due to recombination effects, with the same mechanism that affect collection probability also affecting quantum efficiency⁽²¹²⁾. Front surface passivation affects carriers generated near the surface of the cell. Blue light is absorbed very close to the surface; high front surface recombination will define the lower end of the quantum efficiency⁽²¹⁴⁾. Green light is absorbed in the bulk of the solar cell and a low diffusion length will affect the collection probability, therefore the quantum efficiency for green⁽²¹⁴⁾. The quantum efficiency can be described as the collection probability due to the generation profile of a single wavelength, integrated over the device thickness and normalized to the incident number of photons.

External Quantum Efficiency (EQE), for a solar cell is the ratio of extracted free charge carriers to incident photons⁽²¹²⁾. (EQE) includes the optical losses of the cell. Internal quantum efficiency assesses the quantum efficiency post optical losses. Internal efficiency refers to the efficiency which photons that are not reflected or transmitted out of the cell can generate collectable carriers⁽²¹²⁾. By measuring the reflection and transmission of a device, EQE curve can be corrected to acquire the internal quantum efficiency curve^{(212) (214)}.

3 - Thin Film Deposition Techniques & Processes

Thin films are a continually growing area of research and commercial application. Developments of integrated circuits for micro-electronics has given birth to a whole wealth of thin film technology. Ranging from semiconductors for computing, displays devices (Fluorescent, LCD, LEDs, Plasma, OLED, Electrochromic)^{(20) (180) (215)}, optical coatings (anti-reflective, TCOs)^{(216) (88)} and data storage⁽²¹⁷⁾ (magnetic materials, solid state devices, compact disc, digital versatile video, Blu-ray)^{(218) (216)}.

Thin film technology is tailored to the requirements of the application with consideration of industrial limitations. Suitability of a deposition technique is assessed during research and development processes to not only produce the required materials possessing the desired film characteristics, but explore the possibility of commercial exploitation. Described by Seshan⁽²¹⁸⁾ is that deposition technologies may be classified into four major categories as shown in Table 5. The main process we are concerned with is chemical vapour deposition, an overview of this technique discussed through this section involving the nature of film deposition from nucleation to film development.

Evaporative Methods	
Vacuum Evaporation Conventional vacuum evaporation Electron-beam evaporation	Molecular-beam epitaxy (MBE) Reactive evaporation
Glow Discharge Processes	
Sputtering Diode sputtering Reactive sputtering Bias sputtering (ion plating) Magnetron Sputtering Ion beam deposition Ion beam sputter deposition Reactive ion plating Cluster beam deposition	Plasma Processes Plasma-enhanced CVD Plasma oxidation Plasma anodization Plasma polymerization Plasma nitridation Plasma reduction Microwave ECR plasma CVD Cathodic arc deposition
Gas Phase Chemical Processes	
Chemical Vapor Deposition CVD epitaxy Atmospheric pressure CVD (APCVD) Low pressure CVD (LPCVD) Metalorganic CVD (MOCVD) Photo enhanced CVD (PHCVD) Laser induced CVD (PCVD) Electron enhanced CVD	Thermal Forming Processes Thermal oxidation Thermal nitridation Thermal polymerization Ion implantation
Liquid Phase Chemical Techniques	
Electro Processes Electroplating Electroless plating Electrolytic anodization Chemical reduction plating Chemical displacement plating Electrophoretic deposition	Mechanical Techniques Spray pyrolysis Spray on techniques Spin on techniques Liquid phase epitaxy

Table 5 – Deposition technologies categories ⁽²¹⁸⁾

3.1 Fundamentals of Chemical Vapour Deposition

Chemical vapour deposition (CVD) is a technique capable of depositing highly pure thin films for a wide range of applications^{(219) (41) (220) (221) (222)}. A principal example of CVD materials emanates from the microelectronic semiconductor industry⁽²¹⁸⁾. Other typical examples of CVD deposited materials are metallic films⁽²²³⁾, optical coatings^{(224) (225)}, anti-corrosion⁽²²⁶⁾ and wear resistant films^{(226) (218)}. Deposition typically is achieved from exposure of the substrate surface to the gas flow of decomposed volatile reactant materials. Interacting with the surface, the materials impinge/react and deposits to develop into a film^{(62) (220)}. Growth requires an activation method, with the simplest and common application using thermal energy^{(218) (220)}. Alternative processes can be employed for deposition which supplies the energy for reaction such as combustion^{(227) (218)}, plasma^{(62) (41)} or photo-activated^{(41) (228)}. A further parameter that characterises the process requirements is the pressure regime, normally classified as either atmospheric or low pressure CVD processes^{(41) (218) (220)}. Atmospheric pressure is favoured in certain fields as it offers cost effective and continuous process conditions for high throughput fabrication with the ability for in-situ process control^{(62) (228)}. Alternatively low pressure systems offer the ability to produce high/ultra-pure films for very delicate film structures with the expense of costly vacuum equipment^{(34) (218) (229) (230) (231)}. Figure 12 identifies the classifications of CVD based on reactor design, conditions, precursors and activation method.. Intel semiconductor processes require these conditions for process control, which is reflected in their latest production line in Vietnam costing over \$1 Billion Dollars⁽²³²⁾.

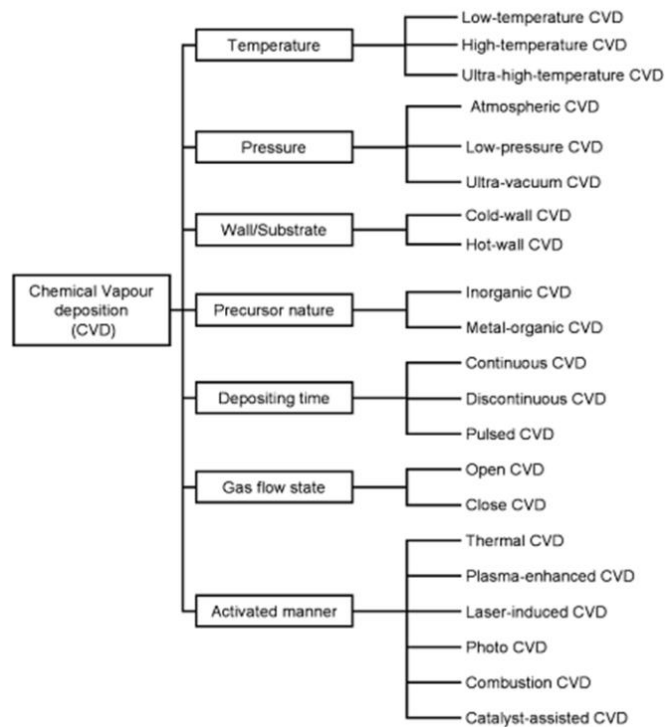


Figure 12 - Classification of CVD Methods ⁽²²⁸⁾

CVD techniques offer multiple advantages compared to other deposition methods. It offers the capability to produce highly pure and dense materials of a uniform composition. This is attained at high deposition rates, offering good adhesion with reproduce results ^{(62) (229)}. As CVD is a non-line of sight process, it offers the possibility for uniform/conformal coating of complex surfaces ⁽²²⁷⁾. Manipulation of process conditions enables control over the crystal structure, surface morphology and orientation ^{(62) (41) (227)}. Considering material requirements, deposition rates can be adjusted to favour growth time or film structure ^{(220) (233)}. CVD is a financially competitive deposition technique due to the nature of coating design, chemical handling and processing steps involved ^{(62) (41) (228)}. It permits high flexibility and offers the use of a wide range of chemical precursors such as halides, hydrides, and organometallics ⁽²²⁷⁾. This enables the deposition of a large spectrum of materials including metals, carbides, nitrides, oxides, sulphides, III-V and II-VI materials ⁽²²⁷⁾. Relatively low deposition temperatures and the desired phases can be deposited at low energies through vapour phase reactions, and nucleation and growth on the substrate surface ^{(218) (226)}. This enables deposition of refractory metals at a small fraction of their melting temperatures ⁽⁴¹⁾.

Chemical vapour deposition is similar to most deposition techniques at a fundamental level, with several key processing steps that define CVD to achieve a film coating. This is

synonymous with many activation methods of CVD, and with alternative deposition techniques. Choy ⁽⁴¹⁾; gave an overview of the key processing steps involved with CVD which is summarized in Figure 13. These denote the steps from specie introduction from the vapour to adsorption and continuous film growth upon the surface.

- Formulation of an active gaseous reactant species.
- Transport of the gaseous species into the reaction chamber.
- Gaseous reactant undergoes gas phase reactions forming intermediate species.
 - High temperatures above the decomposition temperature of intermediate species inside the reactor, homogeneous gas phase reaction can occur where the intermediate species undergo subsequent decomposition and/or chemical reactions forming powders and volatile by-products in the gas phase. The powder will be collected on the substrate surface and may act as crystalline centres and the by-products are transported away from the deposition chamber. The deposited film may have poor adhesion
 - At temperatures below the dissociation of the intermediate phase, diffusion/convection of the intermediate species across the boundary layer (a thin layer close to the substrate surface) occurs. These intermediate species subsequently undergo the following steps.
- Absorption of the gaseous reactants onto the heated substrate and the heterogeneous reaction occurs at the gas-solid interface (i.e. heated surface) which produces the deposit and by-product species.
- The deposits will diffuse along the heated substrate surface forming the crystalline centre and growth of the film.
- Gaseous by-products are removed from the boundary layer through diffusion or convection.
- The unreacted gaseous precursor and by-products will be transported away from the deposition chamber.

Figure 13- Overview of CVD Deposition as Depicted by Choy ⁽⁴¹⁾

Figure 14 describes the multiple processes material atoms/species go through on the substrate surface and gas phase during film development. This is a simplified version of the relevant steps that species may go through during deposition. Figure 15 gives the basic synopsis of chemical processes related to the surface kinetic as the film develops. A more complex overview of the surface kinetics and deposition stages is given in Figure 16.

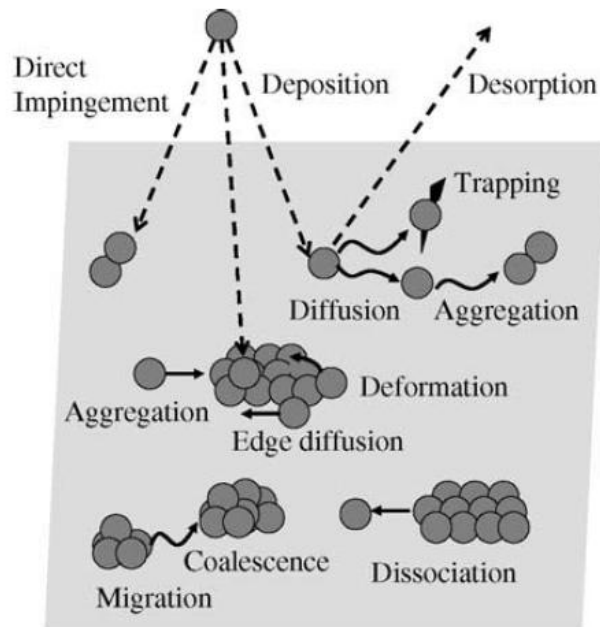


Figure 14 - Schematic illustration of process steps involved in CVD ^{(62) (234)}

These processes have a critical impact on the resultant properties of the deposited material. Variation in growth conditions can influence film characteristics to suit a particular application. For example, dense coatings can be achieved by tailoring heterogeneous reactions at the gas-solid interface ^{(41) (218)}. Porous coatings are developed from homogeneous gas phase reactions ^{(41) (218)}.

$ML_x(g) \rightarrow ML_{x-n}(g) + nL(g)$	Partial decomposition, activation
$ML_{x-n}(g) \rightarrow ML_{x-n}(s)$	Diffusion to surface
$ML_{x-n}(g) \rightarrow ML_{x-n}(s)$	Adsorption
$ML_{x-n}(s) \rightarrow M(s) + (x-n)L(s)$	Surface reaction
$(x-n)L(s) \rightarrow (x-n)L(g)$	Desorption of by products
$M(s) \rightarrow M(l)$	Surface diffusion to lattice site

Figure 15 - Idealised and simplified model of CVD process ⁽⁶²⁾

Precursor materials that are to be employed require careful consideration of the following criteria ⁽²²²⁾ ⁽²²⁷⁾;

- Substance is stable at room temperature.
- Precursors in liquid form should have low vaporisation temperature and high saturated vapour pressure.
- Produce vapour that is stable at a low temperature before decomposition or reacting at a higher temperature within the reaction chamber.
- Possess suitable deposition rates for the intended application.
- Precursors must decompose or react at temperatures which do not destroy or degrade the substrate material.
- Preferentially low hazard chemicals utilized for safe handling and disposal of waste materials/by-products.

Stages of film evolution

Nucleation

- Adsorption of adatoms and IS*
- Development of adatom population
- Migration of adatoms and IS
- Clustering

Crystal Growth

(of individual dispersed crystals on the substrate)

- Migration of adatoms and IS on the substrate
- Self structure diffusion of adatoms
- Monolayer crystal growth
- Adsorption and incorporation segregation of IS
- Formation of SCL**
- Repeated nucleation on SCL

Coalescence

- Sintering – GB*** formation

Complete

- Restructuration by GB migration
- Segregation of IS
- Formation of SCL

Type I - Fast, Liquid-like

- Contraction, free substrate surface area
- Secondary nucleation on free area

Type II – Slow

Incomplete

- GB incorporation
- Impurity coverage of GB

Secondary Nucleation Growth and

Coalescence of Secondary Crystals and Islands

Filling the Channels

- Crystal growth
- Coalescence

Growth of Continuous Film

- Crystal Growth –
(Collective activated nucleation at pure GB-s)
 - Monolayer crystal growth
 - IS incorporation or segregation
 - SCL formation
- Restructuration by GB movement
- Repeated nucleation on SCL

Structural preconditions

Substrate

- Atomic Structure
- Defects
- Chemical Composition
- Homogeneity
- Adsorbed impurity layer

Clusters

- Distribution, number density
- Phase state
- structure
- Orientation

Discrete Single Crystals - Primary Crystals

- Distribution, average distance
- Size
- Orientation
- Surface conditions - SCL

Discrete Single Crystals - Primary Crystals

- Size
- Orientation
- Surface conditions - SCL

Discrete Single Crystals - Secondary Crystals

Polycrystalline Islands

- Orientation of crystals
- GB-s, type, purity
- Surface conditions -SCL

Channels

- Width
- Surface conditions of islands - SCL

Continuous Film

- Crystal orientation
- GB-s, type, purity
- Surface conditions - SCL

Growth Morphology

Grain Size Distribution

Texture

Surface Topography

GB-s type, contamination

Micro Chemistry Phases

Defect Structure

* IS – Impurity species ** SCL – Surface covering layers *** GB – Grain Boundaries

Figure 16 – Deposition processes for film growth ⁽²³⁵⁾

3.2 Mass Transport

Vaporised precursor materials are transported to the reaction chamber by an inert carrier gas. Laminar flow conditions are preferred for precursor transportation to ensure consistent coatings, through uniform gas distribution ^{(62) (222)}. Alternatively, turbulent flow may be encountered. This exhibits irregular conditions and follows unstable circulations in the gas flow with vortices and eddy currents ^{(222) (228)}. In most cases, effort is taken to ensure that flow conditions remain laminar; however realistically this is not always possible thus a certain degree of turbulence may be expected. In certain circumstances turbulent flows may be beneficial to break down the established boundary layer to ensure high growth rates and uniform deposition ⁽²²⁸⁾. An example of this type of system is Pilkington's K-glass lehr coater. This system induced turbulence to combat boundary layer effects that laminar flow cannot penetrate, aiding uniformity and accelerating gas flows to reduce pre-reaction ⁽²³⁶⁾.

Reynolds number R_e is a dimensionless parameter used to interpret the flow conditions of the system. It is calculated from equation (5.3) ^{(62) (227)}.

$$R_e = \frac{\rho UL}{\mu} \quad (3.1)$$

ρ – Density of the gas

U - Average Velocity

L - Length (physical dimension of system)

μ - Viscosity

Alternatively we may determine the flow conditions encountered by calculation of the Knudsen number which is assessed by the pressure of the system and mean free path of the gas molecules.

Knudsen number can be calculated from equation ^{(226) (227)}.

$$K_n = \frac{\lambda}{d} \quad (3.2)$$

K_n - Knudsen Number

λ - Mean free path

d - Diameter of component

It is common to encounter multiple variations in specified numbers for either determination of flow regime. As a rule of thumb guide we can estimate genuine laminar flow to be encountered when $R_e < 10 / K_n < 0.01$ or extremely turbulent conditions when $R_e \gg 1000 / K_n > 1$ ^{(62) (227)}. Unfortunately it is very difficult to assume a transitional period between the two states of flow as gradual progression is noted ^{(220) (227) (237)}.

A further difficulty found in flow condition determination is system dimensions ⁽²²¹⁾. Various gas types and compositions can affect the flow state as suggested by the R_e number. As the gas encounters the reaction chamber the flow conditions change. Knudsen number is critically defined by the system dimensions exemplified in Figure 17;

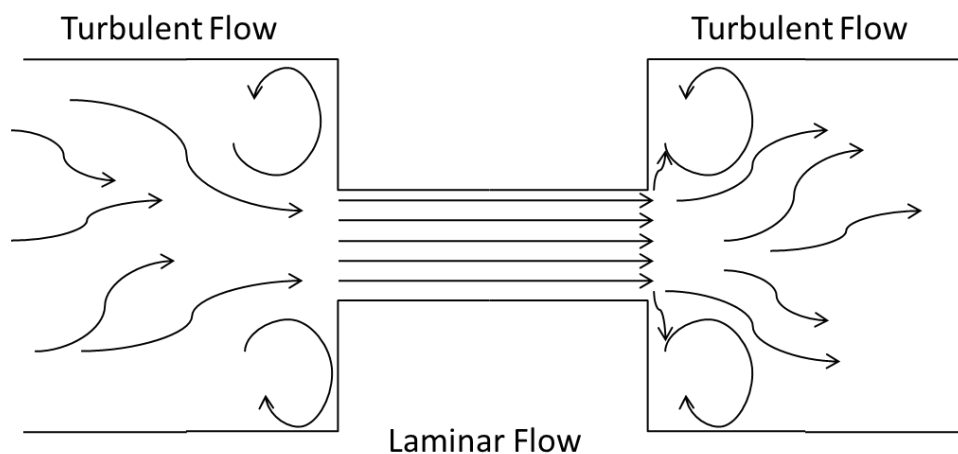


Figure 17 - Examples problem of gas flow entering and leaving pipe dimensions

As represented in Figure 17 the turbulent flow is forced into ordered flow due to the reduced dimensions, however the expansion into the larger dimensions returns the turbulent conditions ⁽²²¹⁾. The reaction chamber is usually much larger than the delivery systems and can pose an issue if strictly laminar flow conditions are required for the deposition. Additionally interaction between gas flow and the system wall produces a boundary layer ⁽⁶²⁾ ⁽⁴¹⁾. Under laminar flow conditions we expect uniformity with a natural development of a velocity distribution in the pipe. Gas flow that interacts with the pipe will suffer a viscous drag effect, which affects only a relatively thin layer in the flow ⁽²²¹⁾. Loss of velocity due to friction extends through the flow resulting in a Poiseuille flow ⁽²²⁶⁾ ⁽²³⁸⁾. The existence of this flow characteristic causes a boundary layer to be formed next to the walls and the substrate surface with a faster stream evolving in the centre of the flow. Figure 18 is a representation of the flow characteristic that establish with a boundary layer.

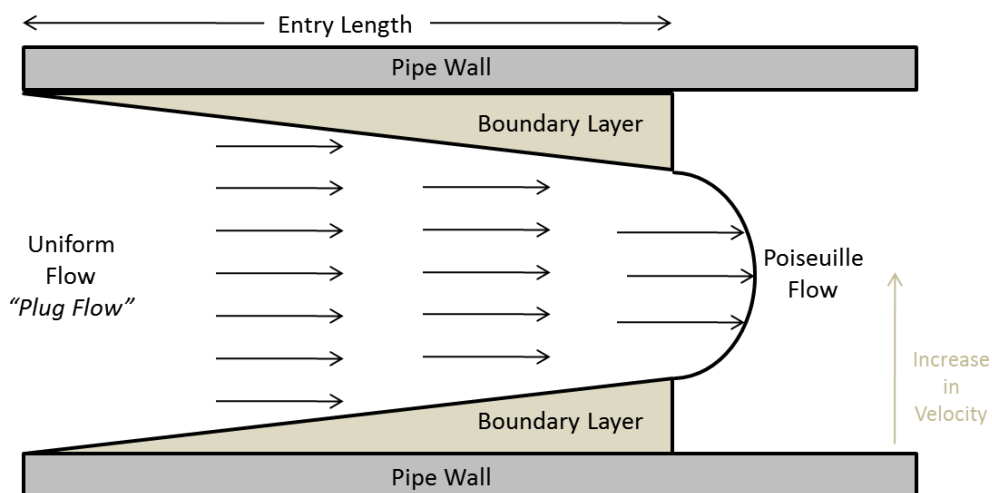


Figure 18 - Boundary layer flow development ⁽⁶²⁾

Gas flow is generally laminar but may be disturbed by convective gas motion becoming turbulent ⁽²²¹⁾. The boundary layer is the region in which the flow velocity increases from zero at the wall to that of the free moving bulk gas ⁽²¹⁹⁾. Entry length defines the depth of the boundary layer and the overall flow conditions at a specific position within the system. Fully developed layers may not be experienced if the entry length is greater than the distance to the reaction chamber.

We encounter two transitional flow types as we pass reactive species through the system to the reaction, convection and diffusion ^{(219) (62) (221)}. Convective flux is encountered whilst the reactants flow through the system under fluid dynamic conditions. When the reactant species reach the impermeable substrate surface no convective flux is encountered due to the boundary layer formation ^{(221) (228)}. Diffusive flux is experienced from the concentration gradient where by species are transported between the surface and gas flow ^{(221) (228)}.

Adsorption and desorption processes occur at the substrate with the deposition of reactants and an increase in by-products left in the concentration gradient of the boundary layer ^{(41) (233)}. Growth rate is therefore dependent upon the rate of diffusion from the free flowing main stream region to the slow moving boundary layer ^{(219) (221)}. Consequently two major limiting factors occur; the growth rate becomes either surface limited or mass transport limited ^{(62) (220)}. Surface limited deposition is suffered when the rate of diffusion is greater than the reactant adsorption rate at the surface ⁽⁴¹⁾. Mass transport limited deposition develops when the adsorption rate is greater than the delivery from the rate of diffusion ⁽⁴¹⁾. Figure 19 shows the two limiting cases for deposition rates which is manipulated by substrate temperature and growth rate.

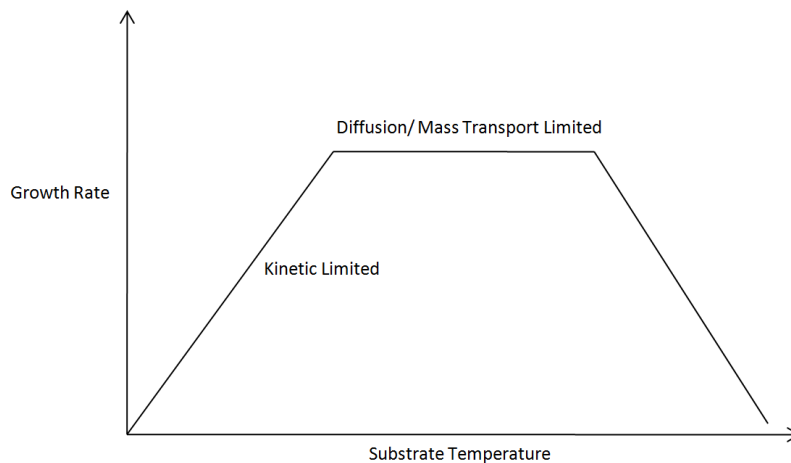


Figure 19 - 'Volcano Curve' depicting deposition limits ⁽⁶²⁾

At low temperatures the molecular reaction at the surface determines the film growth rate. Increasing the temperature incurs a radical change in growth rate which is explained by the

Arrhenius theory of reaction kinetics^{(62) (41) (233)}. Growth rate may be calculated from equation (5.3)^{(41) (233)}.

$$\text{Growth Rate} = A \exp(E_A/RT) \quad (3.3)$$

E_A – Activation Energy

R – Gas Constant

T - Temperature

We reach a plateau region where growth rate is dominated by the supply of molecules delivered to the surface under the diffusion or mass transport limited regime⁽²³³⁾. The regime encountered is determined by the boundary layer conditions and is only slightly influenced by the temperature^{(62) (233)}. Beyond this point the temperature is sufficient to degrade the film and materials explaining the reduction in growth rate⁽⁴¹⁾. Many processes aim to operate in the diffusion/mass transport limited regime as fluctuations in temperature are not as significant to the growth rate as found in the kinetic controlled region^{(62) (41)}.

3.3 Nucleation and Film Growth

Nucleation theories are applied to identify a particular growth mode in the initial stages of deposition^{(239) (234)}. Principally to be able to apply any of these models, identification of surface kinetics is required. Figure 14 represents the main processes active during the initial stages of deposition. Film growth occurs when species adsorb onto the surface (known as adatoms), diffuse, then coalesce to form an island or captured into an existing island^{(219) (41) (239)}. It is important to note that the adsorbed species not only adsorb onto the substrate but also onto the growing islands, this mechanism is known as direct impingement^{(41) (221) (239)}. The substrate can capture diffusing adatoms through surface defects. Importantly islands may migrate across the surface, deform their shape and possibly dissociate^{(220) (234)}. Adsorption of an incident species upon the substrate surface is defined by the probability of the sticking

coefficient (s)⁽²²⁸⁾. It is defined by the ratio of number of atoms adhering to the substrate to the number of atoms arriving^{(239) (240)}.

$$s = \frac{\text{Rate of atoms absorbed}}{\text{Rate of Collision}} \quad (3.4)$$

Conditions of the surface and the reactivity of the impending precursor species have a significant effect over the sticking coefficient^{(241) (240)}. Successful adsorption and desorption is one of the main mechanisms that contribute to conformal coatings of three-dimension substrates^{(41) (233) (239)}.

The incubation period is active during the first instances of growth until continuous growth is assumed⁽²³⁴⁾. During this incubation period deposition is slower compared to continuous growth and develops exponentially with time⁽²³⁴⁾. This implies that the deposited material enhances deposition, which is known as autocatalysis. Mass transport and chemical reactions are the main CVD mechanisms which occur in the vapour phase and film surface^{(219) (221)}. Studies of the incubation period in effect, indicate that the transport processes determine the overall incubation period during deposition^{(227) (234)}.

Surface area energy is always positive with an increase in surface area increasing the energy of the system⁽²²⁷⁾. Homogenous gas phase reactions are hindered by this as the precursor consists of small spherical size particles which exhibit a large surface to volume ratio⁽²⁴¹⁾. The total energy of the particle is broken down into two core components

1. Positive surface free energy - this is equal to $4\pi r^2\gamma$, where r is the radius of the particle and γ is the specific surface free energy.
2. Negative free energy of formation - this is represented by ΔG_V with a volume, V .

The system free energy ΔG is shown by equation (5. 3), which relates the net free energy associated with the formation of a solid spherical cluster^{(219) (226)}.

$$\Delta G = 4\pi r^2 \gamma + \frac{4}{3} \pi r^3 \Delta G_V \quad (3.5)$$

ΔG – Change in free energy

$4\pi r^2 \gamma$ – Free surface energy (Positive)

$\frac{4}{3} \pi r^3 \Delta G_V$ – Volume free energy (Negative)

During the primary stages of deposition the atomic accumulation is much smaller than the surface free energy. The accumulated clusters must reach a critical size before the volume term overcomes the surface term allowing for stable nuclei formation. Beneath a critical radius the nucleus is expected to return to the gas phase. Beyond this once the radius is reached, further growth produces a stable particle from a reduction in the free energy available. This is represented by Figure 20;

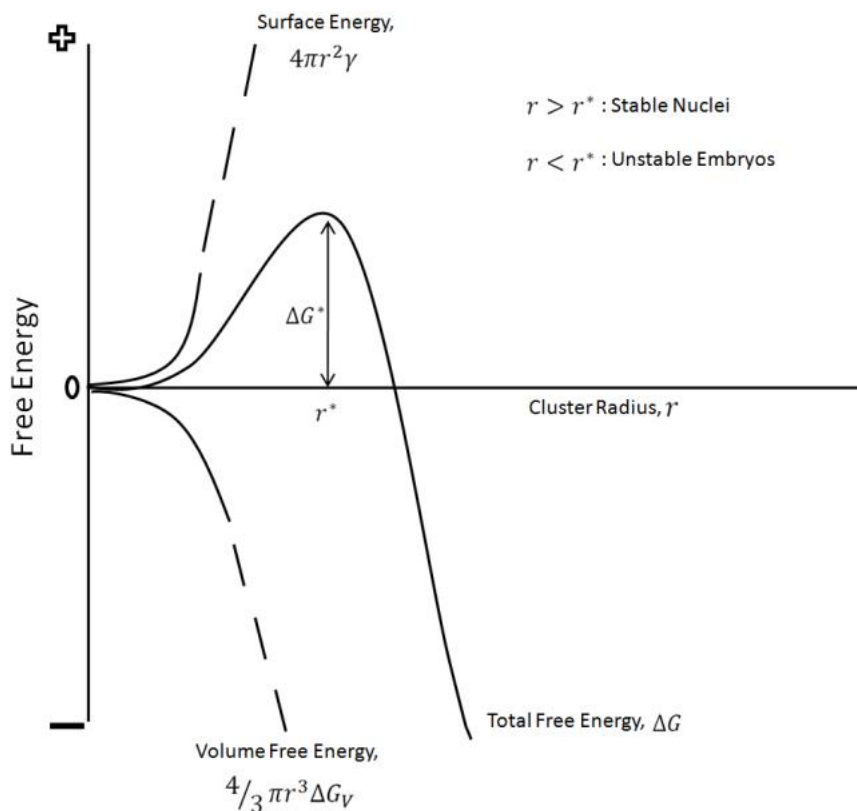


Figure 20 - Free energy against the radius of a spherical nucleus ⁽²²¹⁾ ⁽²²⁶⁾.

Heterogeneous nucleation is supported by the solid substrate surface and promotes a reduction in the total surface energy^{(41) (228)}. Visualisation of the nuclei upon the surface can be assumed to take a domed profile. We encounter a reduction in the critical nucleus size, which catalyses the nucleation process on the substrate⁽²²⁶⁾. Application of contact angles using liquid droplets allows interpretation of the free surface energy⁽²³⁵⁾. Most preferred is where complete wetting of the surface occurs representing a contact angle near to zero⁽²²⁶⁾. Alternatively with a contact angle of up to 180 degrees the substrate contributes nothing to the nucleation process which is comparable to homogenous nucleation. Substrate selection can preferentially affect the film formation through promotion/suppression of heterogeneous nucleation⁽²¹⁸⁾. Three growth modes are used to describe the initial stages of film deposition, Volmer - Weber growth, Frank Van Der Merwe and Stranski – Krastanov^{(235) (221) (222)}.

Volmer - Weber (VW) growth exhibits three dimensional island growth supported by direct nucleation of small clusters to the substrate surface. Island formation occurs from three dimensional expansions of these clusters, resulting in coalescence into a continuous film. We find evidence of this growth mechanism when deposited atoms experience stronger bonding with each other as opposed to the substrate. Two dimensional layer by layer growth is exhibited if the bonds between atoms is less than or equal to that of the substrate. This mechanism is known as Frank Van Der Merwe growth. A third mechanism combines both these mechanism known as Stranski - Krastanov. Initial growth forms one or possibly multiple monolayer's until this two dimensional growth becomes unfavourable, where by three dimensional island growth resumes. Current theory suggests that this mechanism may dominate due to disparity between substrate lattice and the energy within the developing film. Figure 21 highlights the characteristic of each of the growth modes.

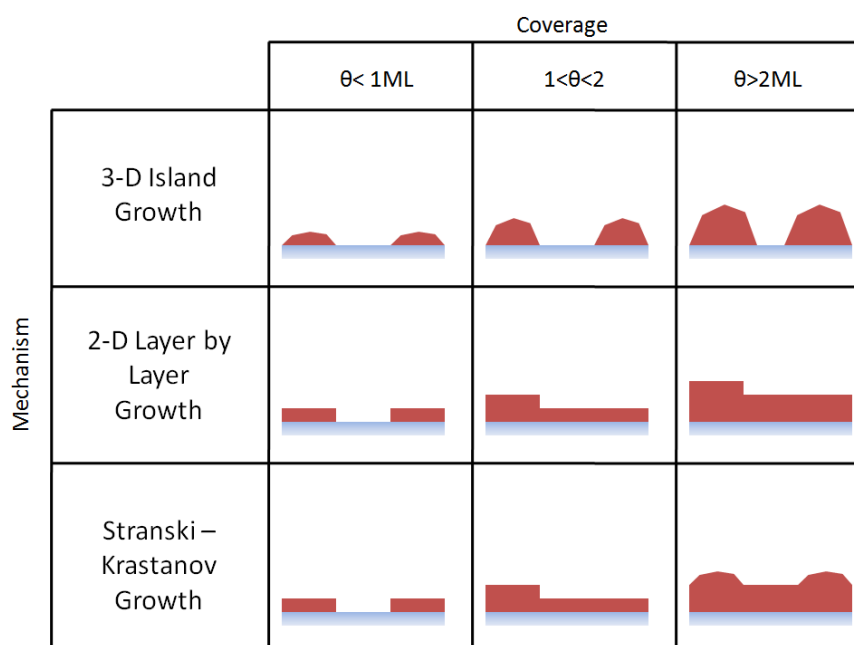


Figure 21 - Schematic representation of growth modes. (θ represents the over layer coverage in monolayer's)
(235) (221) (222) (241)

3.4 Chemical Vapour Deposition Activation Methods

Initiation of the chemical reaction requires an energy source for the deposition to occur. This is known as the activation method for the deposition process. Commonly employed are four main activation methods which are; thermal⁽²²⁸⁾, plasma enhanced^{(242) (243)}, photo-assisted⁽²²⁷⁾ and combustion^{(62) (227)}.

3.4.1 Thermal Activation

Thermal is the most commonly encountered method for activation which initiates the chemical reaction leading to film deposition. This process can operate at atmospheric pressure or reduced pressure dependant on the requirement of the system parameters. Reactor designs fall under the categories of either hot or cold wall design. Cold wall designs have only the substrate heated whilst hot wall reactors have the complete systems at an elevated temperature. Elevated temperatures may be required for certain precursors to maintain them in the vapour phase and reduce the risk of condensation before reaching the reaction zone.

Several methods may be employed for heating the substrate for example; RF heating, Infra-red radiation and Joule resistive heating of the susceptor plate. A range of temperatures from as little as 200°C to in excess of 1500°C are operated for activation. Temperature selection is specific to the precursor material and the process control the user wishes to influence over the resulting deposited film. Unfortunately the elevated temperature range constrains the types of material compositions that can be exploited. Sensitive substrates materials such as plastics have coerced the investigation into alternative activation technique.

3.4.2 Plasma Enhanced Activation

Plasma activation permits growth at significantly reduced temperatures compared to traditional thermally activated sources. Traditional thermally activated methods rely on the substrate to be heated on a susceptor via Joule resistive electronic heating. As the process temperatures are only subjected from the interactions within the activation method, it facilitates the deposition of films upon temperature sensitive substrates. Breakdown for deposition of a combination of material components that may possibly degrade at elevated temperatures is achieved through this method. Additional benefits incorporate reduced energy expenditure and due to energetic charged particle collisions in the plasma, subsidiary effects may take place with metastable species formation, new reaction pathways and production of previously unattainable species (species not found in thermal activation). Reactant species must overcome the activation energy for the reaction to transpire. In spite of this, the presence of charged particles generated by the electric field and the formation of excited species permeating from collisions formulates the possibility of new reaction paths that require reduced activation energy. Consequently reactions develop at lower substrate temperatures or amplified rates for the equivalent temperature.

3.4.3 Photo Assisted Activation

Photo assisted activation seeks to exploit the absorption of incident light to instigate the decomposition or chemical reaction for film deposition. Generally it is found that photo assisted activation encompasses two mechanisms, photo-thermal and photolytic.

Photo-thermal activation is applied for the localised selective heating of a substrate area using a pulsed laser system. Localised surface heating is employed to selectively deposit particular areas of the substrate. The main benefit of this method is that it allows for deposition without bulk material heating. This avoids damage to the material whilst providing a mechanism for deposition through the high transient temperatures available.

Photolytic activation employs ultra violet light for activation. This method induces non-thermal decomposition and the formation of radicals from chemical precursors. Activation via ultra violet lights permits deposition at temperatures lower than those utilized in photo-thermal processing. Contrary to photo-thermal, photolytic activation is administered in the gas vapour phase prior to film growth, which results in non-localised deposition.

3.4.4 Combustion Activation

Combustion activation involves the delivery of precursors in the form of either liquid or gas that are injected into a flame. In the heated environment of the combustion it facilitates the vaporisation, decomposition and chemical reactions. Substrate heating via the susceptor is commonly involved in conjunction with combustion. This allows the successful diffusion/mobility of adsorbed species during deposition. Flames at elevated temperatures promote the homogeneous gas phase reactions and the creation of powders; however reduced temperatures allow the deposition of films.

3.4.5 Typical Deposition System Process

Despite the employed activation method the general principle of deposition remains the same. Figure 22 gives a simple representation of the system involved for CVD.

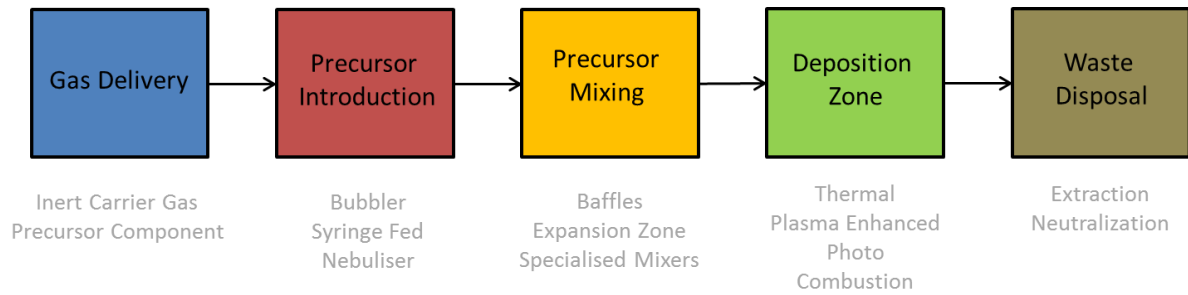


Figure 22 – General System for CVD

4 - Plasma General

4.1 Introduction

Plasma is the fourth state of matter, essentially an ionized gas and constitutes to more than 99% of the universe ⁽²⁴⁴⁾. It comprises of electrons, ions and neutrals which are in fundamental and excited states. Macroscopically the plasma appears to be electrically neutral, closer observation shows that it contains free charge carriers and is electrically conductive ⁽²⁴⁴⁾. Plasmas are created by the application of energy to a gas which consequently reorganises the electronic structure, producing excited species and ions. This induced energy may be invoked thermally, or carried by either an electric current or electromagnetic radiation ^{(245) (244)}. For the purposes of this report we will be mainly discussing electrically induced atmospheric pressure plasmas.

As part of this research we are interested in the etching properties of plasmas. Etching the film topology is achieved by bombarding the surface with ejected particles from the plasma. Two principle processes exist for etching, either sputtering by ion bombardment or chemical interaction ⁽²⁴⁶⁾.

4.2 Fundamentals of Plasmas

4.2.1 Plasma Generation

Plasma's are chemically active medium consisting of ionised gas particles ⁽²⁴⁴⁾. Their classification falls under two categories of cold and thermal plasmas, where each state is dependent on the working power and associated activation method ⁽²⁴⁷⁾. Generated plasmas may exist at low or very high temperatures, which denotes there classification (examples given in Table 8). Encompassing a wide temperature range enables a diverse range of applications for plasma technologies. Typical applications are surface coatings ^{(218) (226)}, waste destruction ^{(244) (246)}, gas treatments ^{(248) (249)}, chemical synthesis ⁽²¹⁶⁾, machining ⁽²²⁶⁾ and many more potential applications ^{(245) (247)}.

Unfortunately not all plasma techniques have been extensively implemented into commercial processes. Further development in plasma technologies will hopefully reduce traditional

methods, imposing cleaner and more efficient industrial processing⁽²⁴⁸⁾. An example of this is described by Roth with regards to the treatment of wool for the dyeing and printing in the clothing industry⁽²¹⁶⁾. Thermal plasmas have found substantial industrial uses predominantly in the aeronautical sector with the application of arc plasmas to weld aerofoil seams⁽²⁴⁵⁾. Generation of cold plasma technologies have increased and adopted into microelectronics manufacturing, however their development has been stunted by the requirement for specialist vacuum equipment^{(246) (248)}. Several research groups are currently trying to transpose the vacuum processes into atmospheric pressure conditions resulting in several successes^{(245) (248)}.

Within the electric field energy is transmitted to the most mobile charged species, the gas electrons. Through collisions the electronic energy is transmitted to the neutral species. This follows probabilistic laws and may be categorized under elastic or inelastic collisions^{(245) (244)}. During elastic collisions the internal energy of the neutral species remains the constant, but encounters a small rise in their kinetic energy. With sufficiently elevated electronic energy, inelastic collisions cause a modification of the electronic structure within neutral species, creating excited species or ions, if the collisions are energetic enough. The majority of excited species have especially short lifetimes and return to the ground state through photon emission^{(245) (247) (244)}. Metastable species are also excited states with prolonged lifetimes due to their decay through radiation emission being impeded due to no allowed transitions departing from the respective state. This denotes that decays may only occur through energy transfers during collisions^{(244) (246)}. Figure 23 shows the constituent parts of the plasma.

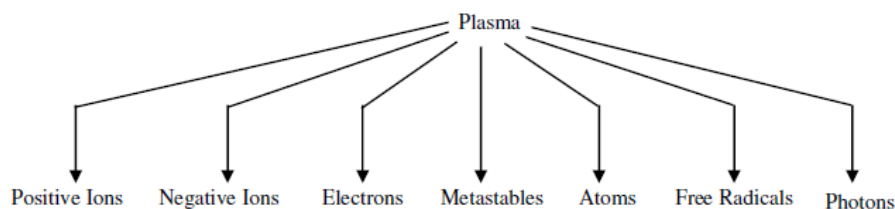


Figure 23 - Constituents of Plasma⁽²⁵⁰⁾

4.2.2 Chemistry of Plasma and Origin of Species

The chemical reactions that take place in a plasma are complex and involve a number of elementary processes⁽²⁵⁰⁾. Reactions within the volume are divided into two categories of homogenous and heterogeneous. Homogenous reactions transpire in the gaseous phase as a result of inelastic collisions between electrons and heavy species. Heterogeneous reactions occur between the plasma species and the solid surface in contact with the plasma. A list of the typical homogenous and heterogeneous reactions has been detailed in Table 6 and Table 7.

Name	Reactions	Description
Excitation of atoms or molecules	$e + A_2 \rightarrow A_2^* + e$ $e + A \rightarrow A^* + e$	Leads to electronically excited state of atoms and molecules by energetic electron impact.
De-excitation	$e + A_2^* \rightarrow A_2 + e + h\nu$	Electronically excited state emits electromagnetic radiations on returning to the ground state.
Ionization	$e + A_2 \rightarrow A_2^+ + e$	Energetic electrons ionize neutral species through electron detachment and positively charged particles are formed.
Dissociation	$e + A_2 \rightarrow 2A + e$	Inelastic electron impact with a molecule causes its dissociation without ions.
Dissociative attachment	$e + A_2 \rightarrow A^+ + A + e$	Negative ions are formed when free electrons attach themselves to neutral species.
Dissociative ionization	$e + A_2 \rightarrow A + e$	Negative ions can also be produced by dissociative ionization reactions.
Volume recombination	$e + A + B \rightarrow A + B$	Loss of charged particles from the plasma by recombination of opposite charges.
Penning dissociation	$M^* + A_2 \rightarrow 2A + M$	Collision of energetic metastable species with neutral leads to ionization or dissociation.
Penning ionization	$M^* + A \rightarrow A^+ + M + e$	
Charge exchange	$A^+ + B \rightarrow B^+ + A$	Transfer of charge from incident ion to the target neutral between two identical or dissimilar partners.
Recombination of ions	$A^- + B^+ \rightarrow AB$	Two colliding ions recombine to form a molecule.
Electron-Ion recombination	$e + A_2^+ + M \rightarrow A_2 + M$	Charge particles are lost from the plasma by recombination of opposite charges.
Ion-ion recombination	$A^+ + B^- + M \rightarrow AB + M$	Ion-ion recombination can take place through three body collisions.

Table 6- List of Gas Phase Reactions Involving Electrons and Heavy Species⁽¹³⁹⁾

Name	Reactions	Description
Etching	$AB + C_{solid} \rightarrow A + BC_{vapour}$	Material erosion.
Adsorption	$M_g + S \rightarrow M_s$ $R_g + S \rightarrow R_s$	Molecules or radicals from a plasma come in contact with a surface exposed to the plasma and are adsorbed on surfaces.
Deposition	$AB \rightarrow A + B_{solid}$	Thin film formation.
Recombination	$S - A + A \rightarrow S + A_2$ $S - R + R_1 \rightarrow S + M$	Atoms or radicals from the plasma can react with the species already adsorbed on the surface to combine and form a compound.
Metastable de-excitation	$S + A^* \rightarrow A$	Excited species on collision with a solid surface return to the ground state.
Sputtering	$S - B + A^+ \rightarrow S^+ + B + A$	Positive ions accelerated from the plasma towards the surface with sufficient energy can remove an atom from the surface.
Polymerization	$R_g + R_s \rightarrow P_s$ $M_g + R_s \rightarrow P_s$	Radicals in the plasma can react with radicals adsorbed on the surface and form polymers.

Table 7 - List of Surface Reactions from Plasma Species ⁽²⁵⁰⁾

4.3 Plasma Classification

We find that depending on the type and amount of energy transmitted to the plasma, the electronic density and temperature properties are defined ⁽²⁴⁵⁾. Therefore we are able to distinguish between plasmas and categorize them based on these two parameters. The categories are represented in the Figure 24 ;

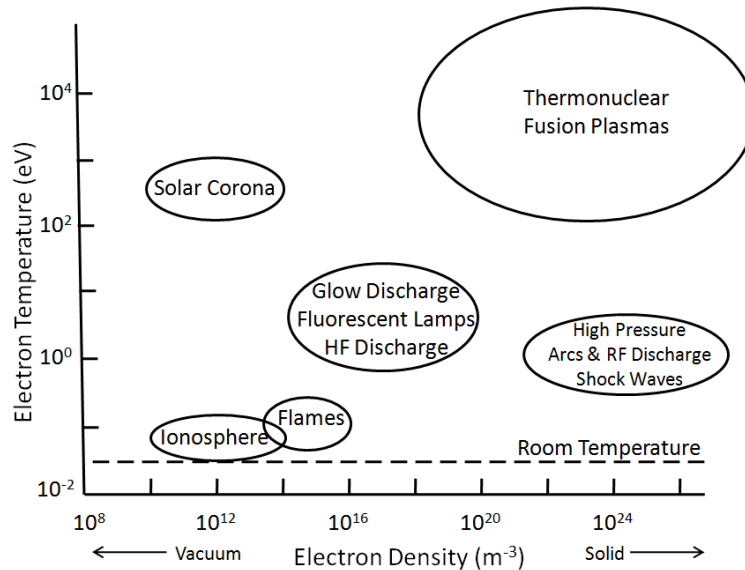


Figure 24 - Classification of plasmas with respects to electron temperature and density ⁽²⁴⁵⁾.

For atmospheric pressure plasmas we generally encounter the glow discharge and arc region ^{(245) (216) (248)}. Within this classification a clear distinction can be made between local thermodynamic equilibrium (LTE) plasmas and non-local thermodynamic equilibrium (non-LTE) ^{(245) (247)}. Consideration of local thermodynamic equilibrium is paramount for the spectroscopic analysis, as plasma parameters (particles distribution functions; electron, excitation, vibration, temperature etc.) enable us to distinguish which state the plasma exist within ^{(245) (246)}.

4.3.1 LTE Plasmas

LTE plasma dictates that transitions and chemical reactions are administered only from collisions, with collision phenomena being micro-reversible ⁽²⁴⁵⁾. This indicates that essentially every collision must be balanced by its inverse; excitation/deexcitation,

ionization/recombination and kinetic balance^{(247) (244)}. A further prerequisite of LTE is that local gradient of plasma properties; temperature, density and thermal conductivity, are small enough to permit a particle within the plasma to achieve equilibrium^{(245) (247)}. This prescribes that the diffusion time is equal or higher than the time required for a particle to equilibrate. Within LTE plasmas, the heavy particles temperature is nearing the electrons temperature^{(245) (247)}. Under the Griem criterion^{(245) (251)}, an optically thin homogeneous plasma is in LTE if the electron density satisfies:

$$n_e = 9.10^{23} \left(\frac{E_{21}}{E_{H^+}} \right)^3 \left(\frac{kT}{E_{H^+}} \right) (m^{-3}) \quad (4.1)$$

E_{21} - Denotes the energy gap between the ground state and the first excited level

E_{H^+} - Equal to 13.58 eV, representing the ionization energy of the hydrogen atom

T - is the plasma temperature

Griem criterion depicts a relationship between the electron density for LTE and the energy of the first excited state. Due to the rigorous nature of LTE, we discover that most plasmas deviate from LTE, notably all types of low density plasma in laboratories.

4.3.2 Non-LTE Plasmas

Digression from LTE plasmas occurs when we diverge from the Boltzmann distribution, representing the density of excited atoms. Certainly for low-lying levels, the electron-induced deexcitation rate of the atom is generally lower than the corresponding electron-induced excitation rate, due to a significant radiative deexcitation rate⁽²⁴⁵⁾. A subsequent digression from LTE ensues from the mass difference between electrons and heavy particles⁽²⁴⁷⁾. Fast and light, these mobile electrons are most likely to govern collisions and transition phenomena; whereas heavy particles are considered static^{(245) (247)}. Strong gradients in the plasma coupled with diffusion effects, further impart the difference from LTE plasmas. Examples of partial LTE distribution have been noted, whereby LTE is verified for the levels close to the ionization threshold, known as pLTE (partial LTE)⁽²⁵²⁾.

Non-LTE plasmas may be depicted by a two-temperature model: an electron temperature (T_e) and a heavy particle temperature (T_h). Plasma temperature is fixed by T_h due to the disparity in electron and heavy particle mass. Further digression from LTE, increases the disparity between T_e and T_h ^{(245) (247) (253)}.

Table 8 highlights the main characteristic between LTE and non-LTE plasma.

	LTE plasmas	Non-LTE plasmas
Current name	Thermal plasmas	Cold plasmas
Properties	$T_e = T_h$ High electron density: $10^{21} - 10^{26} \text{ m}^{-3}$ Inelastic collisions between electrons and heavy particles create the plasma reactive species whereas elastic collisions heat the heavy particles (the electrons energy is thus consumed)	$T_e \gg T_h$ Lower electron density: $< 10^{19} \text{ m}^{-3}$ Inelastic collisions between electrons and heavy particles induce the plasma chemistry. Heavy particles are slightly heated by a few elastic collisions (that is why the electrons energy remain§ very high)
Examples [117]	Arc plasma (core) $T_e = T_h \approx 10,000 \text{ K}$	Glow discharges $T_e \approx 10,000 - 100,000 \text{ K}$ $T_h \approx 300 - 1000 \text{ K}$

Table 8 - Main characteristics of LTE and Non-LTE plasma ⁽²⁴⁵⁾

4.4 Atmospheric Pressure Plasmas

Low pressure regimes between 10^{-4} to 10^{-2} kPa form non-LTE plasmas ⁽²⁴⁵⁾, consisting of an elevated electron temperature compared to the heavy particle ⁽²⁴⁷⁾. Inelastic collisions involving the electrons and heavy particles are excitative or ionizing; however they do not elevate the heavy particles temperature. Coinciding with ascending pressure is an intensification of collisions, inducing plasma chemistry through inelastic collisions and heavy particle heating during elastic collisions. Reduction in the disparity between T_e and T_h causes the plasma to tend towards but does not achieve LTE ^{(245) (247) (244)}. Considerable gradients

within the plasma properties prohibit a particles movement through the discharge, denying equilibrium.

The plasma state, either LTE or non-LTE, is influenced by the density of the feeding power. High power densities induce LTE plasmas such as arc plasma, where low density power or pulsed power supplies produces non-LTE plasmas. Equilibrium is disrupted using short pulse cycles in pulsed supplies, preventing it being achieved ^{(245) (247) (244)}.

Operating at atmospheric pressure, a remote dielectric barrier discharge (DBD) ^{(245) (247)} is employed to establish the plasma. This enables the film surface to be remotely etched by the plasma afterglow. This favourable technique does not require a complex reactor design, allowing the process to be operated in situ with deposition ⁽²¹⁶⁾. Benefits of this configuration stem from its simple sample exposure which incorporates low surface charging effects, multiple gas operation and without the requirement of vacuum equipment ^{(216) (248)}.

Corona discharge is a non-LTE discharge exhibiting low current density ⁽²⁴⁵⁾. Coronal discharge may be attained by applying a pulsed DC power supply to the cathode wire and anode, whereby the anode is the surface under treatment ⁽²⁴⁷⁾. This is portrayed in Figure 25,

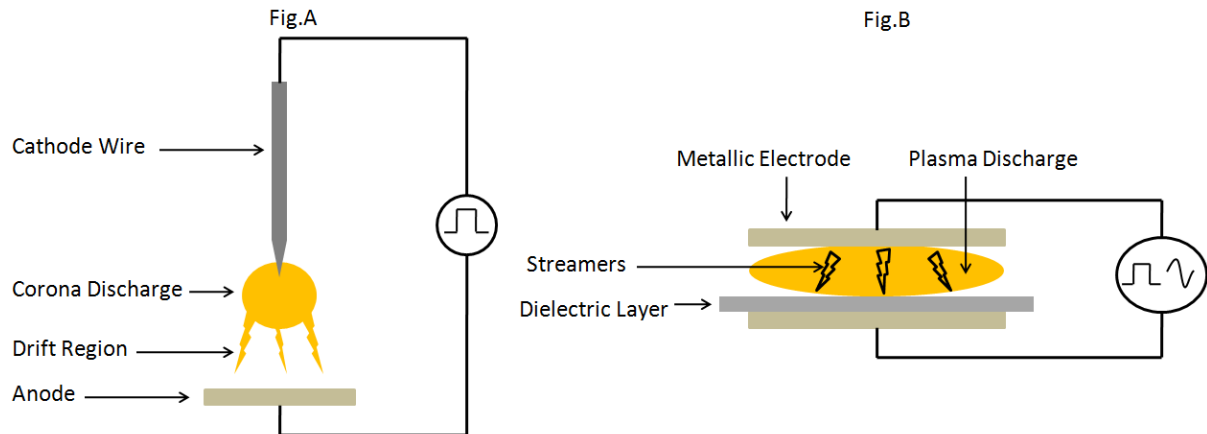


Figure 25 – Fig. A – Principle of a corona discharge & Fig. B - Principle of a dielectric barrier discharge.

The plasma generates a lightning “crown” within the gap, (crown hence corona, distinguished by the shape of generated plasma) ⁽²⁴⁷⁾. Application of a high negative voltage to the wire generates a negative corona discharge. Under this regime positive ions are

accelerated towards the wire, liberating secondary electrons that accelerate into the plasma. This produces a moving front of high-energy electrons (up to 10eV), tracked by a tail of lower energy electrons called streamers (approximately 1eV) ⁽²⁴⁵⁾. Inelastic collisions involving the high energy electrons and heavy particles induce the formation of chemically reactive species ⁽²⁴⁴⁾. Pulse duration in the plasma is shorter than the time required for arc creation. As each pulse ends the discharge extinguishes, preventing the plasma from becoming too conductive, avoiding the transition into a spark. This process involves a very low current discharge from 10^{-10} to 10^{-5} amps ^{(245) (254)}.

Positive corona may also be established; as in this case the wire acts as the anode ⁽²⁵⁴⁾. A shortcoming of corona discharge is the size of the plasma volume, which is minute allowing for only small surface areas for treatment ⁽²⁴⁵⁾. Multiple electrodes may be implemented for large scale coverage, but this can lead to non-uniform interaction on the sample surface. Circumventing the issues involving treatment area, the wire can be replaced with a planar electrode ⁽²⁴⁷⁾. Planar electrodes are set up parallel to the treated surface generating micro arcs perpendicular to the gap between the electrodes ⁽²⁴⁸⁾. Streamers initiate from the same place on the electrode, causing a non-homogeneous treatment on the material surface ^{(245) (248)}. The dielectric barrier discharge configuration was developed to overcome these issues in surface treatment ^{(245) (247) (248) (254)}.

The dielectric barrier discharge (DBD) comprises of a unique electrode construction, generally existing in a plane parallel configuration shielded by a dielectric layer ⁽²⁴⁵⁾. A dielectric medium is one which is non-conductive however is polarised in an electric field. This property is particularly useful for plasma generation, as gaseous breakdown may be established without developing an arc transition ⁽²⁴⁵⁾. Originally the use of this configuration was investigated for the creation of ozone for water treatment, and remains its primary application ^{(255) (256) (257)}.

Multiple electrode configurations may be created with singular dielectrics, two dielectrics & geometries. Working gas flows through the electrode separation, where the discharge is established. Separation of the electrodes is only permitted up to several millimetres to ensure a stable discharge ^{(245) (256)}. Ignition of the plasma discharge utilizes either a sinusoidal or

pulsed power supply (sinusoidal may also be pulsed) which are encapsulated by the two categories of wave form control and temporal^{(258) (259) (260)}. Typically the AC voltage applied for discharge is sustained at frequency between 500 Hz – 30 kHz^{(216) (256)}. DC supplies cannot be used in the DBD configurations, as it cannot dissipate charge accumulation to sustain the plasma⁽²⁵⁸⁾. Dielectric barriers are generally made from glass, quartz, ceramics or polymers; materials which exhibit a low dielectric loss and high breakdown strength⁽²⁵⁶⁾.

Plasmas developed in DBD's may form either a filamentary or glow discharge. The condition is dependent and manipulated by the gas composition, the voltage and frequency excitation^{(256) (257) (258)}. Filamentary discharges form on the dielectric layer surface, resulting from micro discharges or streamers. Glow discharge can be established by alteration of the working powers and frequencies or variation in plasma gas composition. Helium is usually employed to establish a glow discharge as it readily breaks down at modest frequencies, promoting a stable discharge reducing the filamentary aspects formed in the plasma⁽²⁵⁷⁾. DBD may be operated using an array of gases typically involving helium, nitrogen or argon under static or flowing regimes^{(255) (258)}. Design of the barrier may consist of one or both electrodes being covered by the dielectric material⁽²⁶¹⁾. Dual coverage of the electrodes reduces the prospect of streamer formation under atmospheric pressure conditions. Further reduction of streamer formation is typically achieved by increasing the working frequency of the plasma⁽²⁵⁸⁾. With higher frequencies of applied power ranging into the microwave region, streamers can be considerably diminished which enables the generation of a glow discharge for most molecular gases⁽²⁵⁸⁾.

Filamentary discharges are initiated when the application of a high voltage is applied between the electrodes^{(256) (262)}. The applied electric field upon the gas in the gap is equal or greater than its breakdown strength. Atmospheric pressure breakdown of gasses is initiated in a large number of independent current filaments, commonly called micro-discharges^{(256) (263)}. Electron emission from the dielectric surface is stimulated by the UV photoemission, are accelerated in the electric field to energies equal or greater than the ionization energy of the neutral gas⁽²⁶²⁾. Micro-discharges are formed by channel streamers exhibiting a complex

dynamic structure, repeatedly striking the same position until the polarity of the applied voltage is changed⁽²⁵⁶⁾.

As electrons strike the neutral gas this creates an electron avalanche as electron numbers double per ionization collision. The high mobility of the electrons compared to the ions means that they are able to migrate across the gap in nanoseconds. Remaining are the slower ions and other generated species that may go through additional chemical reactions. As electrons accumulate on the opposing electrode, they spread out over the insulating medium and counteract the positive charge on the instantaneous anode^{(256) (262)}. The electric field is reduced around the filaments due to the remaining ions in the gap, which extinguishes further ionization. Conductive channels are established in the gap to the dielectric surface. Electron accumulation prevents new avalanches and streamers from being created. When the polarity is reversed the electron accumulation facilitates new avalanches and streamers, and the process resumes again until the next polarity reversal^{(256) (262)}.

Ignition voltage of micro-discharges is only slightly higher from its extinction level. A consequence of this short lived current within micro-discharges leads to low heat dissipation and the DBD plasma remains strongly non-thermal⁽²⁵⁶⁾. At atmospheric pressure a cold discharge typically contains multiple micro-discharges with a radius within the order of 100 μ m. It will only remain a cold plasma if the current is limited in intensity, which the dielectrics permit⁽²⁶⁴⁾. The memory effect is noted as the sites where discharges emanate on the dielectric from residual charge after the initial discharge⁽²⁵⁸⁾. Dielectrics disperse the micro-discharge across the entire surface, limiting the amount of charge and energy deposited per discharge⁽²⁵⁸⁾.

Under specific conditions we are able to establish a diffuse glow discharge, which has a primary application for uniform surface treatment⁽²⁶⁵⁾. Atmospheric pressure glow discharges (APGD) have been significantly investigated by Donohoe in 1976 using pulsed excitation in helium/ethylene mixtures^{(265) (266)}. In 1987 Okazaki et al developed barrier discharges utilizing 50Hz sinusoidal A.C voltage. Implementing an electrode formed of metal foils and metal mesh with ceramic dielectrics, they were able to establish glow discharge with helium, nitrogen, air, oxygen and argon without organic admixtures^{(265) (267) (268)}. Massines et al

investigated the glow discharge using helium and nitrogen, and subsequently contributed to the better understanding of APGD⁽²⁶⁵⁾. The generation of stable diffuse barrier discharges at atmospheric pressure requires conditions that are significantly determined by the properties of the feed gas⁽²⁶⁵⁾.

Importantly for diffuse discharges is effective pre-ionization, Penning ionization via metastables and primary ionization at low electric field⁽²⁶⁵⁾. Diffuse discharges are sensitive to impurities, admixtures, metastables and residual ions. Densities of residual species remaining from the previous half period cycle are able to initiate the diffuse discharge for the subsequent half cycle. Therefore the feeding voltage frequency has a significant effect on the transition into a diffuse discharge⁽²⁶⁵⁾⁽²⁶⁹⁾. Certain dielectric materials are able to accumulate significant charges uniformly distributed on the surface, which are released during polarity switching, initiating diffuse discharge⁽²⁶⁵⁾. Diffuse discharges can be easily maintained using helium, neon and nitrogen.

Massines et al in their 2005 paper⁽²⁷⁰⁾ discusses the nature of discharges utilizing various atmospheres. The paper is centered on the electrical characteristic of homogenous discharge of helium, argon and nitrogen, and the exhibited regime. Figure 26 shows the typical voltage-current characteristics expected for low temperature DBD discharges.

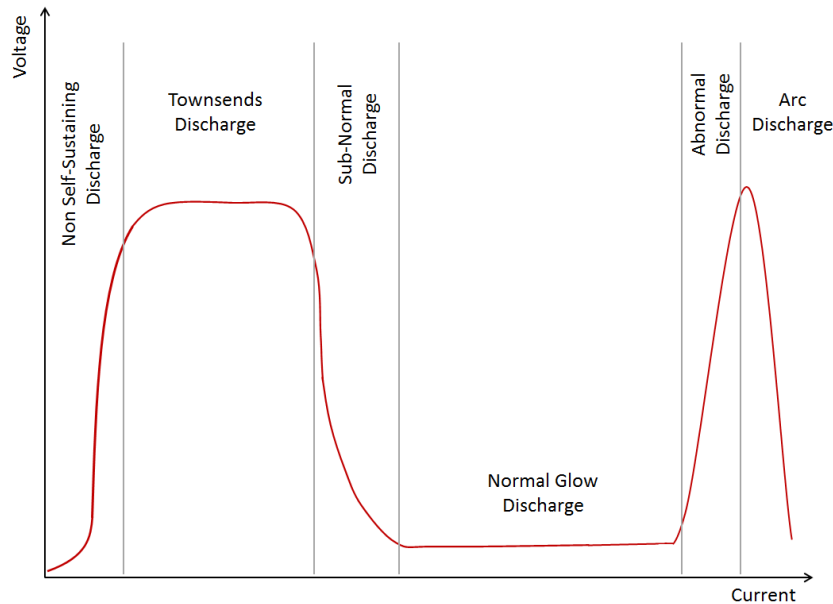


Figure 26 - Voltage-Current Characteristics of Low Temperature DBD ⁽²⁷⁰⁾

Observation of discharge current as a function of the voltage applied to the gas demonstrated a distinct difference for nitrogen. With helium and argon a transition from the non-self-sustained discharge to a Townsend discharge then to a sub-normal glow discharge is exhibited during the initial current increase. Contrary to this in nitrogen the ionization level is too low to induce a localization of the electric field and a glow regime cannot be achieved. Nitrogen exhibits a Townsend discharge at atmospheric pressure (APTD). Furthermore what is contradictory to the typical occurrence of Townsend regime is that the established discharge is far from dark, and in fact quite a bright discharge. This is attributed to the specific conditions of the nitrogen discharge, showing a quasi-uniform electric field during the Townsend region and density of energy carrying species in the plasma. Figure 26 shows various types of discharge created through variation of current and voltage.

Massines showed by the consideration of the species available in the nitrogen discharge, the evolution of the bright APTD ⁽²⁷⁰⁾. Ion density increases to a maximum which is too low to induce localisation of the electric field, being in a quasi-uniform field distribution. Electron density also increases, with a corresponding low ionization rate which remains in agreement with Townsend discharge. The electron density always remains lower than the ion density due to the difference in mobility and absence of a neutral plasma region. Electron density

follows the discharge current shape but never equals zero, with a maximum density being experienced at polarity switch. When the electric field is low the electrons are trapped in the gas. The increase in electron density may be explained if a continuous source of electrons is given. This source has to be independent of the field, related to the energetic neutral particles from the previous discharge and have a high concentration when the polarity is switched. N₂ metastable specie density is still very high when the polarity changes, but is unable to produce Penning ionization in pure nitrogen. These species largely diffuse to the dielectric surface and may induce secondary emission of electrons. A further requirement of APTD is that the energy of electrons is high in accordance to the high electric field. Electron energy is almost equal through the gas gap and remains so for the duration of the discharge. However considering the large density disparity between electrons and N₂ metastable specie, metastable states also largely participate in the energy transfers like all species which have a life longer than the time separating two charges. This is probably a reason why the APTD is bright.

Production of a visually diffuse discharge at atmospheric pressure requires consideration of the electrical circuitry. Impedance matching the system enables resonance for plasma generation to be achieved at a lower driving frequency. Effective implementation of resonance ensures that maximum power is delivered to the plasma, and not wasted heating the transformer. The inductive elements of the primary side were matched to the capacitance of the secondary, to account for the plasma's "capacitive" nature. With the implementation of high frequency filters, ability to reduce the filamentary aspects by reducing the current spikes is seen in the discharge. This enabled the production of a visually diffuse discharge at atmospheric pressure in pure nitrogen.

5 - Etching Methods

Etching of materials has been conducted for many years using an array of techniques, be it physical chiselling or chemical processing. Industrial fabrication of electronic devices involve generally multiple etching processes to pattern the materials, manipulating the physical properties of the device. Two prominent sectors that involve such processes are the integrated circuit board (ICB) and semiconductor manufacturers ^{(244) (218) (226) (216)}. Correct application of etching allows the development of the internal circuitry leading to the desired electrical properties. The following section will concern itself with several etching concepts and discuss the traditional methods of device fabrication.

5.1 Chemical Etching and Photolithography

Production of patterned films may be produced using the combination of chemical etching and photolithography ^{(244) (226) (271) (272)}. In its simplest terms the desired pattern is cut into a mask and the film surface is coated in resist material. Exposure to ultra violet light polymerises the resist not protected by the mask and the remaining un-polymerised material is removed with a suitable solvent ⁽²⁷¹⁾. Application of acid etch removes the material not protected by the resist, leaving the originally desired pattern corresponding to the photographic image. Figure 27 shows the simplified processes steps involved in photolithography etching.

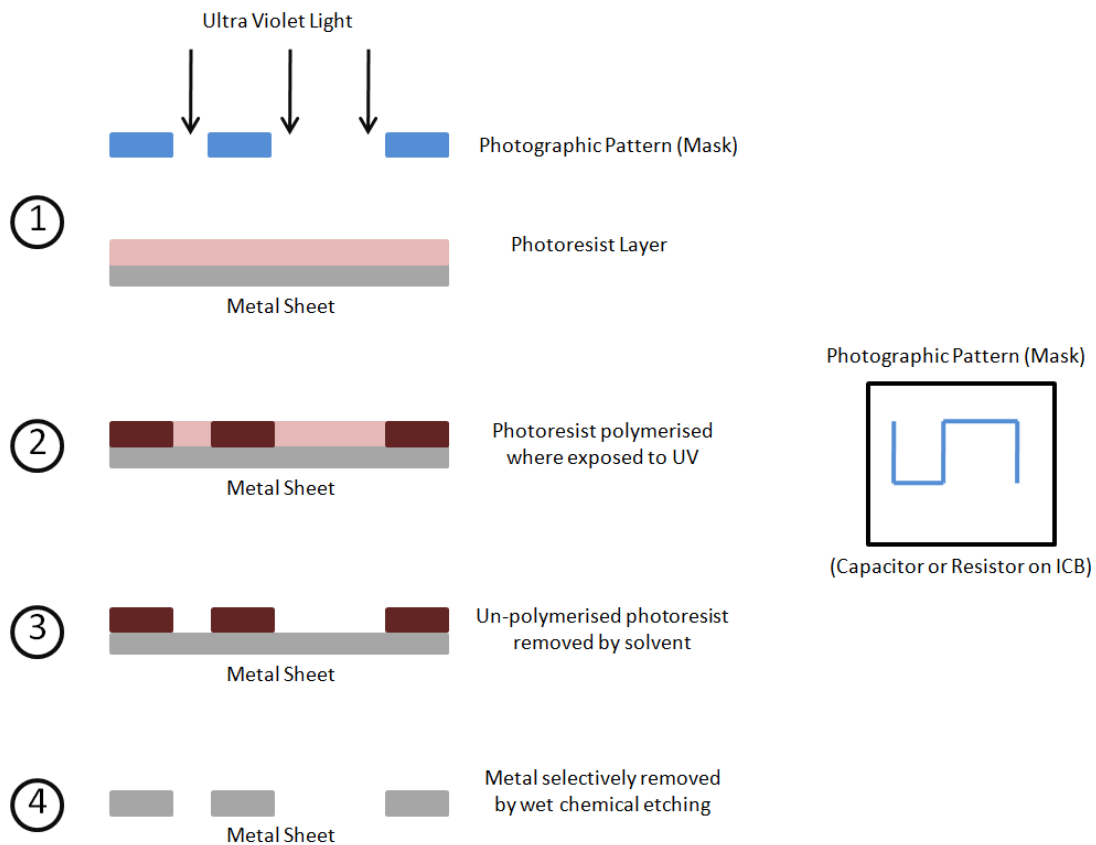


Figure 27 - Simple metal mask etching using photolithography and wet chemical etching

5.2 Resist Masking

Higher masking definition may be achieved using a direct photolithographic treatment. Photoresist is divided into two families, positive and negative resist^{(244) (226)}. Positive resist operates whereby the area of photoresist film exposed to ultra violet is removed by the solvent wash⁽²⁷¹⁾. Negative resist the opposite, whereby the exposed film remains after the solvent wash. Early adoption of resist techniques favoured negative resist; however positive resist is now most commonly employed^{(244) (226) (271) (272)}.

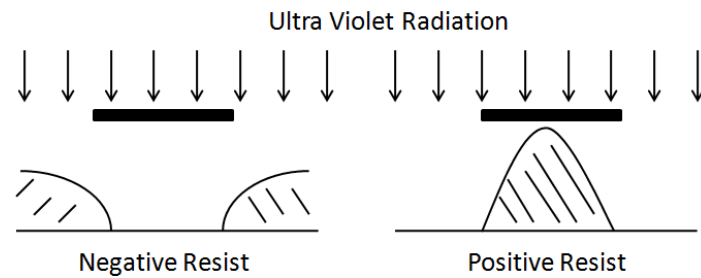


Figure 28 - Resist profile after development from ultra violet exposure

As resolution has improved and line widths have reduced for circuit board manufacturing, an essential upgrade to the lithography method needed. Figure 28 shows the differences in profile between positive and negative resist solutions. This was achieved by avoiding contact between the photograph and the resists and employing accurate optic systems to project the blueprint onto the resist (Figure 29)^{(226) (272) (273)}. Unfortunately glass optics do not transmit ultra violet light and the fabrication of the lenses requires it to be made from quartz⁽²⁷²⁾.

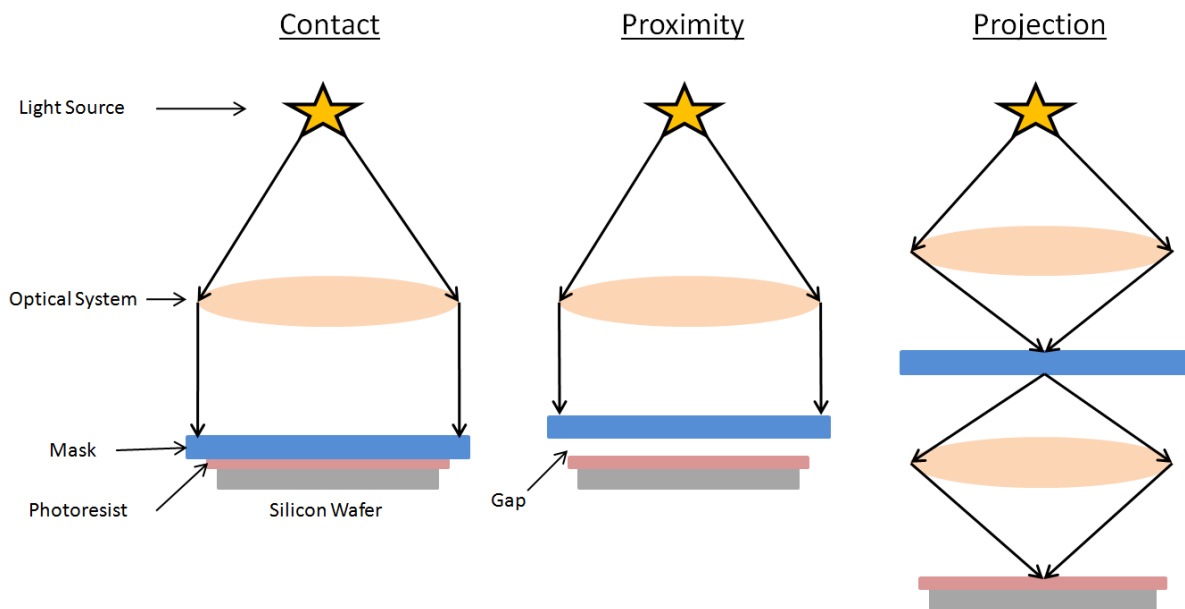


Figure 29 - Photolithography masking techniques

With the resist techniques the edge definition is limited only by the etch undercutting the resist and the definition of the photograph. Alternative manufacturing to the photographic negative is the application of a computer controlled laser or electron beam to incise the pattern in the surface of chromium coated glass slide^{(271) (272)}. This process is extensively

utilized for integrated circuit manufacturing, both in device fabrication and in interconnections. However, in active device fabrication (transistors, diodes and integrated circuits etc.) process temperatures exceed the photoresist tolerance and degrade. In this situation the resist is used to transfer the pattern to a silicon oxide layer to act as the mask, which can endure severe temperatures up to 1500°C^{(226) (271)}. These processing steps permit sub-micron definition on a routine basis^{(274) (275) (276)}.

5.3 Reactive Ion Etching and Deep Reactive Ion Etching

Reactive ion etching (RIE) is very closely related to sputtering processes, although it is administered to etch the target rather than deposition of a film⁽²⁷⁷⁾. Gas type and quantity depend on the etching service, for instance sulphur hexafluoride is universally exercised in the etching of silicon^{(274) (278)}. Vacuum equipment is required for the process to occur with the pressure typically maintained between a few millitorr and a few hundred millitorr^{(274) (277)}.

Deep reactive ion etching (DRIE) is a highly directional (anisotropic), enabling deep high aspect ratio trenches to be excavated, predominately used in the silicon industry^{(272) (279)}. Aspect ratios greater than 20:1 or even 40:1 may be developed^{(280) (281)}. This technique is called High Aspect Ratio Micro Structures (HARMS), and was developed primarily for manufacturing microelectromechanical systems (MEMS)⁽²⁸²⁾. Computer memory has adopted this technique for advancing its technology, permitting the precise engineering of high density capacitors for DRAM (Dynamic Random Access Memory)⁽²⁸²⁾. Application of DRIE for silicon has seen two competitive methods being developed, the cryogenic and Bosch method⁽²⁷⁹⁾. Combination of both of these mechanisms allows for deep truly vertical structures to be fabricated materials.

Cryogenic deep reactive ion etching (Cryo-DRIE) involves the wafer being cooled to approximately 163K/-110 °C, where by the reduced temperature slows down the chemical reaction that produces isotropic etching^{(283) (284)}. Tachi et al⁽²⁸⁵⁾ first introduced the Cryo-DRIE method, which utilized a low-bias fluorine based high density plasma for etching⁽²⁸⁶⁾. Sidewall protection was attained in a twofold method by producing an inhibitor layer whilst

reducing the reaction probability of radicals. Reducing the probability of radical etching the silicon requires the temperature to be low. Subsequent work discovered that the addition of O_2 into the plasma working gas was essential for the inhibitor layer (SiO_xF_y)⁽²⁸⁷⁾ deposition that permits directional etching⁽²⁸⁶⁾. During this process ions continue to bombard upward-facing surfaces and etch them away, producing trenches with vertical sidewalls. Introduction of O_2 into the SF_6 working gas has been shown to exhibit high sensitivity to the anisotropy of Si etching. Etch profiles may be tapered either positive or negative dependant on the application of the working gas⁽²⁸⁶⁾.

Alternatively for DRIE is the Bosch process, also referred to as pulsed or time-multiplexed etching⁽²⁸¹⁾. Bosch processing alternates repeatedly between two phases to attain nearly vertical structures, whereby etching is performed directly after deposition. In the etching cycle a portion of the previously deposited sidewall polymer is removed via off-vertical ion impact, being re-deposited in the developing trench⁽²⁸⁸⁾. Specific reactive ions can be utilized from the plasma, specifically selected from the working conditions and gas composition. Silicon has typically employed sulphur hexafluoride for its etching medium. Application of the polymer enables local anisotropy etching to be exhibited⁽²⁸⁸⁾. Following the etching phase the chemically inert polymer is deposited as the passivation layer, usually C_4F_8 ⁽²⁸⁹⁾. Etching and deposition stages occur for several seconds at time, enabling the deep trenches to be excavated.

Excavation is developed as the passivation layer is broken down in the base of the trench by the highly directional ions, exposing the silicon substrate. Exposure of the substrate to the etchant enables the trench to be developed further through subsequent cycling. Bosch method is essentially the series of numerously small isotropic etches that develops into an anisotropic trench. An element of roughness remains on the sidewalls, which is indicative of the irregular process. Cycle times may be adjusted, with short cycles producing smoother walls and long cycles yielding increased etching rates⁽²⁸³⁾. Bosch etching compared to cryogenic technique operates at room temperature and exhibits a very high selectivity to standard photoresist materials⁽²⁸¹⁾.

5.4 Surface Activation and Etching via Plasma's

Application of plasmas for etching has been employed into the DRIE processing, which offers energetic particles capable of removing material from its bulk ⁽²⁷⁹⁾ ⁽²⁸³⁾. Plasmas have been implemented into many commercial processes, generally involving high temperature arcs for welding ⁽²⁴⁵⁾ ⁽²⁶⁰⁾. In addition to these processes, "cold" plasmas are involved in the commercial processing of temperature sensitive materials; a prime example of this is surface activation of plastics ⁽²⁵⁷⁾. Plasma species interact with the surface of plastic polymers and rupture the surface, activating it for printing. Without conditioning of the surface the printing process would struggle to work, as the ink or charged toner would not have an energy free surface to adhere.

Surface etching involves in the removal of material from the treated sample surface. Numerous parameters contribute to the etching rate: plasma composition, substrate nature, working conditions (power, gas flow, substrate position) ⁽²⁴⁵⁾ ⁽²⁴⁴⁾. Stable discharges offer a higher degree of uniformity during the etching process with DBD being favoured. Metastable energetic species enhance the etching efficiency and they provide an essential role in the excitation, ionization and dissociation phenomena ⁽²⁴⁵⁾ ⁽²⁷⁰⁾. Comparison between atmospheric pressure plasma etching techniques are shown in Figure 30.

Excitation	Source	Plasma	Substrate	Etching rate	Observations
Low frequency	DBD	He/O ₂	Organic materials	0.2 μm min ⁻¹	Not uniform etching
Radio frequency	APPJ	He/O ₂	Kapton	8 μm min ⁻¹	Chemical process: influence of the oxygen metastable species and atoms
		He/O ₂ /CF ₄	SiO ₂	1.2 μm min ⁻¹	
			W	1 μm min ⁻¹	
	Cold plasma torch	He/CF ₄	Ta	2 μm min ⁻¹	Emission intensity (OES) of F* is related to the etching rate of Si
		Si	0.3 μm min ⁻¹		

Figure 30 - Surface etching by atmospheric pressure plasma ⁽²⁴⁵⁾

5.5 Microelectronics Plasma Etching

Microelectronics have been extensively manufactured for approximately 50 years with an evolving production system and resultant technologies ⁽²²¹⁾. Sophisticated electronics and computing power are imbedded into modern culture, sustaining the quality and ease of our

lives. The persistent reliance on these technologies has readily accelerated fabrication techniques, forcing strict measures to define and create smaller, faster electronics ^{(282) (286)}. Globally we have truly entered an electronic revolution from the initial creation of semiconductors coinciding with integrated circuit boards for sophisticated computers for global communication, entertainment and unprecedented scientific benefit.

Current generations of microelectronic fabrication require meticulous attention to cleanliness in their process. Achieving this requires vacuum equipment throughout processing and clean rooms within which the production line is assembled ^{(218) (226) (290)}. Low pressure CVD techniques are employed to deposit the film layers, using masking techniques to produce the desired patterning for components. Plasma etching is used as a post treatment technique to enhance the film layers by selectively etching sections of the film ^{(279) (283)}. Masking techniques are also employed into this method to etch the desired pattern. Dry plasma etching was adopted in favour of previous wet chemical techniques for several reasons, but essentially due to the limitations of definition ⁽²⁸²⁾. Wet processing has a tendency to etch the film layer vertically but also horizontally, undercutting the mask and reducing the side wall definition. Plasma etching is thought to involve mostly straight line propagation of species (within a vacuum), that interact in almost vertical direction for anisotropic etching.

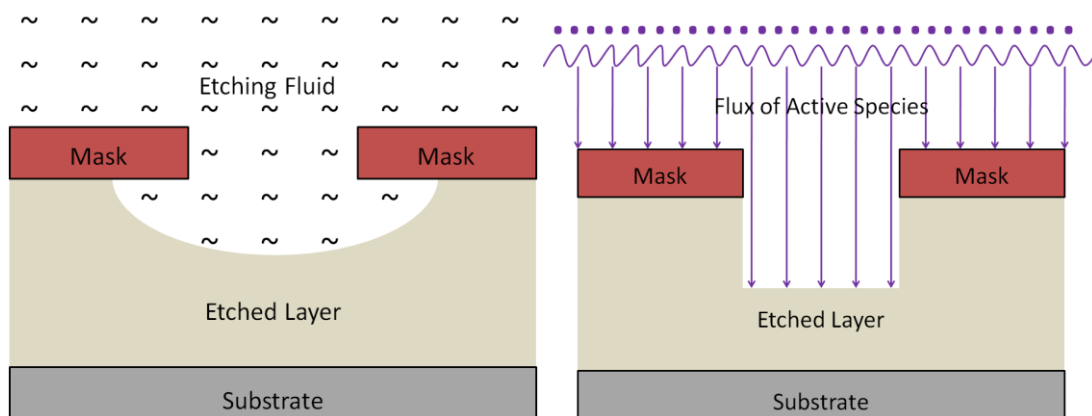


Figure 31 - Wet Chemical Etching Vs. Dry Plasma Etching

Critically with this technique is the ability to reduce the size of features produced under the etching regime. Particular components have reduced to such a size whereby they enter the sub-micron region ^{(281) (286)}. Wet chemistry is unrefined compared to plasma etching, enabling

greater definition and advancement in micro-machining. Optical masking techniques also become compromised as diffraction effects with small features, which results in the requirement of short wavelengths for masking and alternative sources for microlithography (226) (216) (280).

Dry plasma etching of microelectronics is accomplished by permitting the interaction of a relatively inert molecular gas and the plasma discharge, usually RF glow discharge (282) (283). This interaction breaks down the molecular gas into its component forms which are active species. These species propagate in an anisotropic or ideally vertically, interacting and etching the desired film layer whilst the mask remains undeterred by the process (279). Ions and photons developed in the plasma promote the etching effects, whilst the chemical active species are chiefly responsible for etching (244). The imparted high energy possessed by the ions sponsors' increased chemical interaction on the film surface for higher etching rates. Accompanying this is the selectivity of the etching process by careful selection of the working gas, for the component break down to affectively interact with the specified layer (287). Important to this process is the by-product formed after the etching cycle, which is readily removed by the vacuum equipment. If the resultant materials are not effectively removed this can cause contamination on the surface or produce in efficient products (216).

5.5.1 Microelectronics Plasma Etching Process Overview

This section outlines the components, proprietary mechanism for plasma etching and process considerations as described by Roth⁽²¹⁶⁾. An overview of the etching process is shown in Figure 32.

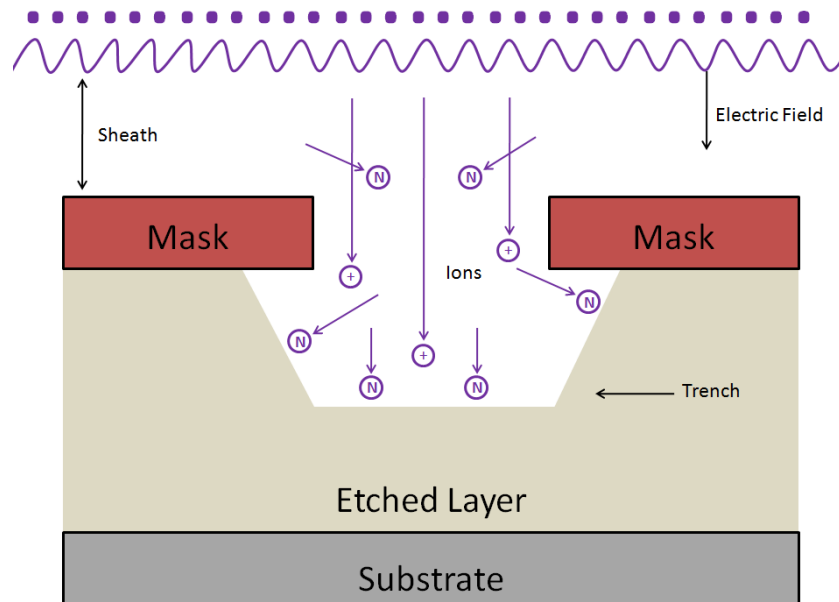


Figure 32 – Overview of Etching Process in Microelectronics

The plasma Generation is typically generated by RF or Microwave glow discharge. Active species emanate from the plasma and through subsequent interactions. Energetic ions generated promote heterogeneous etching reactions. A sheath region is the region between the plasma and the mask, which presents an electric field in the direction of the working material. Ions are accelerated towards the substrate due to the electric field, whilst electrons are retained in the plasma. Generally the sheath is 10-100 times greater intended etching dimensions. Previously described in the photo-lithography techniques, the protective mask outlines the required pattern to be etched into the material. It's essential that the mask is impervious to the plasma etch, whilst being easily removed during post processing. Removal is typically known as stripping or ashing.

The etchant layer is the working layer to be etched situated directly under the mask. Layer thickness depends on its application, typically being around one-half to a few microns. As

etching continues a void is developed through the etchant layer and mask known as the trench. The substrate must be selected so that it is not adversely affected by etching process as the trench deepens. The neutral working gas can comprise of singular or multiple mixtures of gasses introduced into the plasma to form the active species for etching. Generally the working gas does not react with the etchant layers. Chemically reactive species produced react with the etchant material. These may constitute the active species of the plasma, neutral working gas or the reaction products formed by the etching. Active species created in the plasma discharge which may include ions, electrons, free radicals, excited states, molecular fragments, atomic species and photons. Any of the active species may promote the etching towards the bottom of the trench but involving no sidewall interaction. Other active species may serve directly as an etching agent of the layer.

Effective trench etching requires promotion of the reactions from constant precursor's delivery in conjunction with high energy particle interaction. Ions accelerated by the sheath offer energy to promote the etching reactions. Photons originating from the laser illumination or electron beams may also provide energy for reactions, as well as additional ions from beam sources. Deposition of energetic ions, electron or photons exclusively at the bottom of the well is one of the principle factors permitting the directionality of the plasma etching of microelectronics. In accordance with the enhanced etching rates, these promoters may also prevent unwanted polymerization on the etchant surface and the mask.

Neutral reaction products are the resultant products from etching reactions. Importantly these products should be volatile for effective extraction from the system in order to not accumulate or contaminate the newly etched surface. Heterogeneous reactions responsible for etching are initiated with the adsorption of etching species upon the working layer. Dissociation from the surface may occur if the active species is molecular. A consequence of the species interaction is the formation of a new product molecule, from either singular or multiple atoms of the working layer and active species. Completing the etching cycle, the new product molecule desorbs from the surface and is removed from the system.

The etching system comprises of multiple tools that encompasses the complex equipment involved for maintaining the working environment and the tools involved throughout the

process. Advanced vacuum systems of chemically resistant materials is vital for safe and extensive lifetimes of use. In conjunction with the primary vacuum systems are subsystem that permits the maintenance of pressure levels, gas introduction and electrical inputs for establishing the plasma discharge. A consequence of operating under low pressure requires batch processing of samples.

5.5.2 Benefits and Drawbacks of Microelectronic Plasma Etching

At present, plasma techniques are the only commercial viable method for etching microelectronics. Plasma etching systems suffer from performance issues, consideration of these issues and looking to the future helps nurture new improved techniques.

Dry plasma etching techniques certainly present significant advantages beyond the scope of previous wet chemical practices. It benefits significantly from the ability to produce highly directional, almost vertical trenches with the possible potential to be scaled into automated production line technology^{(282) (283)}. The definitive etching limit is only defined by the quality of the mask, as further reduction in masking technology would allow the plasma to etch reduced feature size^{(218) (280) (281)}. A reduction on the environmental impact is noted using dry against wet techniques, as the plasma etching is a clean processes resulting in extremely low toxic or unwanted waste products⁽²¹⁶⁾. In contrast to the wet chemical cycles fewer speciality gasses are mandatory for the etching cycle to occur. Overall the by-products as a consequence of the etching cycle have minimal impact on the environment due to their non-harmful nature⁽²¹⁶⁾.

In light of the benefits offered by the vacuum environment, the major drawback is design configuration^{(250) (291)}. The systems are particularly expensive due to the sophisticated manufacturing methods taken to produce the components, material construction to be resistant to the etching process and the automation required for successful etching^{(257) (292)}. Further strain has been added by the necessity to reduce the design rule for features less than one micron emerging. Need for higher sophistication of production design has led to the further reduction in vacuum pressures^{(216) (283)}. Prior to this design level the pressures were within the medium vacuum range, but these have extended into the high / ultra-high vacuum region, requiring superior vacuum technology which results in increased pump-down times

(218) (216). Furthermore the implementation of these vacuum systems at significantly reduced pressures forces batch processing methods (244) (264). Automated systems require wafers to remain in controlled environments throughout production increasing turnaround time and cost (292). Certain procedural constraint insists the removal of the wafer from the vacuum for further processing, greatly increasing the production time. A consequence of a batch routine introduces hindrances during particularly lengthy procedures (216).

5.6 Four Basic Low Pressure Etching Processes

Four basic mechanisms are encountered for the removal of material from its surface under low pressure conditions:

- I. Sputtering
- II. Pure chemical etching
- III. Ion energy driven etching
- IV. Ion inhibitor etching.

A basic overview of each of the process characteristics is shown in Figure 33.

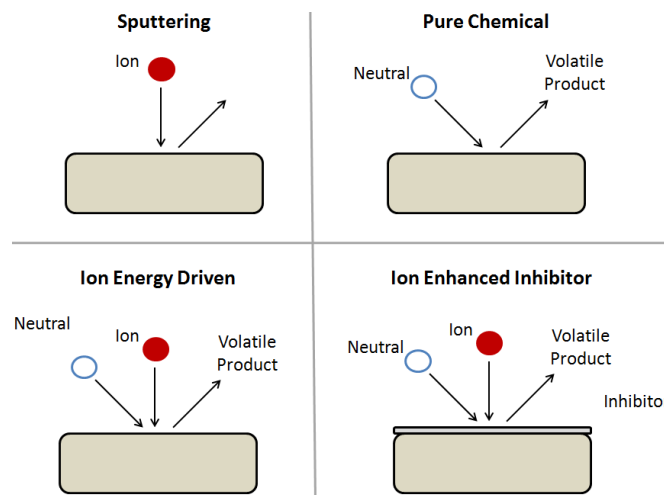


Figure 33 – The Four Basic Etching Mechanism at Reduced Pressure

Sputtering is an unselective, anisotropic etching process that is strongly dependent on the incident angle of the ion (244). Maximum etching yield is generated at the normal to the

surface with little effect at a grazing angle, achieving nearly vertical etching ⁽²¹⁶⁾. This mechanism depends on the energy imparted by the incident ion. Ions need to break the binding energy of the surface atoms, resulting in a rate of one ion for atom removal. Sputtering is particularly useful for removal of involatile target atoms, but by its nature is very slow ⁽²⁴⁴⁾.

Pure chemical etching (PCE), species are supplied from gas phase reactions in the plasma ⁽²⁴⁴⁾. This process is inevitably highly chemically dependent and exhibits isotropic profiling ⁽²¹⁶⁾. Isotropic interaction describes the etchant atoms arriving in a near uniform angular distribution through the reduced pressure. Conformal etching of the surface is attainable with these conditions. This state remains unless a particular resistant crystal orientation exhibited, and the etching preference is developed ⁽²⁴⁴⁾. Subsequently etch rates are high with a substantial flux of etchant species, but the limiting factor is dependent on the complex chemical interactions at the surfacing leading to the etchant product.

Ion enhanced energy driven etching, delivers both the etchant species and ions to the working surface ⁽²⁴⁴⁾. Effective blending of these treatments offers a superior etching process greater than sputtering and pure chemical etching individually ⁽²⁹³⁾. Investigation into this etching mechanism shows that it is predominately chemically etched, with a reaction rate determined by the ion bombardment ⁽²⁴⁴⁾. Etching rate increases in coordination with increased ion energy above a threshold energy of a few volts. Volatile etching products are produced as they are for pure chemical etching, combined with bombarding ions possessing high energy. These ions propagate through the medium with a highly directional angular distribution promoting highly anisotropic etching. Ion contribution to the processes may have a reduced selectivity, so careful consideration of the etching characteristics are required to develop a balance between anisotropic and selectivity ⁽²⁴⁴⁾ ⁽²⁹⁴⁾. The associated mechanism for etch product formation is not well understood and comprehension of this is given by an empirical model.

Ion enhanced inhibitor etching involves the delivery of the etchants, energetic ions and inhibitor precursor from the plasma discharge ⁽²⁴⁴⁾ ⁽²⁸³⁾. The inhibitor molecules absorb or deposit on the substrate surface forming a protective layer or polymer film. Specific selection of the etchant material is taken in order for the chemical etch process to occur at high etching

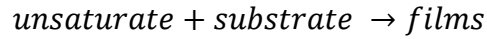
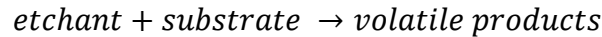
rates in the absence of ion bombardment or inhibitor layer ⁽²⁸¹⁾ ⁽²⁸²⁾. Ion bombardment prevents the inhibitor layer from developing or eradicates its current formation, revealing the surface for the chemical etchant. Regions that avoided the ion flux protect the surface from chemical exposure due to the remaining inhibitor layer. Inhibitor precursor molecules deposit to form polymer films on the surface, as interaction of ions expose an area for chemical etch, the side walls are re-deposited with the inhibitor to produce anisotropic etch condition ⁽²⁸⁸⁾. Careful selection of precursors, gas mixtures and conditions allow the etching process to occur without significant defects, becoming synonymous with the ion enhanced etching technique ⁽²⁴⁴⁾ ⁽²⁹⁵⁾.

5.7 Chemical Framework of Semiconductor Etching

Carrier gasses for establishing the plasma discharge that deliver the etchant source creates a complex configuration based on etch rate, selectivity to the mask & under layer and anisotropy. In conjunction with the introduced materials, the carrier gas becomes dissociated in the plasma generally into more reactive species, aiding or prohibiting the etching process. Flamm ⁽²⁹⁶⁾ summarised the chemical constituents and the dissociated products formed from the carrier gas;

- Saturates: CF₄, CCl₄, CF₃Cl, COF₂, SF₆ ...etc.
- Unsaturates: CF, CF₂, CF₃, CCl₃ ...etc.
- Etchants: F, Cl, Br, O ...etc.
- Oxidants: O, O₂ ...etc.
- Reductants: H, H₂ ...etc.
- Nonreactive Gases: N₂, Ar, He ...etc.

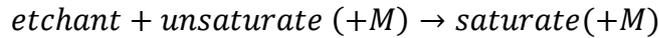
It is found that these species are utilized for the etching process, reacting in the gas phase or upon the sample surface. Generally encountered are the following reactions;



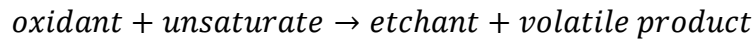
In the case of particular substrate compositions a situation is encountered where the unsaturates become an etchants for example SiO₂;



Three bodied reactions are experienced are at low pressures;



These reactions may not be as important in the gas phase, becoming significant during surface interaction or at higher gas pressures. If oxidants or reductants (O₂ or H₂) enter the feed gas or exist with the gaseous composition, further reactions can arise;



Principally the overriding process parameter for the etching mechanism is the ratio of etchant to unsaturate flux at the substrate surface, with a high ratio leading to isotropic etching while a low ratio may permit film deposition ⁽²¹⁶⁾. An intermediate phase is experienced if a controlled level is maintained; promoting the ion inhibitor process whereby sidewalls are coated and the trench is excavated ⁽²⁸⁸⁾. This anisotropic regime may be induced by the introduction of etchants (Cl₂, Br₂) into the feed gas mixture to enhance the etchant/unsaturate ratio or by introducing oxidants that incinerate the unsaturates ^{(244) (296)}. Contrary to this is the suppression of this ratio as it is utilized to promote the protection of sidewall. Inert gases may added to the feedgas to control the electrical discharge of the plasma and substrate temperature, dilute the etchant mixture or to adjust the gas-phase chemistry through invoking

mechanism such as Penning ionization or excitation⁽²⁵⁰⁾. Alternative substitutions involved in the gas mixture can rupture the protective oxide layers and to remove contaminants on the sample.

5.8 Chlorine as an Etchant Source

Chlorine and fluorine are the two main species utilized for microelectronic fabrication etching^{(244) (222) (246) (216)}. Two factors of this etching medium are of particular advantage. The prominent crystallographic effects and large doping effect^{(244) (246)}. The later effect is a particular facet concerned with the vacuum etching of doped silicon wafers, where the concentration of the dopant species has an effect on the etching properties (mainly the etching rate)⁽²⁴⁴⁾. A strong reliance on the dopant density suggests that Cl⁻ atoms formed on the surface are critically responsible for etching. Etchant rate dependence on the crystallographic orientation can be attributed to the different location densities of silicon atoms (Si-Si bonds) at the surface. Within silicon the <111> orientations possess a greater density over the <100> orientation, which reduces the Cl or Cl⁻ penetration into the lattice for <111>, resulting in a decreased etch rate⁽²⁴⁴⁾. Pure silicon presented with Cl₂ guides the dissociative chemisorption on the surface, saturating around one monolayer with continued exposure resulting in gradual growth of silicon chloride. This particular scenario is of no benefit in the standard etching process; etching rates are low at room temperature for Cl₂ although they can operate as feedstock for Cl atom etching^{(244) (216)}.

Surface examination of the ion assisted etching interaction with Cl₂ molecules has seen numerous studies although Cl atoms have received little attention⁽²⁹⁵⁾. With regards to silicon etching waste products, SiCl, SiCl₂, SiCl₄ and Si₂Cl₆ have been noted⁽²¹⁶⁾. Ion beam induced mixing and recoil implantation^{(221) (222)} of dissociated Cl₂ molecules on the surface promotes the formation of a SiCl_x layer of approximately several monolayer's' thick. This is comparable to the effects of pure chemical Cl etching⁽²⁴⁴⁾. Ion assisted etching for chlorine atoms has higher etching rate for Cl atoms compared to Cl₂ atoms approximately two to three times. Ion energy driven etching is therefore very reliant on both Cl and Cl₂ atoms for effective etching rates⁽²⁴⁴⁾.

6 - Analytical Techniques

Accurate film monitoring enables process refinement, through the application of an array of analytical equipment. Recognition of developments within film structures and properties involves an in depth understanding of the analysis techniques. Therefore it is necessary to have a broad understanding of the principles to understand the characteristics of the films and routes in which to improve them. Key focus areas are the structural, electrical, optical and composition analysis^{(297) (298)}. This section will give a brief overview of the theories involved with the techniques and their operation in respects to conducted analysis.

6.1 Atomic Force Microscopy (AFM)

Atomic force microscopy is the principal analysis tool utilized in modified surface research. This tool allows accurate and immediate detailing of the surface topology with analysis of the surface roughness in conjunction with 2D and 3D imaging. AFM was developed (1985 Binnig, Quate and Gerber)⁽²⁹⁹⁾ to overcome a fundamental flaw with surface tunnelling microscopes (STM), the lack of ability to image non-conductive surfaces^{(300) (301) (302)}. With AFM analysis, practically any surface type may be is imaged including ceramics, glass, composites, ceramics and biological samples⁽²⁹⁸⁾. Surface characterisation is taken at the microscopic level with a resolving accuracy from approximately 1 μ m to sub-nanometer⁽²⁹⁸⁾. AFM operates by the utilization of incredibly fine sharp tips that trace the sample surface either in contact or near proximity (0.2-10nm)⁽³⁰³⁾. Tips are of the order of several microns long and less than 100 \AA in diameter located on the free end of a flexible cantilever of approximately 100-200 μ m long⁽³⁰²⁾. Interactive forces between the tip and the surface either attract or repel the tip, with the resulting deflections being recorded and processed as a computer image^{(297) (298)}.

Tip (probe) is placed on the cantilever, where the amount of force administered between the probe and sample is dependent on the spring constant of the cantilever and the tip to sample separation. This force is described using Hooke's Law in equation (5.3)⁽³⁰¹⁾;

$$F = -k \cdot x \quad (5.1)$$

F - Force

k - Spring Constant

x - Cantilever Deflection

The spring constant for a cantilever is usually between 0.1-1 N/m⁽³⁰⁰⁾. If this spring constant is less than equivalent spring between the atoms of the sample, the cantilever will bend with the resultant deflection (open air deflection 10⁻⁶ to 10⁻⁹) being monitored electronically⁽³⁰⁰⁾. Modern AFM design exploits a laser beam deflection system for sensitive measurement of the probing tip as shown in Figure 34⁽²⁹⁸⁾. The laser emits a beam upon the back surface of the travelling probe, with a position sensitive detector tracking its movements as it scans across the material surface. This particular configuration proves useful in terms of resolution, as the minute deflection in the tip is registered by contrast as significantly large deflections in the lasers path length⁽³⁰¹⁾. Advancements in tip composition and design further aid the resolution attained by the AFM with standard cantilevers being microfabricated from Si or Si₃N₄ with a typical tip radius <10nm^{(300) (303)}.

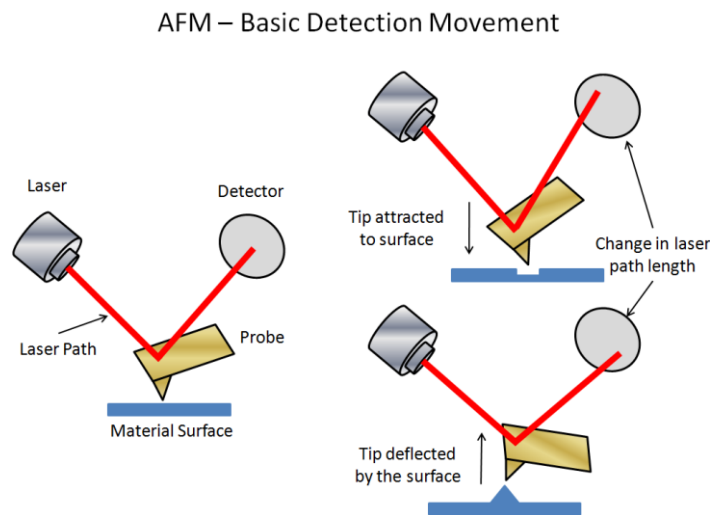


Figure 34 - AFM basic detection method with changes in laser path length due to tip deflection

Probe motion is monitored by a feedback loop system with piezoelectric scanners to maintain probe height or contact against the surface ⁽²⁹⁷⁾. Van der Waals interactions dominate the small probe to surface force interaction. During contact with the sample the probe experiences repulsive Van der Waals forces deflecting the tip, this is known as contact mode ⁽³⁰¹⁾ ⁽³⁰³⁾. As the tip loses contact from the surface it experiences attractive Van der Waals forces, known as non-contact mode ⁽³⁰³⁾. Figure 35 depicts the AFM mode with respects to probe to sample separation and force ⁽³⁰⁰⁾.

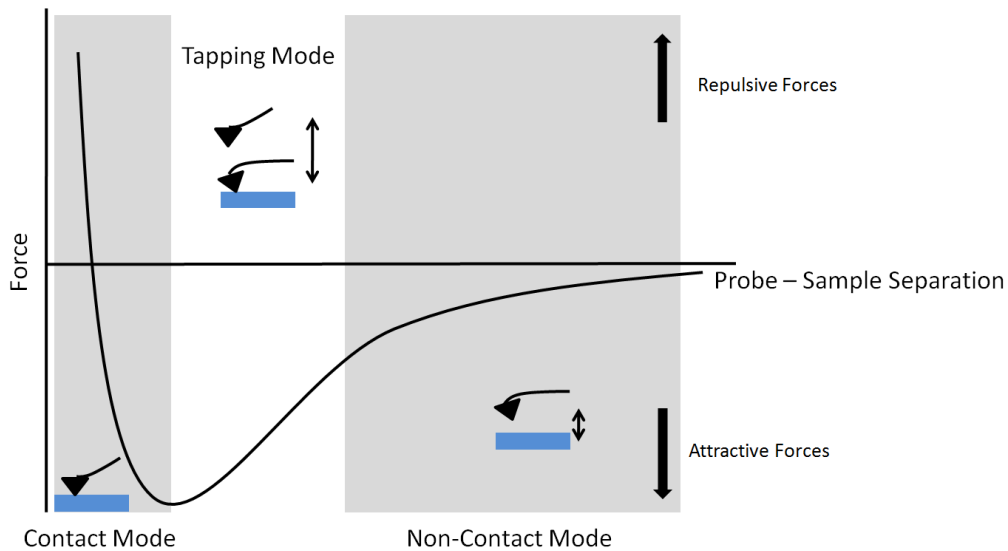


Figure 35 - Force as a function probe-sample separation ⁽³⁰⁰⁾

There are three primary operation modes for AFM imaging, contact, tapping and non-contact ⁽³⁰⁰⁾.

1. Contact mode mainly functions using repulsive Van der Waal forces. As the spring constant is less than that of the atoms on the sample surface the cantilever bends with a repulsive force resulting on the tip. Constant cantilever deflection is maintained by a series of feedback loops and the forces required maintaining said deflection, results in an image being obtained. This mode is good at scanning rough surfaces at fast rates and provides good analysis for frictional properties, but the contact may result in soft sample damage.

2. Tapping (Intermittent) mode is similar to contact operation; however the tip is oscillated at its resonant frequency. Due to the movement in the probe, the tip taps the surface during scanning. Maintenance of stable oscillation amplitude permits a constant tip-sample interaction, allowing imaging of the surface. This mode gives high resolution of samples that may be easily damaged or soft surface adhesion (particularly cellular biological samples). Due to the nature of the intermittent tapping of the surface, slower scan rates are required.
3. Non-contact mode utilises the attractive Van der Waals forces experienced between tip and sample. Samples have a designated liquid absorbed on the surface for scanning or maybe conducted under Ultra High Vacuum conditions. The probe oscillates above the fluid layer during scanning and using a feedback loop monitors amplitude changes due to the attractive forces. The ultimate change in forces results in the imaging of the surface topology. With this method there is a very low force exerted on the sample, a consequence of this is low resolution and contamination of the surface. Generally this technique requires vacuum for best imaging due to the surface interference with oscillation and contaminants.

Resolution of AFM is limited significantly by the aspect of the tip^{(297) (298)}. It's difficult to obtain true surface topology on the atomic scale using the AFM methods as there will always be a degree of error due to the tip width⁽²⁹⁷⁾. We generally encounter the absolute resolution determination as the interaction between the probe and surface, this is described as tip convolution^{(297) (303)}. The shape of the tip does not affect the resultant image feature height but alters the lateral resolution. Figure 36 shows an example of how the perceived feature differs based on probe aspect ratio.

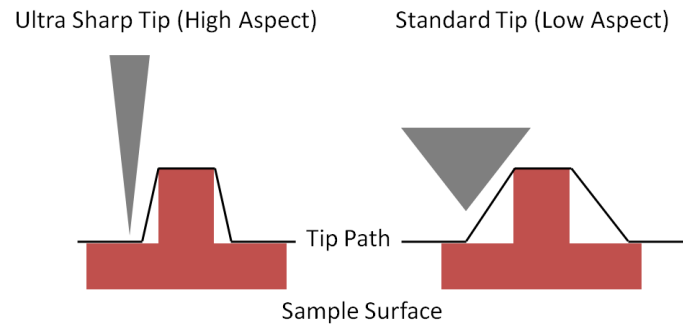


Figure 36 - High and Low aspect ratio tips resolution variation ⁽³⁰⁰⁾.

Roughness data is a useful measurement of the sample surface, enabling characterization of films. Specifically for TCO applications rough films are required with smooth features to prevent defects in final solar cell construction. Therefore the desired films should exhibit large smooth features which reflect a high roughness value. Typically as the film thickness is reduced the roughness and therefore sharpness of the features is reduced. Texture of the film may be visually assessed with roughness being calculated from the AFM probe data. Multiple methods can be applied to determine AFM roughness depending on how the data is handled. Roughness average (R_a) is the most commonly applied measurement for AFM. Root mean square (RMS) is primarily applied in this investigation as this is commonly used within the field of TCO assessment.

Roughness average (R_a) is the arithmetic mean of the absolute values of the height of the measured sample surface. It is calculated from equation (5.2) ⁽³⁰⁴⁾.

$$R_a = \frac{1}{L} \int_0^L |Z(x)| dx \quad (5.2)$$

$Z(x)$ is the function that describes the surface profile analysed in terms of height (Z) and position (x) of the sample over the evaluation length “L”.

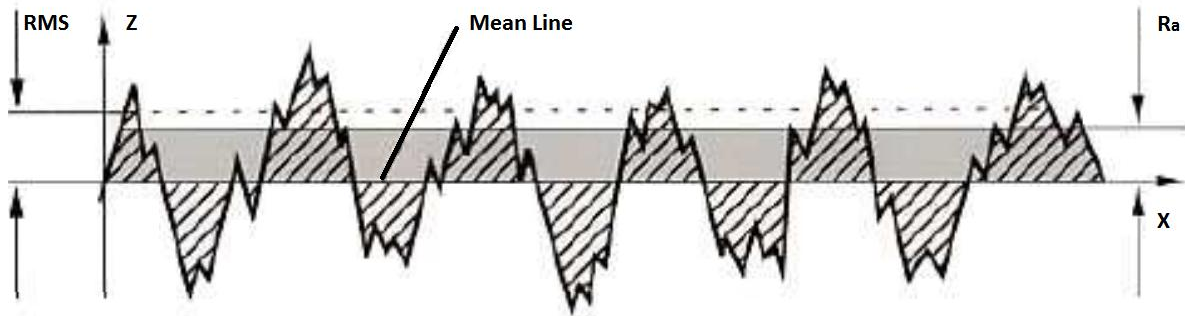


Figure 37 – AFM Measurements and Roughness Determination ⁽³⁰⁴⁾

This value is just the mean absolute profile which makes no distinction between the valleys and peaks of the sample. Therefore samples of various different structures/textures can exhibit identical roughness values. *RMS* determination is a statistical measurement, taking the square of the measurements. The *RMS* function is defined in equation (5.3) ^{(299) (305)}.

$$RMS = \sqrt{\frac{1}{L} \int_0^L |Z^2(x)| dx} \quad (5.3)$$

RMS measurements are therefore more sensitive to the valley and peak information compared to the roughness average due to the amplitude squaring during calculation. This type of assessment is therefore more suited for TCO films for comparative assessment.

6.2 Scanning Electron Microscope (SEM)

The scanning electron microscope (SEM) is a multipurpose and commonly employed electron beam mechanism. Its reputation in scientific world developed from its simple interpretation methods of the generated micrographs, variety of information types that it can produce and combination of images with their analytical information counterpart ^{(306) (307) (308)}. SEM's are used for material characterization involving image and quantitative data representation. It offered an insight into the two dimensional and three dimensional imaging of the microstructure, chemical composition, crystallography and electronic properties ^{(306) (307) (308) (309)}.

Light microscopes (LM) operate using light to illuminate the surface to observe the structure; this limits resolution of these microscopes to the wavelength of light ⁽³⁰⁸⁾. Optical microscopes generally observe an optical limit around 300nm, whereas electron microscopes (EM) offer atomic resolution ^{(306) (308)}. De Broglie theorised in 1925 that all particles assume a corresponding wave like property dubbed wave-particle duality. Particles like the electron therefore had a momentum p which could be related to its wavelength λ via a constant, Planck's constant h ^{(306) (308)}.

$$\lambda = \frac{h}{p} \quad (5.4)$$

λ – Wavelength

p – Momentum

h - Planck's constant

Davisson, Germer, Thomson and Reid experimentally verified the existence of the electrons wave nature properties during the electron diffraction research ⁽³¹⁰⁾. Knoll and Ruska in 1932 constructed a practical example of an electron lens which leads to the original electron microscope, the transmission electron microscope (TEM) ⁽³¹¹⁾.

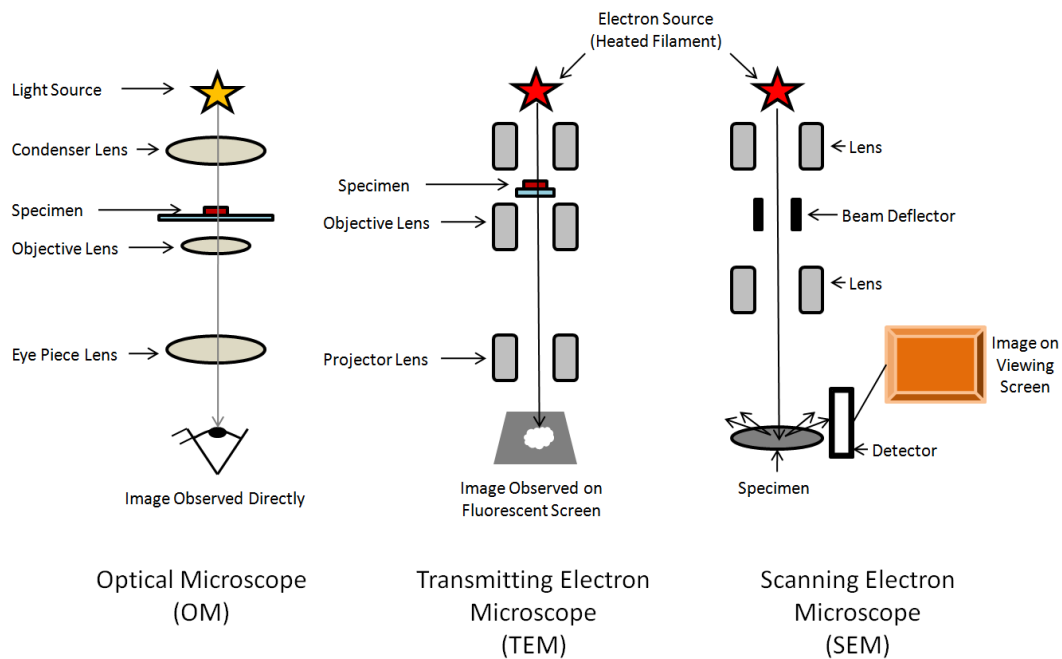


Figure 38 - Optical, Transmitting Electron, Scanning Electron Microscope Instrument Comparison

They were awarded the Nobel Prize in Physics for this magnificent achievement in 1986⁽³¹²⁾. Scanning electron microscopy was unveiled in 1938 with its first wave of commercial instruments available from 1965⁽³⁰⁸⁾⁽³¹¹⁾. The delay in release was due to the advancements in electronics which permitted the scanning of the electron beam across a sample⁽³¹¹⁾. Figure 38 shows the simplified schematics for OM, TEM & SEM. Several key improvements evolved through SEM characterization analysis compared to existing methods⁽³⁰⁸⁾;

- Topography - Surface texture and features.
- Morphology - Size and shape of the material composing particles.
- Composition - Elements and compounds that compose the material with the relative quantity.
- Crystallographic - Atomic arrangement

Analysis of these areas allows the interpretation of their direct effect on the materials properties, resulting in an atomic comprehension of the material. We find significant benefits from using the SEM over traditional optical microscopes.

Type	Magnitude	Depth of Field Resolution
OM	4x – 1400x	0.5mm ~ 0.2mm
SEM	10x – 500Kx	30mm 1.5nm

Table 9 - Optical Microscope Vs. Scanning Electron Microscope ⁽³⁰⁶⁾

SEM operates with a large depth of field permitting a large expanse of the sample to be focussed on ⁽³⁰⁸⁾. This results in an overall better image that allows a representation of the three-dimensional facets of the sample. Combining the higher magnification with the greater resolution, over a larger depth of field in conjunction with compositional and crystallographic information endorses SEM as a very versatile tool for sample analysis.

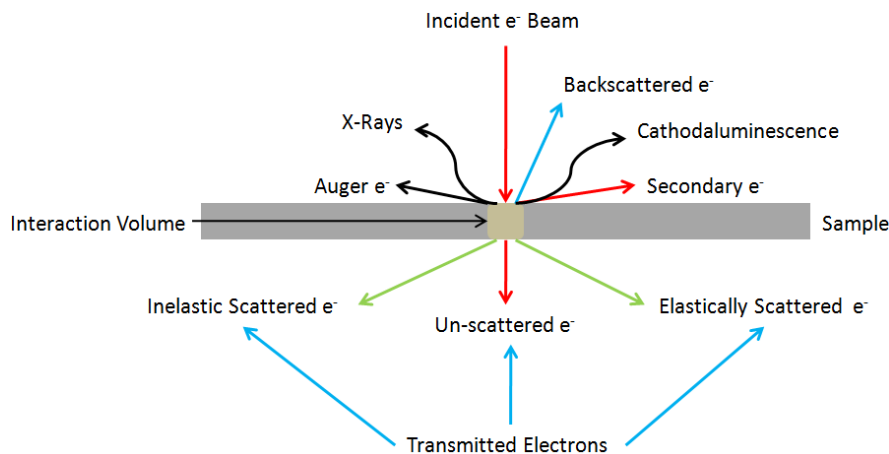


Figure 39 – Interaction Signals Generated by Electron Beam ^{(307) (313)}

As the incident electron beam strikes and interacts with the surface sample, many signals are generated based on the interaction events. Figure 39 illustrates the interaction of the electron with the sample and its consequences, of which is utilized to generate useful information based on the sample. Broadly the signals generated may be divided into two categories, electron and proton ⁽³⁰⁶⁾. The central point of the electrons interaction is within the titled “Interaction Volume”, which is affected by several properties ⁽³⁰⁷⁾. The atomic number of the examined sample affects the volume, as higher atomic numbers absorb or prohibit more electrons reducing the interaction volume ⁽³⁰⁷⁾. Higher acceleration voltages allow deeper penetration into the sample yielding a larger interaction volume ⁽³⁰⁸⁾. The incident angle of the

electrons determines the introduced interaction volume, as greater deviations from the normal produce a smaller volume⁽³⁰⁸⁾.

Vital to the employment of scanning electron microscopy is the mechanism of electromagnetic lenses (EML) in order to manipulate the trajectory of the incident electrons^{(307) (311)}. Traditional microscopy utilizes optical lenses to guide the light path for source focus and illumination. The employment of electromagnetic lenses permits the refinement of focus and affective illumination of the surface details for SEM. A basic depiction of the EML is a tunnelling configuration whereby the electron beam is projected between an array of magnets and balanced forces between the magnetic field stabilises their trajectory⁽³⁰⁷⁾. The foundation of this is reliant on the Lorentz force principle (5.3)^{(306) (311)}.

$$F = q_o v \times B \tag{5.5}$$

F – Force

q_o - Electron Charge

v - Velocity

B - Magnetic Field

Several lenses are operated to help refine the electron flight path, the condenser and objective lens. Primarily the condenser lens helps collimate the electron beam whilst the object lens seeks to control the final focus⁽³⁰⁷⁾. Manipulation of the electrons is achieved by variation of the magnetic field, enabling refinement of the focus. Contained within the lens is the stigmator and aperture which enables greater control over the final focus⁽³¹¹⁾. The stigmator helps correct minor imperfections experienced in the objective lens and the aperture is employed to reduce the “spray” of electrons through the lens aiding refinement^{(306) (311)}. SEMS allow for penetration into greater resolution of microscopy, offering several considerations due to the lens configuration when compared with traditional optical lenses⁽³⁰⁸⁾.

- Electrons never touch the lens therefore there is no definite interface.
- Electrons rotate in the magnetic field.
- Electrons repel each other.
- Focus and magnification controlled electronically, therefore containing no moving parts.
- Lenses may only comprise of positive elements in order to operate (always converging).
- Cannot correct the electron lens aberration (unlike compound optical lenses).
- Electron lenses always operate with a small aperture.

Resolution is the ability to distinctly resolve two closely spaced points. This is different to magnification, as this is the ability to observe objects of smaller size whilst resolution offers the ability to focus on the object at the set distance⁽³¹¹⁾. A method employed to improve the resolution of the SEM is to reduce the size of the electron beam projected on the sample surface⁽³⁰⁶⁾. This may be calculated from the following set of equations (5.6) (5.3)⁽³¹⁴⁾;

$$d_{min} = 1.29C_s^{1/4}\lambda^{3/4}\left\{7.92\left(\frac{iT}{J_c}\right) \times 10^9 + 1\right\}^{3/8} \quad (5.6)$$

This may be reduced to, for low currents;

$$d_{min} = 1.29C_s^{1/4}\lambda^{3/4} \quad (5.7)$$

d_{min} – Minimum electron beam width

C_s - Spherical aberration

J_c - Current density of the source

λ – Electron wavelength

i - Current

T – Temperature

Several other mechanisms may be utilized to further improve the resolution of the SEM. Increasing the strength of the condenser lens aids beam refinement ⁽³¹⁴⁾. Decreasing the objective aperture and working distance between the sample and objective lens aids resolution ⁽³⁰⁷⁾. The height of which the sample is within clear focus is known as the depth of field. SEM has a natively large depth of field with permits the three dimensional texturing nature visible on the images. Depth of field is improved by introducing a larger working distance, smaller objective aperture and by introducing lower magnifications ⁽³⁰⁸⁾. A consequence of improving the depth of field by working distance variation follows a reduction in the resolution possible, due to reciprocal nature between resolution and depth of field ^{(306) (308)}. In certain cases it may be beneficial to sacrifice the resolution to gain crucial information held within the depth of field.

6.3 Four Point Probe and Hall Effect Measurement

6.3.1 Four Point Probe

Electronic analysis of conductive films utilizes primarily two techniques, four point probe and Hall Effect. Four point probe analysis offers an insight into the conductivity of the film by measurement of its resistivity ^{(315) (316)}. Hall Effect comprehends the mobility of the carriers enabling sample conductivity to be characterized ^{(315) (316)}. Predominately we are concerned with TCO semiconductor materials with accurate interpretation of the electronic properties after growth and post treatment.

Conductivity measurements for semiconductors are typically interested in the bulk material compared to the thin film properties. Conductivity may be calculated from equation (5.3) ⁽³¹⁷⁾.

$$\sigma = \frac{1}{\rho} \tag{5.8}$$

σ – Conductivity (S/cm)

ρ – Specific Resistivity (Ωcm)

The conductivity may be calculated from the basic semiconductor properties within the case of electron dominated conduction (equation (5. 3)), and if both carrier types are considered (equation (5. 3))⁽³¹⁷⁾.

$$\sigma = q\mu n \tag{5.9}$$

$$\sigma = q\mu_n n + q\mu_p p \tag{5.10}$$

q - Electron Charge

μ – Carrier Mobility ($\text{cm}^2/(\text{V}_s)$)

n – Carrier Density (cm^{-3})

p – Hole Density (cm^{-3})

Specific resistance determined four point probe, which is an established analytical technique engaged to measure the average resistance of a thin film or sheet⁽³¹⁷⁾. A measurement head consists of four spring loaded needles which are placed upon the measured surface, with the pin spacing being equal. The pressure applied to the surface is sufficient to ensure good near-ohmic contacts, without excessive force in order to avoid damaging the material surface.

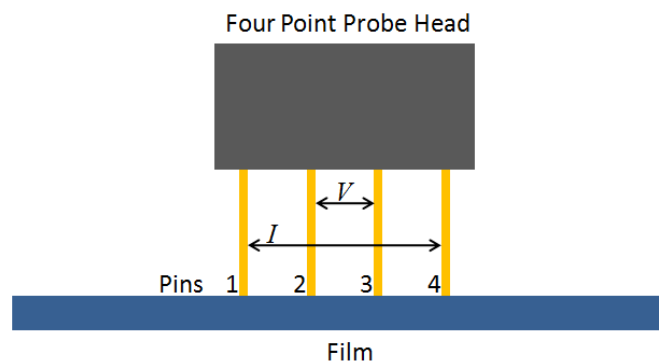


Figure 40 – Four Point Probe Standard Design

A current is passed through the outer probes whilst monitoring the voltage developed across the inner probes⁽³¹⁷⁾. We assume that the current source exhibits a near infinite source

impedance and a voltage meter with nearly infinite input resistance, any possible contact voltages at the needles due to the induced current flow can be neglected⁽³¹⁷⁾. The specific resistance of the sample is given in equation (5.3)⁽³¹⁷⁾.

$$\rho = \frac{V}{I} c \quad (5.11)$$

ρ – Specific resistance

V – Voltage

I - Current

c – Geometry Correction Factor

Geometry correction factor, c , is dependent on the geometry of the sample dimensions and probe needle separation. Several criteria have to be obeyed in all sample configurations for accurate measurements of low inaccuracies sub 1%⁽³¹⁷⁾;

- Nearly ohmic contacts between the probe needles and the sample surface
- Negligible heating of the sample from the measurement current
- No excess injection of carriers, which would lead to excess conduction (dark measurement)
- No extreme surface potential induced surface band bending, otherwise leading to stronger surface accumulation or surface inversion layers which would affect the bulk conduction

For the measurement of thin layer samples, we require special consideration of the geometry correction factor. If the probes are applied to a laterally infinitely extended thin layer of thickness d the determination of specific resistance ρ grown on a semi-insulating substrate can be calculated from equation (5.3).

$$\rho = \frac{V}{I} d \frac{\pi}{\ln 2} \quad (5.12)$$

Error in the evaluation of the sheet resistance approaches 1% if the layer thickness is half the distance between the probe separations. Consequently this error would increase to approximately 8% if the layer thickness was equal to the separation of the probes ⁽³¹⁷⁾. Typically needle separation is around 1mm, therefore layer thickness of 1 - 10µm can be measured with a negligible error. The numerical coefficient is specific to the ratio of probe distance to the sample dimensions, for a very thin and infinite layer, $\alpha = \pi/\ln 2 \approx 4.5324$ ⁽³¹⁶⁾.

6.3.2 Mobility Measurements

Assessment of the mobility of the main carriers is performed utilizing van der Pauw test structures, with the ideal measurement structure being geometrically symmetrical ⁽³¹⁷⁾. Primarily specific resistance is measured followed by determination of the carrier concentration. These properties may be assessed using the same van der Pauw structure; however the application of current and therefore voltage measurement is altered. Mobility is then calculated from equation (5.3) ⁽³¹⁷⁾.

$$\mu = \frac{\sigma}{qn} = \frac{1}{qn\rho} \quad (5.13)$$

μ – Mobility

In this equation the expression $|1/qn|$ is the Hall constant, which is related to the specific carrier concentration of the measured sample ⁽²⁰³⁾. Rearrangement of the hall constant into the previous expression permits the mobility to be determined from equation (5.3) ⁽³¹⁷⁾.

$$\mu = \frac{R_H}{\rho} = R_H\sigma \quad (5.14)$$

R_H – Hall Constant

Hall Effect is polarity sensitive with respect to conduction type, hence the sign of the Hall constant signifies whether the sample is n-type (negative sign) or p-type (positive sign) ⁽³¹⁷⁾.

6.3.3 Hall Effect involving van der Pauw Structures

The Hall Effect was discovered by Edwin Hall in 1879 and permits the determination of mobility carrier properties within a sample. Hall voltage is denoted by V_H and described as the voltage upon a long thin sample of length a , where a current I is driven through the long axis and a magnetic field \mathbf{B} is applied perpendicular to the sample⁽³¹⁷⁾. Denoted by the balance of the Lorentz force (5.3) and the electric field force induced due to the Hall voltage, we are able to comprehend the Hall voltage for an n-type sample when integrating over the transverse field E_H ⁽³¹⁷⁾;

$$V_H = -\frac{1}{nq} \frac{1}{d} IB \quad (5.15)$$

V_H – Hall voltage

B – Magnetic field

From this equation the term $-1/nq$ is known as the Hall constant R_H for a given sample, from which the sign dictates whether the measured sample is n-type or p-type⁽³¹⁷⁾. A positive sign for this constant would describe a p-type semiconductor; therefore the Hall Effect is useful for the determination of dominant carrier and conduction type. The Hall voltage equation can therefore be rewritten as shown in equation (5.3).

$$V_H = R_H \frac{1}{d} IB \quad (5.16)$$

Following this, when the Hall constant is determined the carrier concentration may be calculated n-type (5.17) and p-type (5.3) semiconductors⁽³¹⁷⁾.

$$n = \frac{1}{qR_H} \quad (5.17)$$

$$p = \frac{1}{qR_H} \quad (5.18)$$

Mobility can be calculated if the corresponding four point probe measurements have been determined as well. It is not practical to measure these properties separately and the van der Pauw method resolved corresponding measurements from the same contact points ⁽³¹⁷⁾ ⁽³¹⁸⁾. Van der Pauw demonstrated that a disk of arbitrary shape may be employed for both four point probe and Hall assessment. Practically rectangular shapes are preferred (manufacturing and measurement considering), but van der Pauw exemplified this on configuration showed in Figure 41.

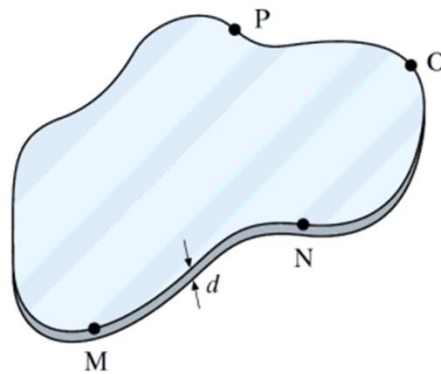


Figure 41 - van der Pauw Test Sample of Specific Resistance ρ , Disc of Arbitrary Shape of thickness d with Infinitesimal Small Contacts M, N, O, P at its periphery ⁽³¹⁷⁾.

Criteria for the measurements specify the sample may contain no holes. The sample is measured using two configurations in the van der Pauw arrangement for specific resistance and carrier concentration.

For specific resistance, a current I is passed across contacts M, N and the voltage V is observed through the remaining contacts P and O . Consequently this measurement configuration may be adjusted through 90° to obtain a secondary voltage measurement through alternative contact pairs, developing two resistances for the sample $R_{MN,OP}$ and $R_{NO,PM}$ ⁽³¹⁸⁾. Van der Pauw demonstrates that by conformal mapping that the sample specific resistance obeys equation (5.3) ⁽³¹⁸⁾.

$$e^{[-(\pi d/\rho)R_{MN,OP}]} + e^{[-(\pi d/\rho)R_{NO,PM}]} = 1 \quad (5.19)$$

Deduction of the specific resistance for the preferred rectangular geometry may be determined from equation ⁽³¹⁸⁾.

$$\rho = \frac{\pi d}{\ln 2} R_{MN,OP} \quad (5.20)$$

Due to the nature of the symmetrical sample geometry, multiple measurements may be taken and averaged. The $I - V$ configuration may be rotated four times through 90° ; current polarity may be also switched resulting in eight total measurements ⁽³¹⁷⁾.

Hall measurement is applied for carrier concentration assessment in the van der Pauw configuration. Alternatively the $I - V$ application is applied so that current and voltage contacts are crossed ⁽³¹⁷⁾. In this arrangement the Hall constant is determined by forming the average out of two measurements as shown in equation (5.3) ⁽³¹⁸⁾.

$$R_H = \frac{d}{B} \left(\frac{R_{NP,OM} + R_{OM,PN}}{2} \right) \quad (5.21)$$

Accuracy of this value may be improved upon with additional averaging over eight Hall resistance terms as given by (5.15), with carrier mobility being determined by (5.14) and (5.21) together with (5.20) ^{(317) (318)}.

6.3.4 Hall Measurements

Characterisation of the electrical properties of materials progressed with new levels of understanding in the early 1800's ⁽³¹⁶⁾. Resistance and conductance became measureable physical quantities through two-terminal current and voltage measurements ⁽³¹⁹⁾. Investigation of resistance from these measurements did not account for structure shape of the sample, and further comprehension of resistance was sought after. Formulated was an intrinsic material property called resistivity (or conductivity) that was not influenced by the geometry of the sample, allowing for quantification of current-carrying materials and classification/comparison between them ⁽³¹⁶⁾. Resistivity is not a fundamental material parameter, dissimilar materials possess similar resistivity. Notably the resistivity of a material can be influence through varying synthesis methods. This was distinctly true for semiconductors, as the resistivity of the material did not coincide with the observed

properties⁽³²⁰⁾. Electron conduction was well theorised until the opening of quantum mechanics, where no acceptable solution to the electrical transport was offered. Evolving from this problematic situation was the definition of carrier density and mobility permitting a higher sophistication of practical electrical measurements^{(316) (320) (321) (322)}.

Application of the Hall Effect permits the determination of the mobility of carriers in the film. We find that several factors can affect the mobility; temperature, crystal defect density and the impurities present in the structure^{(320) (319)}. Essentially the Hall Effect is underpinned by the physical effects of the Lorentz force^{(317) (316)}. Model Hall effect systems consist of a uniform piece of electrically conductive material, uniform current density flowing through the material in the presence of a perpendicular magnetic field. Charge carriers are deflected to one side of the sample from the Lorentz force, which induces an electric field perpendicular to the current density and magnetic field^{(317) (316) (320)}. The Hall coefficient is the ratio of the perpendicular electric field to the product of the current density and magnetic field. Resistivity is the ratio of the parallel electric field to the current density^{(317) (316) (320) (323)}.

Determination of the materials actual transport properties requires a considerable deviation from the idealised model. Direct measurement of the electric field or the current density inside a sample cannot be obtained⁽³¹⁷⁾. We therefore resolve the current density from the total excitation current and the geometry of the sample^{(317) (316)}. Determination of the electric field is obtained through measurements of the voltage difference between the electrical contacts on the sample surface^{(317) (316) (323)}.

Commonly we find two applied geometries for Hall measurements;

1. Long, narrow Hall Bar geometries
2. Nearly square or circular van der Pauw geometries

Each variation possess its own advantages and disadvantages, however both types of samples are measured by the same mechanism. Hall voltage V_H is developed perpendicular to a current and an applied magnetic flux⁽³¹⁷⁾. Our practice of thin film measurements utilizes the calculation of the Hall properties using the van der Pauw technique.

6.3.5 The Van Der Pauw Technique

Resolving the mobility μ and sheet density n_s (number of charge carriers) of a sample requires the resistivity and Hall measurements to be determined⁽³¹⁷⁾. Van der Pauw technique is convenient and widely adopted in the semiconductor industry for resistivity measurements of uniform samples. Van der Pauw conceived technique involves an arbitrarily shaped conducting film of a continuous nature (no defects or voids in the conducting film), with four very small ohmic contacts situated out the outer regions of the sample^{(317) (318)}. Figure 42 gives an example of Van der Pauw measurement geometry for thin films.

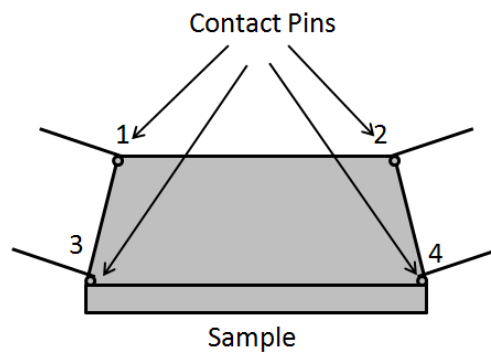


Figure 42 – Van der Pauw Analysis of Thin Film's

Resistivity measurements are obtained in order to resolve the sheet resistance R_s of the sample. Van der Pauw verified the exhibition of two characteristic resistances R_A and R_B ⁽³¹⁸⁾. These resistances correspond to the probes on the sample surface and their configuration of measurement giving two resistances relating to surface and the sheet resistance R_s . We obtain the Van der Pauw equation through which R_s maybe solved numerically and used to ascertain the bulk electrical resistivity (5. 22)^{(317) (318)}.

$$\exp\left(-p \frac{R_A}{R_S}\right) + \exp\left(-p \frac{R_B}{R_S}\right) = 1 \quad (5. 22)$$

R_s – Sheet Resistance

R_A and R_B – Characteristic resistances

The characteristic resistances are measured through applying a DC current through pin 1 & out of pin 2 (I_{12}) whilst measuring the voltages from pin 3 & 4 (V_{43}). Secondary measurement is taken by applying the current through pin 2 & out of pin 3 (V_{14}) whilst measuring the voltages on pin 1 & 4 (I_{23}). They are then determined from equation (5.3)⁽³¹⁷⁾
(318).

$$R_A = \frac{V_{43}}{I_{12}} \text{ and } R_B = \frac{V_{14}}{I_{23}} \quad (5.23)$$

The intention of the Van der Pauw technique is to ascertain the sheet carrier density n_s by the measurement of the Hall Voltage V_H ⁽³¹⁷⁾ (318). Hall measurements are depicted through series measurements of voltage with a constant current I and magnetic field B (perpendicular to the sample). Hall voltage is measured by forced current being applied through opposing contact pairs (1 & 3 or 2 & 4), with the Hall voltage being measured through the remaining two contacts. Once the Hall voltage is ascertained the sheet carrier density maybe calculated from equation (5.3)⁽³¹⁷⁾ (318).

$$n_s = IB/qV_H \quad (5.24)$$

n_s - Sheet Carrier Density

Several practical considerations must be accounted for during these measurements;

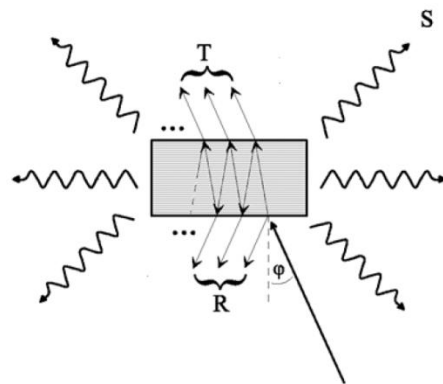
- Ohmic contact quality and size
- Sample uniformity and thickness accuracy
- Thermomagnetic effects
- Photoconductive and photovoltaic effects

A further note for equipment configuration, it is necessary that the contact pins are much smaller than the sample and its corresponding thickness. Accurate calculation of the Hall voltage, carrier density and resistivity demands precise determination of the temperature, magnetic field, current and voltage⁽³¹⁷⁾ (320) (318) (324).

6.4 Optical Measurements

Consideration of the optical properties is a key property for TCO's, solar cells and thin film technologies. This is not only for performance reasons but considered also for the cosmetic appearance of the deposited material. Implementation of any layer into a photovoltaic stack must take into consideration the optical properties with respects to refractive index matching, transmission, reflection, absorption, scatter and further specifics relating to the property of intended captured light. Throughout this next section we will discuss in classical electrodynamics terms the optical properties of light with respects to thin film materials.

Incident light has to penetrate the surface of an object to interact with the bulk material. It is therefore clear that the optical properties of surfaces and interfaces are of critical importance when observing the optical behaviour of a system ⁽³²⁵⁾. Light that has interacted with the sample may be ejected from the sample in several ways, as described by Figure 43;



To the definitions of T , R , and S . φ is the incidence angle

Figure 43 - Interaction of Light in a Sample ⁽³²⁵⁾

Observation of the light trajectories shown in Figure 43 develop the following categories of light ⁽³²⁵⁾;

- Transmitted – Light passes through the sample with a well-defined direction only varied by refractive index changes.
- Specularly Reflected – Light reflected from the sample
- Diffusely Scattered – Deviated light scattered by the sample surface or in its volume
- Absorbed – Light absorbed by the bulk material or at the surface.

By contemplation of only the intensities of the light interaction we are able to define these four terms. Transmittance of a sample is shown to be the ratio of the intensity of the transmitted light I_T and incident light to the sample I_E (5.3)⁽³²⁵⁾.

$$T \equiv \frac{I_T}{I_E} \quad (5.25)$$

T – Transmittance

I_T – Transmitted light intensity

I_E – Total incident light

Corresponding with the transmittance, the reflectance R is defined as the ratio of the intensity of specularly reflected light I_R and the incident light (5.3)⁽³²⁵⁾.

$$R \equiv \frac{I_R}{I_E} \quad (5.26)$$

R – Reflectance

I_R – Specularly reflection intensity

Following the laws of energy conservation if none of the incident light is either diffusely scattered or absorbed by the sample, the transmittance and reflectance must be equal to a value of one. In practice this is not the case, as a proportion of the light will go through diffuse scattering or be absorbed. Developed from this situation is the definition of the optical scatter S , which is defined as the ratio of intensities for light scattered and incident total light (5.3)⁽³²⁵⁾.

$$S \equiv \frac{I_S}{I_E} \quad (5.27)$$

S – Scattered light

I_S – Intensity of scattered light

Equally we are able to define the term for absorbance A as the ratio of intensity of light captured from the incident total (5.3)⁽³²⁵⁾.

$$A \equiv \frac{I_A}{I_E} \quad (5.28)$$

A – Absorbed light

I_A - Intensity of absorbed light

The conservation energy law is satisfied when absorption and scatter is taken into consideration whereby the total value of light interaction equals one (5.3)⁽³²⁵⁾.

$$T + R + A + S = 1 \quad (5.29)$$

Each term maybe determined independently, however these terms are not independent of each other. Determination of three terms in principle will allow the fourth term to be defined. Typically the algebraic sum of the absorption and scattered is referred to as the optical loss L (5.3)⁽³²⁵⁾.

$$L \equiv A + S = 1 - T - R \quad (5.30)$$

All of these values are characteristic for a given sample in a specific experimental system, whereby sample material and geometry (involving experimental geometry) determine the measured signal response⁽³²⁵⁾. Wavelength of light also has an impact upon these values, as material interaction with specific wavelengths varies.

Being principally concerned with TCO materials the optical characterization is critical. Predominantly we focus on the transmission, absorption, haze and scattering properties of the deposited films over multiple discreet wavelengths (455nm, 530nm, 627nm, 870nm). Classification of these properties allows the performance of the optical abilities of the TCO material to be assessed.

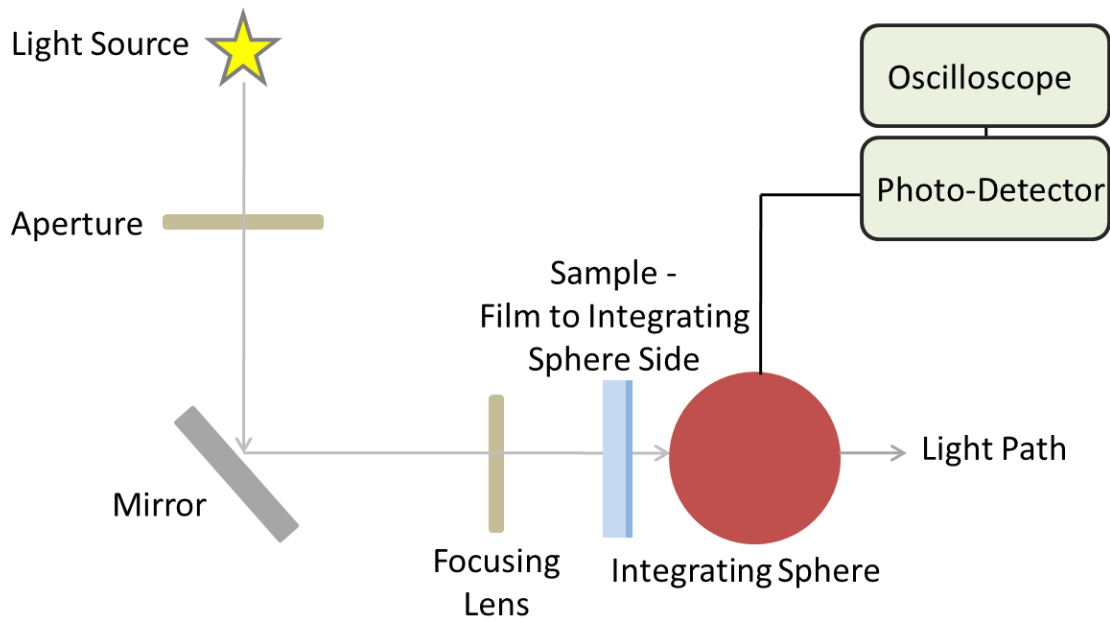


Figure 44 – Optical system configuration

Optical characteristics are determined using the arrangement shown in Figure 44. In Figure 45 a schematic of the measurements taken are shown. Conducting these seven measurements we are able to determine the films transmission, forward/reverse haze, specular reflection and absorption. Observation of the haze and specular reflection values gives an indication of the scattering capability of the film.

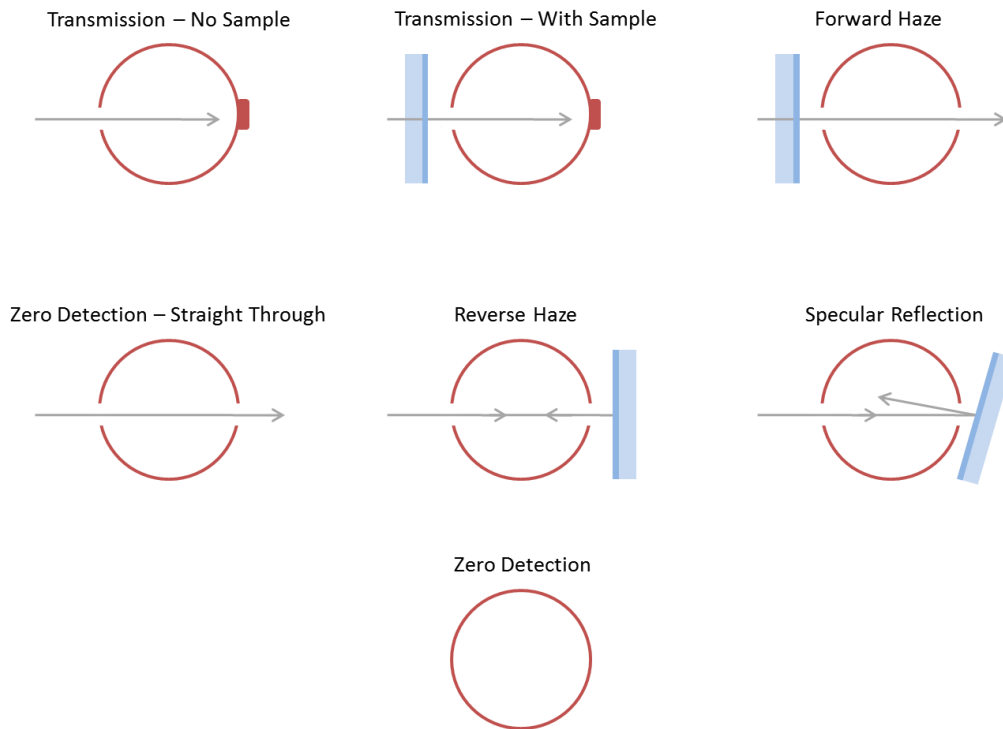


Figure 45 – Optical measurements taken for TCO characteristic determination

Transmission is calculated from the quantity of light detected through the film compared to the total light administered to the film as calculated from equation (5.3).

$$Transmission = \frac{I_t - Zero}{I_0 - Zero} \quad (5.31)$$

Forward haze is the light scattered through the front of the film surface. $H_f(I_0)$ calculates the haze from the film surface without accounting for transmission loss through the film (5.32), $H_f(T)$ includes the film transmission (5.3).

$$H_f(I_0) = \frac{H_f - Z_0}{I_0 - Zero} \quad (5.32)$$

$$H_f(T) = \frac{H_f - Z_0}{I_t - Zero} \quad (5.33)$$

Reverse haze is light scattered back from the film surface. $H_r(I_0)$ calculates purely the haze of the surface (5.34), $H_r(S_p)$ incorporates the reflected light (5.35).

$$H_r(I_0) = \frac{H_r - Z_0}{I_0 - Zero} \quad (5.34)$$

$$H_r(S_p) = \frac{H_r - Z_0}{S_p - Z_0} \quad (5.35)$$

Specular reflection is the total amount of light directly reflected from the surface (5.3).

$$Specular\ Reflection = \frac{S_p - H_r - Z_0}{I_0 - Zero} \quad (5.36)$$

Absorption is calculated from the optical loss in the system from passing light through the sample (5.3).

$$Absorption = (1 - Transmisson - H_r(I_0) - Specular\ Reflection) \quad (5.37)$$

A separate optical fibre system is operated to determine transmission and reflection. A major difference with this system is that transmission and reflection are observed over the visible spectrum (400-800nm). Utilizing this system we are able to analyse the peak performance across the wavelength and observe the reflection dependency with frequency and film thickness.

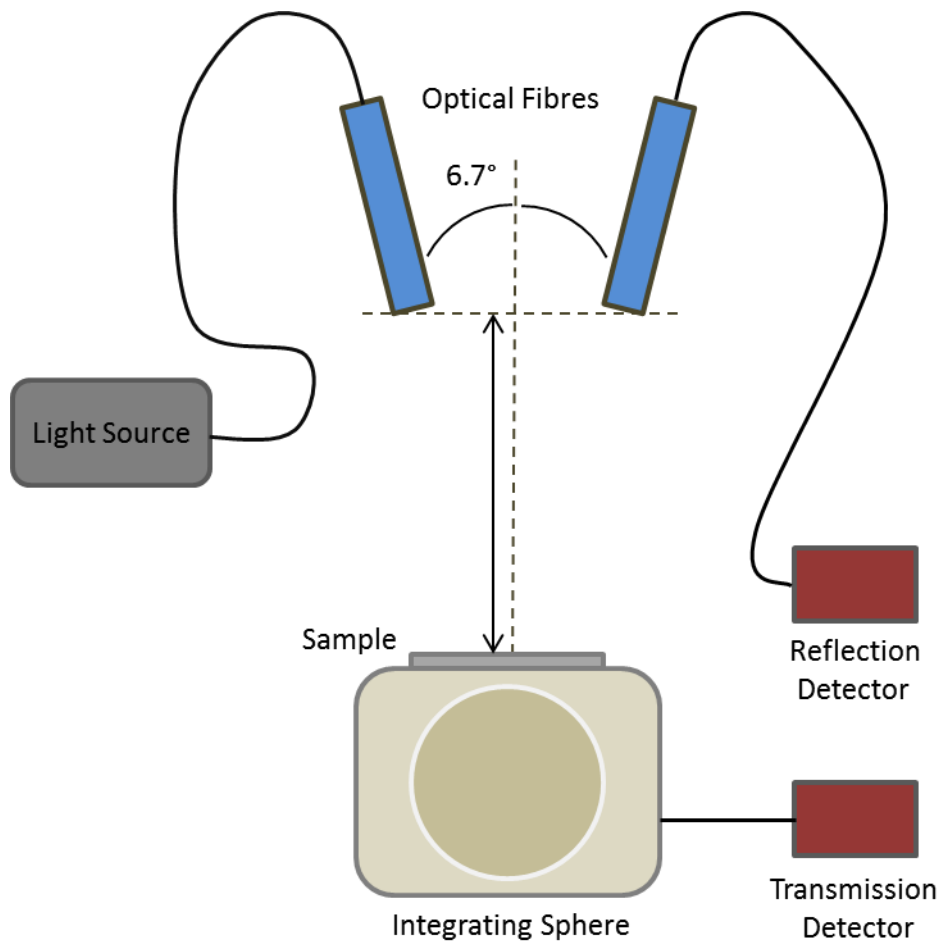


Figure 46 - Ocean Optics Optical Fibre System

In this arrangement transmission is captured by the integrating sphere, reflection is observed at a known angle at a given height above the surface. Capturing the data using the standard Ocean Optics Spectra Suite we are able to deduce the information in relation to a given standard.

6.5 X-Ray Diffraction (XRD)

XRD is an essential experimental technique employed for inquiries into the crystal structure of solids. It enables assessment of lattice constants and corresponding geometry, material identification (including unknown specimens), single crystal orientation, preferred orientation of polycrystals, defects, stresses etc. ⁽³²⁶⁾.

Diffraction occurs when light is scattered by a periodic array with long-range order, producing constructive interference at specific angles. It is regarded that electrons in an atom coherently scatter light acting as point scattering source. The scattering factor is proportional to the electron number surrounding the atom. XRD analysis is performed by a collimated beam of X-rays of wavelength typically between 0.7 - 2Å incident on a specimen surface. The wavelength of X-rays is comparable to the spacing between atoms. The beam is diffracted by the crystalline phases in the specimen according to Bragg's Law as shown in equation (5.3) ⁽³²⁶⁾;

$$\lambda = 2d \sin\theta \quad (5.38)$$

Denoted by this equation is d , the spacing between atomic planes in the crystalline phase and λ is the X-ray wavelength. Intensity of the diffracted X-rays is measured as a function of the diffraction angle 2θ and the specimen's orientation ⁽³¹⁷⁾. Observation of the diffraction pattern is used to identify the specimen's crystalline phases and measure its structural properties. It is important to note that amorphous materials such as glass do not possess a periodic array with long range order, and consequently do not produce a diffraction patterns ^{(326) (327)}.

Two critical advantages of X-ray diffraction for thin film analysis are ^{(326) (327)};

1. The wavelengths of X-rays are of the order of atomic distances in condensed mater, which especially qualifies their use as structural probes.
2. X-ray scattering techniques are non-destructive and leave the investigated sample intact.

The generated diffraction pattern is a product of the unique crystal structure of the material. Comparable material compositions with alternative atomic arrangement therefore produce distinctly different diffraction patterns⁽³²⁷⁾. Unit cells are used to describe the basic repeating atomic order that defines the crystal structure. It contains the maximum symmetry that uniquely defines a crystal structure, and may contain multiple molecules⁽³²⁷⁾. Crystal systems are utilized to describe the shape of the unit cell for example hexagonal, cubic etc. Lattice parameters describe the size of the unit cell. Unit cells are repeated throughout the material to produce crystal grains composing the material.

Crystal structures endeavour to reside in the lowest energy format, which develops symmetry of crystal structures to minimise energy. These symmetries often produce the bulk material properties and behaviour, from which symmetry elements are used to define seven different crystal systems⁽³²⁸⁾. Table 10 shows the seven crystal systems and associated properties.

Crystal System	Bravais Lattices	Symmetry	Axis System
Cubic	P, I, F	m3m	$a = b = c,$ $\alpha = \beta = \gamma = 90$
Tetragonal	P, I, F	4/mmm	$a = b \neq c,$ $\alpha = \beta = \gamma = 90$
Hexagonal	P, R	6/mmm	$a = b \neq c,$ $\alpha = \beta = 90, \gamma = 120$
Rhombohedral	R	3m	$a = b = c,$ $\alpha = \beta = \gamma \neq 90$
Orthorhombic	P, C, I, F	mmm	$a \neq b \neq c,$ $\alpha = \beta = \gamma = 90$
Monoclinic	P, C	2/m	$a \neq b \neq c,$ $\alpha = \gamma, \beta \neq 90$
Triclinic	P	1	$a \neq b \neq c,$ $\alpha \neq \beta \neq \gamma \neq 90$

Table 10 - Seven Crystal System Denoted by Symmetry⁽³²⁷⁾

Miller indices (hkl) are utilized to identify the different planes of atoms, with diffraction peaks relating to the atomic structure and their microstructure of the sample⁽³²⁹⁾. This permits analysis of the unique crystal structure and therefore identification of the specific material. The Miller indices define the reciprocal of the axial intercepts, with crystallographic direction [hkl] is the vector normal to (hkl)⁽³²⁹⁾. Therefore d_{hkl} is the vector extending from the origin to the plane (hkl) and is normal to (hkl)⁽³²⁹⁾. This vector is used in Bragg's law to determine where diffraction peaks will be observed.

Bragg's law determines the angle at which constructive interference will occur from scattered X-rays, with parallel planes of atoms producing a diffraction peak⁽³²⁹⁾. In practice most diffractometers operate with a fixed X-ray wavelength. As a consequence of fixed wavelength, specific planes will only produce a diffraction peak at a given angle of 2θ . Vector d_{hkl} is from the origin of the unit cell that intersects the crystallographic plane (hkl) at a 90° angle, and is geometric function of the size and shape of the unit cell⁽³²⁹⁾. Also required for diffraction determination is that the plane normal [hkl] is parallel to the diffraction vector s . Figure 47 represent the x-ray interaction and the determination of the Miller indices.

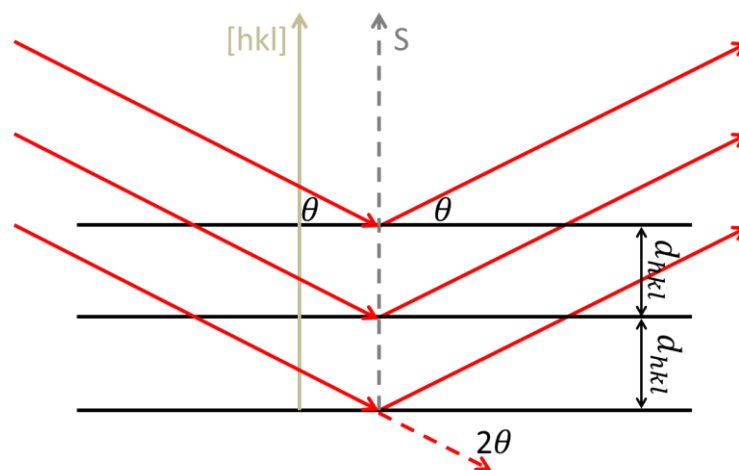


Figure 47 – X-ray Interaction in Sample and Miller Indices Diffraction^{(330) (329) (267)}

Bragg-Brentano geometry (Figure 48) is the conventional diffractometer found in laboratories generally being the most reliable design⁽³³¹⁾. Incident X-ray beam angle is ω , and is defined as the angle between X-ray source and sample. The angle between the incident

beam and detector is denoted as the diffraction angle by 2θ , and ω is always half the diffraction angle ⁽³³²⁾. In the Bragg-Brentano geometry the diffraction vector s is always normal to the sample and bisects the angle between the incident and scattered X-ray beam.

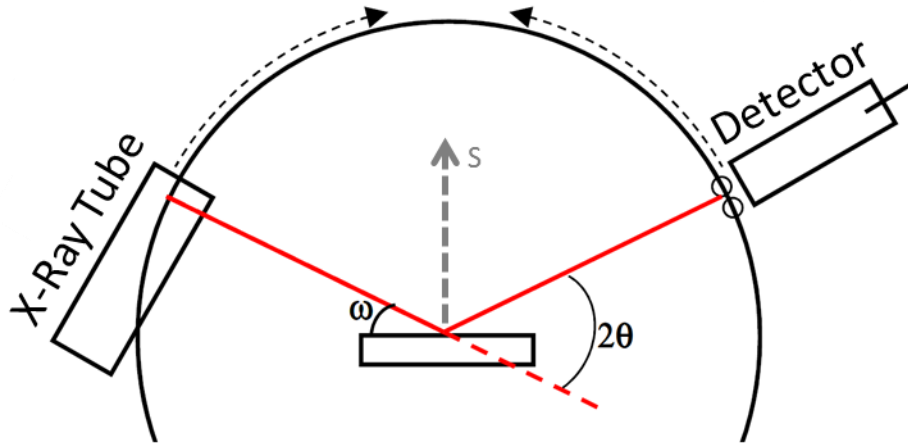


Figure 48 - Bragg-Brentano Diffraction Geometry ⁽³³⁰⁾⁽²⁶⁷⁾

Diffraction peak positions are accurately measured with XRD, allowing for characterization of homogenous and inhomogeneous strains. Homogenous or uniform elastic strain shifts the diffraction peak position. From the shift determination of the d spacing is enabled, which is the result of changing lattice constants under a strain ⁽³²⁶⁾. Inhomogeneous strains vary between crystallites or within a single crystallite, resulting in broadening of the diffraction peak which increases with $\sin\theta$. Peak broadening occurs as well from the finite size of crystallites however under these circumstances it is independent of $\sin\theta$ ⁽³²⁶⁾. If peak broadening is occurring due to both crystallite size and inhomogeneous strains, determination of these separately is possible through analysis of the peak shapes.

In the instance of no homogenous strain the crystallite size, D , can be estimated from the peak width with Scherrer's formula as determined from equation (5.3) ⁽³²⁶⁾;

$$D = \frac{K\lambda}{B \cos\theta_B} \quad (5.39)$$

In this equation λ is the X-ray wavelength, B is the full width of height maximum (FWHM) of a diffraction peak, θ_B is the diffraction angle and K is the Scherrer's constant of the order of unity for a typical crystal⁽³²⁶⁾. Nanoparticles can however distort the results of the Scherrer formula producing results different from the actual particle size, as they often form twinned structures.

XRD is predominately employed to determine the following sample characteristics⁽³²⁶⁾⁽³³⁰⁾⁽²⁶⁷⁾;

- Phase composition of a sample
 - Quantitative Phase Analysis: determine the relative amounts of phases in a mixture by referencing the relative peak intensities
- Unit cell lattice parameters and Bravais lattice symmetry
 - Index peak positions
 - Lattice parameters can vary as a function of, and therefore give you information about, alloying, doping, solid solution, strains etc.
- Residual strain
- Crystal structure
 - By Rietveld refinement of the entire diffraction pattern
- Epitaxy/Texture/Orientation
- Crystallite size and micro-strain
 - Indicated by peak broadening
 - Other defects (stacking faults, etc.) can be measured by analysis of peak shapes and peak width
- In-situ analysis capability to evaluate as a function of time, temperature and gas environment

7 - Experimental Investigation

The primary focus of this research has been the growth and modification of thin films. Film growth was achieved by thermal APCVD and modification post deposition via plasma etching. Development throughout this body of work was simultaneous for growth and etching, with progression points overlapping. The growth of thin film zinc oxide including dopant introduction and investigation of plasma modification are discussed. The first section will introduce the CVD systems employed, followed by the investigation results.

7.1 CVD System

Multiple atmospheric pressure chemical vapour deposition systems were employed to deposit zinc oxide. All systems were principally thermally activated APCVD with various geometries to enable material investigation.

7.1.1 Precursor Delivery

The selected zinc precursor was dimethylzinc triethylamine $[\text{Zn}(\text{C}_2\text{H}_5)_3\cdot\text{N}(\text{C}_2\text{H}_5)_3]$. This adducted form was selected for stability of reaction for APCVD. Introduction of multiple oxidant sources were investigated which included ethanol $[\text{C}_2\text{H}_6\text{O}]$, propanol $[\text{C}_3\text{H}_8\text{O}]$, methanol $[\text{CH}_4\text{O}]$ and ethyl acetate $[\text{C}_4\text{H}_8\text{O}_2]$. Two fluorine doping sources were investigated trifluoroethanol $[\text{C}_2\text{H}_3\text{F}_3\text{O}]$ and tetrafluoropropanol $[\text{C}_3\text{H}_4\text{F}_4\text{O}]$, and Triethylaluminium $[\text{C}_6\text{H}_{15}\text{Al}]$ for aluminium doping. As all of these precursors have a boiling point below 100°C , the delivery lines to the reaction zone were kept above 100°C to ensure they did not condense in the lines delivery the required quantity. Delivery of these precursors was achieved using nitrogen. Inert nitrogen does not interact with the precursor chemistry and is able to safely delivery the precursors to the deposition region.

System flow rates are dependent on coater geometry. Typically for the nozzle and dual flow a total flow of 6L/min of nitrogen is established for effective delivery and uniform coating. The tube coater requires slightly higher delivery of 7-9L/min for uniformity due to the large reaction volume. Susceptor temperatures remain the same for all geometries. Low temperature deposits for zinc oxide occur around $\sim 150^\circ\text{C}$ with higher temperatures reaching

~550°C. Corning Eagle glass was employed as the substrate throughout the investigation. It is a 1.1mm thick borosilicate glass with low impurities suitable for TCO applications.

7.1.2 Nozzle Coater

Nozzle geometry allows for quick investigation into multiple deposition parameters on a single substrate. The susceptor is able to move in X&Y directions allowing for up to ten coatings on a single substrate. For deposition the nozzle is lowered onto the substrate surface, sealed by a graphite ring at the base of the nozzle. Once the nozzle is sealed over the substrate, the precursor mixture is allowed flow through the inlet. As deposition occurs on the surface, the extraction around the inner inlet nozzle pulls the reacted precursor away. The extraction comprises of four feeds connected to an expansion volume to promote uniform extraction. Within the inlet nozzle is a series of waffle packs and baffles to ensure a uniform gas distribution. Deposition is conducted over a specified amount of time.

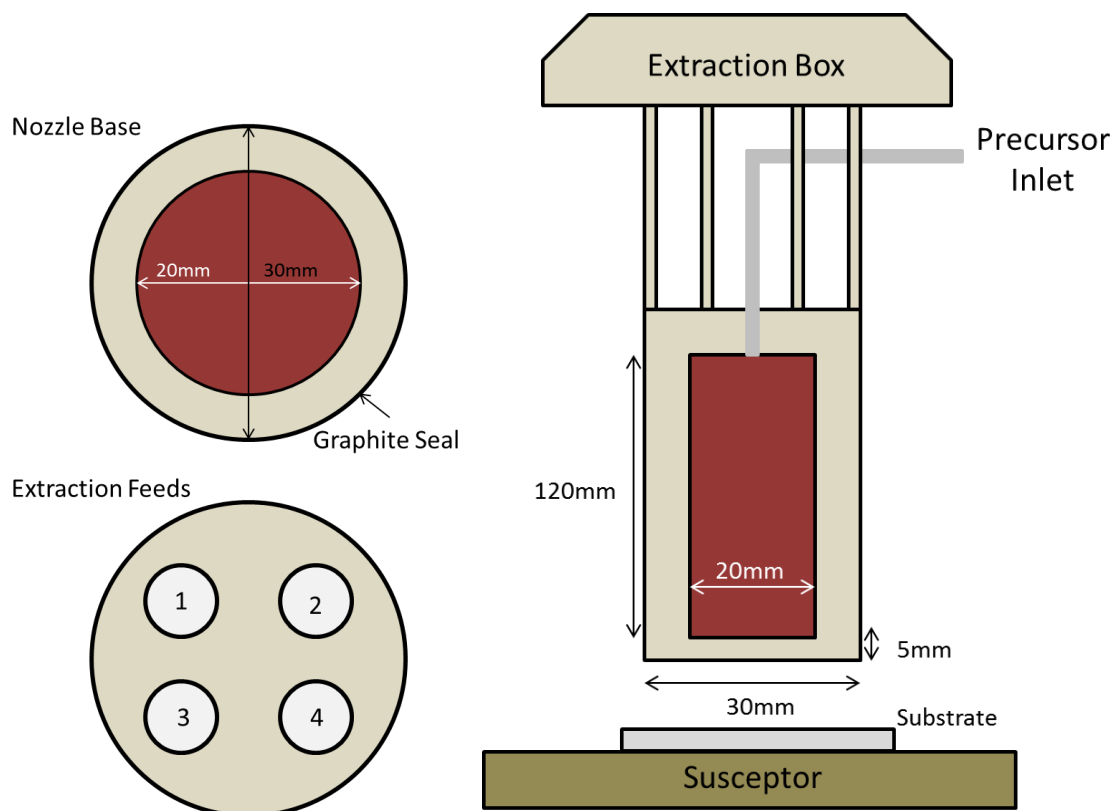


Figure 49 – APCVD Nozzle System

7.1.3 Tube Coater

Tube geometry is useful for assessing the reaction length of the precursor and composition. In this configuration the precursors are fed through the inlet slot and pass over the substrate before being extracted through the exhaust. A quartz tube comprises of the main body, with a machined flat semi-circular graphite susceptor and glass top plate defining the reaction zone. A substrate is placed on to the susceptor by access of the end plates. The CVD head consists of multiple baffles to ensure even gas mixing and distribution. The CVD head slot is machined to be level with the middle of the reaction zone to prevent any unwanted gas distribution. Deposition is conducted over a specified amount of time.

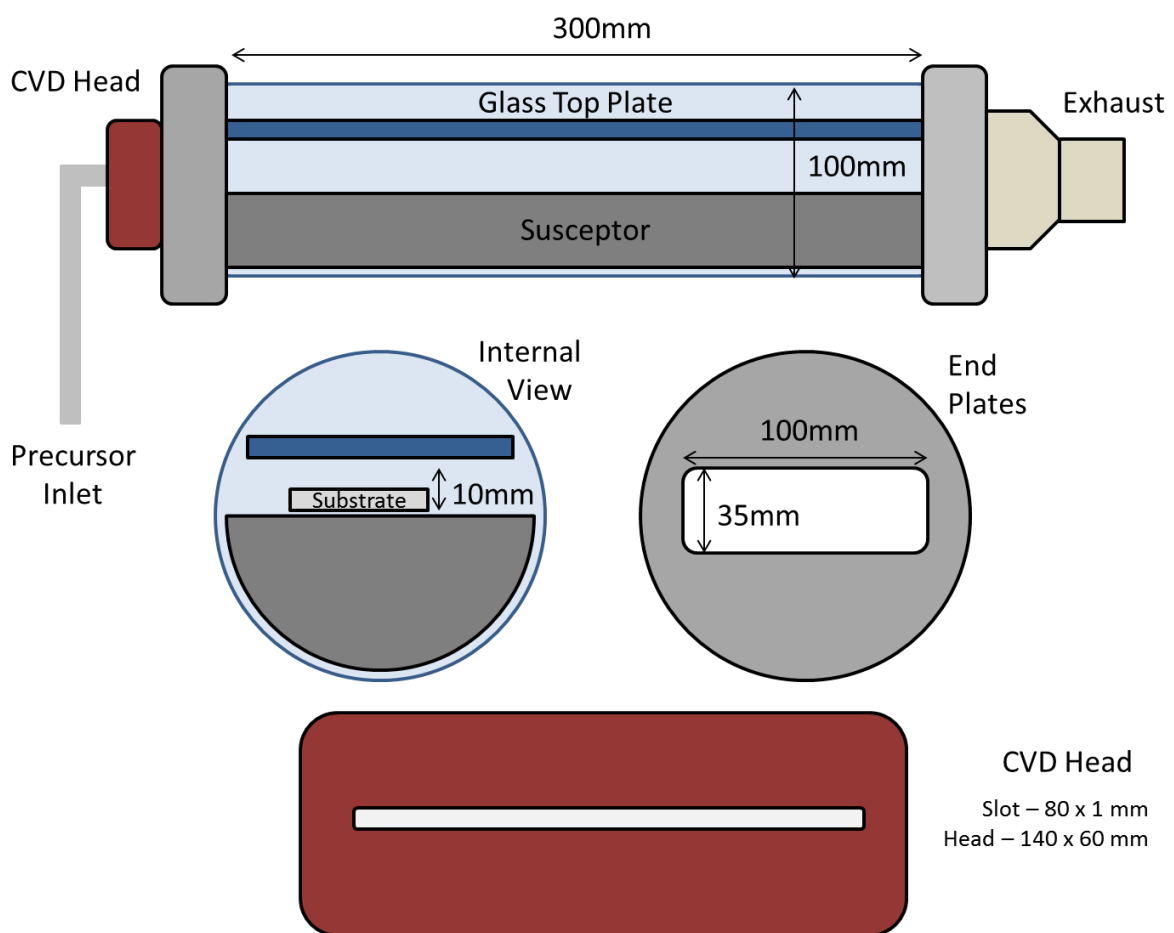


Figure 50 – APCVD Tube Coater

7.1.4 Dual Flow System

Dual flow geometry is synonymous with commercially designed CVD heads. It allows for deposition of uniform samples up to the width of the CVD head. This design essentially comprises of the gas distribution and extraction. Uniform coatings are achieved by translation of the susceptor/substrate underneath the dual flow head. Precursors are delivered through the head and extracted all around the head. The CVD head like the tube coater consist of multiple baffles for equal gas distribution and the extraction hood is equally distanced around the outside. Suitability of the distance from the head slot to the inner extraction is based on the precursors selected for deposition. Deposition is conducted through multiple passes under the head at a given speed.

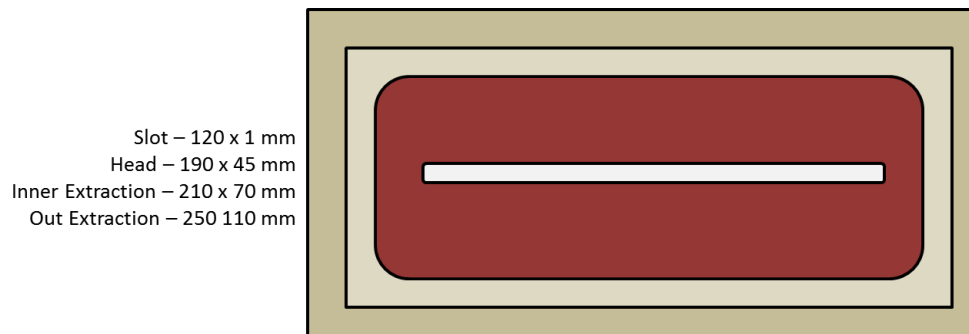


Figure 51 - Dual Flow Slot Design

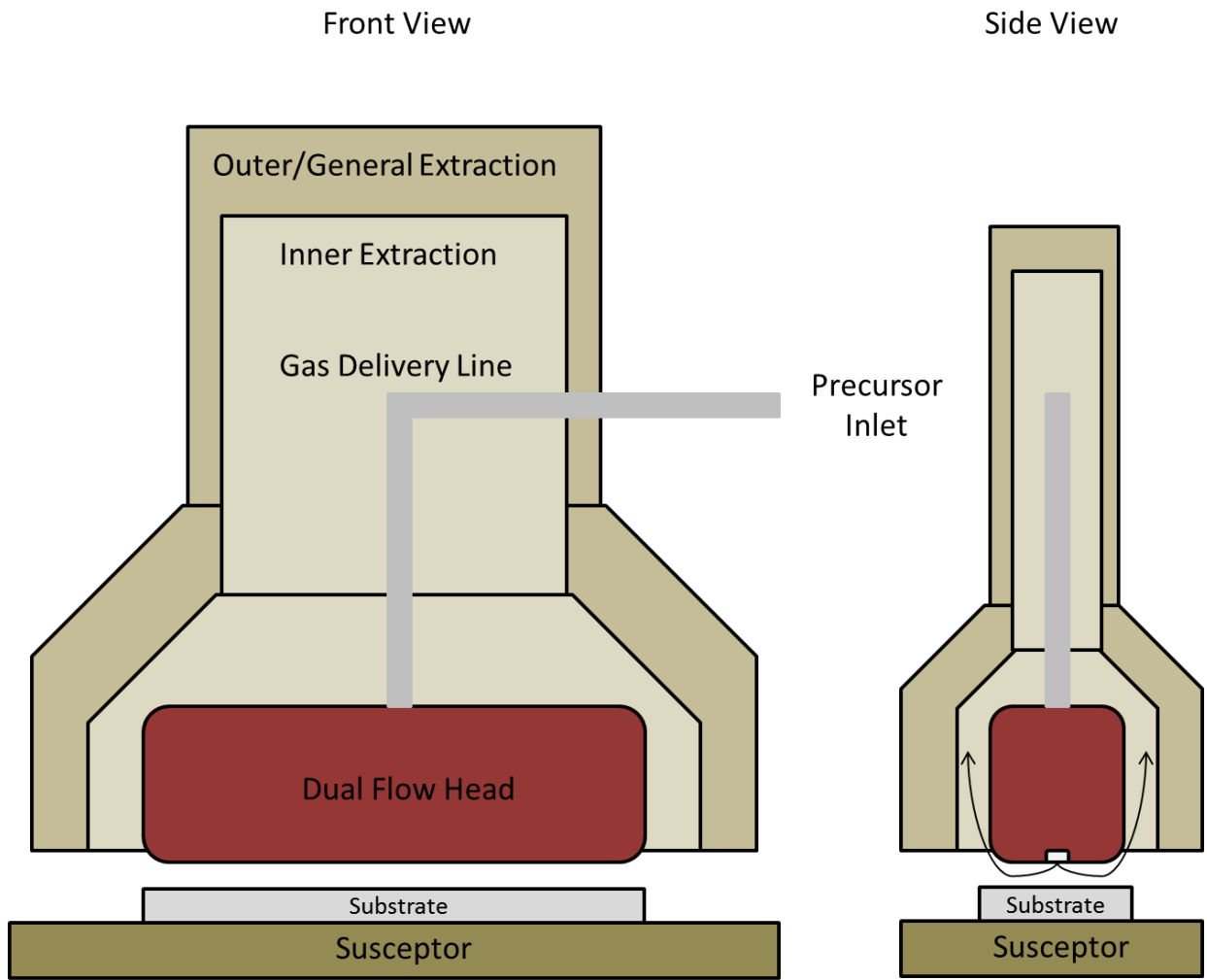


Figure 52 – Dual Flow Reactor Design

7.2 Zinc Oxide Growth – First phase

7.2.1 Initial Stages

To begin deposition the initial phase of characterization was required. This involved the determination of critical growth parameters, deposition conditions and the resultant film properties. Establishing a base line for film deposition enables further investigation for TCO production. Thermal APCVD has witnessed a number of breakthroughs with regards to zinc oxide growth^{(59) (67) (141) (45) (137) (60)}. Focus was on producing ZnO films with high conductivity through doping and optical performance applicable for integration in to PV cells.

Initial investigation with zinc oxide growth showed the development of surface morphology. Substrate temperature was a significant contributing factor influencing the surface texture of deposited films. Low temperatures (200°C) produced smooth films with very low roughness values (Rms = 11.6 nm), as shown in Figure 53.

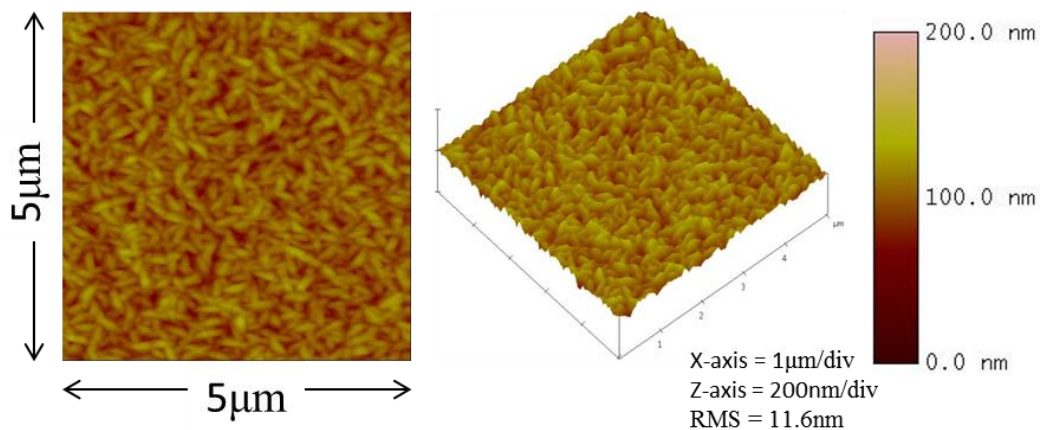


Figure 53 – Test Sample of Low Temperature Zinc Oxide Growth

A consequence of increasing substrate temperature led to pre-reaction in the gas vapour phase, resulting in powdery deposits. The limiting temperature for growth before pre-reaction occurred was approximately 300°C on the substrate surface. Investigation of this pre-reaction indicated the ethanol source to be triggering powder production. Ethanol was used to catalyse the reaction, if contaminated with water it led to the powder formation through gas phase reaction. Water reacts more rapidly than the alcohol at the elevated temperature resulting in

pre-reacted powdered deposits. Water is typically used to accelerate growth rates of oxide materials, and excessive amounts caused undesired properties. Distillation of ethanol reduced the water content sufficiently to avoid the pre reaction. Depositions utilizing the distilled ethanol yielded significantly improved results. Elevated temperature deposition was attainable, enabling production of textured films and greater potential for dopant introduction.

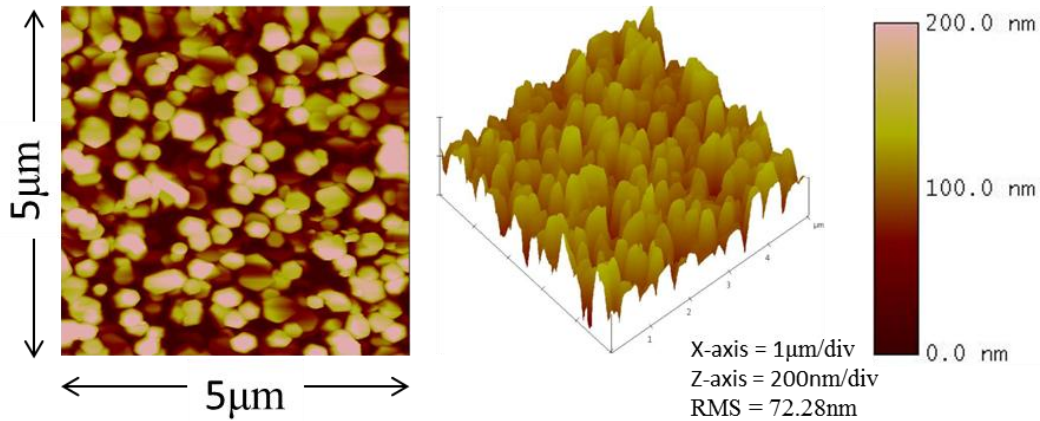


Figure 54 - Test samples of high temperature deposited zinc oxide

Deposition was established with an upper limit of 420°C on the substrate surface (545°C susceptor temperature). Temperatures beyond this limit experienced pre-reaction due to degradation of precursor in the gas phase. Deposition rate were approximately 1 μm/min producing highly textured features contributing to the average surface roughness of Rms = 72nm. Figure 54 shows an AFM image of the higher temperature ZnO deposit. Proceeding deposition iterations established a base line configuration for the system parameters. Low temperature deposits could not replicate the textured films of elevated temperatures, despite manipulation of delivery rates of the precursors.

In an attempt to retain the purity of the distilled ethanol over operational lifetime, a molecular sieve was introduced. However this resulted in unpredictable deposition, exhibiting similar pre-reaction issues as previous. A three angstrom sieve effectively captured water molecules, although it was also effective in trapping methanol from the ethanol content. Methanol may be responsible as an intermediate catalysing phase. Other possible explanations of the powder formation are further water elimination or contamination from the sieve. Water reduction

beyond distillation was unlikely due to the sieves effectiveness, however contamination was viable. R.G. Gordon⁽⁵⁹⁾ in his 1991 paper dealing with APCVD of zinc oxide investigated the introduction of water into ethanol for improved growth. This paper suggested that introducing trace amounts of water improved the surface texture with little effect on growth rate until a saturation point. Water formed an azeotrope with ethanol which makes the distillation of pure ethanol difficult. Standard ethanol has a purity of ~96% with the remaining bulk comprising of water. High purity anhydrous ethanol is approximately 99.5% pure with traces of water $\leq 0.005\%$. Our investigation of water introduction yielded no positive results, with reproducible introduction of water traces being difficult to achieve.

The testing phase of zinc oxide deposition was performed using a nozzle coater. The nozzle sealed a section of glass using a graphite seal and the inlet/outlet infrastructure was within the nozzle housing. Precursors were directed to the glass surface for deposition in the centre section and reacted by-products were extracted by the outer extraction. This design allowed for quick deposition investigation as several spots could be deposited within the susceptor area.

Initially the temperature range was studied to designate the deposition limits. At temperatures between approximately 310°C - 390°C on the substrate surface, unsatisfactory growth was observed. In this temperature window the coatings would have a 'white ring' of deposit as shown in Figure 55.

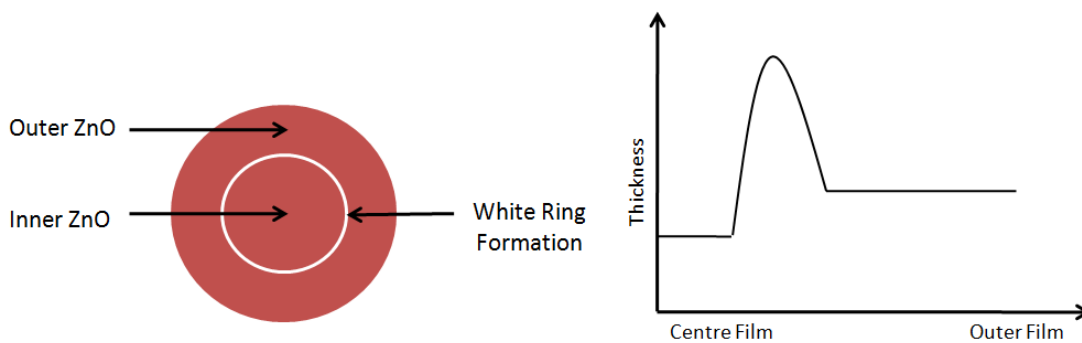


Figure 55 - White ring formation and thickness across the sample

Thickness measurements showed an increase at the ‘white ring’ deposit, with an increase in thickness to the outer edge of the sample. Film thickness was normally concentrated in the centre of exposure and reduced in thickness to the outer edges.

It is anticipated that eddy currents are formed between the gas inlet and extraction due to the sealed environment. The established eddy currents are visible post deposition with the appearance of interference fringes in the film. The lack of a suitable catalyst in the reaction for this temperature regime, suggested that the vapour caught in the eddy currents gathered sufficient thermal energy to decompose and deposit resulting in a dense powdery ring. Several explanations were formulated to identify the source of this issue, but further investigation would be required to fully understand this mechanism (surface kinetics, boundary layer diffusion, eddy currents, ethanol composition etc.). Although this may have been an artefact of the nozzle coater design.

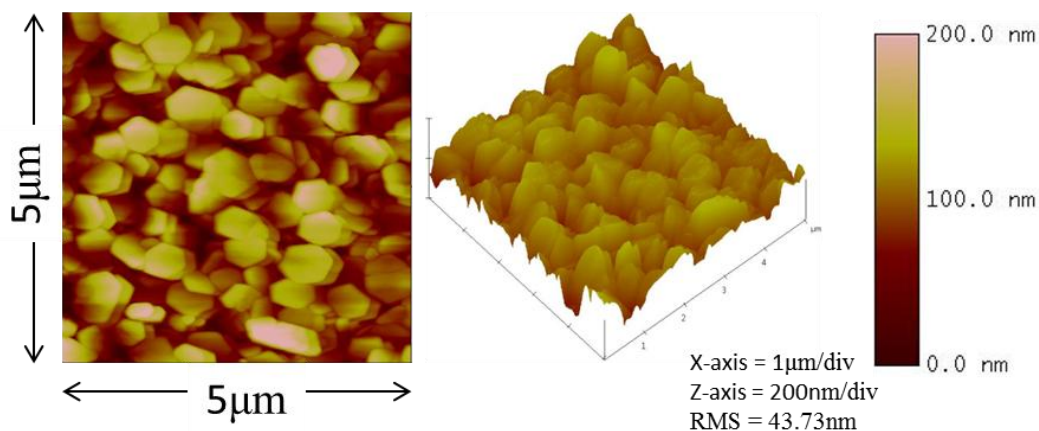


Figure 56 - Analytical grade ethanol grown - 440°C - 1 minute

Temperature was crucial for highly textured deposition and ethanol purity was essential to attain the desired temperature. Regulation of the purity of the ethanol source has led to the use of distilled analytical grade ethanol. Growth rates appeared initially unchanged with the previously established highly textured surface. Figure 56 is an example of the zinc oxide growth with the distilled analytical grade ethanol. The initial stages of deposition were undertaken to establish a set of base line conditions from which to operate. Subsequently zinc oxide production was developed utilizing a thermal APCVD dual flow coater. This system

enabled dynamic deposition under the coating head for uniform film production that replicated an industrial production line.

This initial phase of investigation developed a set of conditions for effective ZnO deposition, revealing some important characteristics of the deposition process. Oxidant purity is critical for film quality and deposition at higher temperatures. With increasing temperatures the surface structure greatly changed, showing large rounded facets. This presented a structure with potential for application in TCOs. Continuing the investigation, alternative oxidant sources was observed to see the effects on the resultant structure and process conditions.

7.2.2 Alternative Oxygen Source for ZnO Growth

Alcohols offer a stable platform for oxygen introduction, allowing for a wider operational control as they break down slowly compared to water in the gas phase. They offer a more stable reaction at higher temperatures. Initial investigations revealed the consequence of water traces in ethanol. Continuing this line of investigation, alternative alcohols were employed to observe their effect. Ethanol, ethyl acetate, propanol and methanol were utilized for comparison. Propanol (2-propanol) and methanol were lab grade alcohols readily available and possessed comparable characteristics to ethanol.

Deposition was performed on an inline coating arrangement, with the baseline conditions previously established using ethanol. The dual flow coating arrangement had a central inlet and twin extracted outlets. The path length of the coating head was denoted by the distance between inlet and outlet. A heated susceptor was translated under the head for deposition of the film to occur. Thickness and uniformity was subject to the number of passes, height of the coating head and levelling. In Figure 57 the dual flow head design is shown and a schematic representation during deposition.

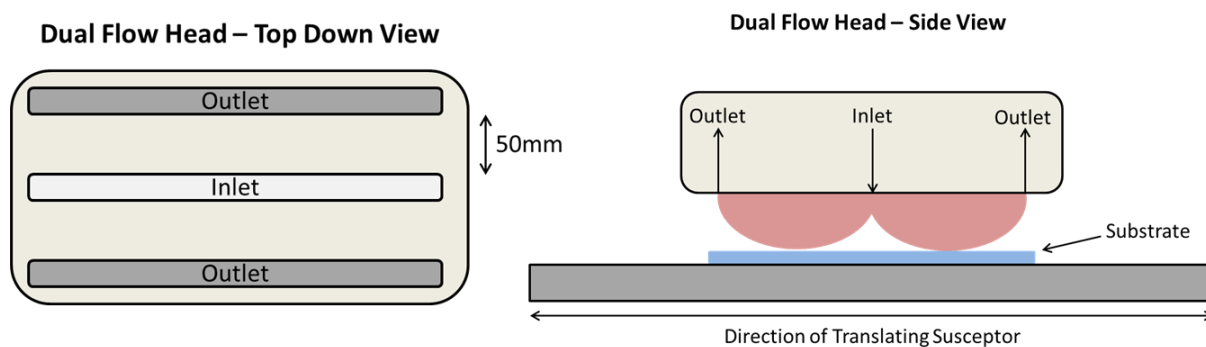


Figure 57 – Dual Flow Coater Schematic

Preliminary experimentation was to establish the number of passes required to attain comparable thickness. All samples were exposed to the same experimental conditions for comparison, which are given in Table 11.

Oxidant	Glass Temperature (°C)	Zinc Molar Flux (Mol/Min)	Syringe Driver (cc/hr)	Syringe Flow (L/Min)	Passes	Thickness (nm)	Thickness per Pass (nm)	Sample ID
Ethanol	420	9.68×10^{-4}	12	0.4	6	360	60	Ezno
Ethyl Acetate	420	9.68×10^{-4}	12	0.4	6	60	10	ETHZno
Propanol	420	9.68×10^{-4}	12	0.4	6	460	77.7	Pzno
Methanol	420	9.68×10^{-4}	12	0.4	6	330	55	Mzno

Table 11 – Growth Conditions to Establish Thickness

Emanating from this series was the similar growth rates experienced by ethanol, propanol and methanol. Ethyl acetate however grew at a significantly reduced rate; continuation with this alcohol was withdrawn from further experimentation. Drafted from these measurements was

approximate thickness per passes for each alcohol. From this the following combinations (Table 12) of passes were planned to deposit comparable thicknesses.

Combination	Passes			Thickness (nm)
	Ethanol	Propanol	Methanol	
1	6	5	7	370
2	8	6	9	480
3	9	7	10	540

Table 12 - Thickness Combinations

Combination 2 was selected for growth as it offered a thickness $\approx 500\text{nm}$ which would be suitable for our experiments. This would allow the structure to be fully developed for modification.

Oxidant	Glass Temperature ($^{\circ}\text{C}$)	Zinc Molar Flux (Mol/Min)	Syringe Driver (cc/hr)	Syringe Flow (L/Min)	Passes	Thickness (nm)	Roughness RMS (nm)	Sample ID
Ethanol	420	9.68×10^{-4}	12	0.4	8	500	19.39	Ezno
Propanol	420	9.68×10^{-4}	12	0.4	6	500	16.28	Pzno
Methanol	420	9.68×10^{-4}	12	0.4	9	500	10.47	Mzno

Table 13 - Growth Conditions for Comparable Thickness

Analysis was conducted with AFM imaging (Figure 58) for the surface structure and XRD (Figure 59) for crystal structure. Each alcohol exhibited a different texture as shown by the AFM, which was confirmed by the presence of alternative crystal structures.

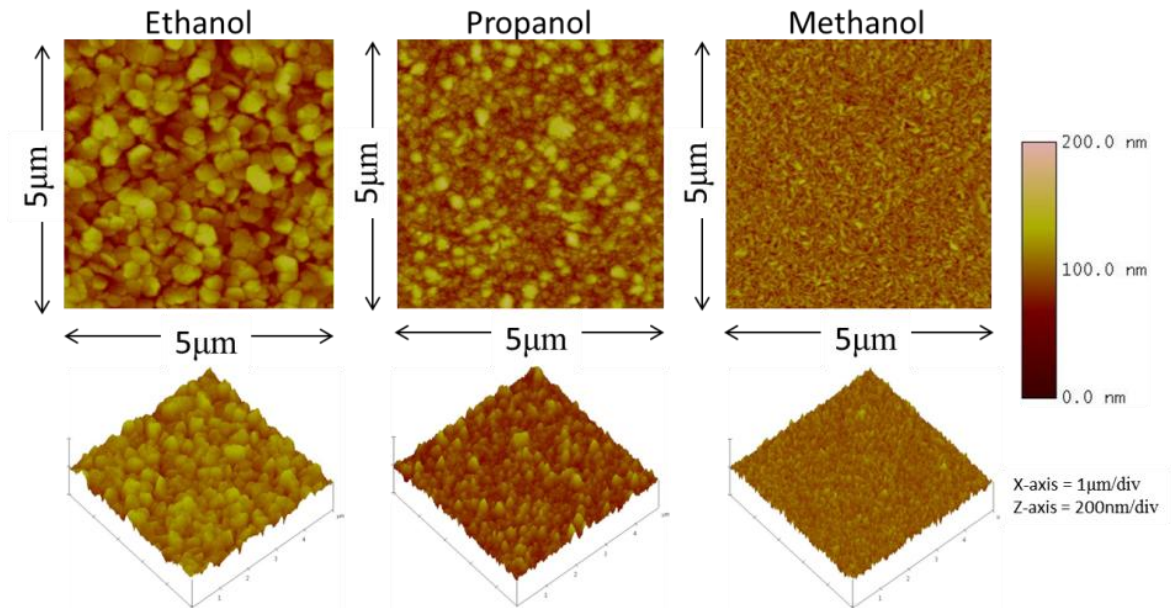


Figure 58 - 2D/3D AFM Images of Deposited ZnO with Various Oxygen Sources

Structurally ethanol and propanol exhibit a dominant $\langle 002 \rangle$ crystal peak, whilst methanol's main peak was in the $\langle 101 \rangle$ orientation. Menthol had several strong peaks but no singular dominance unlike ethanol and propanol. AFM images of ethanol and propanol illustrated the comparable structure, both exhibiting large plate like crystals and high degree of roughness. Imaging of methanol showed a very different needle like structure, corresponding to the array of crystal orientations and associated lower roughness. This also was indicative of lower growth rate, requiring increased deposition time to attain comparable thickness.

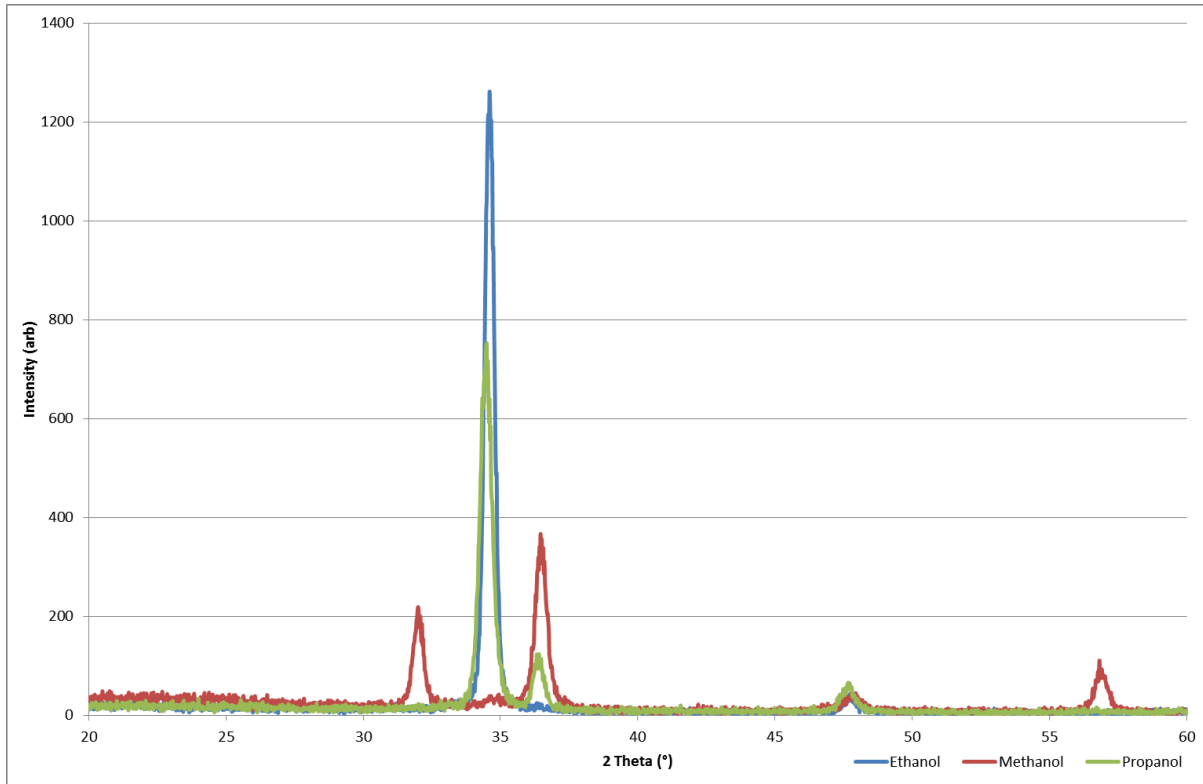


Figure 59 - XRD of ZnO Films

Wavelength (nm)	Ethanol	Propanol	Methanol
870	89.3%	87.1%	89.5%
627	85.3%	75.0%	86.8%
530	77.2%	79.5%	78.1%
455	73.7%	62.2%	79.5%

Table 14 - Transmission Data for Different Alcohols Growths

Optical transmission (Table 14) assessment was conducted on the films to observe any difference between the structures. What was noted from this data was that methanol exhibited the greatest transmission, whilst propanol had the least. Visual evaluation of the films showed a higher absorption for propanol by comparison. Carbon incorporation from the oxidant

source into the film showed as a yellow/brown colour when laid across a white background. This simple method was effective for quick comparison of the films, but full optical assessment would be required to fully interpret the film quality.

This series has revealed some particularly interesting effects with respect to zinc oxide production. It is evident that the oxygen source affected the resultant structure of the film. Crystal structure was significantly changed with methanol introduction, offering a greater number of crystal orientations. The array of crystal orientations had an effect on the resultant optical properties and consequent conductivity. Optically we required crystal features in film thickness approaching the wavelengths of incident light for effective scattering. Enhancing the scattering function of the film ultimately improved the TCO performance. Ethanol and propanol possess a dominant orientation in the $\langle 002 \rangle$ plane. The facets in this dominant orientation are approaching the desired size for effective scattering. However, it may have been the composite configuration of multiple orientation and crystal size that was most beneficial for enhanced TCO layers. Applied plasma etching of films was used to modify the structure for optical performance combined with advanced growth.

Several possible theories have been postulated to describe the mechanism responsible for the alternative zinc oxide structures. Film thickness and process conditions were equivalent; therefore the resultant structures are unlikely to stem from thickness. It would indicate that the subtle variance in decomposition at the temperature for each alcohol has led to the various crystal structures.

Alcohols share a common OH (oxygen & hydrogen) group, with their composition being described by the associated methyl groups. Singular or multiple carbon groups and relative position define the alcohol. Methanol has a single carbon, ethanol two carbons and propanol three carbons attached. The way in which this methyl group is bonded to the OH is a single chain for methanol and ethanol. However propanol can either be 1-propanol or 2-propanol, where by the methyl group is attached in a single chain or separately paired to the OH.

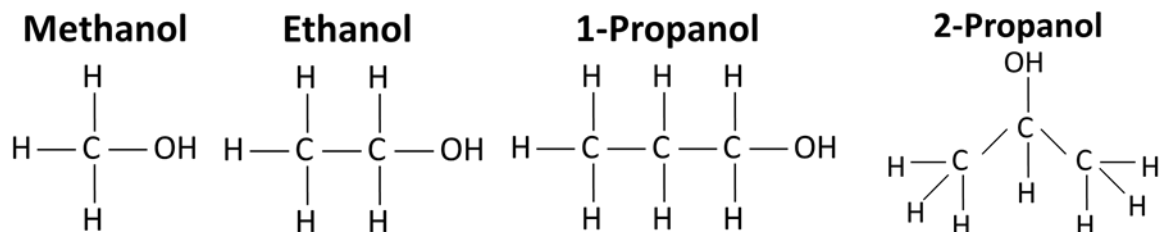


Figure 60 - Methanol, Ethanol, 1-Propanol and 2-Propanol Composition

As each alcohol has a separate configuration with the associated carbon, this may have been the condition needed for alternative crystal preference during growth. Visually what was noted after deposition was the absorption of the films. Carbon content exhibited a distinct brown/yellow absorption on a white background, separate from the colour of the film. Inspection of the films by eye showed that methanol had the least absorption whilst propanol had a significant carbon tinge to the film. Further investigation will be required to determine the optical difference and involve 1-propanol growth to observe its growth pattern. Attempts to drive alternative crystal structures through temperature and precursor variation have shown no effect. Zinc oxide had a distinct set of crystal orientations available; it appeared that the structure was determined by the alcohol incorporated. The intensity of these facets, crystal and texture, was dependent on experimental conditions. However each alcohol exhibited a distinct crystal preference when deposited, dictating the final structure. Further studies intend to introduce dopants into the precursor for developing conducting films. As a consequence of the dopant integration we may note further changes to the crystal structure and surface texture. Investigation into plasma etching will seek to resolve the preferences of etching. Controlling the film structure will prove beneficial, offering greater resolution of the plasma etching effects.

7. 3 Fluorine Doping of ZnO

7.3.1 Initial Stages

Fluorine doping requires higher temperatures for decomposition, not attainable with water contaminated ethanol. This stage of deposition was to investigate how effectively fluorine could be incorporated in the ZnO film. This was assessed by measurement of sheet resistance compared to undoped ZnO, which showed no conductivity. As part of this development a base line set of conditions was to be established for continued investigation.

Two fluorine sources were employed for comparison, trifluoroethanol and tetrafluoropropanol. During the initial investigation these dopants were added by volume ratio into ethanol and deposited using the nozzle coater arrangement. These initial depositions were conducted to test the coating requirements, enabling calculation of process parameters to effectively investigate precursor preference. Tetrafluoropropanol was implemented into the growth with little success, showing little to no conductivity despite a range of doping concentrations, varied Zn/F/Ethanol ratio and temperatures (200-550°C). Application of propanol as the oxidant source also resulted in poor growth that exhibited very limited conductivity.

Contrary to this fluorine was readily incorporated into the deposition using trifluoroethanol into the standard undoped zinc oxide growth conditions. Trifluoroethanol was successfully introduced using a 10% volume mixture into the catalysing ethanol. These films exhibited a growth rate of 1200nm over 3 minutes with a sheet resistance of 8 ohm/□. This deposition occurred at 450°C on the substrate surface, with all other process conditions remaining identical to the non-doped growth.

Block Temperature (°C)	Glass Temperature (°C)	Zinc Molar Flux (Mol/Min)	O:Zn Ratio	F:Zn Ratio	Exposure (min)	Thickness (nm)	Sheet Resistance (Ω/□)
500	450	9.68×10^{-4}	4:1	0.4:1	3	1200	8

Table 15 - Growth Conditions for Initial F:ZnO Testing

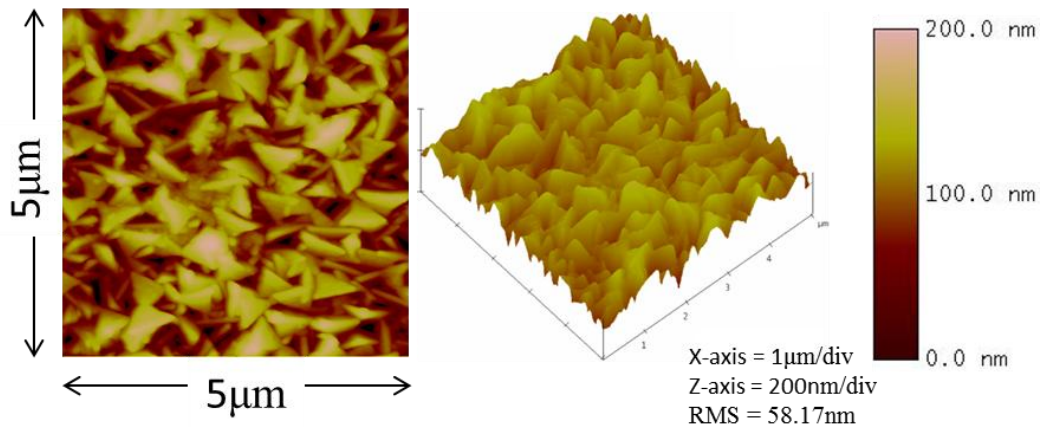


Figure 61 - F: ZnO growth - 450°C

Figure 61 is an AFM of the doped sample, which exhibited a radically changed surface morphology. The texture displayed triangular plates that emanated from the surface, suggesting they lay within the vertical axis. Several papers ⁽⁵⁹⁾ ⁽⁶⁰⁾ propose that the introduction of dopants in the film composition can lead to dramatically altered surface textures. These initial test results gave a positive change towards the desired pyramidal structure, and low sheet resistance in correspondence with thickness. Further advancements of this growth would require large area deposition for effective TCO implementation.

This series has the effective incorporation of fluorine into the ZnO deposition. Effective doping was achieved with trifluoroethanol, exhibiting the properties required for TCO applications. Further investigation will transfer this process onto a dual flow CVD system for large area coatings. As part of this process, further optimization will be required for large area coating and TCO implementation.

7.4 Aluminium Doping of ZnO

7.4.1 Initial Stages

Following the example set by the fluorine dopant, aluminium doping was introduced into the standard growth conditions. Similar to fluorine this initial trial was to assess the feasibility of aluminium doping, establishing a set of growth parameters.

Aluminium like fluorine also necessitated higher deposition temperatures for effective incorporation, with Triethylaluminium being selected as the precursor. Aluminium was configured differently to fluorine deposition, with higher line temperatures and syringe delivery. As the aluminium precursor was highly reactive it was essential to keep it separate, and within its vapour form to reduce risk of condensing in the system. Initial testing for deposition was conducted within a tube reactor. The main difference with this reactor design was that the inlet and outlet are parallel with the substrate. It allowed for better characterisation of the process conditions through observation of the deposited path length.

Path length is the distance down the substrate the film extends. If it went beyond the substrate it indicated that not all the precursor has reacted, if short the film was being deposited quickly. Tailoring the process condition in a tube reactor allowed for optimum determination of the dual flow design to work with (shorter or longer path length coating head to be selected). In Table 16 the testing conditions for aluminium depositions are given;

Sample	Glass Temperature (°C)	Zinc Molar Flux (Mol/Min)	O:Zn Ratio	Al:Zn Ratio	Exposure (min)	Thickness (nm)	Sheet Resistance (Ω/\square)	Roughness RMS (nm)
1	450	9.68×10^{-4}	4.6:1	0.14:1	3	800	15	28.28
2	500	9.68×10^{-4}	4.6:1	0.14:1	3	900	10	34.8

Table 16 - Initial Aluminium Deposition Conditions

AFM imaging (Figure 62) showed that the aluminium doping produced a highly textured surface that exhibited a large degree of roughness. The texture showed a large domed

structure that protruded from the surface; this structure was similar to the undoped material. Increasing the process temperature had amplified the size of the facets, with a corresponding increase in roughness. These films have shown an approximate sheet resistance of 10 ohm/□ at a thickness around 900nm which is suitable for TCO application.

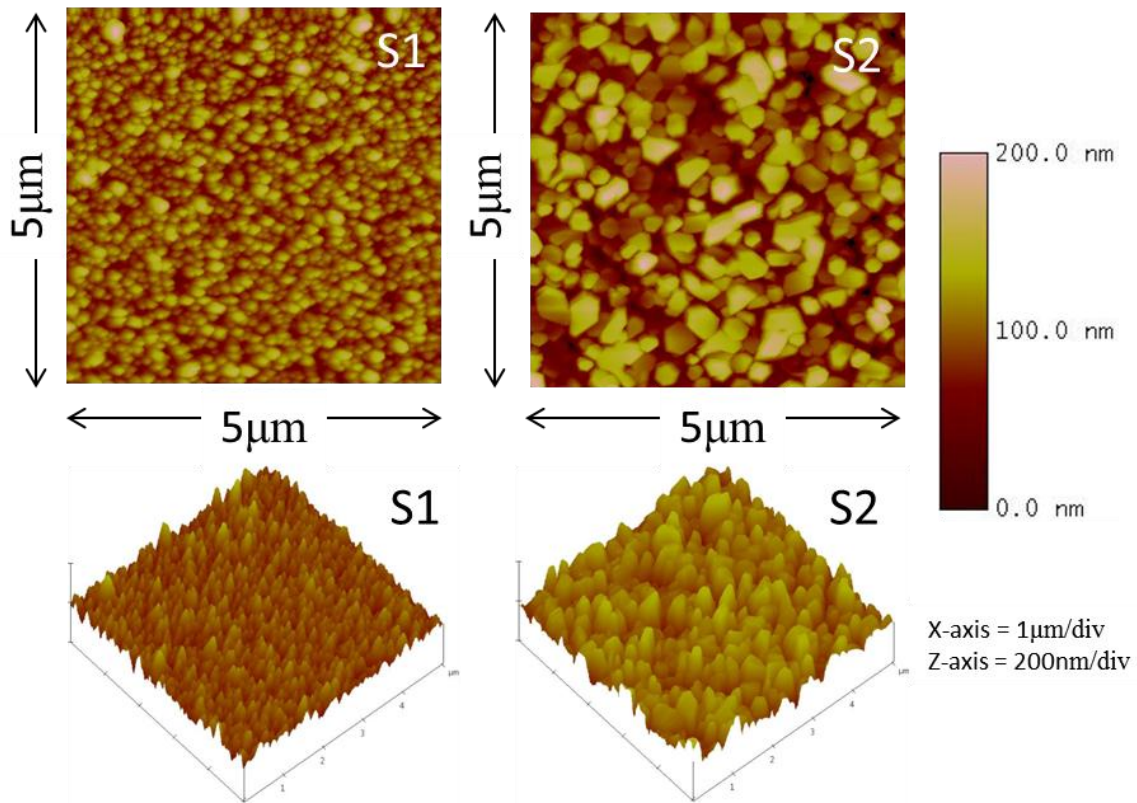


Figure 62 - AFM Images of Aluminium Doped Zinc Oxide

These initial results demonstrated the viability of the precursor as a dopant. It also highlighted that the elevated temperatures play a significant role in tailoring the surface structure. Consideration of the process conditions will be required to improve the film properties to a suitable level for TCO incorporation. A balance of optical and electrical properties will need to be achieved. Continuation of aluminium doping will look at process refinement and deposition utilizing a dual flow arrangement.

7.5 Plasma Etching System

Preliminary observations of the plasma etching system involved characterization of the system and development of a safe working protocol. As part of this the electrical layout was observed and the breakdown voltage was calculated. Residence time was also calculated and spectroscopic measurements were conducted. Determining these initial parameters enabled the continued investigation into the etching system.

Post deposition treatment methods are routinely utilized for removal of unwanted material or to modify a material structure. Chemical etching is commonly employed, which involves the risk of contamination from the hazardous working chemicals. Specialist processing conditions may require elevated temperatures and/or vacuum environment for operation. Combination of the environment and working conditions results in an expensive and potential harmful process (to the operator and external environment).

This research focused on a plasma etching system that utilizes the afterglow from an atmospheric pressure glow discharge. This was a low temperature process, where by activated species were ejected from the glow towards the sample surface. These active species interacted with the sample and etched the surface. The plasma was established by using a dielectric barrier discharge (DBD) arrangement with nitrogen as the main feedgas for discharge. High voltage and frequency discharge permitted the efficient breakdown of nitrogen at atmospheric pressure. Critical for effective etching was the uniformity of the process. This was accomplished by the application of the DBD configuration and glow discharge, which allowed stable uniform discharges for etching.

In this design the discharge was parallel to the sample, to avoid any direct interaction. Gas flow was directed through the plasma region towards the sample. A schematic of the system configuration is given in Figure 63.

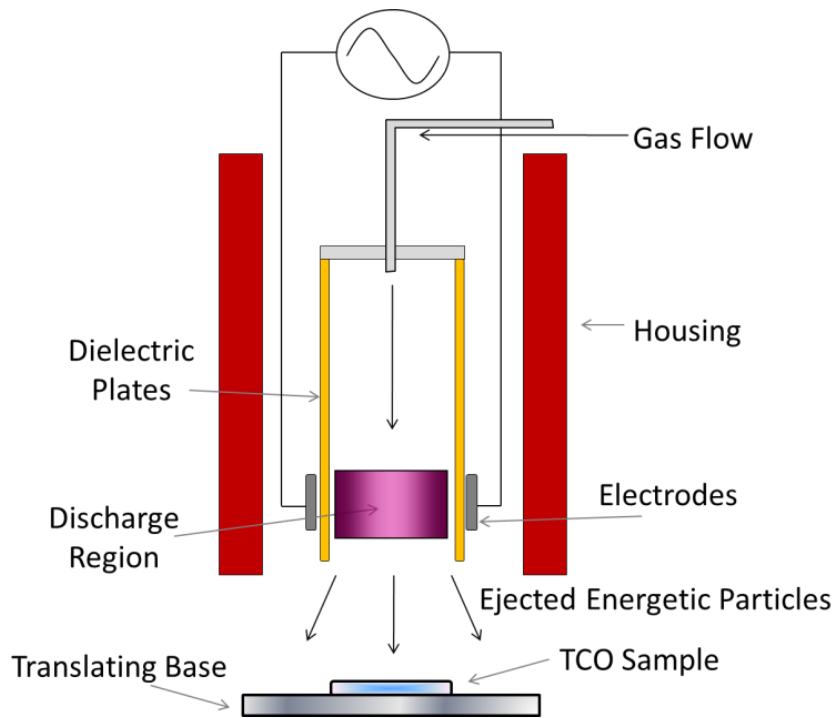


Figure 63 -Dielectric Barrier Discharge Plasma Nozzle System

Dielectrics are a poor conductor but are effective at permitting electrostatic fields. They are employed into the discharge design to localise the plasma without establishing an electrical short. Electrodes are situated on either side of the dielectrics and when the electric field was applied, breakdown of the gas occurred within this region. Nitrogen was the bulk feed gas mixture for the system, and was effectively broken down by the electrostatic field. Excited species generated in the plume were ejected from the plasma due to the gas flow direction. Etching of the sample occurred from interaction of these excited species. Waste by-products were removed by localised extraction in the housing.

Generation of the electrostatic field was from an AC supply that was tuned to first order resonance frequency. Application of resonant frequency enabled maximum transmission of electrical energy into the plasma. This reduced losses in the electrical components through heat and other sources.

To give a brief overview of the system regarding the etching process, the following flow diagram (Figure 64) gives a typical process route taken during experimentation. Additional steps may be taken for specific processing steps for example the HCl introduction and techniques to monitor the process conditions. Note not all steps of the process are explicitly listed.

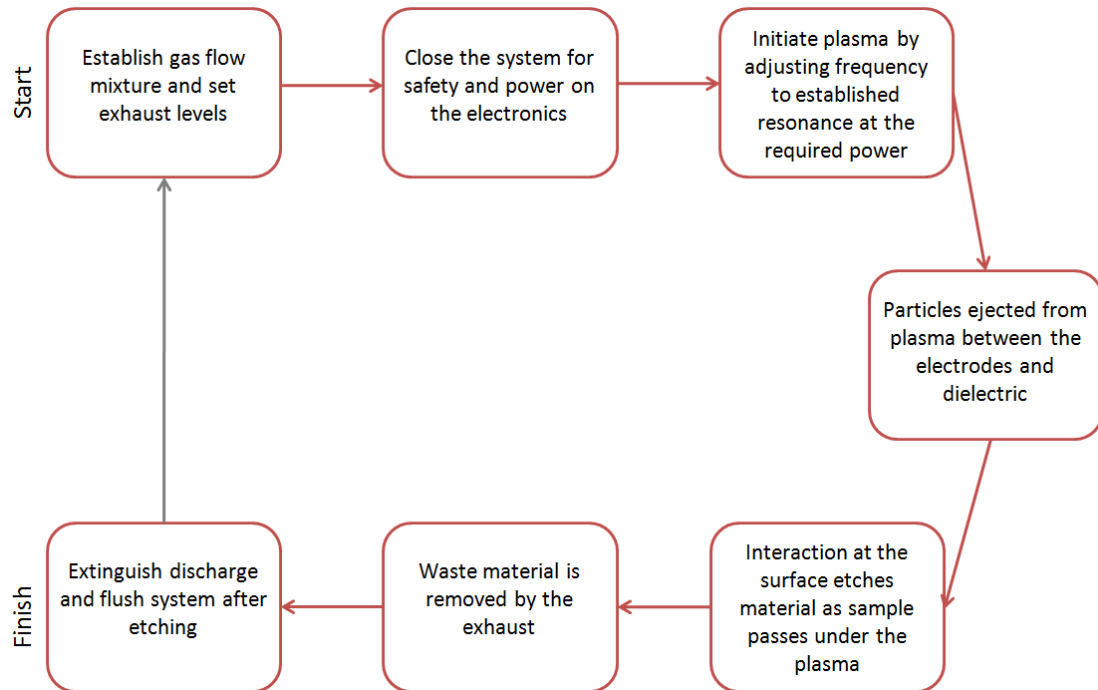


Figure 64 – Flow diagram of plasma etching process

Having conceived a work flow it was important to begin characterisation of the plasma system. The next section of work observed the route taken to refine system parameters and configuration. Within this body of work, the etching investigation was split into two sections, tin oxide and zinc oxide etching. A distinction was noted between these film compositions requiring tailoring of the etching parameters. Small quantities of hydrochloric acid (HCl) were introduced into the nitrogen flow for F: SnO₂ modification. Zinc oxide alternatively established a genuine etching effect operating with nitrogen as the bulk feed gas. The preceding sections focused on the modifications to the plasma system for improved etching followed by tin oxide and zinc oxide modification.

Establishing the plasma required a series of specific electronic components, enabling the discharge, manipulation of process parameters and measurement of the input values. Depicted in Figure 65 is the configuration required to develop and sustain a discharge. Multiple improvements have been made to several parts of the configuration, but the essential layout remained unchanged. Development of this system was conducted in house at the University of Salford by Dr Hodgkinson, and further details of this system are documented in the paper⁽³³³⁾.

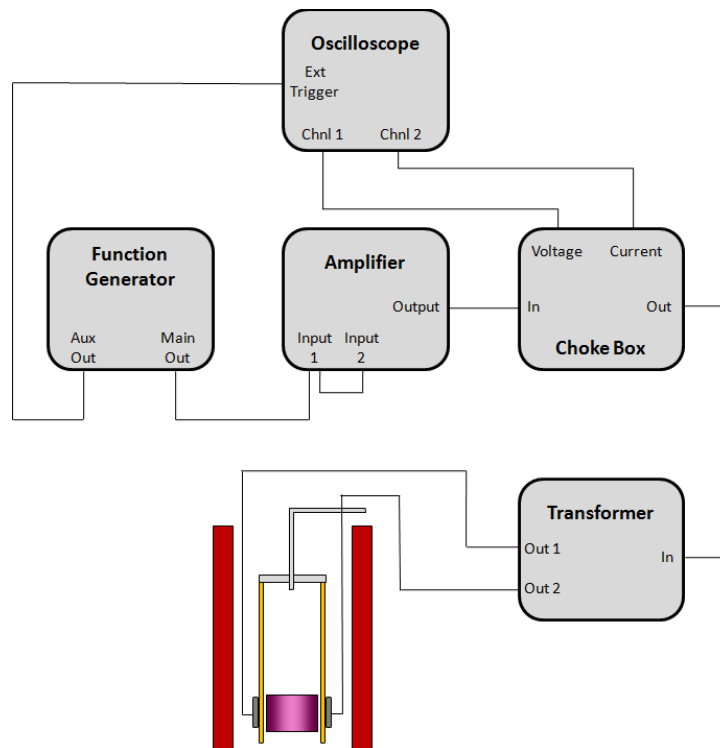


Figure 65 – Flow Chart Diagram of the Electronic Configuration Utilized to Establish the Plasma Discharge

Calculation of the power input involved the standard equations of power in relation to current and voltage. Due to the configuration of the system, measurements of the voltage only assumed half the input voltage (point of measurement takes one half of the signal generator). Power and breakdown voltage can be calculated from equation (6.1) and (5.3) respectively.

$$P = V_{in} \times I \quad (6.1)$$

$$\text{Breakdown Voltage} = 2V_{in} \times 85 \quad (6.2)$$

P - Power

V_{in} – Voltage Input Primary Side

I – Current

Also to note the transformer possesses a turn's ratio of 1:85. The breakdown voltage generated was sufficient to breakdown nitrogen and oxygen at atmospheric pressure. However these idealised calculations did not account for losses due to heat and other sources in the system.

Characterization of the plasma configuration began by uniformity assessment and establishing the residence time experienced by the sample as it travels under the nozzle. Several trial samples etched under the nozzle were analysed by AFM over the entire area. As the plasma width between the electrodes was greater than the sample size and sufficient gas distribution system the samples were uniformly etched. Minimal variation was noted in surface structure and roughness in the AFM data confirming the etching uniformity.

The width of the nozzle was noted as the separation of the dielectrics within the housing as shown in Figure 66. Activated species should be present in this area; this was established as the active etching region. Residence time was therefore depicted as the time taken for the sample to pass through the active region. Residual etching effects were omitted from this

calculation, as their contribution to accuracy was not determinable. The purpose of this measurement was to give an indication of time rendered in the active region per pass. Table 17 shows the measured times of multiple passes under the active region and equation (5.3) gives the calculated residence time.

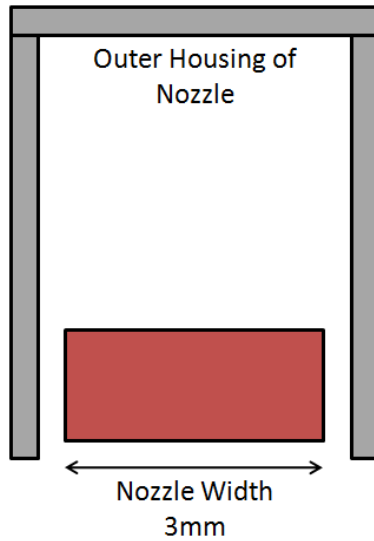


Figure 66 – Side View of Plasma Nozzle

Pass	Time (s)	Interval (s)
1	21.67	21.67
2	43.56	21.89
3	65.55	21.99
4	87.72	22.17
5	109.36	21.64

Table 17 - Residence Time of Plasma Etching System

Length of measured translation – 276mm

$109.36/5 = 21.872$ Seconds' average pass

$$Speed = \frac{276}{21.87} \quad (6.3)$$

$$Speed = 12.62 \text{ mm/s}$$

$$Residence \ Time = \frac{12.62}{3} = 4.206s \quad (6.4)$$

Etching of F: SnO₂ compared to ZnO required a small quantity of hydrochloric acid to be activated in the plasma. Exploration into the plasma discharge composition may indicate the active species responsible for etching. Assessment of the plasma was conducted by spectroscopic analysis. Spectroscopic measurements were taken of the plasma from a line of sight, pointing directly into the discharge, as shown in Figure 67. These measurements were performed by Dr J Cowpe and Dr R Pilkington through the University of Salford.

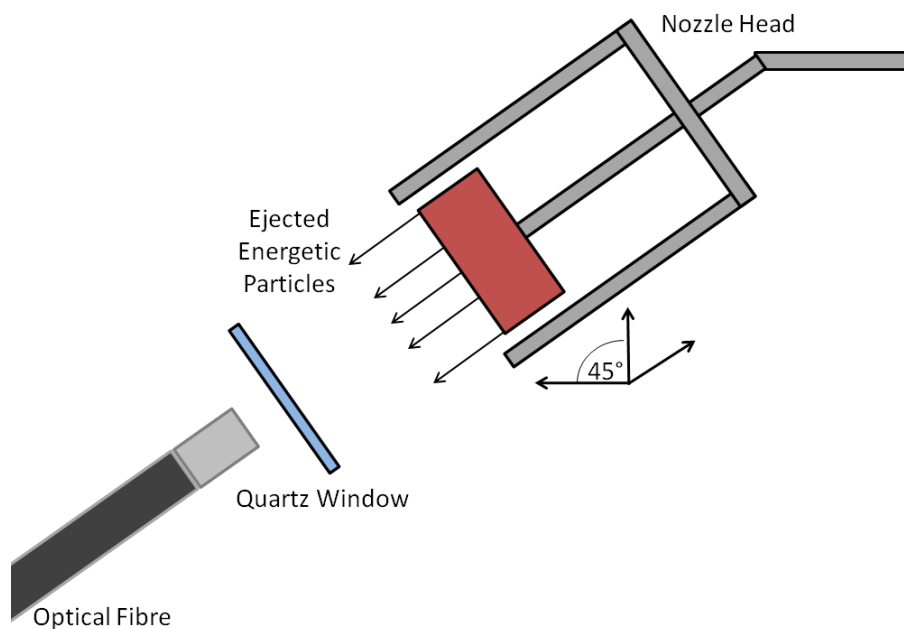


Figure 67 – Spectroscopic Setup for Plasma Analysis

Optimum collection of incident light found the nozzle angled at 45° degrees, with the optical fibre positioned within distance of the plume to fully saturate its 12° catchment angle. Quartz was introduced into the measurement field to prevent any adverse effects on the optical fibre whilst retaining optimal light transmission. Established was a standard discharge of 3.4 kHz where by the spectroscopic measurements were taken.

Analysis of the plasma from narrow slit spectroscopy confirmed the plasma was non-thermal. Observed in the spectral analysis is the high presence of nitrogen, oxygen and traces of aluminium. Interestingly the high traces of oxygen indicated several sources possibly stemming from the nitrogen cylinder, atmosphere or the alumina electrodes. Variation in the intensity of the peaks residing in the higher wavelengths varied with time during the discharge. This may have been due to small developments of filamentary discharges or excitation of oxygen sites upon the alumina plates. Despite the source of the gasses, assuming the high etching rates observed originated from interaction with oxygen and nitrogen in the discharge. Preliminary testing of added oxygen noted an increase in the etching effect, with a saturation point suppressing the effects upon reaching a critical flow level. To note the spectral analysis (Figure 68) shows the suggested species in the discharge and cannot be completely confirmed without further in-depth analysis.

Assessment of the plasma etching system has developed an operational work flow and initial system characterization. Spectroscopic measurements have shown some of the possible etchant species available in the discharge. Consideration of the available species will be critical for effective etching of films. Further work introduces improvements to the waste handling system and develops an upgraded etching environment.

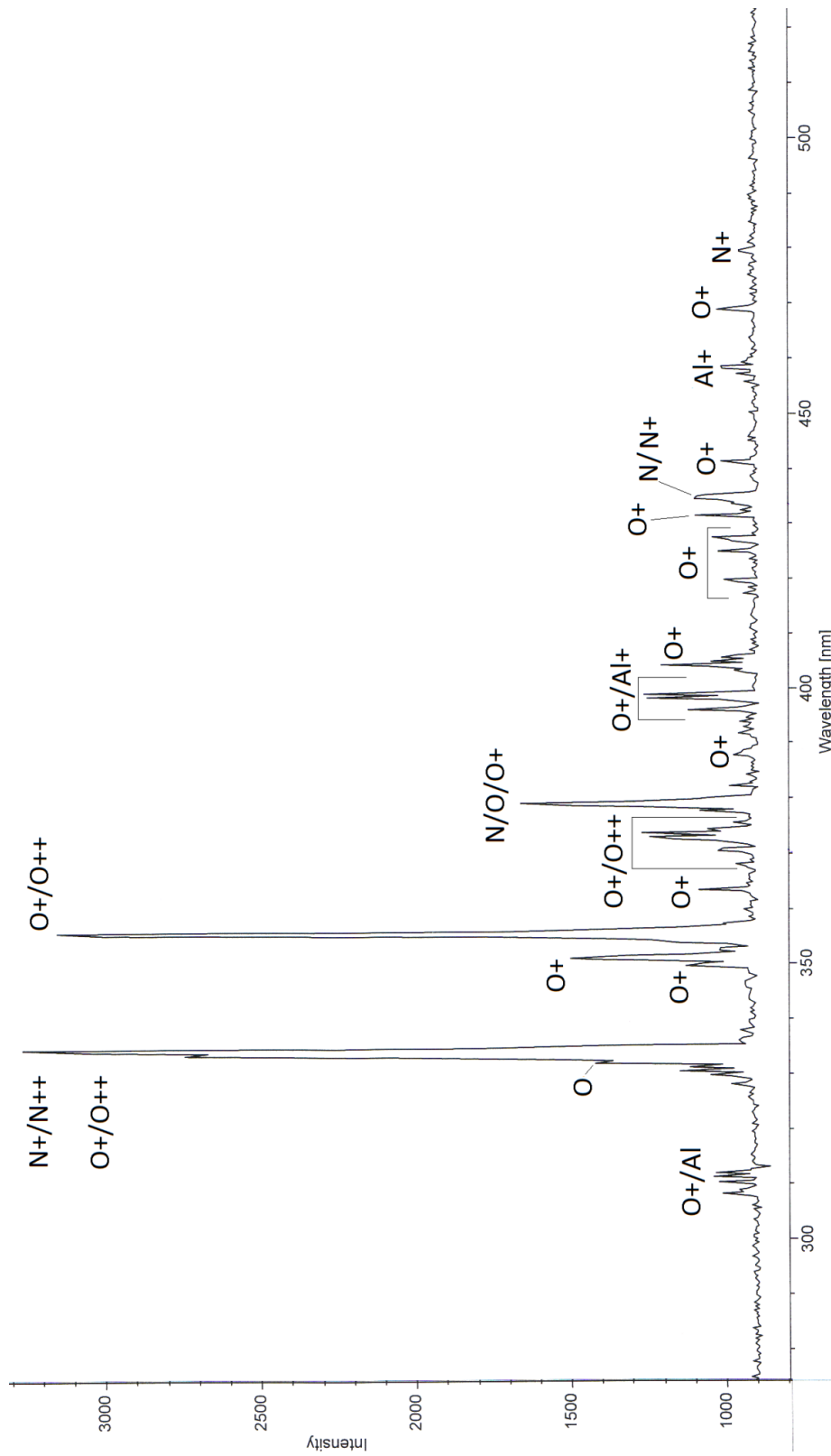


Figure 68 - Spectral Analysis of Suggested Species in the Plasma Discharge

7.6 Plasma System Modification

During the primary system calibration, some weaknesses in the configuration were encountered. Predominately the waste gas management, plasma-sample interaction and maximum flow rate capabilities. Appropriate measures were taken to resolve these issues. The following sections highlight the improvements made to the system, for an enhanced and safe operation.

After multiple cycles of the etching system it was noticed that some of the exhaust mechanism began to corrode. Vulnerable components of the fan that were particularly exposed to the chemical waste products were most affected; predominately the zinc coated screw threads to secure the fans position. Internally this corrosion formed a pool of wet chemical deposit of corroded material. Indicator paper suggested it to be of a mild acidic concentration. Condensation of HCl within the exhaust system poses a danger to the operator and the process. System design dictated that any deviation from a safe working environment was deemed unacceptable and a method to prevent any risk should be taken.

Early modification to the exhaust system introduced a bleed line (Figure 69). The idea behind this was to reduce the concentration of the chemical gas products entering the fan, and hopefully reduce the corrosion. Despite the efforts taken, little effect was gained from this modification.

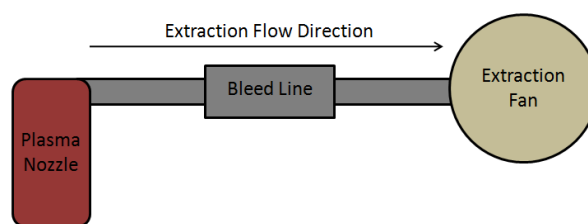


Figure 69 – Bleed line extraction system

Designing a new waste management system was required to address this issue. It was evident a preventative method would be required prior to the waste introduction into the fan. A chemical trap was decided as the best method to remove the harmful waste products from the exhaust flow. Conceived from these requirements was the introduction of a water bath into

the exhaust line (Figure 70). The water bath was positioned between the nozzle and the extraction fan, limiting the exposure of the waste gas to a short exhaust section. Employing a liquid trap enabled the waste products to be saturated by the liquid and neutralised for safe disposal.

Two concepts were introduced simultaneously into the bath design, involving a limited amount of water and marble chips. Marble chips were used routinely in chemical reactions to neutralise acids. Waste gas passing solely through marble chips would not be efficient at neutralizing the waste flow. Combination of the marble chips in water allowed for effective neutralization. This produced an alkaline solution, where by the waste products were forced to flow through, invoking the maximum interaction.

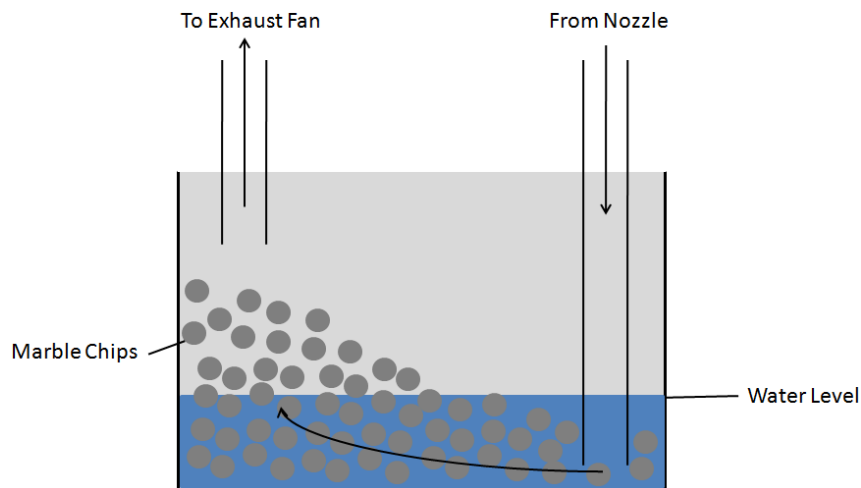


Figure 70 – Water Bath Exhaust System

Filtration of the waste products via this method was very effective, neutralizing most of the waste. This was physically observed by the significantly reduced damage to the exhaust fan, with no signs of deterioration of the metallic parts.

The new filtration system now regulated the rate of extraction which was dependent on the water level within the bath. The pressure differential encountered in the bath drew the waste gas from the nozzle and forced it to bubble through the alkaline solution. If the water level was increased above the saturation point, the pressure differential was not sufficient to break the water surface tension, resulting in no exhaust flow. With no water present in the bath,

interaction between the waste products and marble chips was significantly. Monitoring the solution level permitted optimum exhaust conditions and cleansing of the chemical waste products.

Accompanying the new exhaust/filtration system was a shroud (Figure 71) that encompassed the plasma head. This maintained the chemical gas products within the exhaust system. Reduction in ambient chemical gaseous emission was vital to retain the integrity of the surrounding equipment and any possible inhaling by the operator.

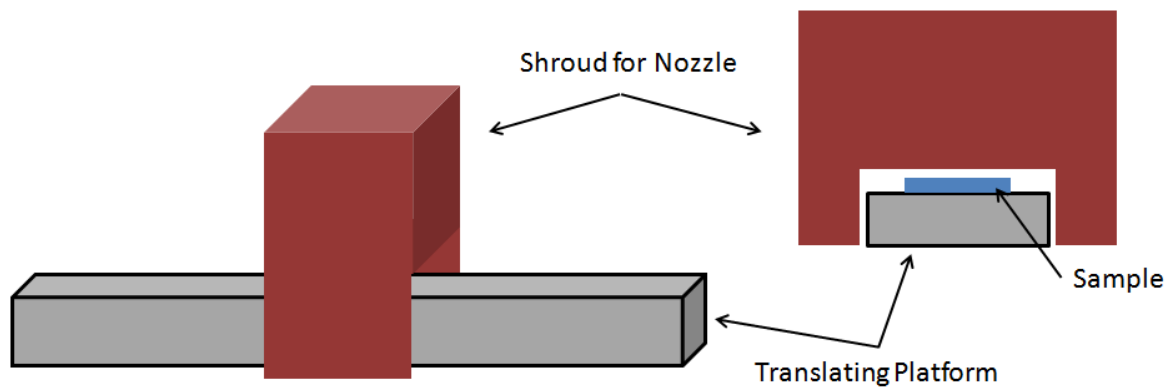


Figure 71 – Plasma Nozzle Shroud

In the course of testing the experimental procedure and process conditions, an adverse effect was discovered. Samples exposed to the discharge were becoming damaged during the cycle resulting in film and equipment degradation. Investigation of the samples under an optical microscope revealed areas of the sample with striking marks, resembling lightning strikes on the surface. Blackout operation of the etching cycle presented the evidence, with clear discharging of the plasma to the sample surface as shown in Figure 72.

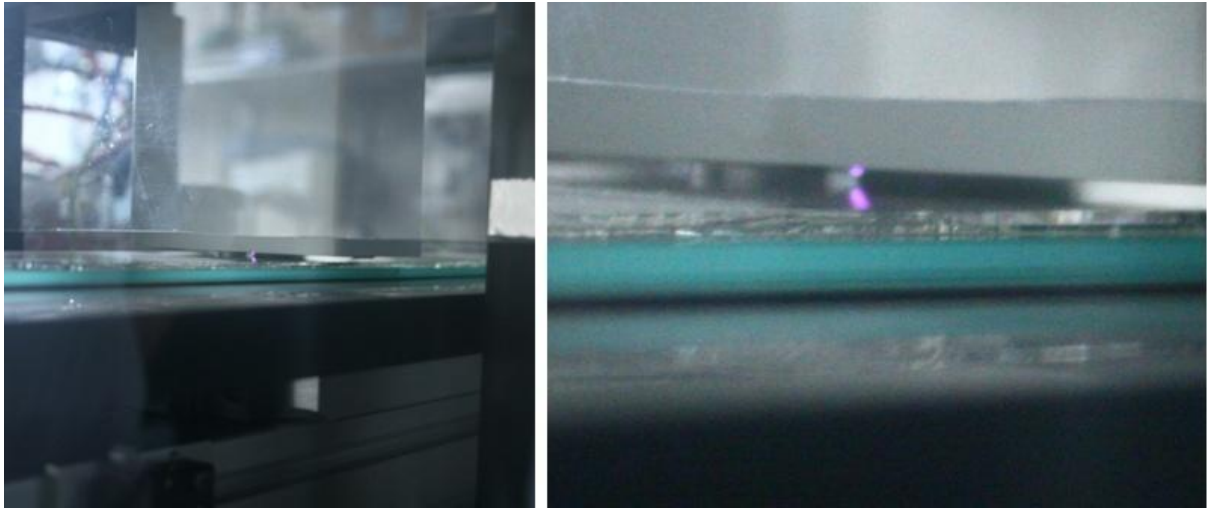


Figure 72 – Discharge Striking the Sample Surface

Adjusting the sample/electrode gap prevents the discharge striking the surface, with a summary of discharges given in Table 18. Variation of the sample spacers was explored to find the optimum distance without discharge interaction. Figure 73 shows the distances in the system configuration. During the operation cycle it was noted the breakdown for discharge predominately occurred from one site on the electrode. This may have been an area of the electrode that contained a defect site or an exposed area of electrode.

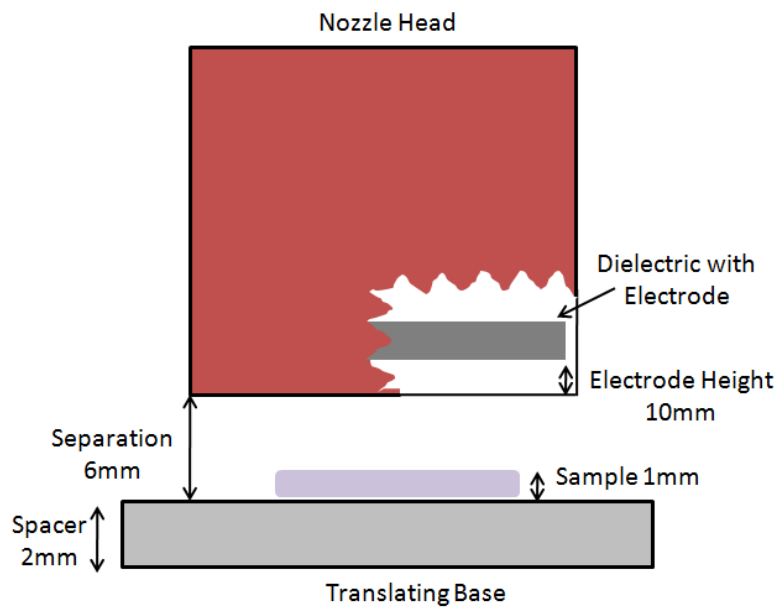


Figure 73 – Dimensions of the Plasma Nozzle with Gap Separations

Spacers Thickness (mm)	Gap (mm)	Surface Strike (Yes/No)
6	11	Yes
5	12	Yes
4	13	Yes
3	14	Yes
2	15	No
1	16	No
0	17	No

Table 18 – Plasma Discharge to Sample Gap for Surface Striking

To resolve this issue a separate head construction was utilized, with the electrodes situated higher on the dielectrics, as shown in Figure 74. This configuration neutralised plasma sample interaction and permitted higher flow rates over the sample as it could be raised closer to the gas ejection. Application of increased nitrogen flow rates above 8 L/min resulted in the sample being dislocated from the translation unit. Higher flow rate conceivably increased the number of active species ejected, enhancing the etching rate.

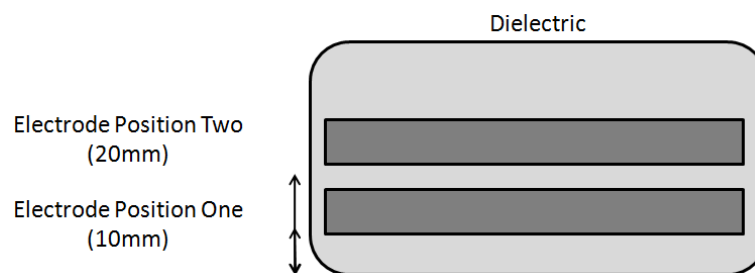


Figure 74 – Electrode Configurations on the Dielectric

Optical microscope imaging (Figure 75) of the sample shows the damage by plasma interaction. Dark contrast areas have been struck by the discharge, resulting in burn like damage to the film.

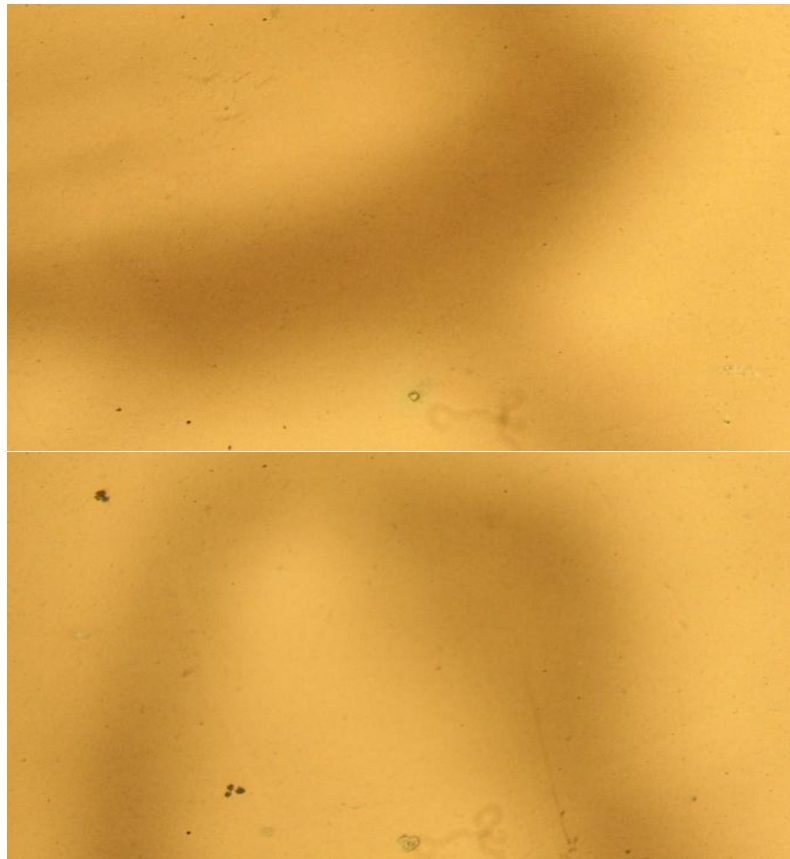


Figure 75 – Surface Burns due to Plasma-Sample Interaction

Improvements from this investigation have developed a superior waste gas handling system, effectively reducing component wear from reactive by-products. Enhancing the waste capturing element of the system, the additional housing aids the effective capturing of waste products. Investigation of the plasma to sample interaction has established the criteria for working distance and the effect of electrode position and gas flow. Further investigation will apply the system in this developed configuration, with application of varying feed gas mixtures, flow and breakdown conditions.

7.7 Plasma Etching of F: SnO₂

7.7.1 Etching of F: SnO₂

The first comprehensive investigation into the effects of plasma etching TCO films was conducted on F:SnO₂. F: SnO₂ is a common TCO product readily available in the market place and implemented in multiple commercial sectors. Preliminary experimentation had established a reference of plasma parameter from which to operate. This was produce by observation of the effects of a nitrogen based discharge, without additives to the feedgas mixture, on F: SnO₂. Table 19 gives the etching conditions for these preliminary samples.

Sample	Voltage (kV)	Current (mA)	Frequency (kHz)	Plasma Power (W)	Nitrogen (L/min)	Oxygen (cc/min)	Passes	Roughness RMS (nm)
Standard (STD)	-	-	-	-	-	-	-	44.73
S1	5.1	520	3.43	15.6	6	20	20	44.75
S2	5.1	510	3.43	15.3	6	50	20	45.09

Table 19 – F:SnO₂ Etching Conditions

AFM imaging (Figure 76) displays the roughness and three dimensional analysis of the samples. Depicted in this analysis there was no significant change to sample topography after exposure to the plasma, corresponding with a minimal change in sample roughness.

Concluded from this experiment set was that the standard discharge did not offer any potential for etching F: SnO₂. Feedstock gas mixture was not effective alone, and additional material may be required. Selection of a reactive medium could offer active species that are dissociated in the plasma for effective etching.

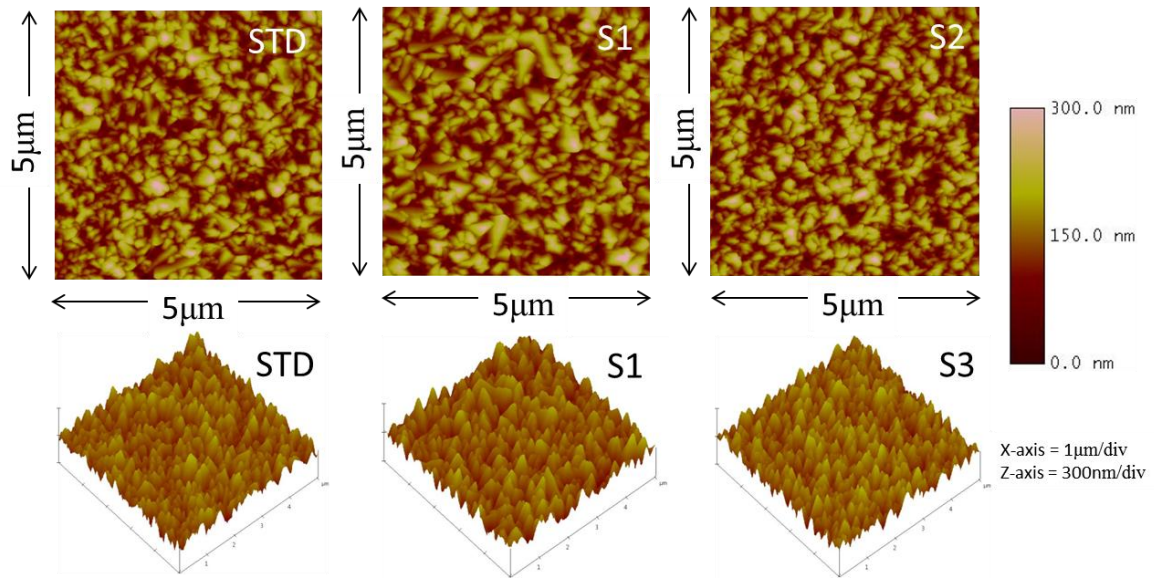


Figure 76 - AFM Images of F:SnO₂ Etching

Chlorine is commonly used for microelectronic etching. Addition of a chlorine source into the feedstock mixture was investigated. Early indications involving trace quantities of the HCl into the feedstock were very distinct, altering the samples surface. Figure 77 is an example of the nature of HCl active etching, and the next stage of investigation was to observe further HCl active etching.

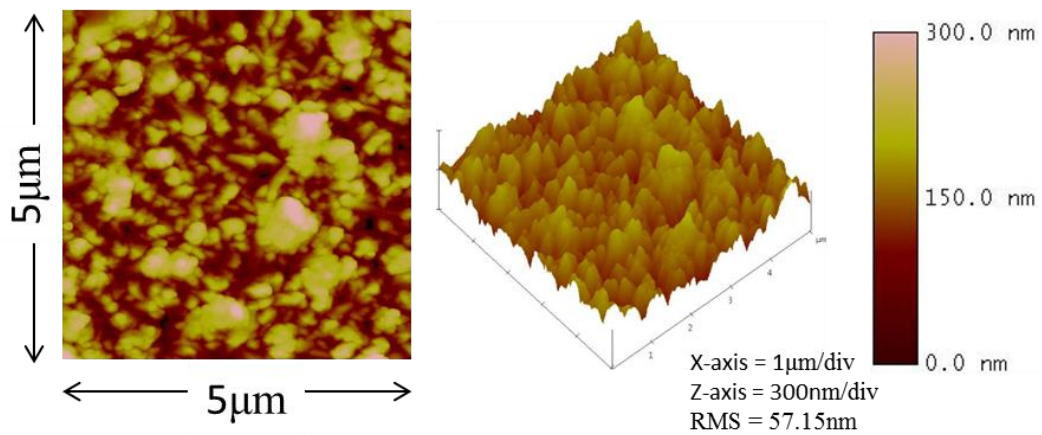


Figure 77 - Initial Trial of HCl Plasma Etching of F:SnO₂

7.7.2 Activated Chemical Etching of F: SnO₂

Chemical activation was required for effective etching of F: SnO₂ via the plasma discharge. Hydrochloric acid (HCl) was the chemical employed, which is dissociated in the plasma. SnO₂ is a resilient material, impervious to wet HCl etching within a reasonable and exploitable industrial time scale. The remote nitrogen based plasma discharge did not etch the material. Application of dissociated chlorine into the etching plume however enabled the effective etching (Published 2011; Journal of Nanoscience and Nanotechnology⁽³³⁴⁾).

Investigation into the etching properties of the HCl activated plasma led to four distinct experiments. This involved manipulation of flow rates, discharge power and sample-discharge gap. Assessment of the samples was conducted primarily by AFM to observe the surface structure, in conjunction with this optical and Hall measurements. Additional analysis included observation by SEM & EDAX for detailed observation and compositional analysis. Four distinct sample sets (Series A-D);

- A. Nitrogen flow rate change
- B. Low and high powered discharge
- C. Reduced sample/electrode gap
- D. Increased sample/electrode gap

Surface modification was of the main criteria of the etching system, and from the above series the most significant results were chosen to be examined further, with the etching parameters shown in Table 20. Exploitation of the etching system with regards to F:SnO₂ demonstrated a subtle etching effect as shown in the AFM images (Figure 78), that primarily etched the smaller surface facets, exposing the larger crystal grains. This was reflected in the roughness analysis of the surface with variation from the standard being noted dependant on the administered etching cycle. Through the series of experiments the most interesting results belonging to Series B, with exaggerated etching effects being exemplified by the low/high powered etching parameters.

Sample	Voltage (kV)	Current (mA)	Frequency (kHz)	Plasma Power (W)	HCl Flow Rate (cc/min)	Nitrogen (L/min)	Passes	Gap (mm)	Roughness RMS (nm)
Standard (STD)	-	-	-	-	-	-	-	-	46.51
A1	6.8	755	2.979	30.3	0.3	6	20	15	48.8
B2	5.1	541	3.314	16.2	0.2	6	20	15	48.76
B3	8.3	735	2.882	35.7	0.3	6	20	15	44.87

Table 20 – Plasma Etching Conditions of Chemically Active Etching of F: SnO₂

Scanning electron microscopy permitted high resolution imaging of the sample (Figure 79). In this selection we compared the etched samples to the un-etched standard film. The high magnification and wide view portrayed in SEM images gave indication to the overall surface texture of the film. Marking of the particular facets of interest permitted inspection of facet size and how the etching parameters influenced them. Furthermore careful inspection of the images gave some early indication of the facets which became readily etched under the plasma influence.

Optical measurements assess the films characteristic before and after exposure to the plasma discharge. Table 21 are the calculated values from the measurements. Observation of the optical data enables assessment of the etched film properties and potential benefits of the etching regime. Subtle variation in transmission, absorption and scatter are witnessed across the several wavelengths as shown in (Figure 80). Despite these samples showing the most significant change in surface features towards larger pyramidal structure, the optical parameters show no significant alteration. Each wavelength has responded differently to the changing surface structure. With variation in wavelength response based on feature size, a trade of in beneficial optical response is noted.

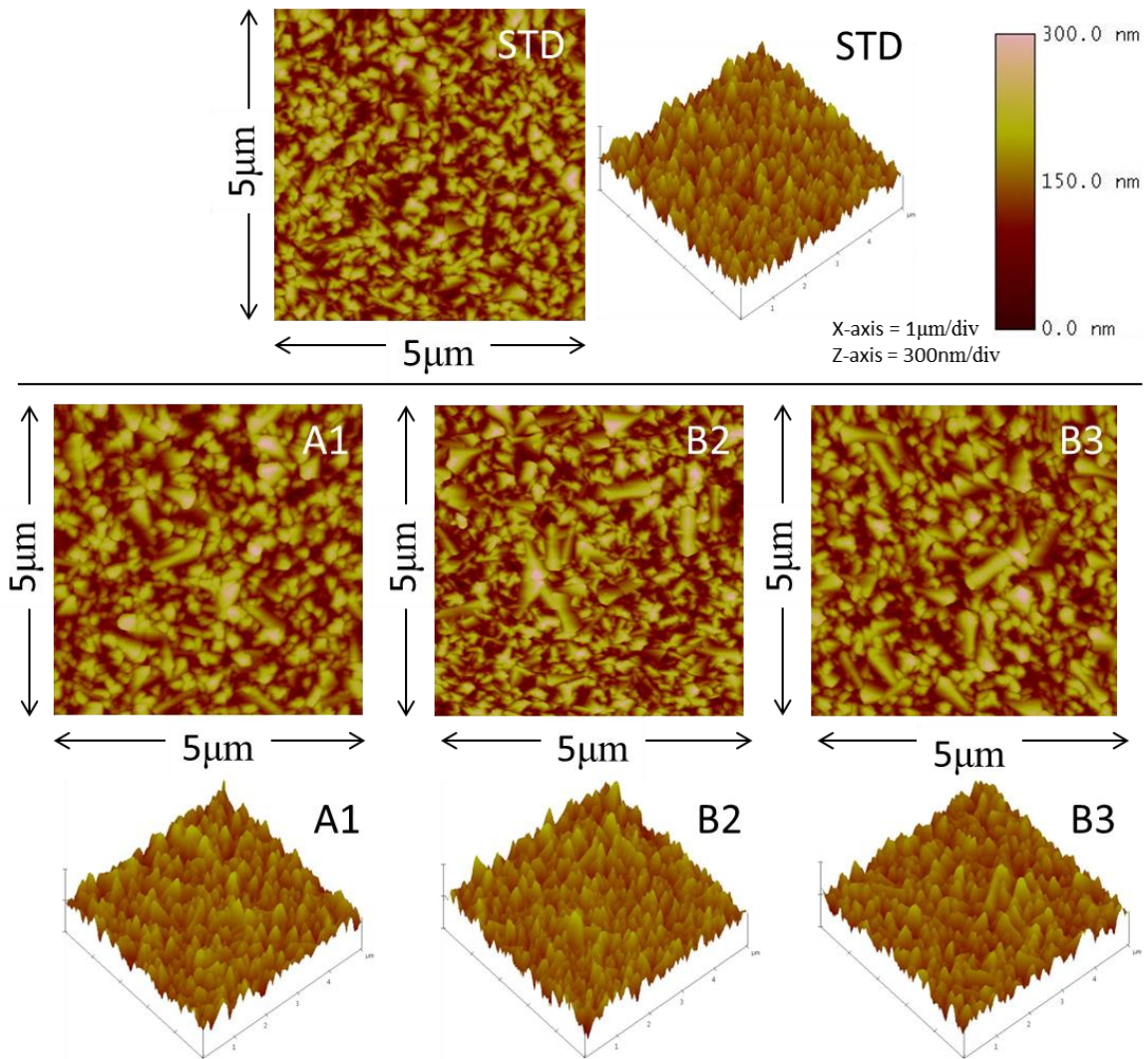


Figure 78 - AFM Imaging of Chemically Active Etching of F: SnO₂

Magnification 100,000x

Magnification 50,000x

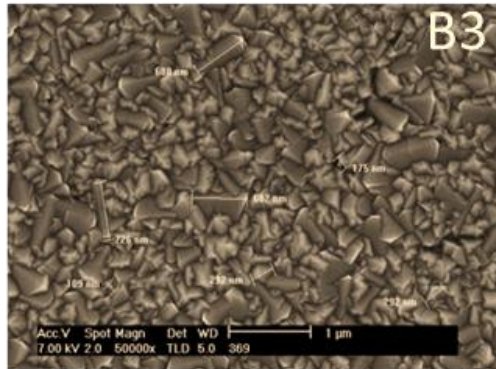
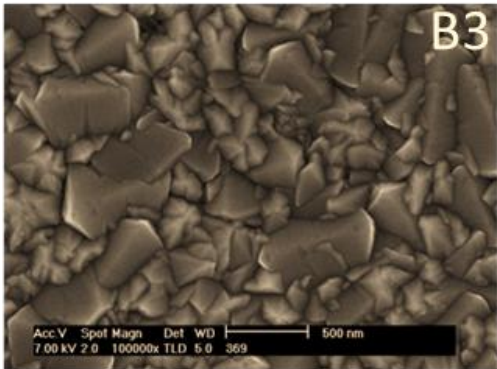
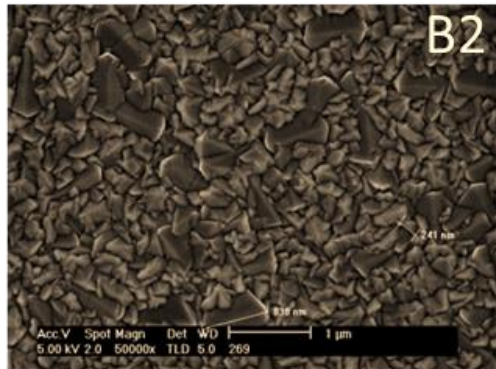
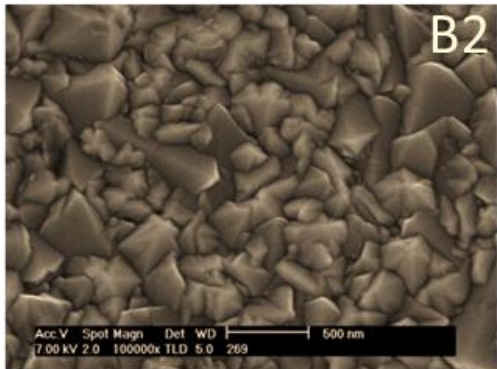
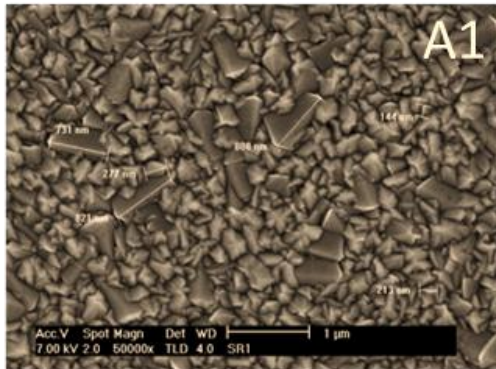
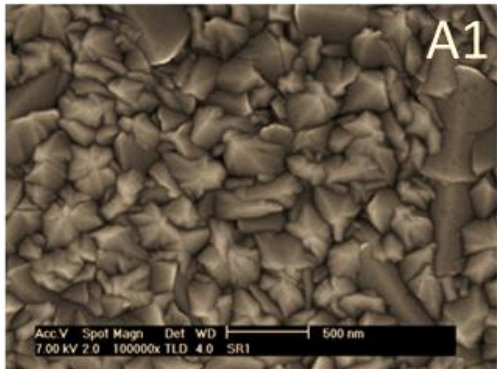
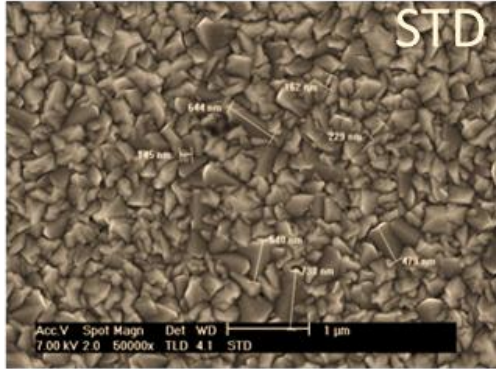
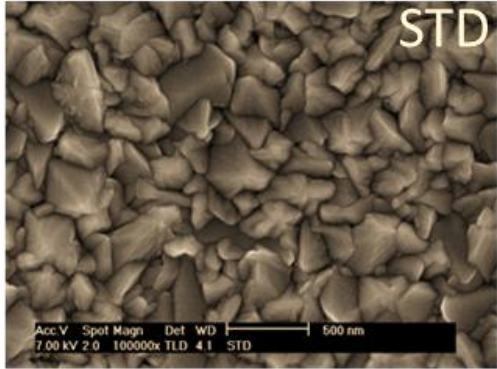


Figure 79 - SEM Imaging of Chemically Active Etching of F: SnO₂

Wavelength 870nm							
	Transmission	Hf(Io)	Hf(T)	Hr(Io)	Hr(Sp)	Sp	Abs
STD	86.80%	1.90%	2.20%	3.00%	47.50%	3.70%	6.60%
A1	85.40%	2.80%	3.30%	0.90%	13.90%	5.80%	7.90%
B2	86.00%	2.70%	3.10%	2.20%	31.50%	5.00%	6.80%
B3	82.90%	1.80%	2.20%	2.10%	24.50%	6.90%	8.10%

Wavelength 627nm							
	Transmission	Hf(Io)	Hf(T)	Hr(Io)	Hr(Sp)	Sp	Abs
STD	80.70%	5.30%	6.60%	3.50%	33.60%	6.90%	8.90%
A1	80.60%	5.30%	6.60%	2.40%	27.40%	6.20%	10.80%
B2	80.60%	7.00%	8.70%	3.30%	36.90%	5.80%	10.20%
B3	82.50%	5.30%	6.40%	2.50%	27.50%	6.60%	8.40%

Wavelength 530nm							
	Transmission	Hf(Io)	Hf(T)	Hr(Io)	Hr(Sp)	Sp	Abs
STD	78.30%	9.10%	11.60%	2.60%	30.90%	10.30%	8.80%
A1	78.40%	9.30%	11.80%	3.20%	41.80%	8.70%	9.70%
B2	77.20%	10.70%	13.90%	4.30%	56.80%	7.20%	11.30%
B3	78.40%	8.10%	10.40%	2.30%	26.80%	10.50%	8.80%

Wavelength 455nm							
	Transmission	Hf(Io)	Hf(T)	Hr(Io)	Hr(Sp)	Sp	Abs
STD	73.40%	14.20%	19.40%	4.10%	55.90%	6.40%	16.10%
A1	72.30%	12.80%	17.60%	3.40%	37.80%	8.60%	15.70%
B2	72.30%	15.30%	21.20%	4.80%	62.70%	6.10%	16.80%
B3	74.90%	13.10%	17.40%	4.10%	51.30%	7.00%	13.90%

Table 21 – Optical measurement calculated data of the F: SnO₂ etching experiment

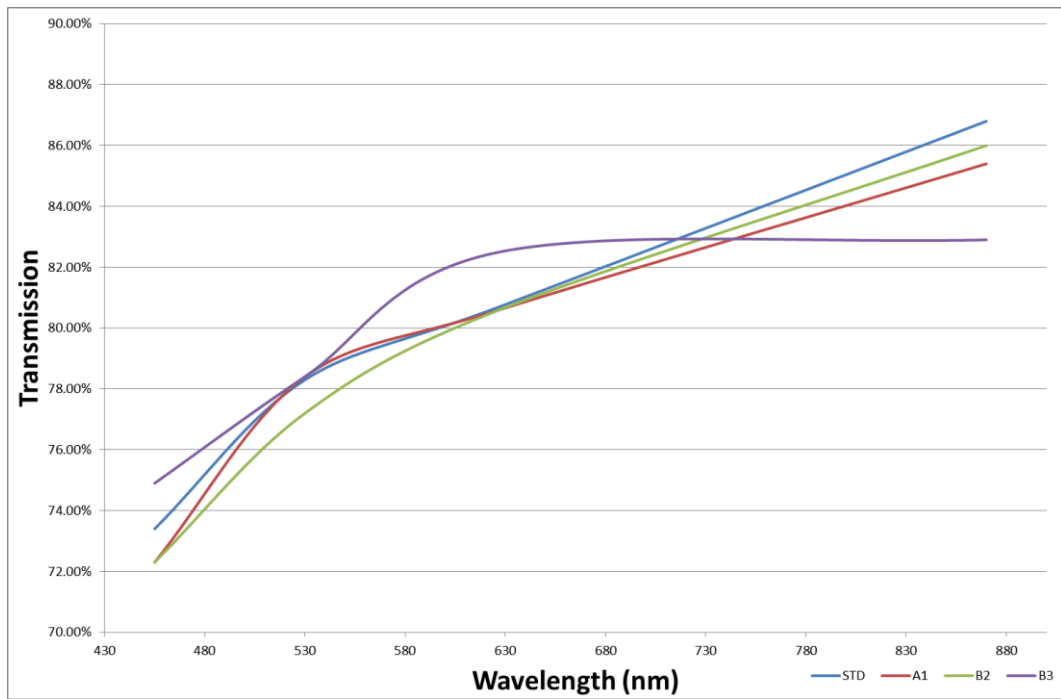


Figure 80 - Transmission of F:SnO₂ Etching

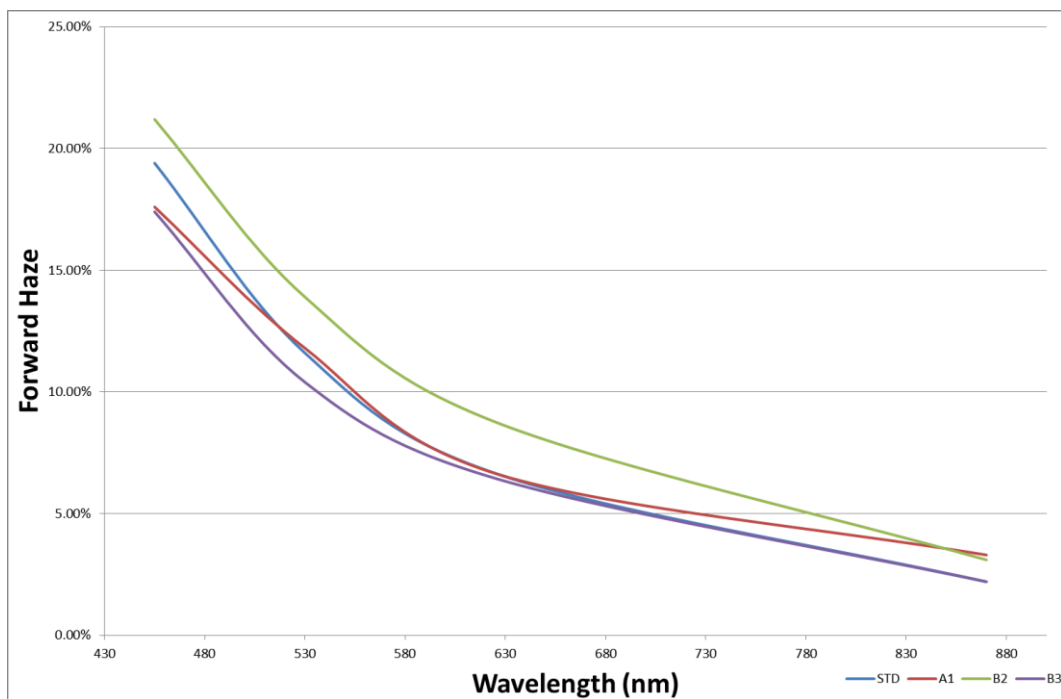


Figure 81 - Forward Haze of F:SnO₂ Etching

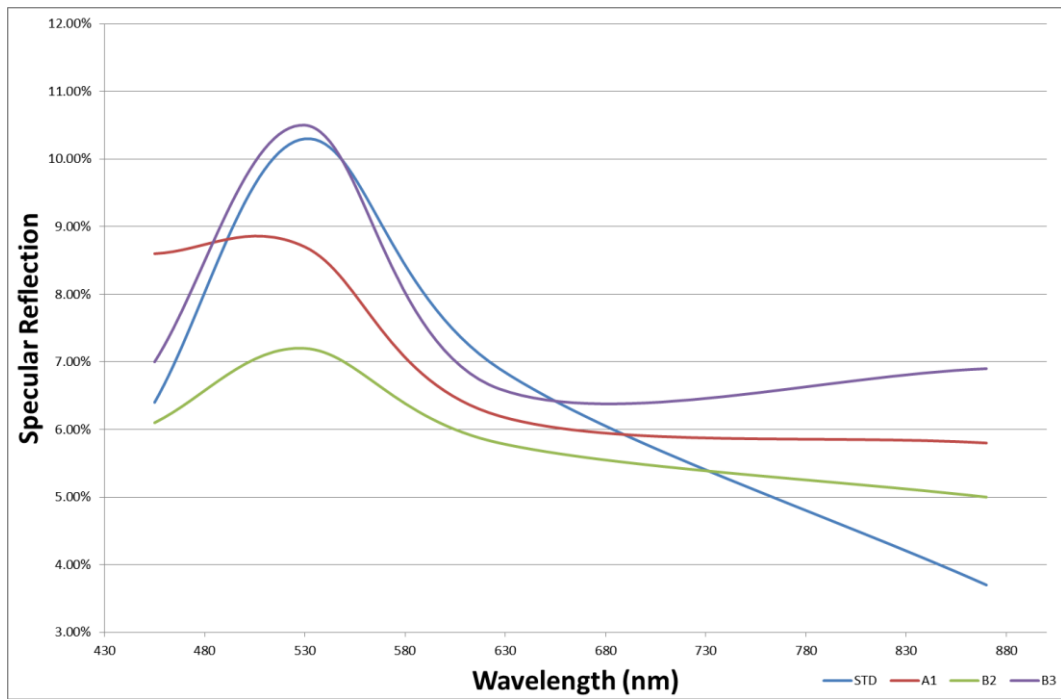


Figure 82 – Specular Reflection of F:SnO₂ Etching

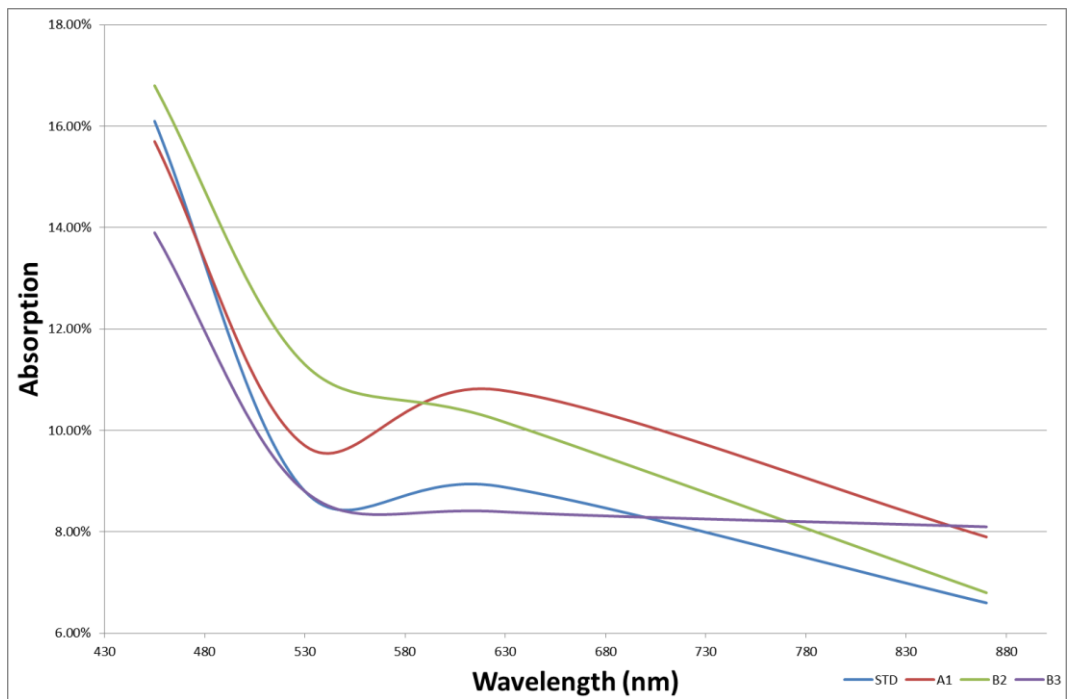


Figure 83 – Absorption of F:SnO₂ Etching

	Standard	A1	B2	B3
Film Thickness (nm)	1000	1000	1000	1000
Hall Voltage (V_H)	9.69E-03	8.66E-03	8.41E-03	8.61E-03
Hall Current (V_I)	2.39E-01	2.58E-01	2.60E-01	2.50E-01
Sheet Resistance (Ω/\square)	1.71E+01	1.42E+01	1.40E+01	1.58E+01
Resistivity (Ωcm)	1.71E-05	1.42E-05	1.40E-05	1.58E-05
Carrier Density (cm^{-2})	1.22E+16	1.47E+16	1.53E+16	1.43E+16
Mobility (cm^2/Vs)	3.00E+01	2.99E+01	2.93E+01	2.76E+01
Carrier Concentration (cm^{-3})	1.22E+20	1.47E+20	1.53E+20	1.43E+20

Table 22 - Hall measurement calculated data of the F: SnO₂ etching experiment

An interesting effect was noted however for the electrical parameters of the series (Table 22). Across the set a reduction of sheet resistance was shown. This was achieved by promotion of the carrier concentration but coincided with a relative decrease in carrier mobility. Several interactions may have affected the electrical properties through the surface modification. Assessment of AFM/SEM showed an increase in larger crystal facets through sample treatment. Larger crystal grains are considered to improve carrier mobility through the reduction of grain boundaries this was considered a beneficial change for increasing carrier mobility by reducing grain boundaries, it appeared that the etched facets had increased carrier concentration but not mobility.

The increase in carrier concentration explained the variation in optical performance, as this directly affected transmission/absorption of the film. The resultant mix of the facet sizes must correspond to the wavelength variation that showed either increased or decreased optical benefits. Further work would intend to promote carrier mobility though tailoring the surface features, which would inherently improve optical performance.

Conclusions of the treated films revealed the emergence of larger features with rounded peaks during the etching cycle. AFM analysis of the low powered etched films suggested a promoted roughness compared to the standard film. However the high power discharge notes

a reduction in this roughness. Under higher power there appeared an alteration in volatile species produced or a preference in the etching regime.

This corroborates the suggested theory⁽²⁴⁴⁾ with respect to vacuum etching, that an increased number of dissociated chlorine atoms enable higher etching rates. These highly active species appeared to preferentially etch the protruding and troughs of the facets, resulting in smoother peaks and wells. This was confirmed by the theory of dissociated molecular species permitting the etching F: SnO₂ film via a chemical mechanism. EDAX (Figure 84) imaging confirmed the chemical composition of the film to be approximately stoichiometric without the presence of any chlorinated by-products or residual effects. No signs of re-deposition from EDAX analysis or imaging of the surface structure was confirmed by the stoichiometry.

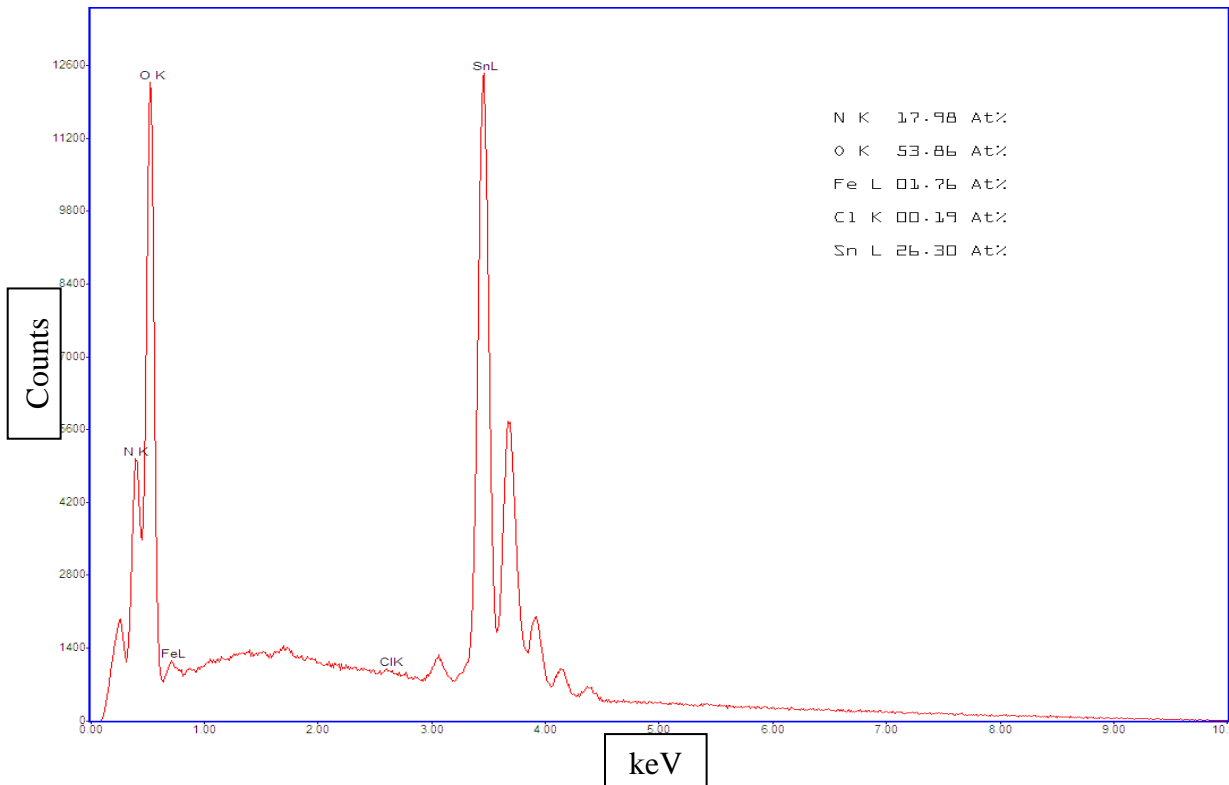


Figure 84 – EDAX Imaging of the Etched F: SnO₂

Evolution of the plasma treatment system has shown thus far the ability to affectively modify the TCO surface. Without any major defects being inflicted or destroying the key beneficial properties of the film. Future progress would attempt to establish a core routine as an etching cycle that produces enhanced optical properties through improved carrier mobility.

7.7.3 Initial Indications of the Plasma Mechanism F:SnO₂

Considering accredited literature about plasma etching, some assumptions may be drafted about the process based on the etching observations. Reflection on microelectronic etching systems currently operated under low pressure regimes was a sufficient platform from which to build the atmospheric pressure plasma system upon.

Preferentially throughout the active plasma etching of F:SnO₂ the smaller surface features in the base of the material experienced greater etching rates. This observation was apparent on the AFM/SEM with the exposure of larger features. Horizontal crystal grains would logically experience an increase in exposure to active species, presenting a larger surface area. Concentration of species occurred in the flat valleys of the material enabling increased activity. Chlorine atoms with respect to silicon etching promoted a crystallographic preference⁽²⁴⁴⁾. Described in the literature⁽²⁴⁴⁾ was the dependence on the bond energy exhibited by the crystal orientation. This served as a point of access for the incident etchant to break the bond liberating the material from the surface. It was also possible that etching was due to a crystallographic preference, eliminating specific weaker orientations (although no evidence at this time can support this for atmospheric pressure plasma etching).

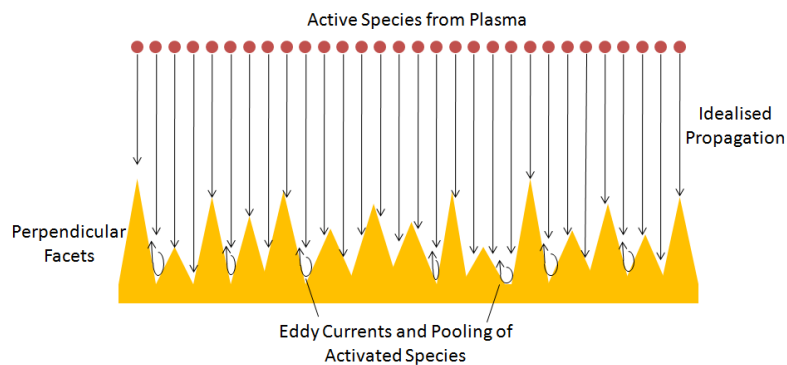


Figure 85 – Idealised Interpretation of Sample and Species Interaction

Figure 85 represents a theoretical depiction of the species interaction, and propagation in terms of the isotropic etching. Propagation under atmospheric pressure would involve specie and atmospheric gas interaction and not exhibit straight line interaction. Combination of species available from the feedstock mixture and atmospheric composition may present

active species that are responsible for etching. The result was that the exposed weaker perpendicular surface was readily etched, whilst the other peaks were rounded during the etching cycle.

The nature of atmospheric pressure operation would indicate that a chemical mechanism takes preference. With a short mean free path, high energy ions would not be able to reach the sample surface given the respective distance. Chlorine and oxygen are commonly employed chemical etching medium and dissociation of these gasses may present active species. Indicated by the experienced etching results is the chemically active nature of the plasma. HCl was required to effectively etch F:SnO₂ and the requirements of the process further underpin the chemical mechanism (time frame, etching preference). Continuing investigation observed the effects of etching on ZnO, assessing the required components for etching.

7.8 Plasma Etching of Zinc Oxide

7.8.1 Initial Investigation

Contrary to the etching of F: SnO₂ which utilizes the HCl activated plasma, exposure of ZnO to an open atmospheric nitrogen based discharge is sufficient to modify the surface. Zinc oxide material composition did not require the activated chemical species, but is enhanced by oxygen. High energy oxygen was sufficient to fine-tune the surface plus, with high exposure, can completely eradicate the thin film. Preliminary investigation demonstrated the severity of etching zinc oxide. Figure 86 shows examples of an un-etched, “light” and “heavy” etched ZnO film. “Light” & “heavy” were the designated names attributed to the severity of the results experienced from the induced etching parameters.

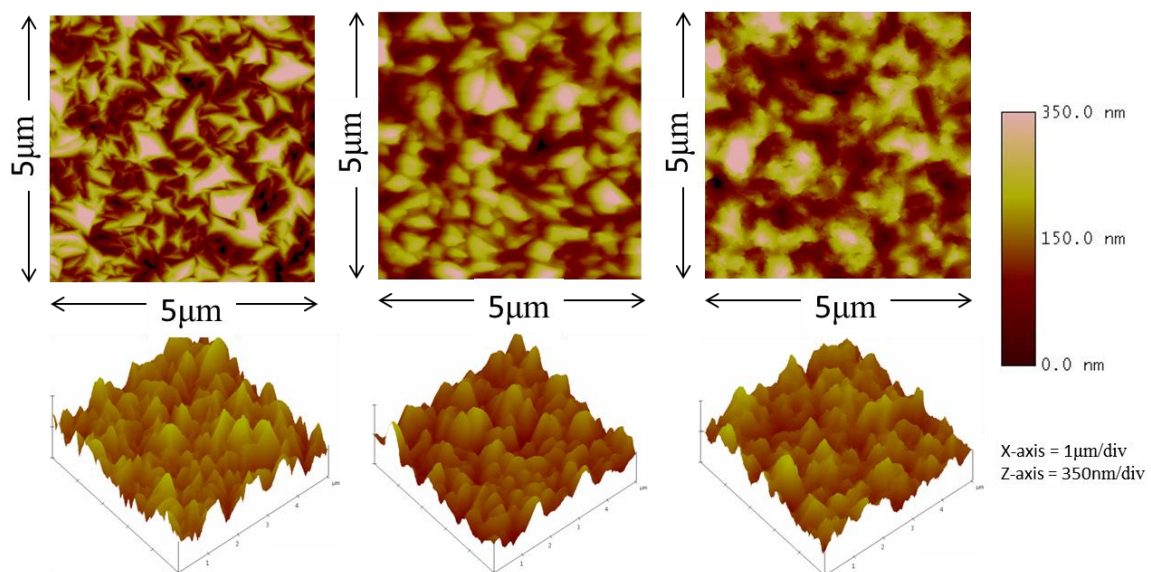


Figure 86 – Examples of physical vapour deposited ZnO Films, un-etched, light etch and heavy etch respectively

Initial investigation of ZnO etching was to establish a baseline of etching parameters for zinc oxide. ZnO etching primarily involved various ZnO surfaces structures and silver over-coated ZnO (Published 2011; Surface and Coatings Technology⁽³³⁵⁾). Silver is impervious to the plasma discharge, which permitted a moderate control over the texturing of zinc oxide through subsequent etching. Deposited using flame assisted CVD (FACVD), silver formed a

spatial layer on the ZnO surface. Application of various quantities of silver on the zinc oxide surface may introduce a controllable measure of etching by varying the spatial distribution.

Smooth ZnO was produced utilizing the low temperature growth process, whilst a highly textured surface was produced from elevated temperatures. Both these surface structures were grown in the initial deposition of ZnO. ZnO was deposited using the nozzle coater arrangement at a glass temperature of 300 °C smooth texture and 450 °C for highly textured. Silver over coating was applied to the smooth ZnO surface, which aided the initial observation of its etching effects. In this series we have shown three etching sets including smooth ZnO (S1), highly textured ZnO (S2) and silver over-coated ZnO (S3). The notation STD signifies the sample before exposure (pre-etch) to the plasma. The process conditions are given in Table 23 .AFM data for S1, S2 and S3 is shown in Figure 87, Figure 88 and Figure 89 respectively.

Sample	Feedgas - N ₂ (L/Min)	Voltage (kV)	Frequency kHz	Primary Current (mA)	Plasma Power (W)	Passes	Roughness RMS Pre-Etch (nm)	Roughness RMS Post-Etch (nm)
S1	6	5.12	3.2	490	14.75	20	13.26	14.6
S2	6	5.12	3.2	490	14.75	20	48.02	47.78
S3	6	5.12	3.2	490	14.75	20	9.64	17.32

Table 23 - ZnO Etching Conditions of Initial Testing

Illustrated by the first series is the etching ability of ZnO. Static samples situated directly under the discharge for several minutes were almost completely obliterated. Samples with moderated exposure showed a significant change to the surface topology. High textured ZnO portrayed a nominal variation in roughness. With prominent surface features it is noted to change with respects to the etching regime. Entire sample modification may have occurred or the structure was more difficult to etch.

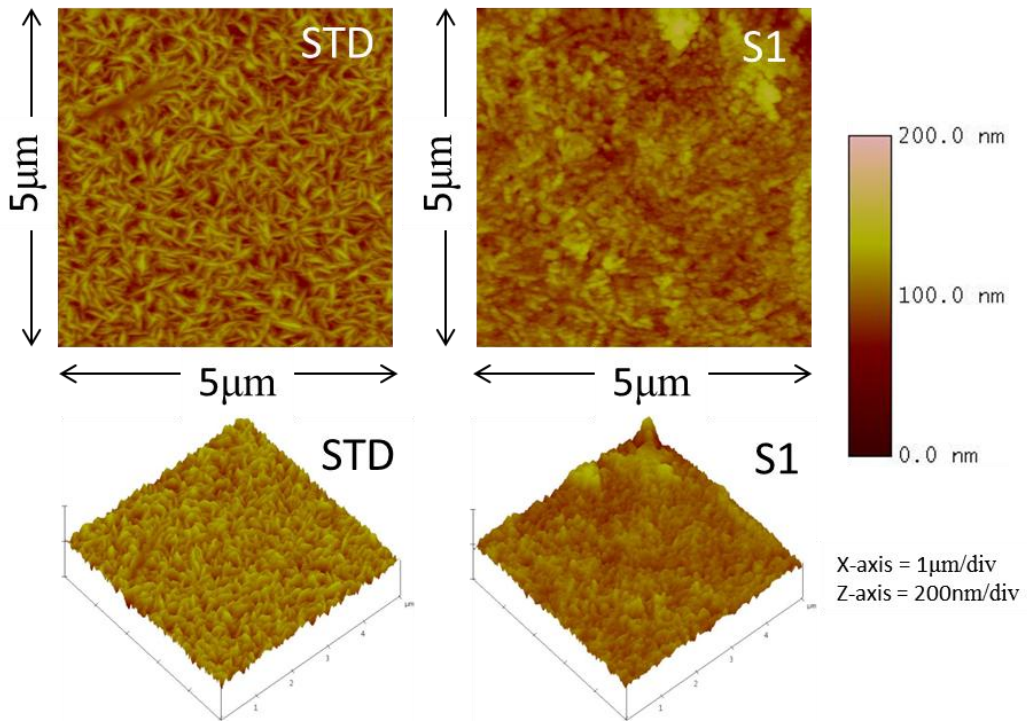


Figure 87 – Smooth ZnO Etching (STD – Before Etch)

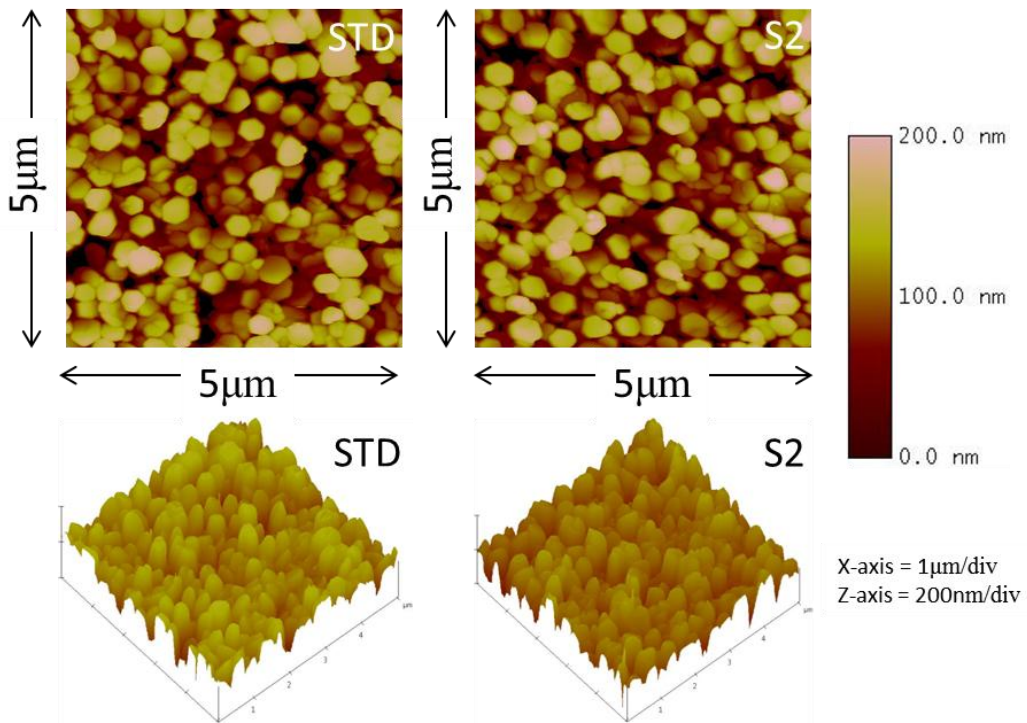


Figure 88 – Highly Textured ZnO Etching (STD – Before Etch)

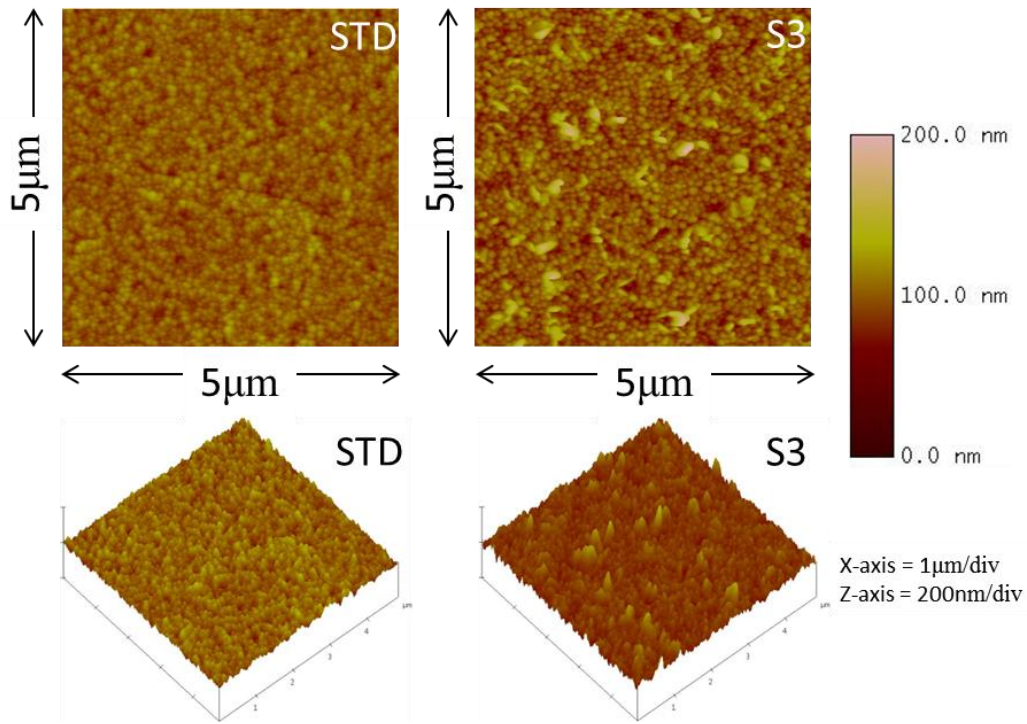


Figure 89 - Silver Top Coat Low Temperature Deposition Etching (STD – Before Etch)

Silver over coating proved moderately effective for tailoring the etching of the zinc oxide layer. A consequence of this method was the difficulty of removing the silver. This resulted in damage to the zinc oxide layer. Delicate peaks were observed in the AFM, which suggested tall peaks of zinc oxide remained under the silver layer. Washing cycles damaged these delicate facets, removing the benefit of silver tailoring. Silver removal required further exploration to develop an improved method. Although it was suggested that the best course of action would be to leave the silver in place, as this may prove to be an enhancement in TCO applications. Introduced silver could assist the conductivity of the film whilst involving supplementary optical benefits. The focus of this work was to principally prove the technique was viable and practically. Non-chemically activated plasma etching proves a significant benefit to production methods, as no harmful products are formed or introduced into the system during the etching phase. Continued investigation observes the effects of feed gas composition for enhanced etching and the working environment. Assessment of the etching environment was conducted to determine which of the feed gas mixtures was critical for ZnO etching.

7.8.2 Plasma Etching of ZnO in a Nitrogen Environment

Initial investigation demonstrated the effective nature of ZnO etching when exposed to the plasma. Developing this process further we required a more intimate knowledge of the process parameters enabling surface modification. Effective manipulation of these parameters enhances the facilitation of tuning the surface properties. Oxygen is well documented⁽²⁴⁴⁾ as an etching medium and open atmospheric pressure operation by its nature will incorporate a portion into the discharge. As the suspected catalyst for the etching regime we investigated the environment gas composition and working gas mixture.

ZnO was deposited using thermally activated chemical vapour deposition at atmospheric pressure, employing a dimethylzinc adduct and ethanol mixture to produce the films. The temperature of deposition was 430°C at the substrate surface, which resulted in natively rough films demonstrating peaks facets typical of the form advantageous for light scattering enhancement. Deposited film thickness was approximately 500nm. These films were subjected to the plasma etching system within a nitrogen environment, to observe the morphology development. Investigation was conducted using plasma etching with various discharge parameters and chemistry mixtures delivering nitrogen, oxygen, air and H₂O. Four distinct series were performed;

1. Open atmospheric etching vs. nitrogen atmosphere.
2. Nitrogen Atmosphere with plasma feedgas of nitrogen and oxygen.
3. Nitrogen Atmosphere with plasma feedgas of air.
4. Nitrogen Atmosphere with plasma feedgas of nitrogen, oxygen and H₂O.

For the H₂O delivery, two approaches were taken. Firstly, the samples were laid on a bain-marie, so that H₂O was available locally without submerging the sample. Secondly, the nitrogen feedgas was passed through a bubbler containing H₂O to transfer vapour into the process gas mixture. The bubbler was at room temperature with no additional heating sources applied.

The etching system was a lab room apparatus and consequently was exposed to atmospheric air. In its current status, due to its size and configuration it was unable to be placed into a vacuum chamber for environment management. Circumventing around this problem a PVC vacuum bag was utilized, completely encaging the system and allowed environment exchanges. The bag was sealed tight around the exhaust system and feed lines to ensure only the working gases could enter the environment. Exercising a pumping line, it was possible to evacuate the bag and back fill with the desired environment. The established environment was maintained through continuous gas introduction to allow a slight positive pressure in the bag to avoid atmospheric gases being introduced. Figure 90 shows the layout of the modified system, with Figure 91 and Figure 92 showing photographs of the apparatus.

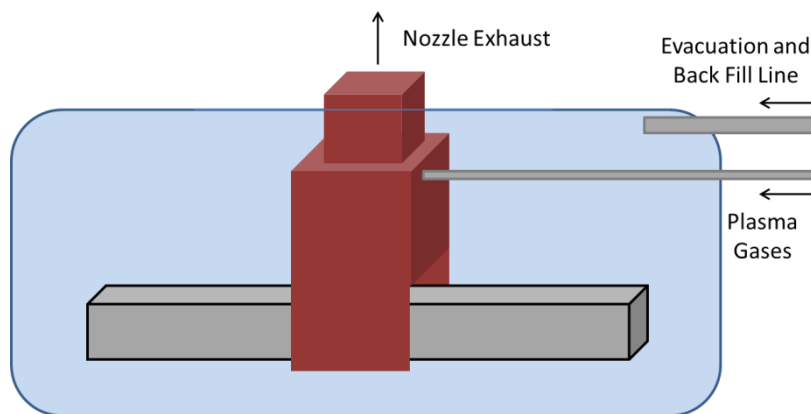


Figure 90 - Plasma Nozzle Housed in the Controlled Environment

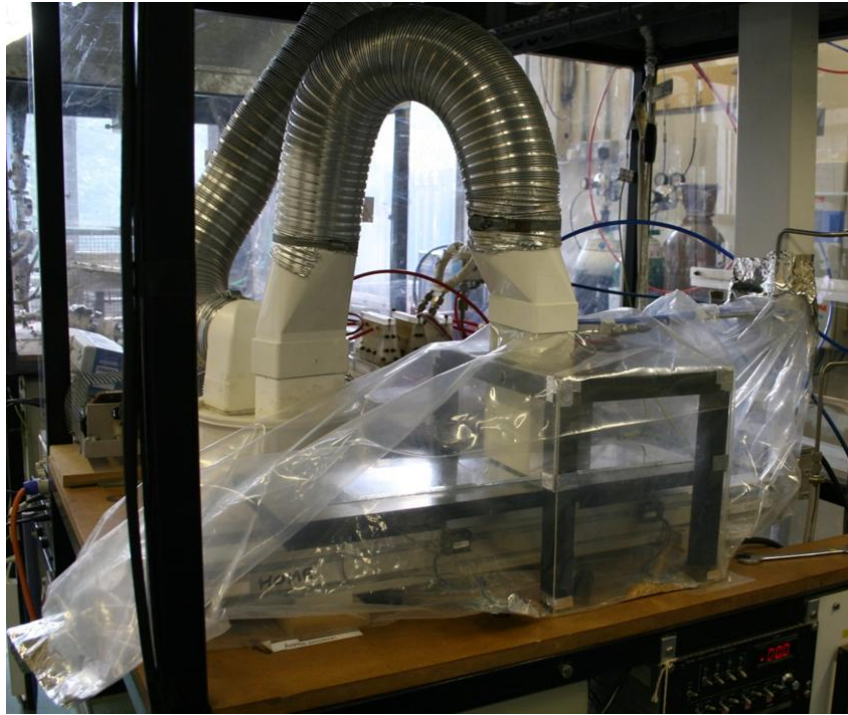


Figure 91 - Photograph of System Side View



Figure 92 - Photograph of System End View

7.8.3 Open Atmospheric Etching vs. Nitrogen Atmosphere

The first investigation was to observe the effect of etching with an open atmospheric lab environment and with a controlled nitrogen environment. Comparatively the plasma discharge was configured identically, as was the feedgas flow rate and exposure time. The etching system comprised the controlled environment, sample translation unit and the dielectric barrier discharge etching head. Environment exchange was achieved by a gas extraction and back filling the environment with the required gas. Figure 90 shows a schematic of system. The controlled environment was nitrogen, reducing the possible oxygen exposure to a minimum. Each pass had a resonance time of 4.2 seconds for the given translation speed Table 24 expresses the etching conditions for this series. Standard (STD) denotes the sample prior to etching for comparison.

Sample	Feedgas - N ₂ (L/Min)	Voltage (kV)	Frequency (kHz)	Primary Current (mA)	Plasma Power (W)	Passes	Nitrogen Environment	Roughness RMS (nm)
Standard (STD)	-	-	-	-	-	-	-	20.41
S1	10	4.95	3.177	515	14.68	50	N/A	21.97
S2	10	4.91	3.264	552	15.62	50	Yes	20.44

Table 24 - Etching Conditions of Open Atmosphere vs. Nitrogen Atmosphere

To compare the effects of the process, AFM images (Figure 93) were taken of an as grown zinc oxide film, standard open atmosphere etched and nitrogen environment etched. It was evident from the AFM images that the nitrogen environment significantly reduced the etching effects.

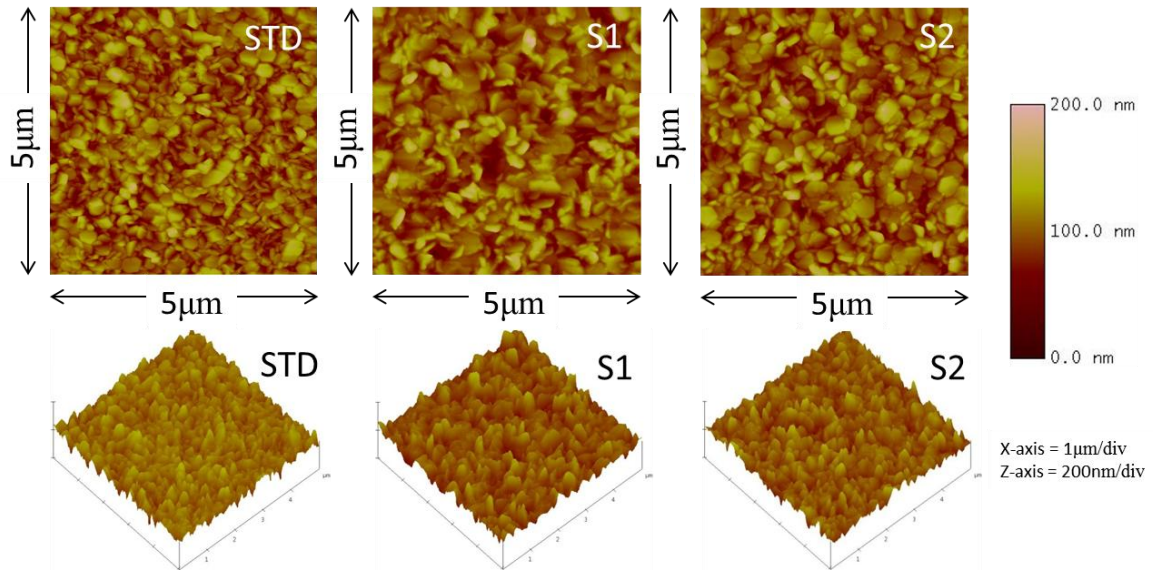


Figure 93 - 2D AFM Images of ZnO Grown and Etched in Various Environments

Minimal visual difference was noted between the grown standard zinc oxide and the sample etched in the nitrogen environment, which showed a nominal difference in measured roughness. However the open atmosphere etching showed a visually different topology and subsequently produced a rougher surface exhibiting a higher RMS. Comparing the two environments it showed that the nitrogen environment required additional components for etching ZnO. Working backwards towards atmospheric conditions, the next series investigates the introduction of oxygen in the feed gas mixture.

7.8.4 Nitrogen Atmosphere with Plasma Feedgas of Nitrogen and Oxygen

Investigation has shown that additional gases are required for ZnO etching. Oxygen is known to be a reactive gas, and would be the significant part of the etching medium in the atmospheric environment ⁽²⁴⁴⁾. This series involved the introduction of oxygen into the feedstock in a ratio mixture comparable to ambient air.

All samples were etched for twenty passes under the nitrogen environment and subjected to a discharge at 5kV with 7 l/min total gas flow. Table 25 shows the conditions of the etching series. Standard (STD) denotes the sample prior to etching for comparison.

Sample	Total Flow (L/Min)	O ₂ Percentage (%)	Voltage (kV)	Frequency (kHz)	Primary Current (mA)	Plasma Power (W)	Passes	Roughness RMS (nm)
Standard (STD)	-	-	-	-	-	-	-	19.26
S1	7	14.3	4.98	3.098	554	15.9	50	17
S2	7	12.5	4.98	3.094	552	15.84	50	17.32
S2	7	20	4.93	3.104	530	15.05	50	18.72

Table 25 - Conditions for Etching with Oxygen in Feedstock Gas Mixture

In Figure 94 the relevant AFM images of each sample are shown. There were visible subtle changes in this series, which may have been due to the sample growth. It is difficult to attribute any significant changes made by oxygen exposure, with little variance in appearance and roughness values. Oxygen delivered in the feedgas demonstrated a subtle change in etching performance, however another component maybe required for the effective etching, gas type, ratio of gases etc. The next series investigates the effects of introducing air as the feed gas for the plasma, offering an 80/20 mix of nitrogen and oxygen.

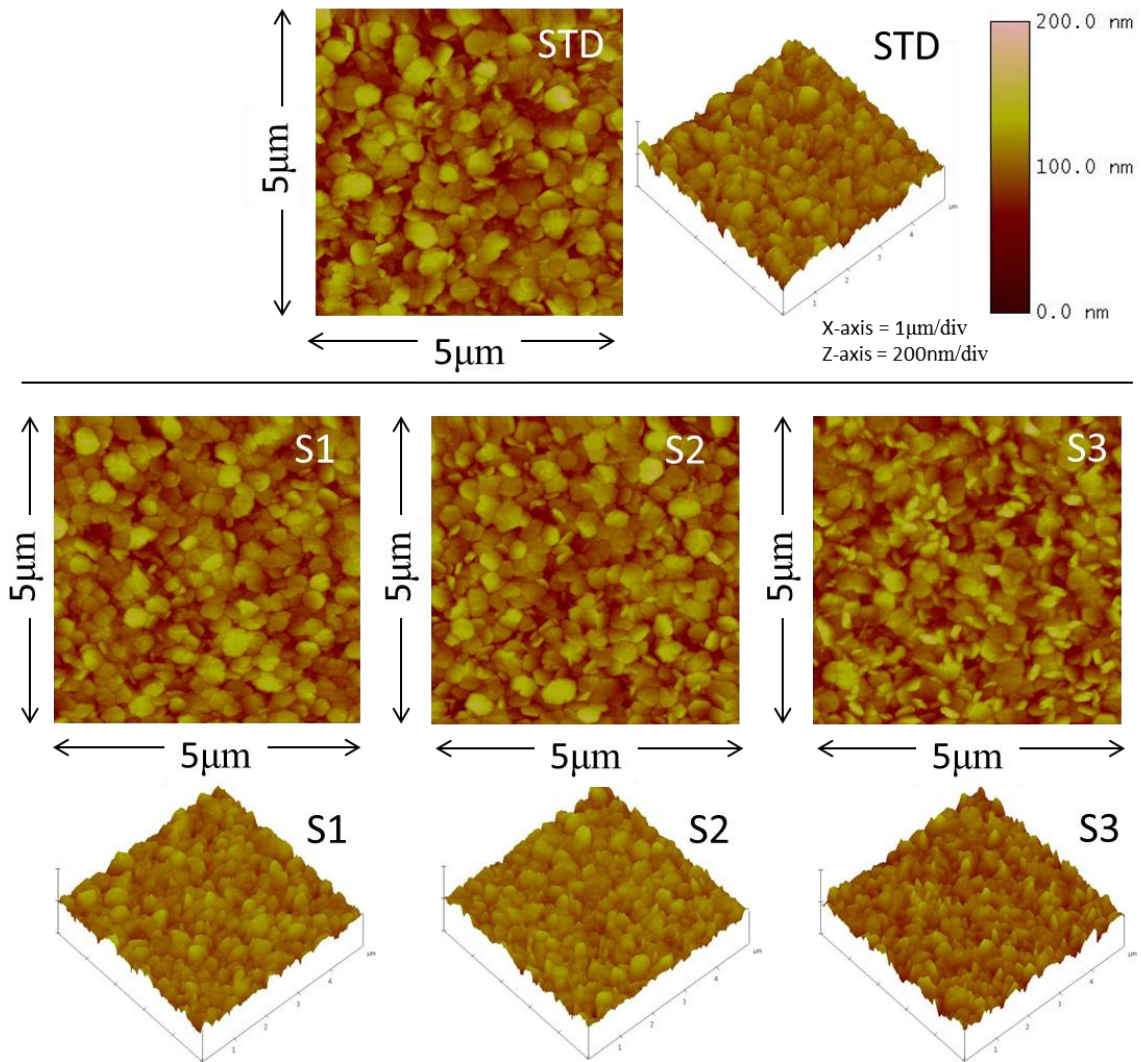


Figure 94 - 2D AFM's of Nitrogen and Oxygen Etching

7.8.5 Nitrogen Atmosphere with Plasma Feedgas of Air

Following the nitrogen and oxygen mixture, standard air (BOC standard) was employed as the feedstock gas. This contained the N₂ for sustaining the discharge and a high ratio of oxygen for etching. In this series the effects of only air feedgas plasma discharge in the nitrogen controlled environment were observed. This exhibited a significantly reduced oxygen availability compared to the open atmosphere & additional oxygen process gas.

Each sample was etched for fifty passes under the nitrogen environment and subject to a 5kV discharge.

Sample	Air (L/Min)	Voltage (kV)	Frequency (kHz)	Primary Current (mA)	Plasma Power (W)	Passes	Nitrogen Environment	Roughness RMS (nm)
Standard (STD)	-	-	-	-	-	-	-	20.48
S1	10	4.93	3.075	528	14.99	50	Yes	19.92
S2	10	4.96	3.075	533	14.99	50	N/A	18.07

Table 26 showed the process conditions, which tested the influence surrounding environment. Standard (STD) denotes the sample prior to etching for comparison.

Sample	Air (L/Min)	Voltage (kV)	Frequency (kHz)	Primary Current (mA)	Plasma Power (W)	Passes	Nitrogen Environment	Roughness RMS (nm)
Standard (STD)	-	-	-	-	-	-	-	20.48
S1	10	4.93	3.075	528	14.99	50	Yes	19.92
S2	10	4.96	3.075	533	14.99	50	N/A	18.07

Table 26 - Conditions for Air Etching

AFM of the treated samples are shown in Figure 95. The AFM data shows little etching effect in the nitrogen environment with air as the discharge feed gas. When the system is operated in an open atmosphere, increased etching activity is noted in the AFM data. This suggests that components available in the atmosphere and not present in the delivery gas enable etching of zinc oxide. Sample two exhibits an increased etch activity with a greater excess of oxygen. This is reflected by the reduction in roughness and exemplified in the AFM data.

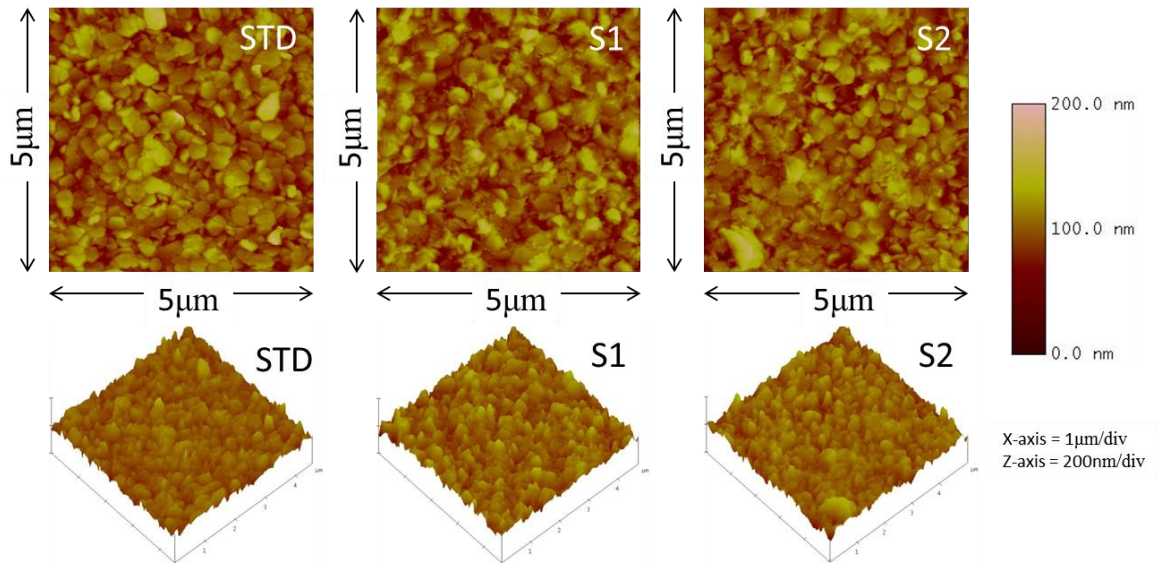


Figure 95 - 2D AFM of Air Feedgas Plasma

Open atmospheric etching showed a significantly greater etching activity compared to the nitrogen environment. Application of air as the discharge medium yielded no positive etching results nor did additional oxygen into the nitrogen discharge. This suggested another component was still required for etching which was not present in the cylinder gases. These gases are very dry, containing little H₂O content compared to atmospheric conditions. The following investigation observes the effects H₂O of introduction into the nitrogen discharge.

7.8.6 Nitrogen Atmosphere with Plasma Feedgas of Nitrogen, Oxygen and H₂O

Open atmospheric pressure conditions show enhanced etching performance. Oxygen showed to be a significant component for etching, therefore H₂O was added as an additional oxygen source. Two designs were implemented for H₂O introduction, a water bath and bubbler. Implementation of an in-line bubbler configuration permits the regulation of H₂O compared to the bath arrangement. Blending these design into the original etching configuration enabled control over the three components for required etching. This series demonstrates the effective etching of the zinc oxide material utilizing a combination of nitrogen, oxygen and H₂O for the plasma feed gases. Neither oxygen nor water alone is able to drastically etch the sample. This series reveals the critical components of oxygen and water is required for etching ZnO.

A water bath (Figure 96) was constructed using a bain-marie structure, so that water was present in the etching environment. Note the sample in this configuration was not submerged in water, and any interaction directly with the plasma was avoided. Additional H₂O would be from evaporation into the environment (no additional heating).

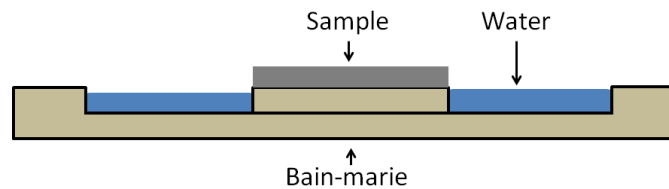


Figure 96 - Water Bath Configuration

The second configuration utilized a bubbler (Figure 97) to supply the water vapour. The bubbler was placed in configuration with the feedgas, this enabled nitrogen to pass through the bubbler. No additional heating was supplied to the bubbler through this series, and the water remained at room temperature.

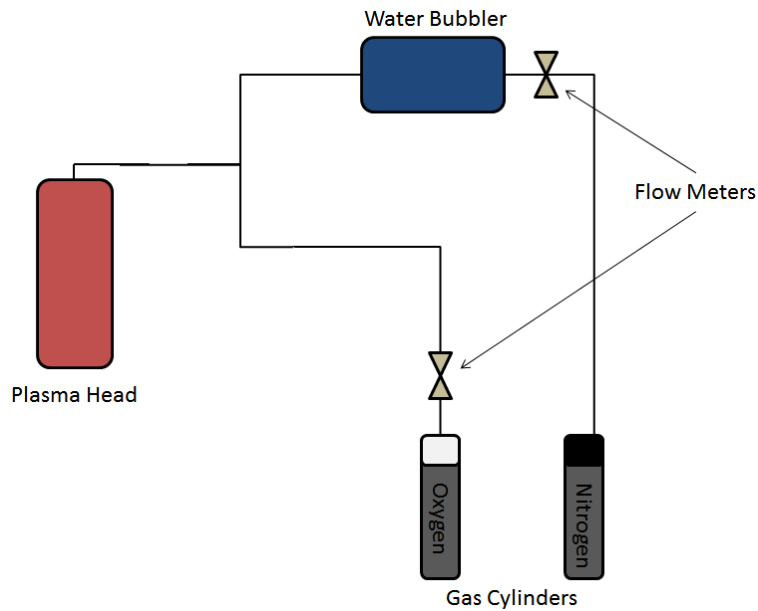


Figure 97 - Water Bubbler Configuration

Each sample was etched for fifty passes under the nitrogen environment and subjected to a 5kV discharge with a total flow of 7 L/Min. Given in Table 27 are the quantities of oxygen added to the feed gas mixture. The bath was filled with 3ml of H₂O and monitored during the etching process. Standard (STD) denotes the sample prior to etching for comparison.

Sample	Total Flow (L/Min)	O ₂ Percentage (%)	Voltage (kV)	Frequency (kHz)	Primary Current (mA)	Plasma Power (W)	Passes	H ₂ O (ml)	Roughness RMS (nm)
Standard (STD)	-	-	-	-	-	-	-	-	17.79
S1	7	0	4.98	3.189	539	15.46	50	3	17.27
S2	7	20	4.95	3.026	544	15.5	50	3	15.14

Table 27 - Conditions of H₂O Bath Etching

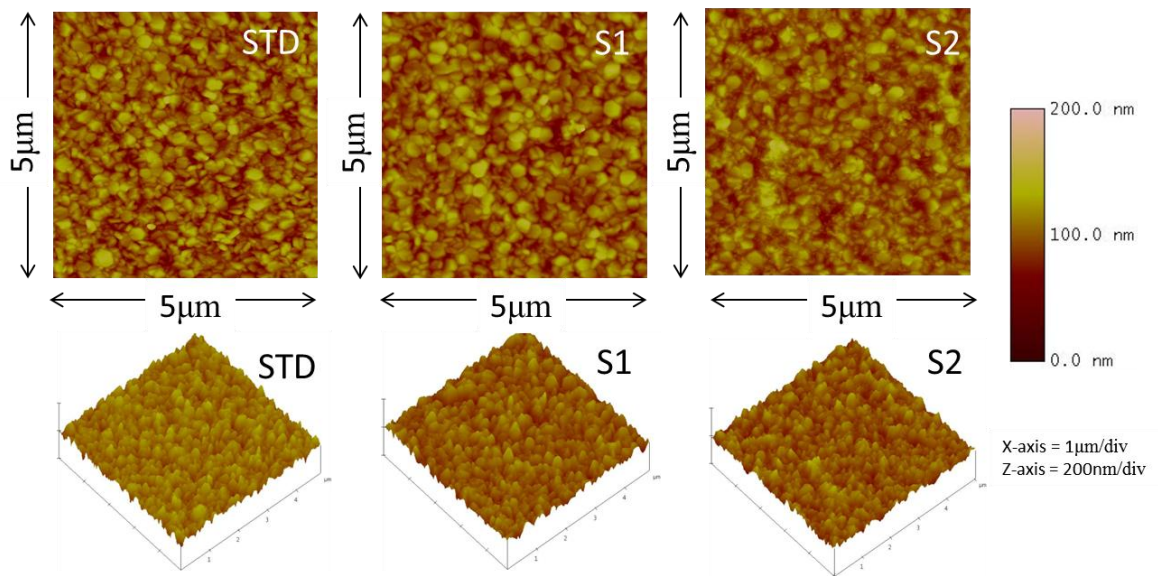


Figure 98 – AFM of H₂O Bath Etching

Introduction of a water bath with a nitrogen discharge showed little effect upon the surface morphology and roughness in the AFM data (Figure 98). Introduction of oxygen into the feed gas mixture showed a considerable effect, with surface roughness being reduced correspondently with a morphology change, indicative of the reliance of oxygen and water for etching zinc oxide. The water bath may not have been the most efficient way to monitor and effectively administer water to the etching environment.

A water bath showed that H₂O was an essential component for the effective etching of ZnO. The design however offered a crude method of control. Implementation of an in-line bubbler configuration permitted the regulation of H₂O introduction. Blending this design into the original etching configuration enabled control over the three components for required etching. In this configuration the water was measured into the bubbler and all of the process gasses were fed through it. In Table 28 the conditions for etching are given and Figure 99 shows the AFM data.

Sample	Total Flow (L/Min)	O ₂ Percentage (%)	Voltage (kV)	Frequency (kHz)	Primary Current (mA)	Plasma Power (W)	Passes	H ₂ O (ml)	Roughness RMS (nm)
Standard (STD)	-	-	-	-	-	-	-	-	17.42
S1	7	0	4.98	2.948	519	14.9	50	50	17.95
S2	7	20	4.93	3.018	514	14.6	50	50	47.34

Table 28 - Conditions of H₂O Bubbler Etching

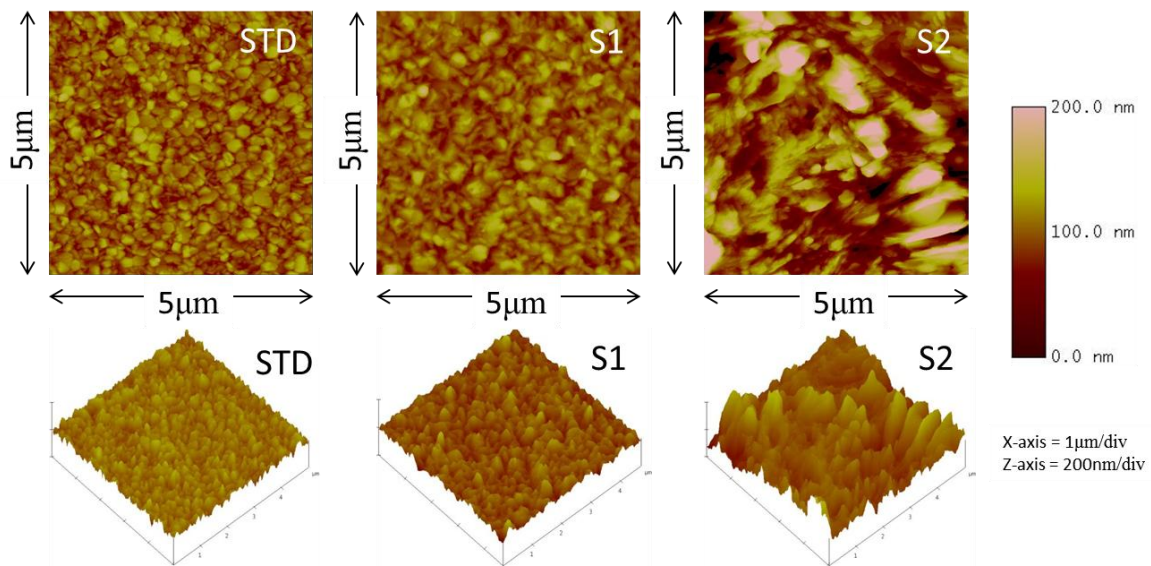


Figure 99 – AFM of H₂O Bubbler Etching

This series demonstrated the effective etching of the zinc oxide material utilizing a combination of nitrogen, oxygen and water for the plasma feed gases. Utilizing the bubbler arrangement, water introduction directly into the feedgas significantly enhanced the etching action whilst retaining a high degree of control. Neither oxygen nor water alone was able to drastically etch the sample. However when combined the resultant etching regime was powerful, resulting in a significant change to the surface morphology and roughness. This series revealed that the critical components of oxygen and water were required for etching. Continued investigation observed the regulated introduction of H₂O into the feed gas mixture.

7.8.7 Plasma Etching of ZnO – Regulated H₂O Etching

A series of experiments involving flow rate adjustment was performed to observe the etching effects with H₂O delivery. Each sample was exposed to 100 passes under the plasma discharge as described in Table 29. The oxygen/nitrogen ratio for the bulk for the discharge remained constant through the series. (Publication 2013; Surface Coating and Technology⁽³³⁶⁾). Figure 100 shows the revised configuration for the etching system;

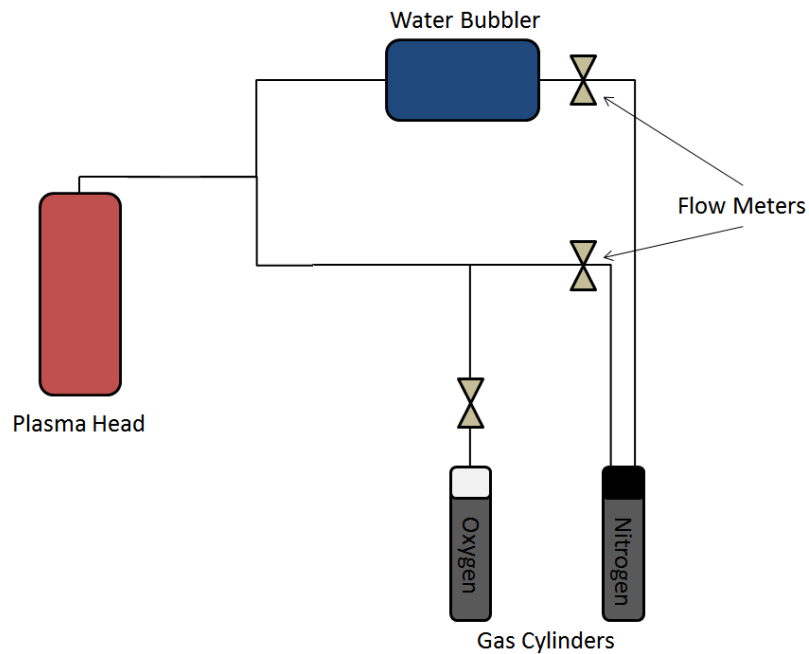
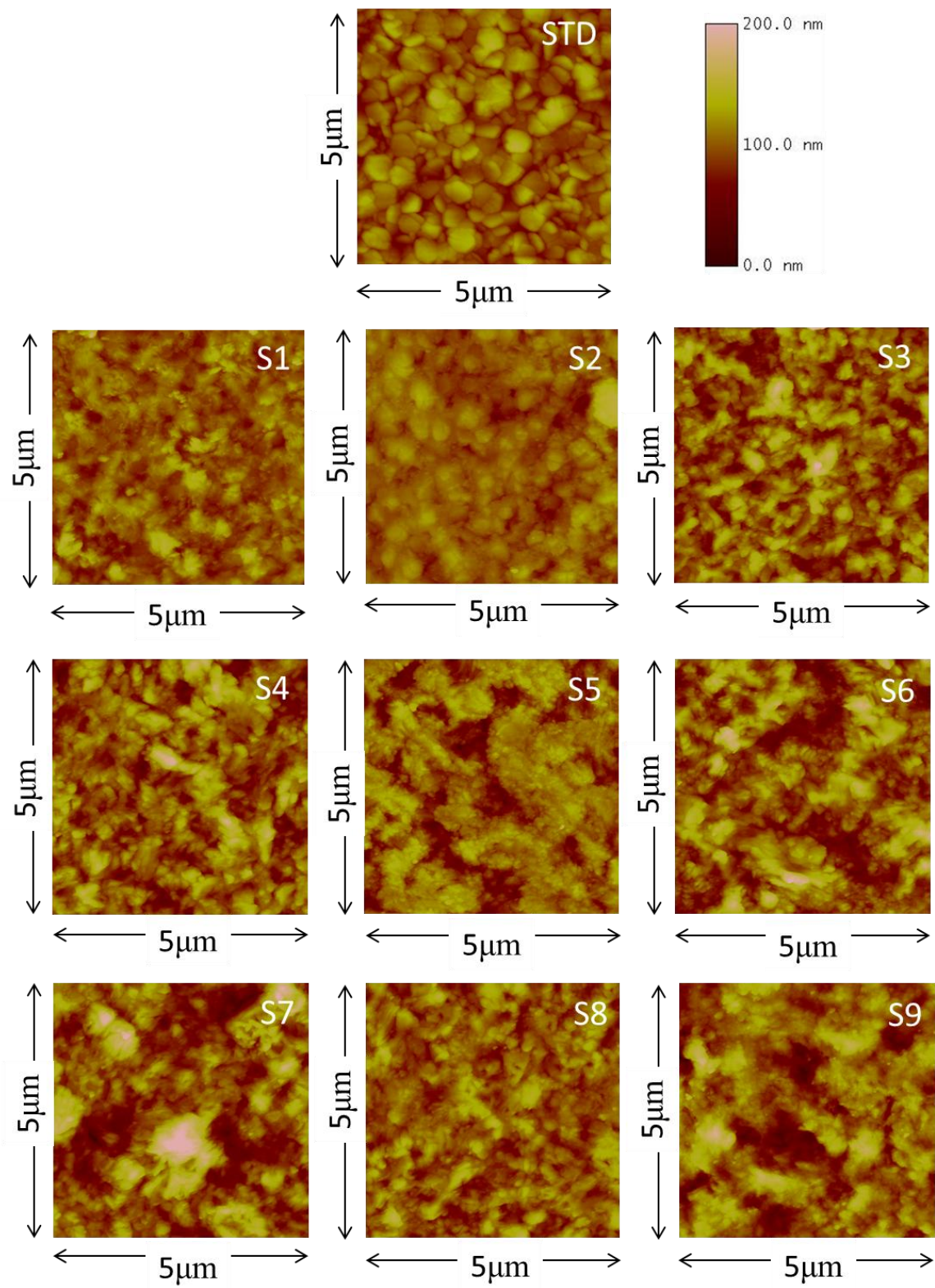


Figure 100 - Water Bubbler Configuration Version Two

Sample	Total Flow (L/Min)	O2 Percentage (%)	Voltage (kV)	Frequency (kHz)	Primary Current (mA)	Plasma Power (W)	Passes	H2O (L/Min)	H2O (ml)	Roughness RMS (nm)
Standard (STD)	-	-	-	-	-	-	-	-	-	21.26
S1	7	14	4.6	3.125	480	13.25	100	0.2	50	19.58
S2	7	14	4.6	3.109	486	13.35	100	0.4	50	16.94
S3	7	14	4.5	3.113	501	13.63	100	0.6	50	27.77
S4	7	14	4.5	3.102	519	14.12	100	0.8	50	28.24
S5	7	14	4.6	3.102	520	14.04	100	1	50	26.49
S6	7	14	4.5	3.108	489	13.25	100	1.2	50	32.06
S7	7	14	4.5	3.102	496	13.54	100	1.4	50	38.3
S8	7	14	4.6	3.125	493	13.51	100	1.6	50	22.55
S9	7	14	4.5	3.109	500	13.6	100	1.8	50	32.04

Table 29 - Etching Conditions for Regulated H₂O Introduction

Illustrated by AFM data (Figure 101) is the effectiveness of the etching cycle upon the ZnO surface. With varying H₂O content in the feedstock gases, various stages of etching are noted. Observed is the reduction and increased roughness for a given gas composition. These samples indicate a scale of control available for tailoring the surface structure. Roughness data showed a decline for sample one and two, with the rest of the samples increasing in roughness. Highest order roughness was shown in sample seven, where it appeared that most of the smaller facets had been removed, leaving the larger more dominant structure behind. Sample 7 optical assessment indicated a comparative drop in performance with respects to the series. This may have been due to the manipulation towards a larger and sparse surface features having an increased absorption, which did not effectively scatter across the measured wavelengths.



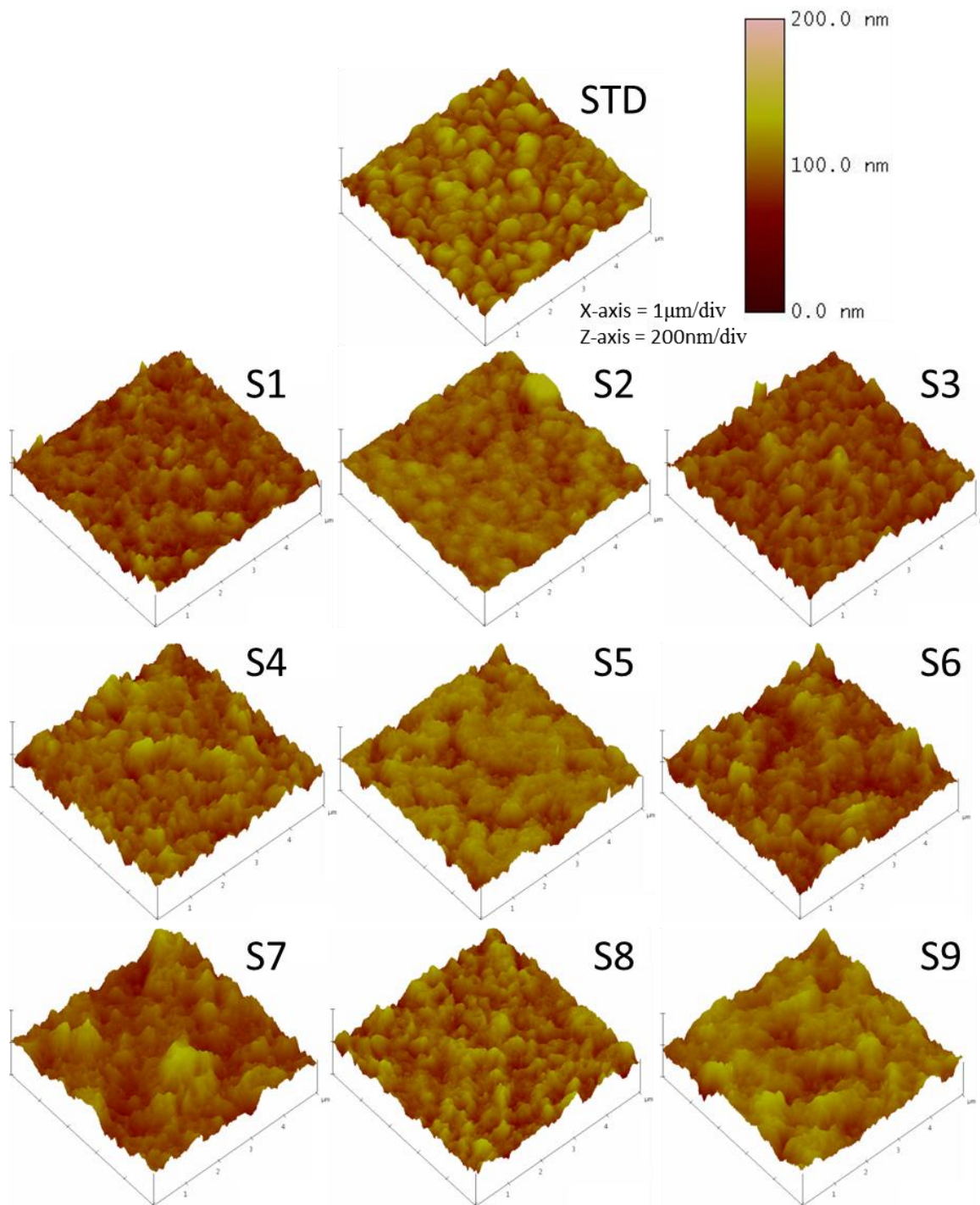


Figure 101 - AFM of Regulated H₂O Etched Samples

Optical analysis of the series has shown that sample five had an increase in transmission across the multiple wavelengths compared to the standard sample, whilst also exhibiting peak scattering properties (increased forward/reverse haze). A corresponding reduction in specular

reflection further indicated the enhanced scattering property. Observation of the AFM data has shown an approximate increase in roughness by 25%, with a morphology exhibiting a more conformal surface. Surface analysis identified a reduction in smaller features whilst retaining larger crystals that are smoothed through processing. This indicated an etching preference towards the smoothing the film surface. Enhancement of both these elements simultaneously was a key advantage for TCOs, and the primary focus of the post treatment.

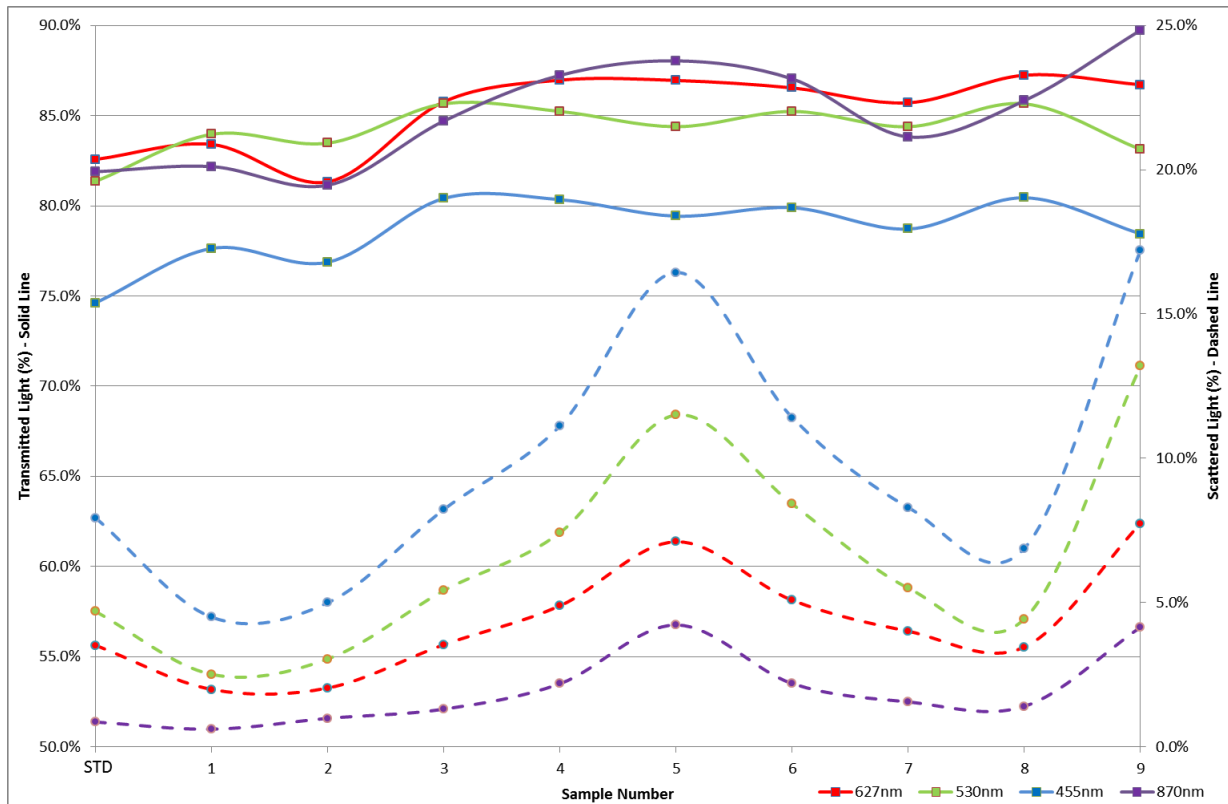


Figure 102 –Optical Transmission and Scattered Across Multiple Wavelengths Against Sample Number Associated to Water Content Delivered to the Plasma Discharge. Conditions Shown in Table 29

Atmospheric pressure plasma etching has been demonstrated as an effective new approach to achieve surface profile control for ZnO thin films. Shown in Figure 102 is an increase in transmission is established in conjunction with an increase in forward/reverse haze, across the target wavelength range. A corresponding reduction in specular reflection further indicates the enhanced scattering property. Surface analysis identifies a reduction in smaller features whilst retaining larger crystals that are smoothed through processing. This indicates an

etching preference towards the smaller facets on the film surface. Resulting from this process are larger features that resemble the desired pyramidal structure.

Plasma feedstock gases have shown to have a significant effect on etching cycle. Water introduction into the standard nitrogen and oxygen mixture has proven essential for ZnO etching. Separately water and oxygen do not offer the same degree of etching activity. It is speculated that a two stage reaction process is occurring with intermediate (e.g. a hydrate or partial hydrate) reacting faster with oxygen. Varying the concentration of H₂O in the plasma discharge showed an evolution of diverse surface structures. Several aspects may be involved during the surface evolution. Etching activity increased with a corresponding increase in H₂O delivery. Equally increasing the H₂O delivery a saturation point may develop, reducing etching activity. If the plasma became quenched with “contaminants”, effective breakdown reduced and therefore the active specie production diminished. Testing involving increased oxygen introduction developed filamentary spikes visibly in the discharge and observed on the oscilloscope.

Further refinement of the system would be to introduce temperature control of the bubbler and system lines. This would permit control over the vapour pressure of water and subsequently define a measureable quantity of introduced H₂O. In conjunction with this modification a heated substrate may also improve the etching efficiency and offer alternative benefits. With the developments of the etching system and control of the etching parameters, the system was ready for etching of TCOs for PV testing. The next stage of developments observed F:ZnO deposition on large area substrate suitable for PV testing.

7.9 Zinc Oxide Growth – Second phase

7.9.1 Fluorine Doped Zinc Oxide

Zinc oxide was the proprietary material researched, with particular interest in the plasma etching properties. Advancing this body of work further required the development of doped zinc oxide for implementation into PV cells. Fluorine doping offers an attractive alternative to dopants traditionally paired with zinc oxide, offering the potential of greater electron mobility with enhanced optical transparency. Initial testing demonstrated the ability to implement fluorine doping utilizing an APCVD system. This process however required a scaling towards large area coatings for PV testing. The intended application of the TCOs would be for amorphous silicon solar cells, manufactured with a collaborator at EPFL.

Precursor combination of dimethylzinc triethylamine $[\text{Zn}(\text{C}_2\text{H}_5)_3.\text{N}(\text{C}_2\text{H}_5)_3]$, ethanol (anhydrous) and trifluoroethanol was selected as in the initial experimentation. Dimethylzinc triethylamine is an adduct-stabilised zinc precursor. It is less prone to gas phase reaction than traditional alkyl zinc precursors and therefore more suitable for atmospheric pressure applications. Vapour pressure was calculated using the Antoine equation (equation (5. 3)), where the components (ABC) are constants for a given material. These values are supplied on the data sheets for the chemical and enabled the determination of molecular flux of a material for a given temperature (T) and flow.

$$\log(P_a) = A - \frac{B}{T + C} \quad (6.5)$$

Concluding from the primary investigation precursor delivery was defined in molar ratio to zinc introduction as shown in Table 30.

O:Zn Ratio	4:1
F:Zn Ratio	0.4:1

Table 30 - Previously Established Standard Working Conditions for Deposition (molar ratio against zinc)

Scaling up the processes required an alternative coating design to be operated to achieve the desired sample size. As in previous growth work the ‘dual flow’ head was utilized. This design permits sample translation under the head, simulating a production process of multiple coating regions/heads. Dimensions of the heated susceptor and coating head allowed uniform deposition of an area up to 100x200mm, with 40x40mm being required for PV testing.

F:ZnO coatings were deposited using a dual flow coating head with a reaction path length of 50mm (inlet to exhaust length). Film thickness of 600nm was achieved by passing the sample multiple times under the head. A consequence of operating in a ‘dynamic’ process was that material exhibited no conductivity. Coatings were deposited in a static position under the head to investigate the loss of conductivity. These coatings exhibited high conductivity underneath inlet slot, but became more resistive towards the extraction slot as shown in Figure 103. Dual flow reactors operate with sample introduction into the exhaust region first, prior to the main coating region. Deposition process and coating arrangement was having a detrimental effect on the sample properties. Consideration of the deposition requirement was assessed.

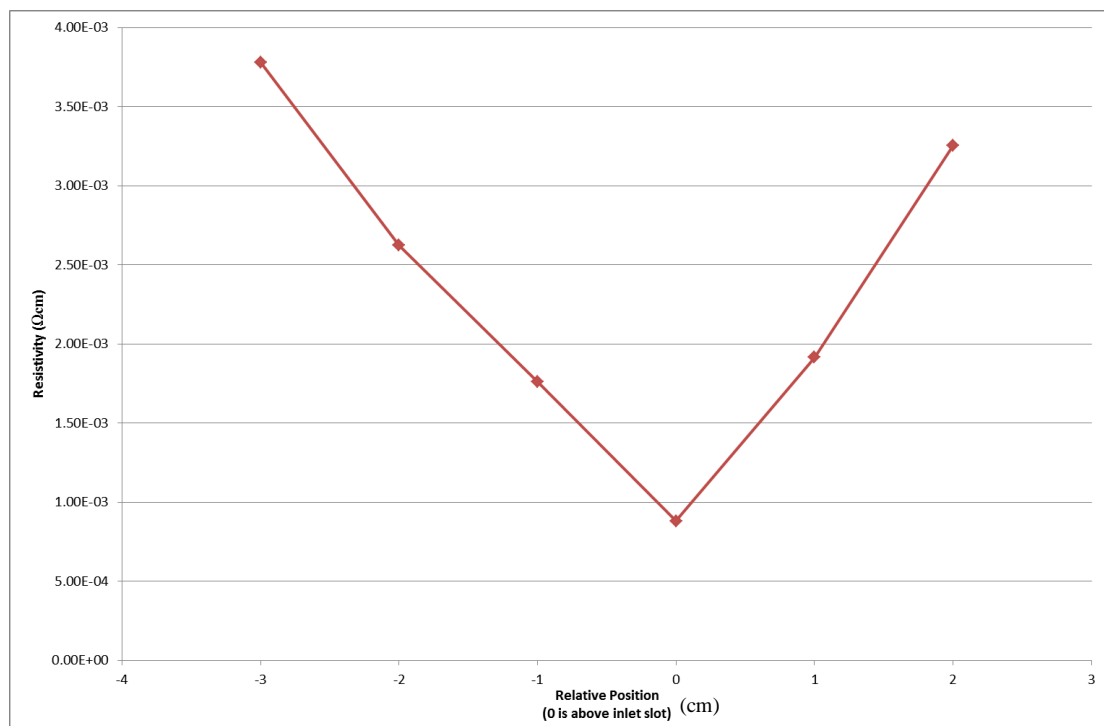


Figure 103 - Film Resistivity against Relative Position of Inlet Slot (Static Coating)

Analysis using Time-of-Flight Secondary Ion Mass Spectrometry (ToF-SIMS) was applied to determine the composition of the film through the width of the coating. SIMS showed an increase in fluorine concentration in the conductive regions (normalized total count of $1: 1.04E^{-2}$), whilst a decrease was exhibited in the non-conductive areas (normalized total count of $1: 3.2E^{-3}$). Considering the coating elements several proposed explanations were offered;

1. Oxidation of the film underneath the extraction due to oxygen ingress from the surrounding atmosphere.
2. Depletion of the fluorine source in the precursor gas.
3. Coating path length was too long, exhibiting over-oxidation of the deposition which prevents fluorine incorporation.

Utilizing a tube coater arrangement permitted investigation into the deposited path length and enabled environmental process control. Deposition in a tube coater aided discovery of processing issues. The tube coater was run initially without a comprehensive seal and subsequently with an air-tight seal after a significant bake out and nitrogen purge. In both cases the coatings yielded films possessing a decent conductivity in correspondence to their thickness of approximately $60 \text{ Ohm}/\square$ around 300nm. Observation of the conductivity down the deposited length of the coating showed an increase in conductivity until a rapid decrease occurred. Conductivity increased in correspondence with increased thickness. The increase and decline in thickness/conductivity showed a peak reaction length for the precursor selection until unfavourable growth developed. Manipulation of the temperature, flow rates and precursor rate did not alter the rapid decline of the peak growth spot (Figure 104). Variation of the trifluoroethanol concentration ruled out depletion of the fluorine dopant, as excessive dopant did not alter the conductive properties.

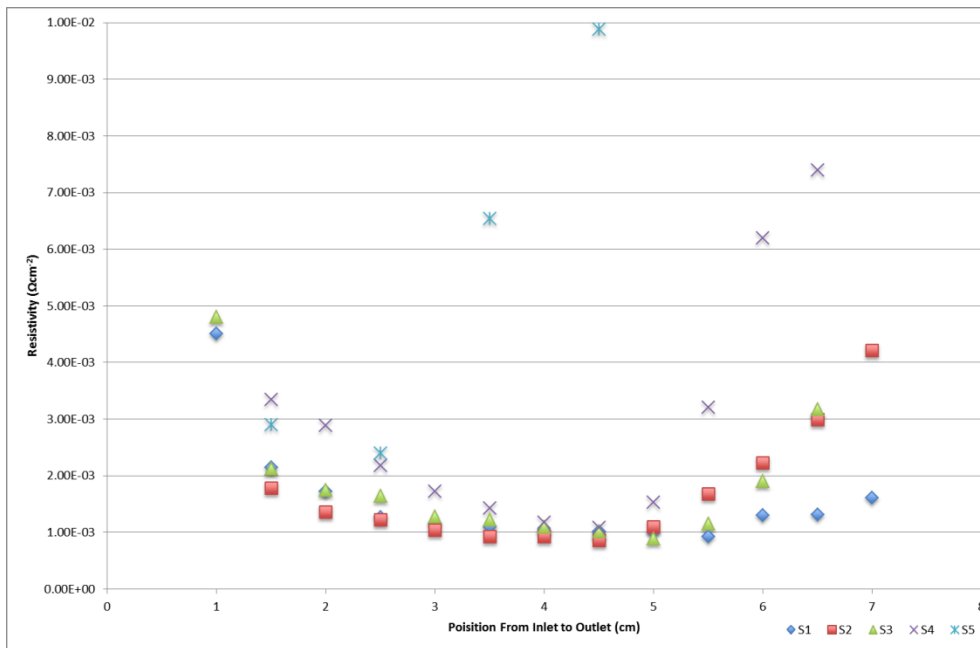


Figure 104 - Resistivity of F:ZnO from Inlet to Outlet of the Tube Coater

Investigating temperature showed that films deposited between 160°C & 390°C were non-conductive, whilst 400°C to 470°C were conductive (temperature of glass surface). These samples still exhibited the rise and decline in conductivity along the sample length. AFM & XRD showed that conductive sections were distinct compared to the non-conductive. F:ZnO had a different structure and surface morphology to undoped ZnO. A similar observation was made with the small area coatings produced on the nozzle coater.

Undoped ZnO exhibited flat plate-like features on the surface, due to a preferred orientation of the hexagonal wurtzite structure along the <002> axis. This axis became dominant as the sample thickness extended beyond 300nm. Through fluorine incorporation the <002> & <101> are of equal presence up to an encountered thickness of 300nm. Beyond this critical limit the structure developed a dominance in the <101> orientation, with AFM data showing a typical needle like structure. These two crystal structures define the undoped and fluorine doped structures being readily identifiable by AFM analysis. Figure 105 identifies the typical progression of an F:ZnO film as the thickness increased.

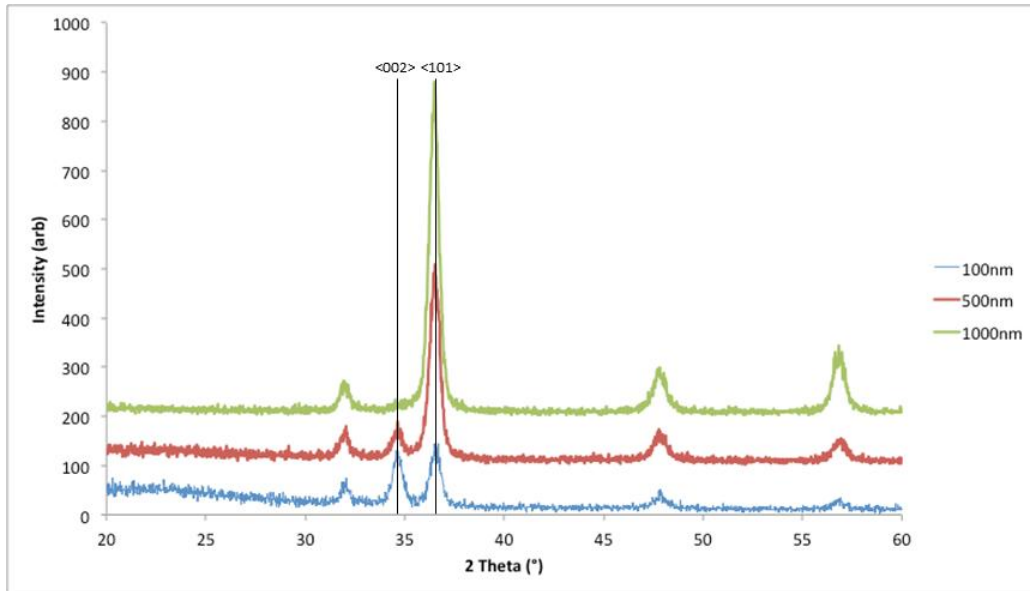


Figure 105 - XRD Spectra for F:ZnO with Increasing Thickness

Path length investigation revealed that development of both structures was present. Deposition in the inlet region reflected the fluorine doped needle structure. Progression of the film towards the exhaust saw a declining fluorine structure towards the undoped ZnO. In the presence of the fluorine structure the films exhibited conductivity up to a maximum, after which this plummeted to no conductivity. Film composition was confirmed in XRD analysis by dissection of the film (Figure 105).

Higher deposition temperatures presented the highest conductivity with the associated benefits of increased growth rate and developed surface structure. The AFM data is shown in Figure 106 and XRD data in Figure 107. Further testing involved the use of fluorinated propanol, albeit with little success with iterations using similar to extreme conditions showing no conductivity. Fluorinated ethanol demonstrated the best capability for producing doped ZnO with the associated limits of the coating apparatus for developing large area samples.

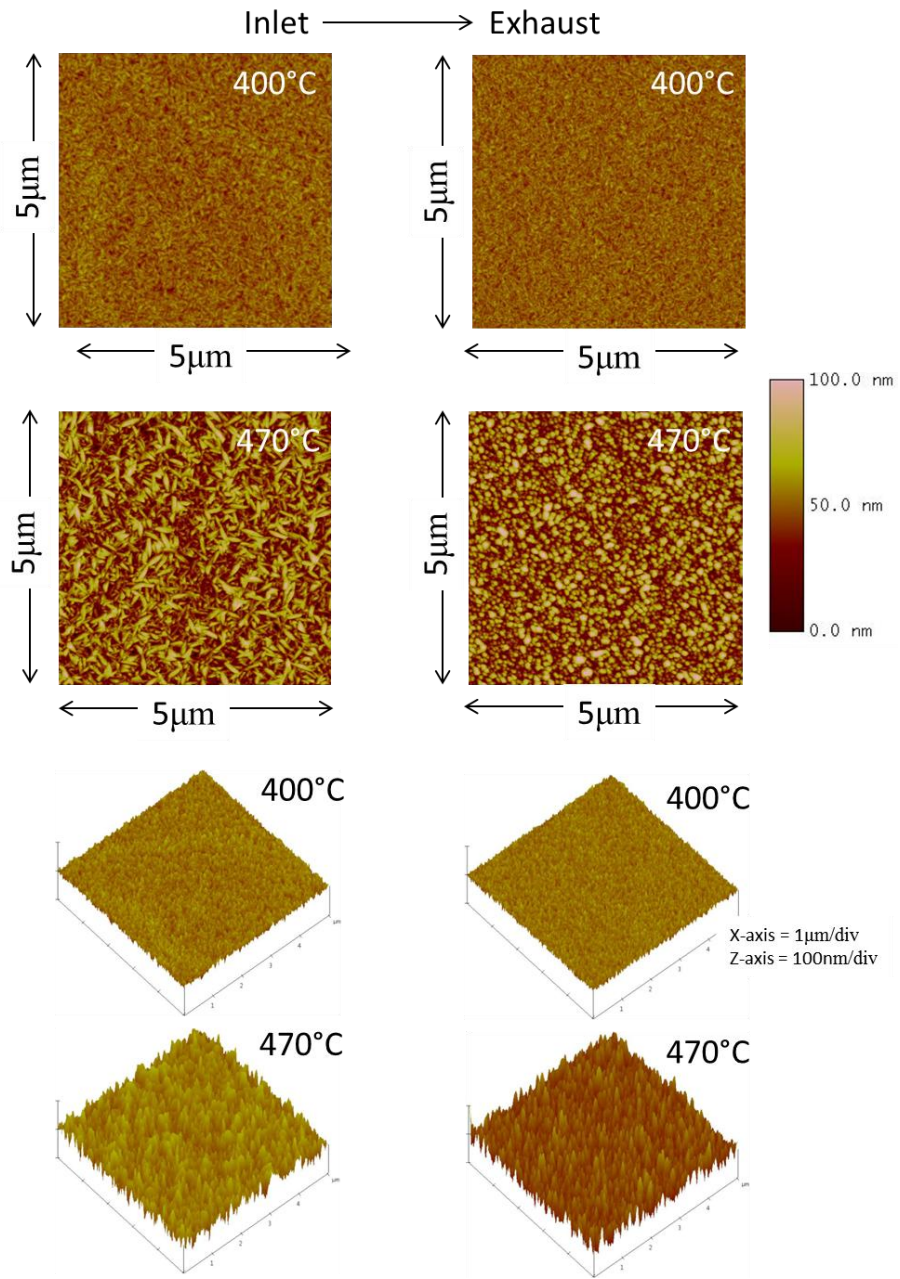


Figure 106 - AFM of Tube Deposition at 400°C & 470°C

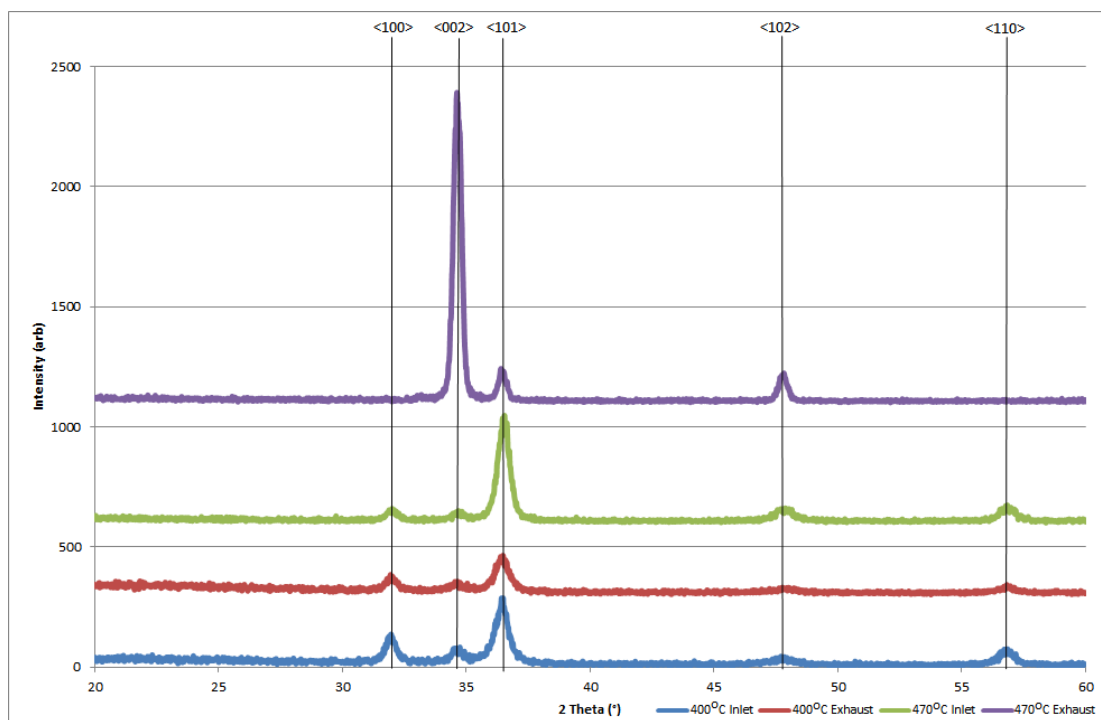


Figure 107 - XRD Data for Tube Deposition at 400°C & 470°C

Analysis of films prepared in the tube coater demonstrated that oxygen ingress was not the issue affecting doping. Discovery of a “sweet spot” in the deposition length of the tube coater indicated the coating design was not suitable for the intended chemistry. The coating head needed to be shorter to suit the deposition phase for fluorine incorporation. Previously the dual flow head employed 50mm path length, allowed for a dominant undoped structure to obtain priority deposition. Implementation of a shorter path length would allow for the fluorine priority development through increasing the resonance time in this reaction phase. Testing utilizing a 25mm path length design confirmed the coating design requirements as depicted in Figure 108.

Sample thickness of approximately 1 μ m was required for effective implementation into PV products; this was achieved by multiple coating passes. This simulates the commercial environment where several heads are utilized to attain the required properties. Deposited film thickness depends on the translation parameters, number of passes and speed.

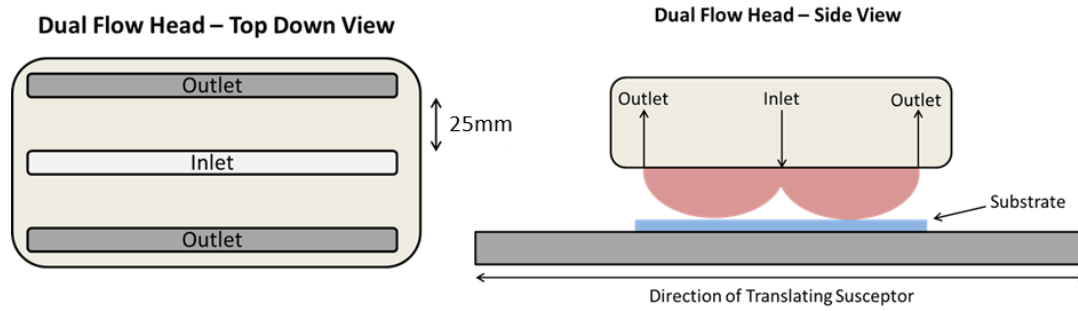


Figure 108 - Alternative Dual Flow Path Length Design

The translation generic controller specified speed in discrete values (0 - 10.0), which do not relate to a specific value. Translation speed is determined by the specific components of the translator (gearing, transitional length etc.). Measurement of translation speed for various settings was conducted in order to determine the residence time experienced shown in Table 31.

Indicated Speed (Translator)	3	2.3	1.9	1.7	1.6	1.55	1.4	1.3
Actual Speed mm/s	5.72	3.89	2.84	2.32	2.05	1.92	1.53	1.27

Table 31 - Commonly Operated Translator Speed and Actual Speed

First the growth conditions were set statically to calibrate the system parameters at 460°C substrate temperature as described in Table 32. Film thickness under the inlet slot was 1.8 µm exhibiting a sheet resistance of 10 ohm/□. Towards the outer region of the coating the thickness dropped to 1µm to with a sheet resistance of 20 ohm/□. Photovoltaic specification requires a TCO film of 800nm to 1µm thick with a sheet resistance below 20 ohm/□, as requested by collaborators at EPFL.

Substrate Temperature (°C)	Zinc Molar Flux (Mol/Min)	O:Zn Ratio	F:Zn Ratio	Centre Thickness (Nm)	Centre Sheet Resistance (Ohm/□)	Outer Thickness (Nm)	Outer Sheet Resistance (Ohm/□)
460	9.68×10^{-4}	4:1	0.4:1	1800	10	1000	20

Table 32 - Static Deposition Conditions

The next series of investigation observed the dynamic operation under the head for large area coatings.

7.9.2 F:ZnO Passes Series

Moving beyond static coatings, we continued with dynamic deposition and started by performing a passes series to determine optimum conditions. The thickness of the films was scaled up to 800-1000nm in order to increase the haze and conductivity of the films for photovoltaic applications. Three different translation speeds were also used with varying number of passes to determine thickness and the further effects upon film conductivity. The process conditions are given in Table 33 for this series.

Sample	Passes	Speed	Substrate Temperature (°C)	Zinc Molar Flux (Mol/Min)	O:Zn Ratio	F:Zn Ratio	Thickness (Nm)	Sheet Resistance Initial/After (Ohm/□)	Cracked
1	1	1.3	460	9.68×10^{-4}	4:1	0.4:1	300	50/50	No
2	2	1.55	460	9.68×10^{-4}	4:1	0.4:1	260	115/160	No
3	4	2.3	460	9.68×10^{-4}	4:1	0.4:1	206	400/600	No
4	6	3	460	9.68×10^{-4}	4:1	0.4:1	295	-	No
5	12	3	460	9.68×10^{-4}	4:1	0.4:1	770	100/430	Yes
6	18	3	460	9.68×10^{-4}	4:1	0.4:1	980	60/350	Yes
7	1	1.3	410	9.68×10^{-4}	4:1	0.4:1	220	65/65	No
8	2	1.55	410	9.68×10^{-4}	4:1	0.4:1	325	45/300	No
9	4	2.3	410	9.68×10^{-4}	4:1	0.4:1	280	85/550	No
10	6	3	410	9.68×10^{-4}	4:1	0.4:1	280	100/300	No

Table 33 - Conditions for Passes Series

From this series the most notable samples were those deposited at 460°C. In this part of the series an increase in passes and film thickness is shown however the initially measured conductivity of the sample diminished over time. An unfortunate problem was encountered when operating in the dynamic mode, where visible film cracking occurred. Samples would decrease notably in conductivity after a 24 hour period, and in certain cases within minutes of leaving the coating equipment.

In Figure 109 the AFM data is shown for a selection of samples with the associated roughness given in Table 34 and the corresponding XRD data in Figure 110.

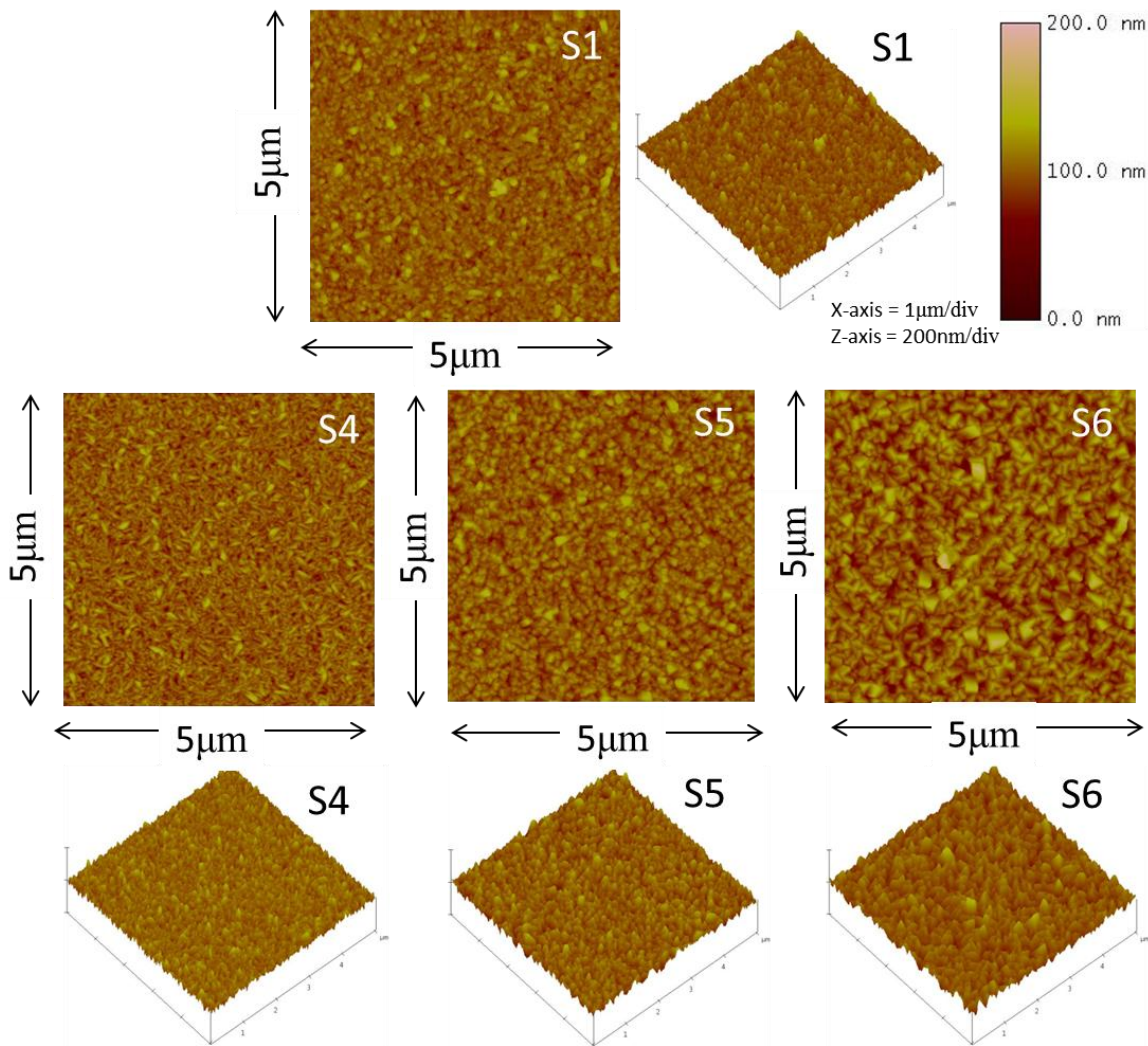


Figure 109 - AFM Images of Passes Series - Sample 1, 4, 5 and 6 respectively

Sample	1	4	5	6
Roughness RMS (nm)	10.07	10.46	11.66	15.46

Table 34 - Roughness Data for Passes Series

Sample 6 demonstrated a thickness of nearly 1µm from eighteen passes with a sheet resistance of 60 ohm/□. Despite having the desired thickness, the conductivity of the sample was too low for TCO requirements as a consequence of cracking.

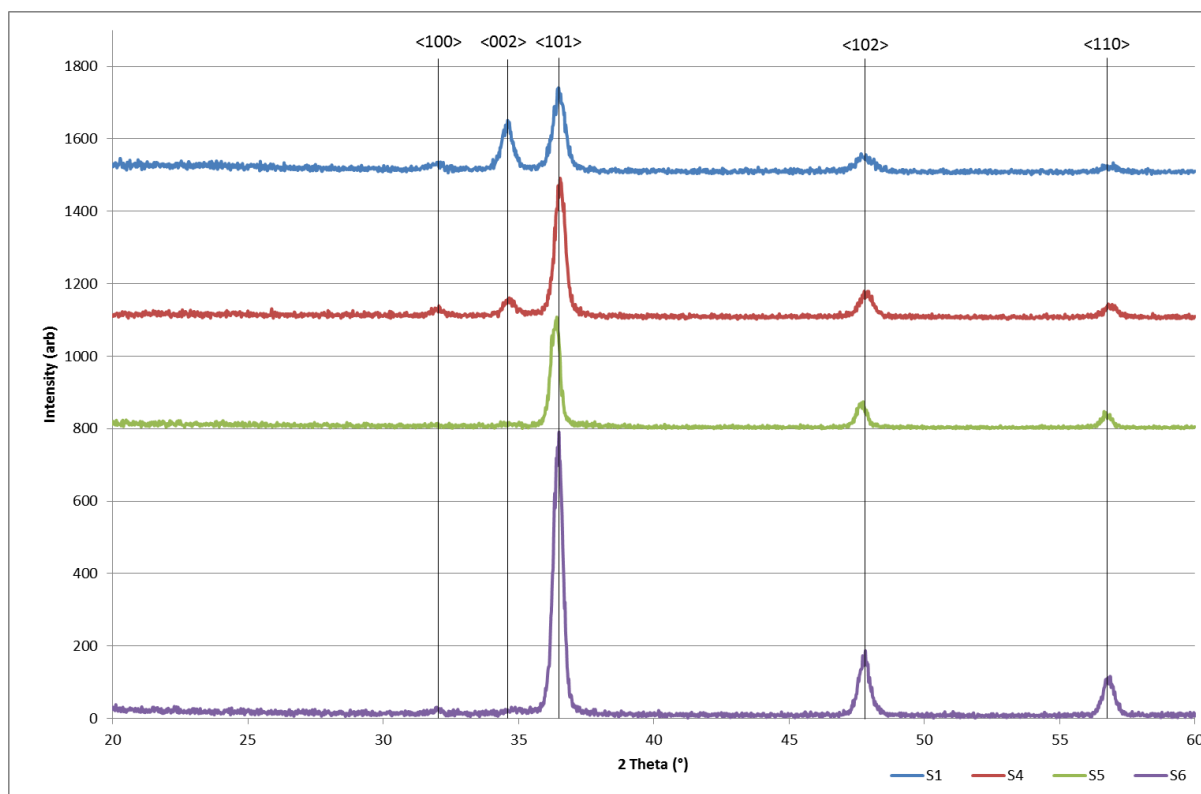


Figure 110 - XRD Data of Passes Series

For one pass approximately 300nm was deposited at a lower translation speed with comparable thickness at higher speeds requiring multiple passes. Despite the equivalent thickness, samples exhibited varying surface structure, crystal preference and conductive properties. This may have been a consequence of the residence time for coating, permitting film development to develop differently attributing to the alternative properties.

Films deposited in the series to achieve the same thickness from fewer passes demonstrated higher conductivity. Increasing the number of passes with a lower substrate temperature appeared to reduce these effects, allowing thicker films to be developed. Following this relationship it was decided that 410°C was the optimum coating temperature to continue the process.

Dynamic deposition of 6 passes at speed 3 was non-conductive. Deposition at a slower speed of 1.3 showed some traces of conductivity. Critically it demonstrated that dopant introduction required a slower transition through the coating region, enabling a higher resonance time. The

route forward was to reduce the number of passes and speed of translation to deposit the required thickness. It appeared that resonance time is critical for the growth rate, dopant introduction or exposure of the chemicals to temperature. Figure 111 shows the relationship between resistivity developed between number of passes and substrate temperature from the series.

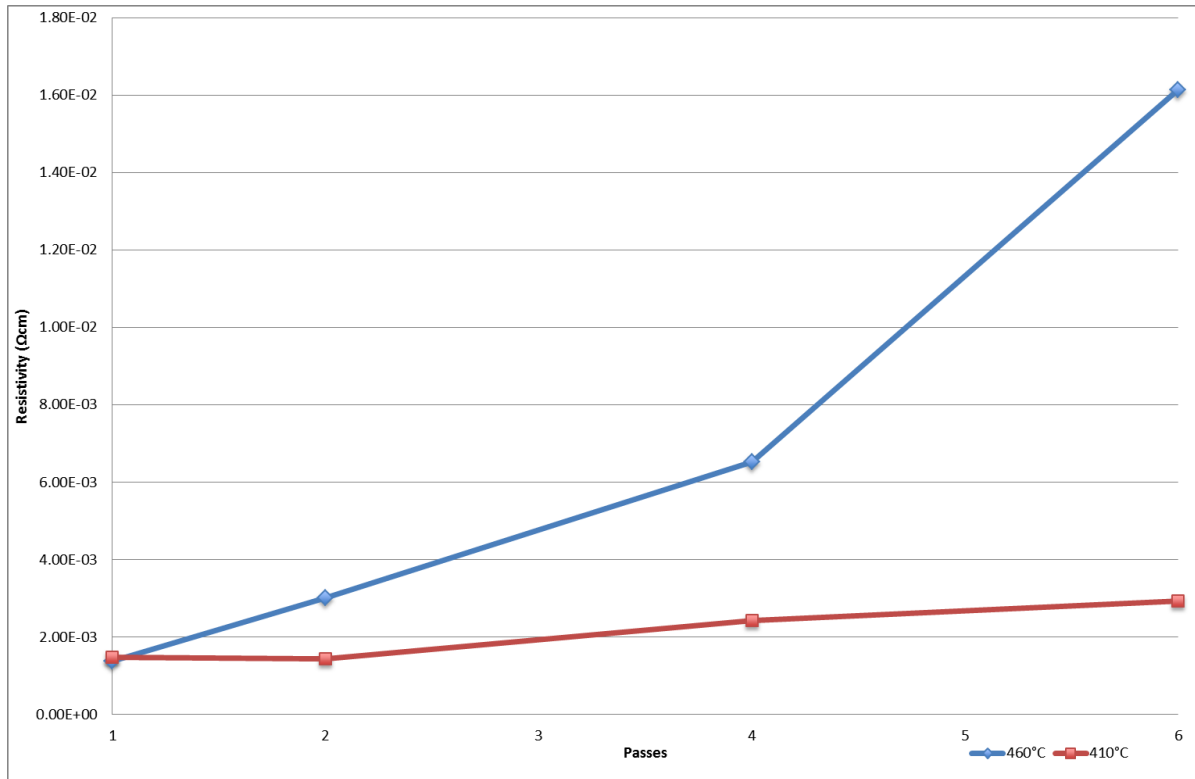


Figure 111 - Relationship between Number of Passes and Resistivity

Reduced number of passes in conjunction with lower deposition temperature may also resolve the cracking issue. Currently at this stage of development it is unknown whether the cracking exists due to stresses in the film from the deposition condition or physically from the dopant. In an attempt to reduce the cracking problem a reduced number of passes and translation speed in conjunction with slow cooling was investigated.

7.9.3 F:ZnO Reduced Passes with Slow Transition Speed

The following series observed the effects of reducing the number of passes for deposition. This was performed in an attempt to prevent the cracking problem, as indicated from the previous experimentation. In Table 35 the conditions for this series are given. Sample 1&2 were removed from deposition immediately (normal operation), whereas sample 3-5 were cooled slowly over several hours.

Sample	Passes	Speed	Substrate Temperature (°C)	Zinc Molar Flux (Mol/Min)	O:Zn Ratio	F:Zn Ratio	Thickness (Nm)	Sheet Resistance Initial/After (Ohm/□)	Roughness RMS (nm)	Cracked
1	4	1.55	410	9.68×10^{-4}	4:1	0.4:1	700	70/820	11.28	Yes
2	6	1.55	410	9.68×10^{-4}	4:1	0.4:1	960	35/1170	17.67	Yes
3	4	1.4	410	9.68×10^{-4}	4:1	0.4:1	750	20/320	17.01	Yes
4	6	1.4	410	9.68×10^{-4}	4:1	0.4:1	1000	12/345	16.11	Yes
5	6	1.55	410	9.68×10^{-4}	4:1	0.4:1	700	22/300	8.94	Yes

Table 35 - Slow Translation Deposition Conditions

Samples 1&2 appeared initially to have increased stability, however after several hours had subsequently cracked eliminating conductivity. As the reduced number of passes failed to resolve the cracking, thermal stress in the film was considered. Samples 3-5 were allowed to cool down over a few hours on the susceptor. These samples were removed when room temperature had been achieved. Initially the results seemed positive with the achieved target conductivity and thickness. However given 24 hours these samples, cracked and degraded the conductive properties. The AFM data for samples 1 and 2 is shown in Figure 112, 3 to 5 in Figure 113 and the XRD is represented for all samples in Figure 114.

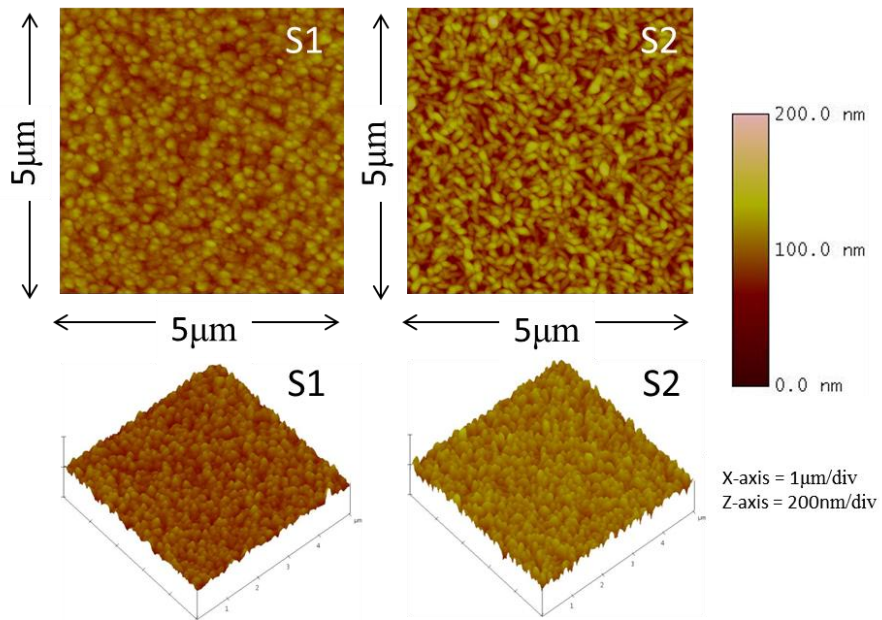


Figure 112 - Sample 1 & 2 Reduced Passes

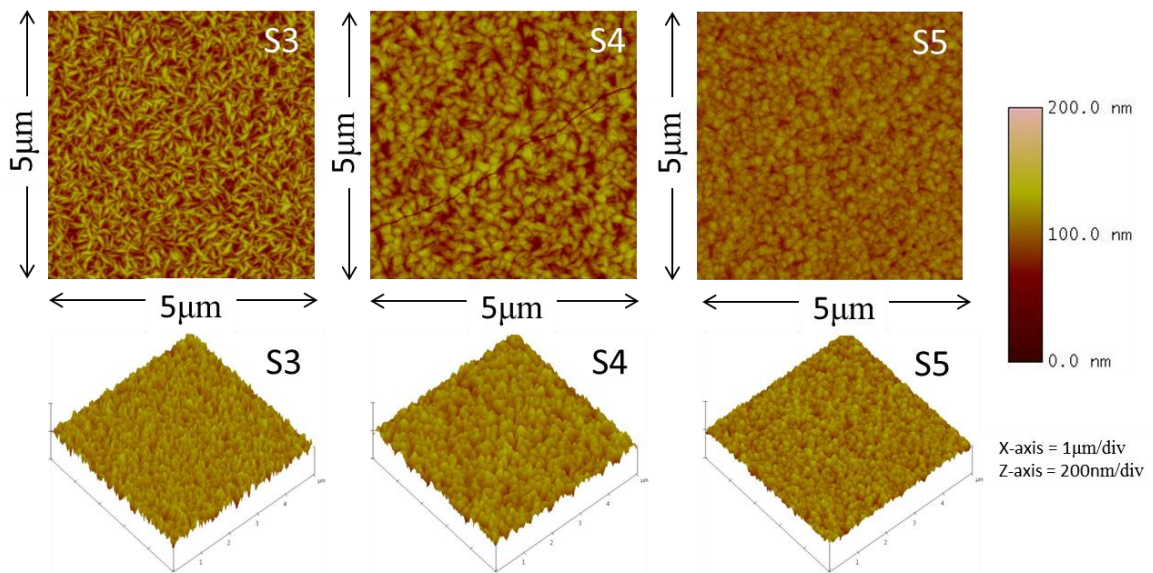


Figure 113 - Sample 3, 4 and 5 Reduced Passes and Slow Cooled

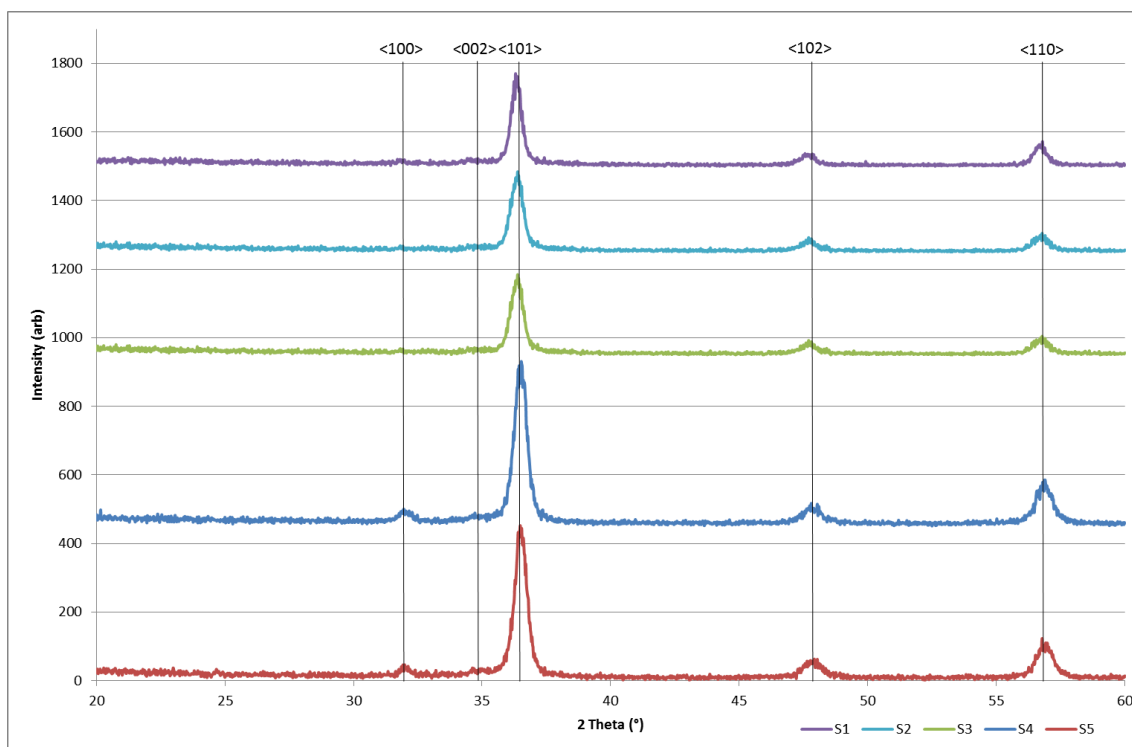


Figure 114 -XRD Data of Reduced Passes Samples 1 to 5

In the AFM data we see effects of altering the translation speed with subtle changes to the morphology. Sample 3 shows a distinct needle structure typical of fluorine incorporation, with all samples showing tendencies towards this morphology. XRD analysis confirms the presence of fluorine with a dominant $\langle 101 \rangle$ peak. Sample 4/5 show a stronger $\langle 101 \rangle$ peak and additional $\langle 100 \rangle$ peak, which may be attributed to the cooling process and sample exposure. Subsequent research will investigate the deposition conditions of translation speed and passes for comparable thickness to observe any structural differences. Imaging of sample 4 shows a distinct crack through the structure. Typically these cracks are easily identifiable using an optical microscope, with the AFM showing the existence of much smaller micro cracks in the film.

7.9.4 Film Cracking Monitoring

Cracking was monitored via an optical microscope, with cracks being the order of microns wide and several microns long clearly visible. Shown in Figure 115 is the progression of cracks on a sample straight after deposition cooling and at hour intervals thereafter.

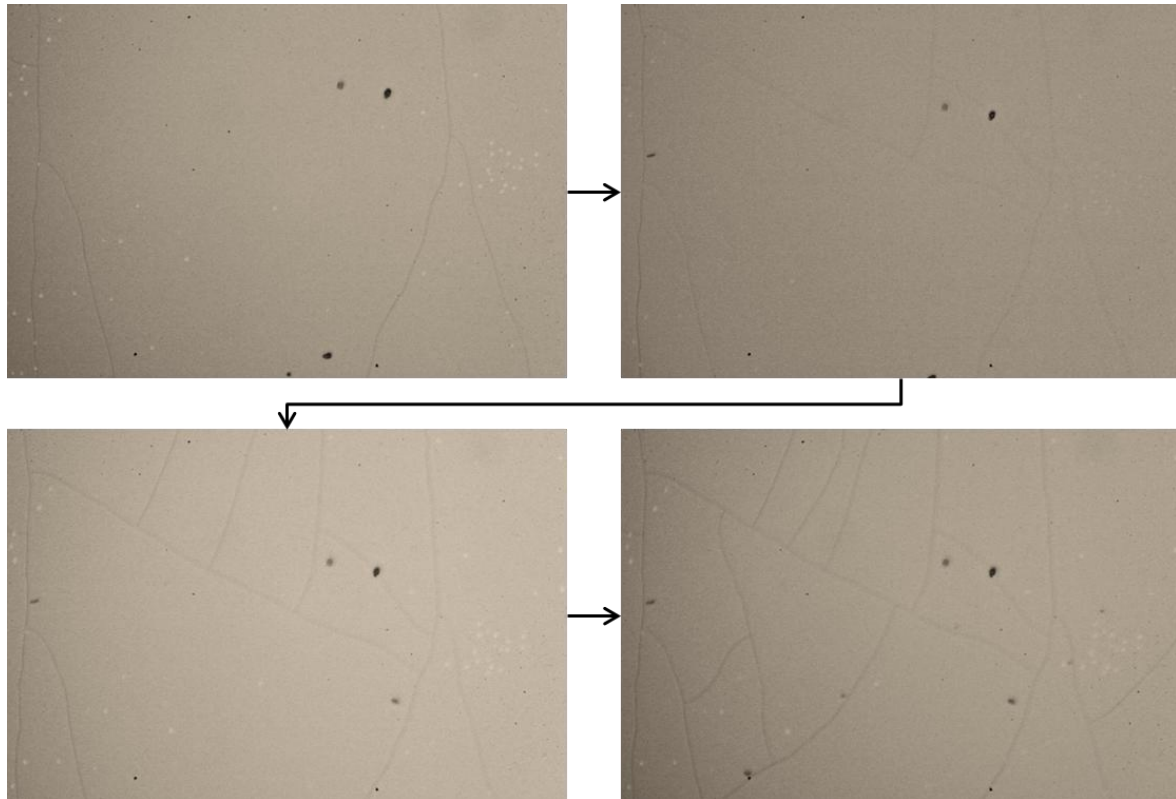


Figure 115 - Advancement of Cracking over One Hour Intervals from Deposition

From the previous experiments, samples exposed to changes in the number of passes, temperatures (between 410°C & 460°C), slow speeds and slow cooling still cracked. Initial observations of these samples indicated the following characteristics for the cracking of F: ZnO;

- Fluorine doped zinc oxide films deposited over 300nm thick ultimately cracked over a 24 hour period, eliminating conductivity.
- Deposited films of 300nm or less remained stable over a 6 month/year period.
- Undoped ZnO could be deposited up to 1000nm without any traces of cracking.

Considering the positive results exemplified by the static coatings, they were observed again to assess their current condition. Coatings deposited via the nozzle system and statically underneath the dual flow arrangement were inspected. These samples were 12-18 months old and originally exhibited a reasonable conductivity. Inspection now showed significant signs of cracking and high sheet resistance. Comparable to the large area coatings of the dual flow arrangement, films below the critical 300nm thickness remained stable. The ZnO films cracked with the introduction of fluorine into the deposition. Further investigation observed the effects of fluorine concentration.

7.9.5 F:ZnO Dopant Series

Initial investigation of the cracking indicated that dopant introduction was responsible, as undoped films were deposited successfully without cracking. Previous deposition utilized a 0.4:1 fluorine to zinc ratio in the oxidant source supplied into the gas phase concentration. Subsequent investigation sought to reduce the fluorine concentration present for deposition in aid of resolving the film cracking.

Dopant reduction would have a corresponding advantage by reducing the carrier concentration present in the films. Current theories with regards to TCOs have shown that maintaining high mobility whilst reducing carrier concentration leads to more efficient solar cells, through reduced free-carrier absorption.

Sample	Passes	Speed	Substrate Temperature (°C)	Zinc Molar Flux (Mol/Min)	O:Zn Ratio	F:Zn Ratio	Thickness (Nm)	Sheet Resistance Initial/After (Ohm/□)	Roughness RMS (nm)	Cracked
1	6	1.4	410	9.68×10^{-4}	4:1	N/A	1000	N/A	23.35	No
2	6	1.4	410	9.68×10^{-4}	4:1	0.04:1	1000	12/75	13.73	Yes
3	6	1.4	410	9.68×10^{-4}	4:1	0.08:1	1000	8.8/60	15.83	Yes
4	6	1.4	410	9.68×10^{-4}	4:1	0.15:1	1000	10/25	11.34	Yes
5	6	1.4	410	9.68×10^{-4}	4:1	0.4:1	1000	12/345	16.11	Yes

Table 36 - Dopant Series Conditions

Table 36 gives the conditions for the series, utilizing fluorine doping of 0% to 0.4:1, with the associated AFM shown in Figure 116 and XRD data in Figure 117. All other conditions through the series remained the same.

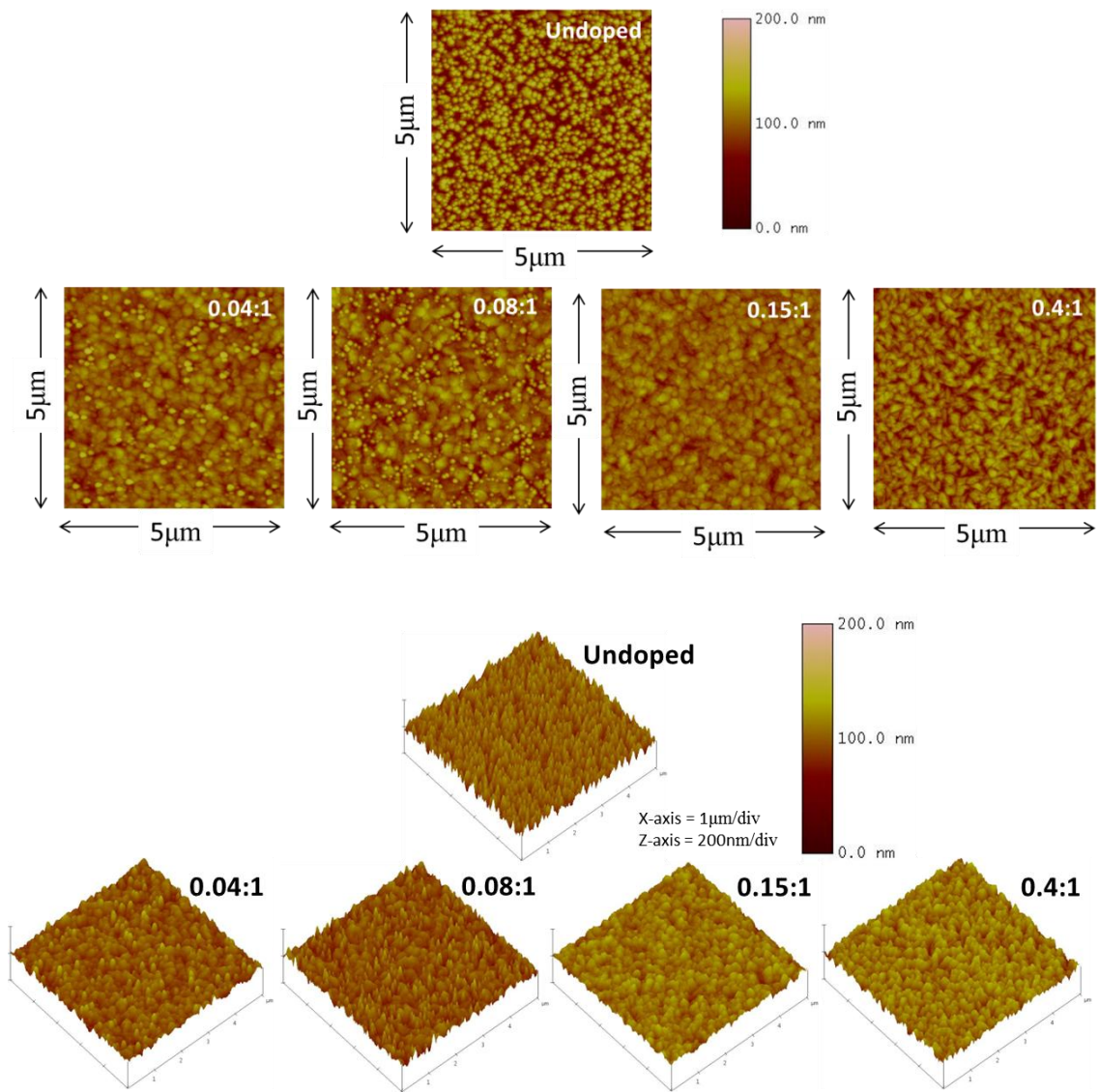


Figure 116 - Dopant Series AFM Data

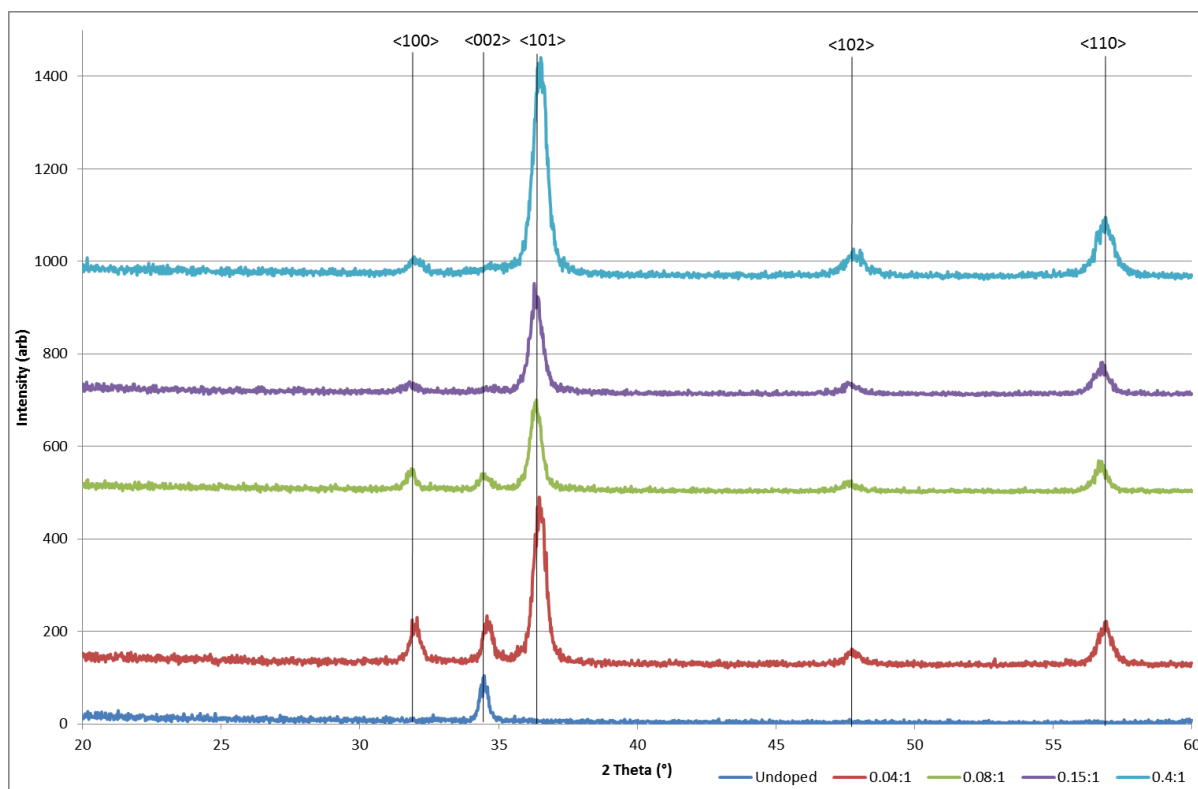


Figure 117 - XRD Data for Dopant Series

Decreasing dopant concentration had a distinct effect on the morphology and crystal structure. Reducing fluorine incorporation the crystal structure reverted back to the <002> preferred orientation of the undoped. This was reflected in the AFM data with the rounded features associated with undoped zinc oxide for this deposition temperature. Initial results were positive showing the dopant reduction did not have a negative impact on conductivity. The 4Mol% concentration demonstrated the target properties of conductivity for a given thickness. Reduction of the carrier concentration whilst retaining high mobility offered enhanced optical properties through reduced losses. Unfortunately as experienced with previous depositions, each doped film subsequently cracked after 24 hours. Following investigations observed the effects of the Zn:O ratio and fluorine incorporation. Optimization of the zinc, oxidant and fluorine ratio was observed in the following series.

7.9.6 F:ZnO Oxidant Introduction Series

In this series the optimization of the zinc to oxidant ratio is observed. Standard ethanol introduction was used throughout the previous series with a molar ratio of O:Zn of 4:1. In this series it was reduced to a 1:1 ratio and increased up to 40:1 to investigate its effects on the film characteristics and if this could resolve the film cracking. Continuing with the results of the dopant series the fluorine was reduced to 0.04:1. This series was split into two sections, with the investigation of lower and higher oxidant ratios with the conditions given in Table 37.

Sample	Passes	Speed	Substrate Temperature (°C)	Zinc Molar Flux (Mol/Min)	O:Zn Ratio	F:Zn Ratio	Sheet Resistance Initial/After (Ohm/□)	Roughness RMS (nm)	Cracked
1	6	3	410	9.68×10^{-4}	1:1	0.04:1	-	4.23	No
2	6	3	410	9.68×10^{-4}	2:1	0.04:1	-	5.36	No
3	6	1.55	410	9.68×10^{-4}	4:1	0.04:1	22/300	8.94	Yes
4	6	1.55	410	9.68×10^{-4}	10:1	0.04:1	-	3.27	No
5	6	1.55	410	4.84×10^{-4}	20:1	0.04:1	-	7.03	No
6	6	1.55	410	4.84×10^{-4}	30:1	0.04:1	50 / -	15.76	Yes
7	6	1.55	410	4.84×10^{-4}	40:1	0.04:1	60 / -	22.03	Yes

Table 37 - Oxidant Series Conditions

The first samples AFM data is shown in Figure 118 had a molecular ratio 1:1 and 2:1 respectively. Neither of these samples appeared to be conductive, reflected by the dominant

<002> XRD peak typical of an undoped film as represented by Figure 119. Coinciding with this data both samples remained stable without any signs of cracking on the surface.

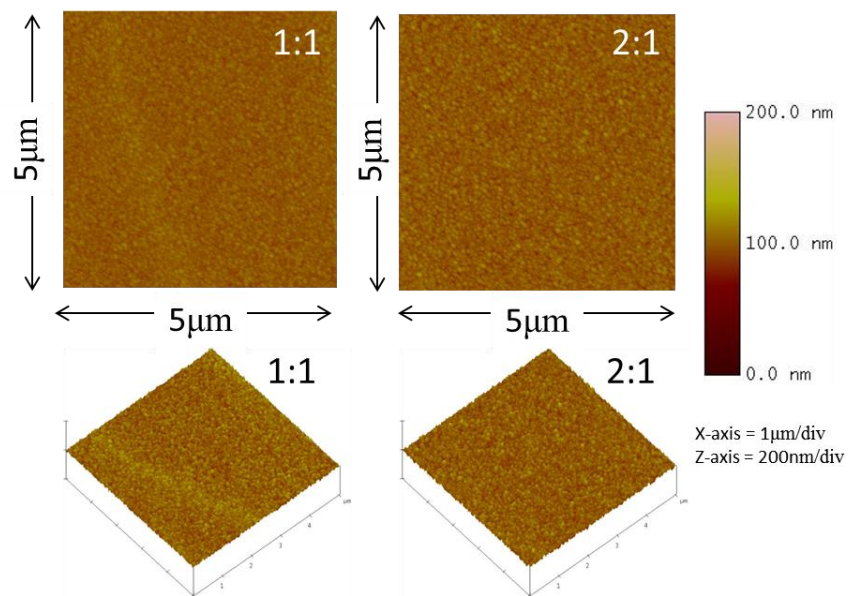


Figure 118 - Low Oxidant Series AFM

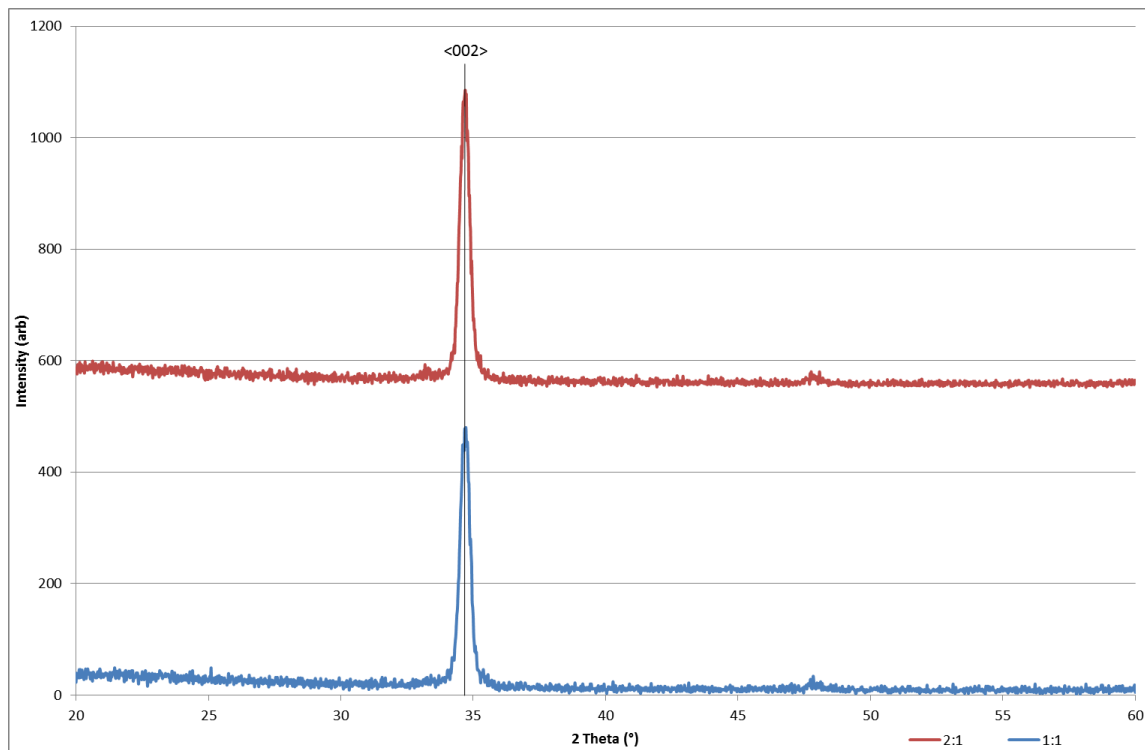
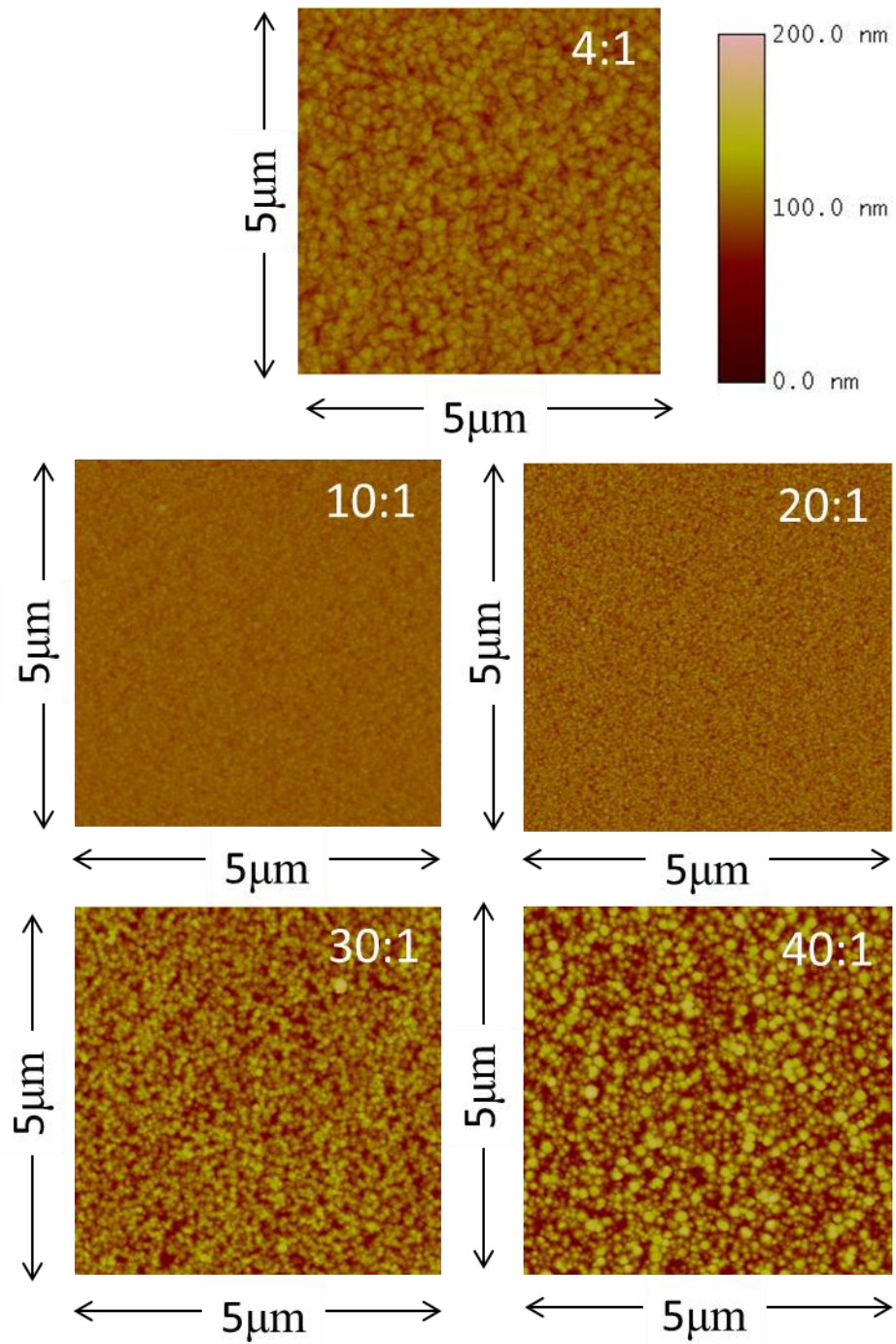


Figure 119 - Low Oxidant Series XRD

Films appeared visually very yellow upon a white background, indicative of excessive absorption through high carbon incorporation. Optically these films were not beneficial for TCO applications and the lack of conductivity showed that oxidant reduction was not a viable method.

The second phase of this series introduced higher ratio of oxidant into the deposition chemistry. Preceding samples were deposited with the 4:1 ratio of oxidant to zinc, used as a reference for this series. The AFM data is shown in Figure 120 and the XRD data is represented in Figure 121.

AFM data showed a transition of a doped morphology from the low oxidant ratio to a significantly rounded surface of the higher ratio. It was indicative of reduction of fluorine incorporation as the sample structure tended towards the undoped. This also was reflected by the XRD data as the preferred doped orientation $\langle 101 \rangle$, to the undoped orientation of $\langle 002 \rangle$. Surface roughness also increased with oxidant, indicative of the $\langle 002 \rangle$ orientation development (c-axis). With excessive oxidant the undoped structure was preferentially deposited. Optical assessment was conducted utilizing the fibre optic system with the transmission data shown in Figure 122 and reflection in Figure 123, with the average values calculated in Table 38.



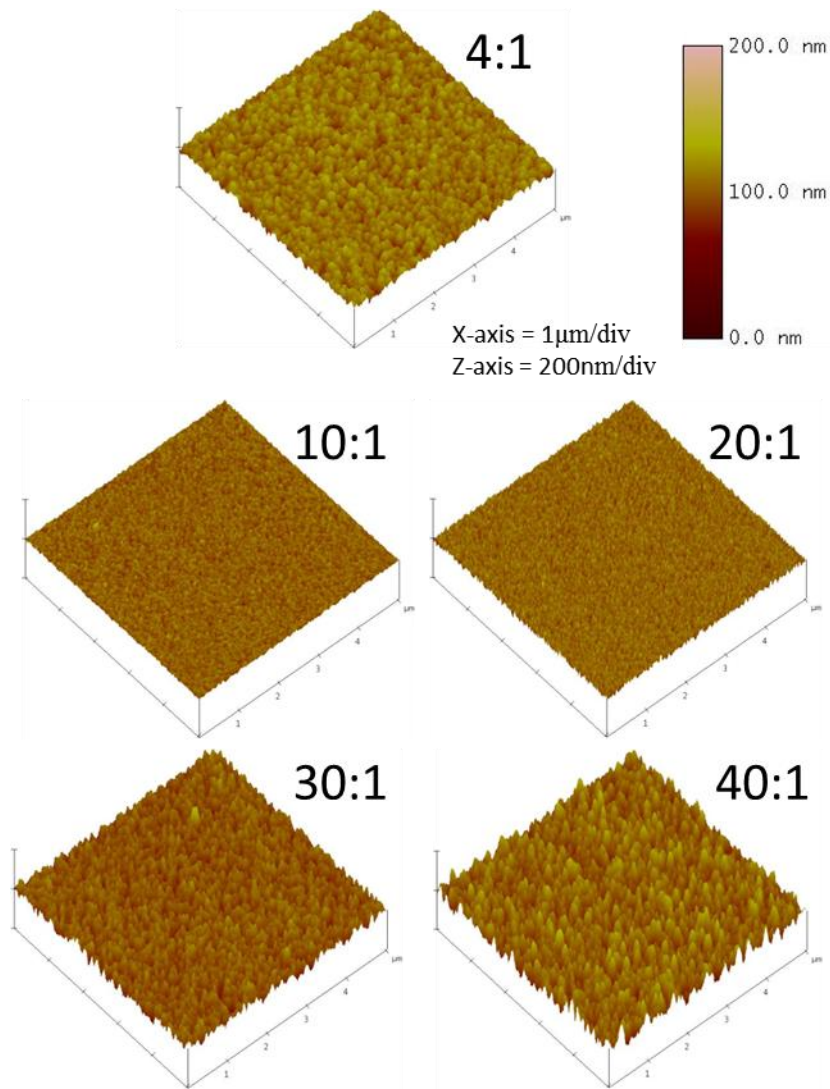


Figure 120 – High Oxidant Series AFM Images

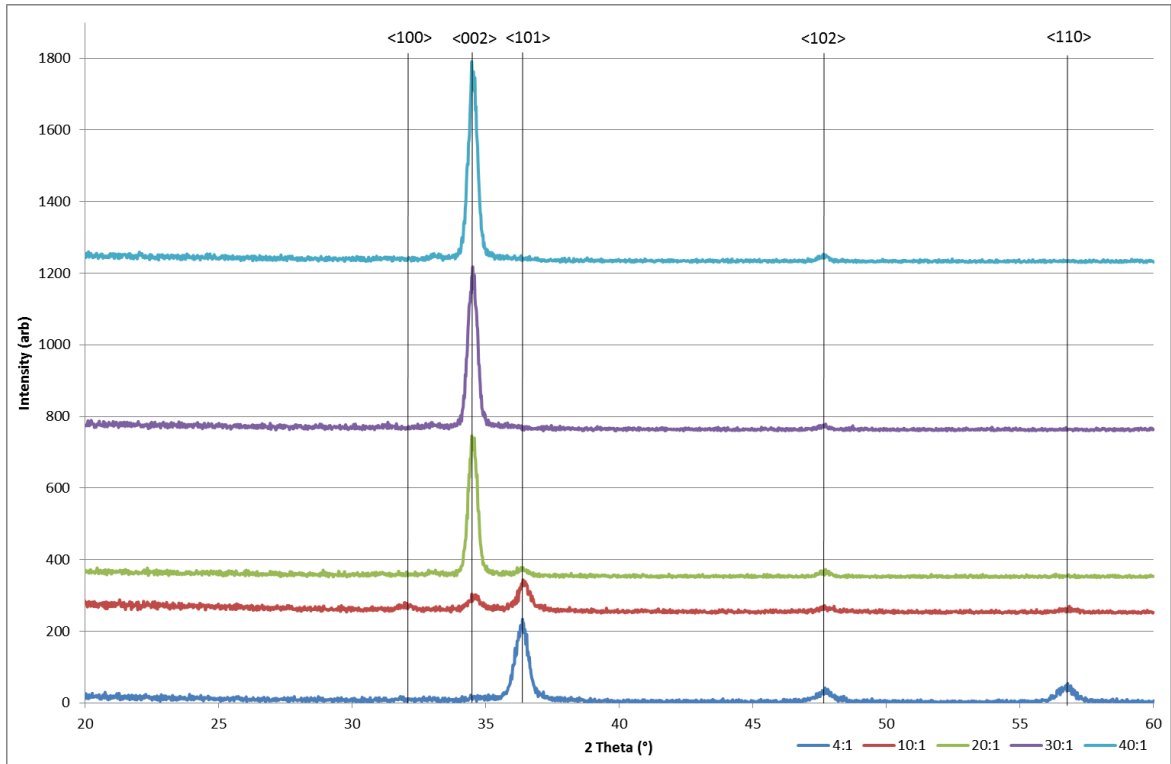


Figure 121 - High Oxidant Series XRD

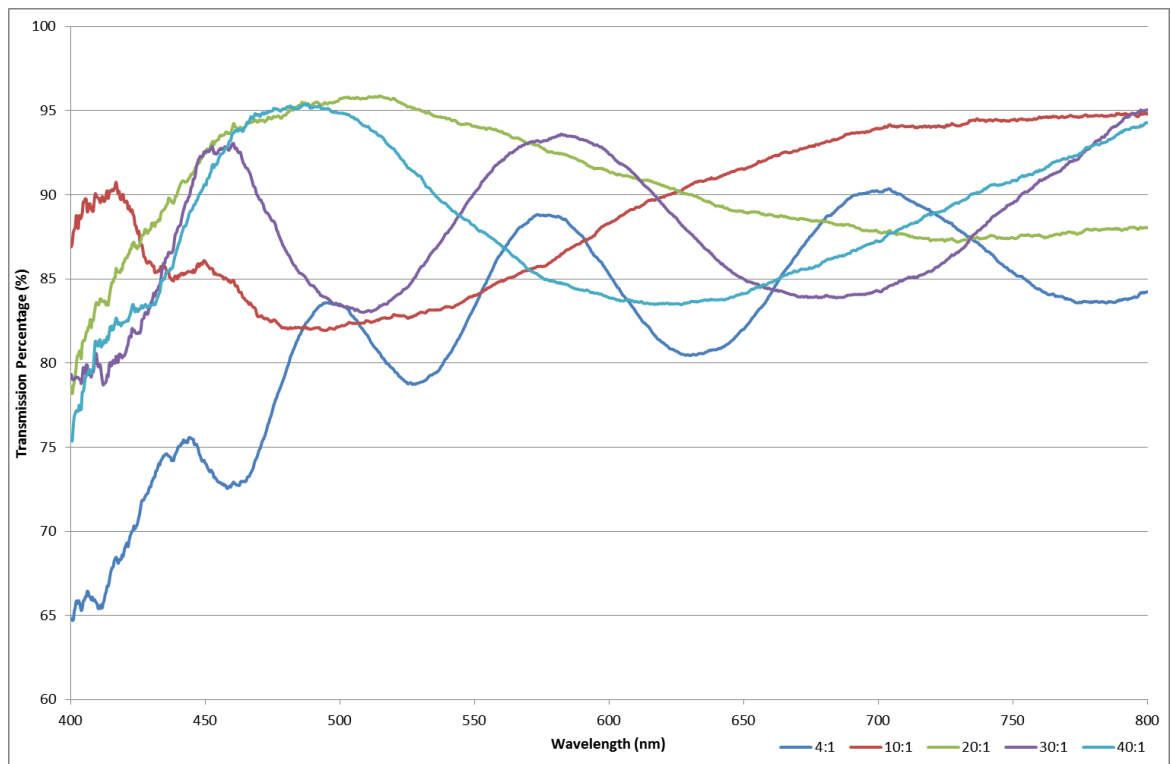


Figure 122 - Transmission of Higher Oxidant Samples (400nm - 800nm)

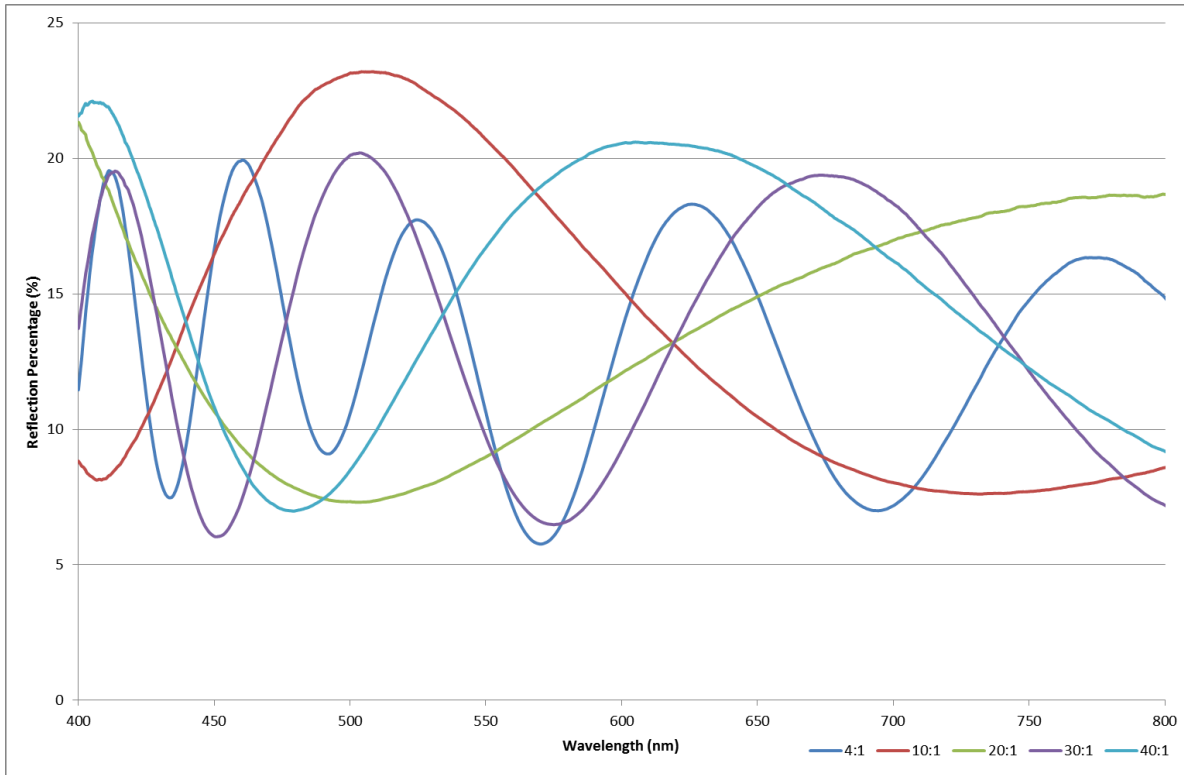


Figure 123 - Reflection of Higher Oxidant Samples (400nm - 800nm)

Sample	4:1	10:1	20:1	30:1	40:1
Transmission %	82.34	89.09	90.32	87.77	88.3
Reflection %	13.02	13.55	13.63	13.58	15.08

Table 38 - Optical Assessment of Higher Ratio Deposition (Average over 400-800nm)

Visual assessment of the samples showed a significant reduction in absorption, as the yellow tint to the films was greatly reduced. Samples were assessed using an Ocean Optics standard configuration for transmission and reflection. The visual observations corresponded with a notable increase in transmission over standard conditions. A peak gain of 8% transmission was recorded for the 20:1 ratio, and a minimal increase in reflection of 0.6%. This was a significant advantage for TCO production being able to increase optical efficiency of the layer. However these films after a 24 hour period subsequently cracked, losing the beneficial conductivity.

During the oxidant series it was noted that ratio of 20:1 was optimal for optical properties and suited the performance related capabilities of the system. Controlling the deposition of higher oxidant ratio's in the current system configuration became increasingly difficult due to syringe delivery limitations. An interesting observation was noted with varying sample exposure to the high ratio delivery, the sample feature size altered greatly. Maintaining the slowest growth possible, large platelet features were grown. Increasing the speed reduced the feature size, producing a sharper overall structure. Figure 124 shows the variation of feature size through AFM observation.

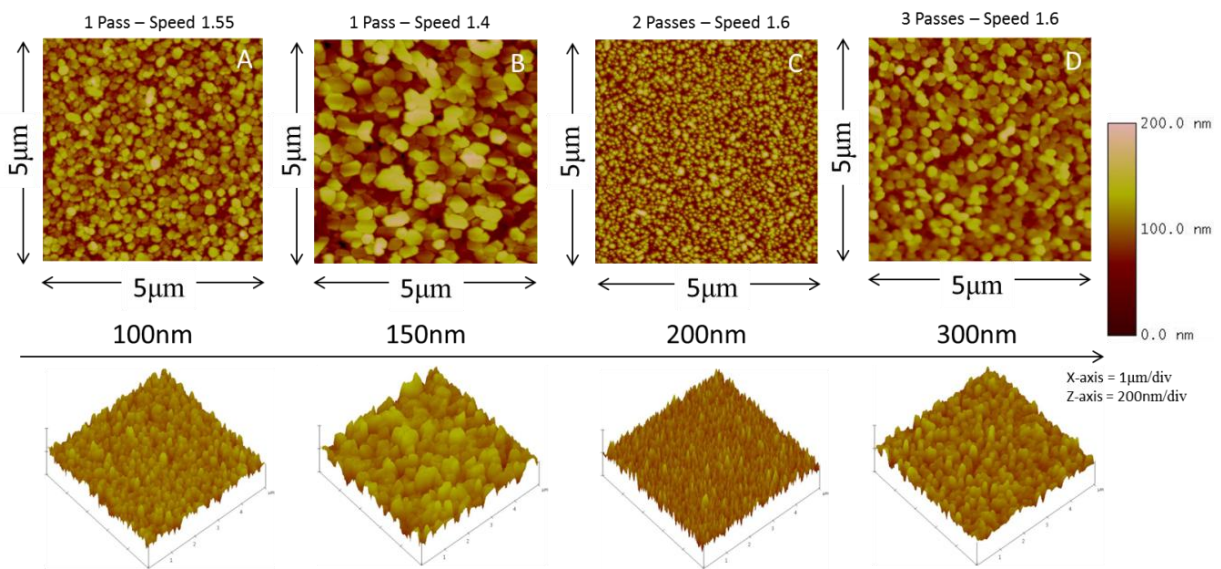


Figure 124 - Variation of Feature Size through Exposure Manipulation

Observation of all these samples showed a preferred orientation in the $\langle 002 \rangle$ axis although they exhibited a range of structures. This may be a useful tool for tuning the surface morphology for a specific application that requires rougher or smoother films.

Sample	A	B	C	D
Roughness RMS (nm)	24.88	33.78	24.67	23.61

Table 39 - Roughness Values for Changing ZnO Morphology by Exposure

7.9.7 F:ZnO Growth Current Status

Cracking persisted despite manipulating the dopant concentration, deposition temperature, cooling regime, zinc to oxidant ratio, translation speed and passes. Film cracking was typically associated with stress in the film. These experiments indicated fluorine introduction into these films induces stresses that cannot be removed easily. Shown in the oxidant ratio series, even trace quantities in the deposition permits conductivity but subsequently cracks after a given period.

Additional attempts to resolve the cracking involved alternative fluorine sources of trifluoroacetic acid (TFA) and tetrafluoropropanol (TFP). Utilizing TFA produced powdery deposits on the glass surface and conditions to alleviate powdery deposits suffered very low growth rates (sub 10nm thick with a long residence time). TFP as shown previously not to be a suitable alternative as films deposited exhibited little to no conductivity.

Methanol was also employed as the base oxidant with trifluoroethanol as the fluorine source. Samples produced were predominantly very thin and showed limited conductivity. These films also subsequently cracked.

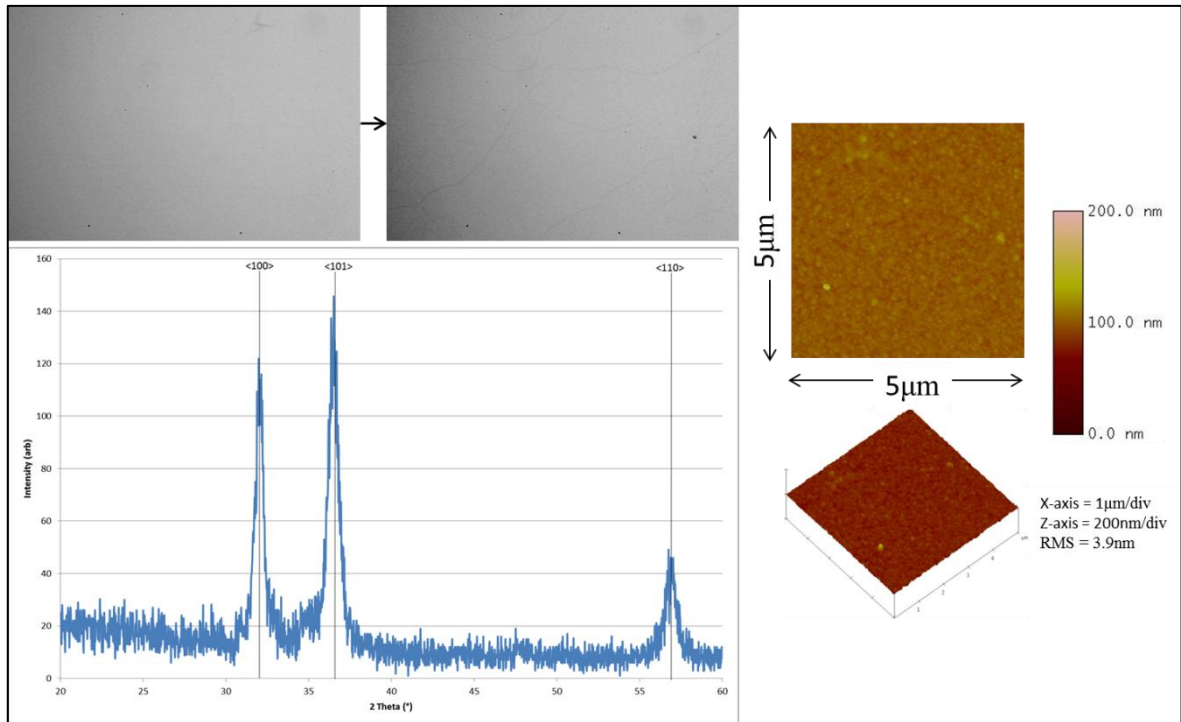


Figure 125 - Methanol Oxidant for F:ZnO Growth

Currently it appears that a method to produced F:ZnO via APCVD is not possible beyond 300nm without cracking on glass. Utilizing another substrate may enable the film growth to develop without the stresses that are the source of cracking. Further investigation observed the effects of an seeding layer for F:ZnO growth, which intended to reduce the cracking through disruption of the initial phases of growth.

7.10 Seeding Layer for Fluorine Zinc Oxide Growth

7.10.1 Initial Investigation

Corning bora silicate is the standard glass employed for deposition research. All attempts to deposit stable F:ZnO on bora silicate failed. Implementation of an alternative substrate or seeding layer may offer a possible solution to the film fracturing. Utilizing a seeding layer may disrupt/influence an alternative growth structure/mechanism that resist cracking whilst offering target properties. Previously deposited thin F:ZnO films were initially employed as a seeding layer, with a subsequent growth of an undoped top layer for bulk thickness. The 300nm doped films have shown to be stable over several months, being highly doped they could offer carrier diffusion through the film. Table 40 demonstrates the conditions for deposition of the seeding layer and Table 41 highlights the best samples produced from seeding layer over coating. Over-coating used the previously standardized 4:1 O:Zn ratio for undoped ZnO bulk deposition.

Sample	Passes	Speed	Substrate Temperature (°C)	Zinc Molar Flux (Mol/Min)	O:Zn Ratio	Oxidant	F:Zn Ratio	Thickness (Nm)	Sheet Resistance (Ohm/□)
Seeding	2	1.55	410	9.68×10^{-4}	4:1	Ethanol	0.4:1	300	85 to 100

Table 40 - Condition for Seeding Layer

Sample	Passes	Speed	Substrate Temperature (°C)	Zinc Molar Flux (Mol/Min)	O:Zn Molar %	Oxidant	Thickness (Nm)	Sheet Resistance Initial/After (Ohm/□)	Cracked
1	4	1.55	410	9.68×10^{-4}	4:1	Ethanol	700	47 / 300	Yes
2	10	1.55	410	9.68×10^{-4}	4:1	Methanol	700	68 / 600	Yes

Table 41 - Conditions for Seeding Layer Over-coating

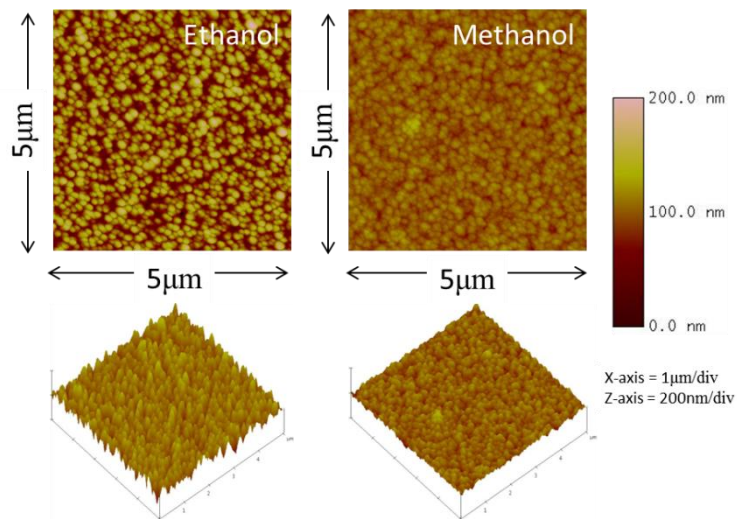


Figure 126 - AFM of Over-Coating Undoped ZnO Seeding Layer

Sample one utilized ethanol as the bulk oxidant source, with sample two using methanol. Both samples were prepared to a comparable stack thickness of 700nm. Initially after deposition sample one saw a decrease in sheet resistance from 100 to 47 ohm/□, sample two from 85 to 68 ohm/□. Subsequently both these films have cracked eliminating the conductivity. Despite the bulk material being undoped, cracking persists from the seeding layer. Interestingly from this series is the drop in sheet resistance through an additional undoped bulk layer. This would be beneficial for implementation into an alternative seeding layer. The next development observed the effect of an F:SnO₂ seeding layer.

7.10.2 F:SnO₂ Seeding Layer

F:ZnO with a bulk stack of ZnO demonstrated that carrier diffusion was present throughout the composite layers. This proved to be a beneficial property with the experienced cracking of doped ZnO. Implementation of F:SnO₂ as the seeding layer was explored as a possible solution to the cracking and as an alternative TCO composition. This material combination approach has several advantages. Utilizing F:SnO₂ to form part of the total composition may reduce the overall cost of the TCO coating. Furthermore applying ZnO/F:ZnO as the top layer permits easy adaptability of the morphology through the growth and etching capabilities. Additionally ZnO is also known to have increased stability against hydrogen plasmas which is used in subsequent cell processing. These facets could lead to an improved TCO layer for enhanced solar cells.

Investigation of this seeding layer employed a research group standard 900nm F:SnO₂ sample, which offered an approximate 12 ohm/□ conductivity. Initial deposition utilized the previously standardized F:ZnO deposition conditions of a 4:1 zinc to oxidant ratio with trifluoroethanol as the fluorine source. Deposition of the F:ZnO layer was kept under 300nm to ensure the film remained stable. The deposition conditions for this series are given in Table 42 and associated AFM image in Figure 127 and XRD represented in Figure 128.

Sample	Passes	Speed	Substrate Temperature (°C)	Zinc Molar Flux (Mol/Min)	O:Zn Ratio	F:Zn Ratio	Thickness (Nm)	Sheet Resistance Initial/After (Ohm/□)	Roughness RMS (nm)	Cracked
1	2	1.6	410	9.68×10^{-4}	4:1	0.4:1	900/200	11.8/8	31.67	No
2	1	1.55	410	9.68×10^{-4}	4:1	0.4:1	900/100	11.3./10	36.67	No

Table 42 - Conditions for Initial Over-coating on F:SnO₂

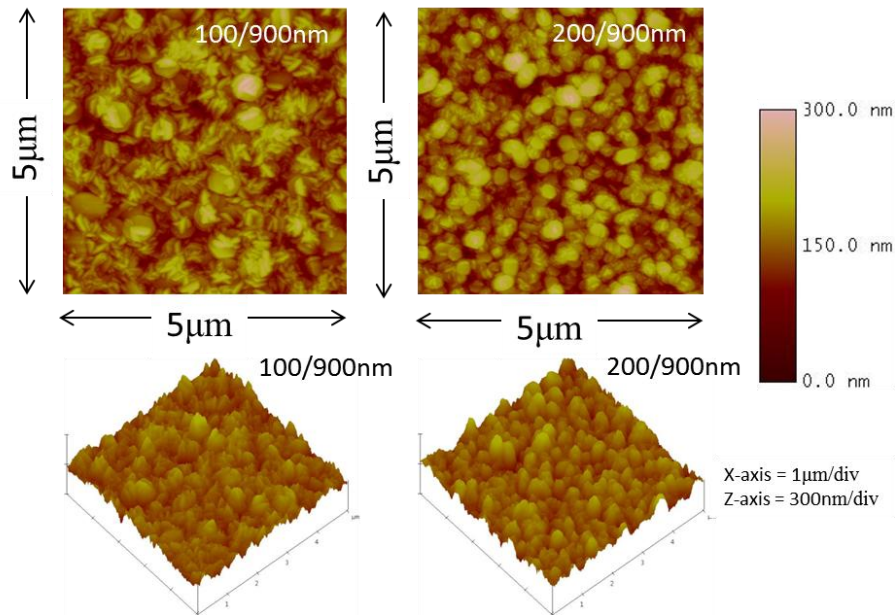


Figure 127 - Initial F:SnO₂ Over-Coating AFM's

The AFM images show that the ZnO layer grew upon the F:SnO₂ facets. This was an interesting effect as it develops on the facets opposed to the valleys of the structure. As the thickness increased the ZnO layer developed across the surface to form a continuous film. In the XRD data, the typical associated peaks of ZnO are seen with the additional SnO₂ peaks, <002> was still the dominant peak indicating the potential stability of the material. Optical assessment was performed using the fibre optic system with the transmission data represented in Figure 129 and reflection data in Figure 130.

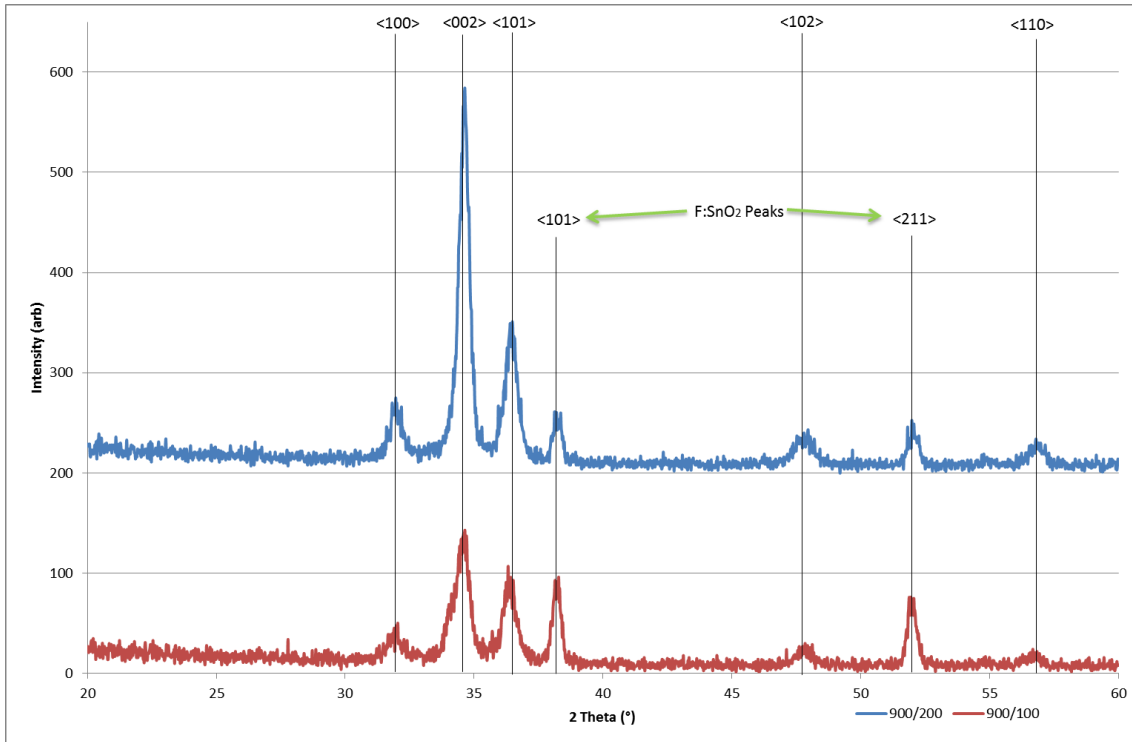


Figure 128 - XRD of Initial F:SnO₂ Over-Coating

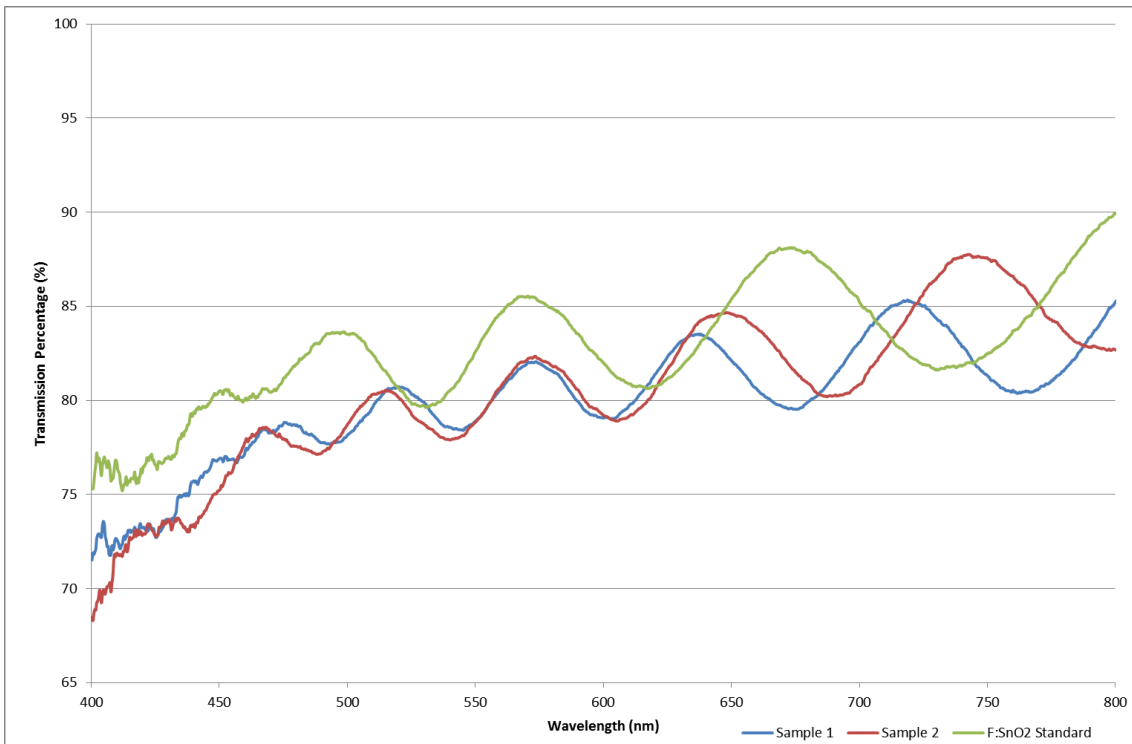


Figure 129 - Optical Transmission of F:SnO₂/F:ZnO Over coated

A subtle change in optical transparency and reflection was noted. Average transmission was on the lowest part of acceptability of approximately 80%. This was possibly due to the stack composition with an associated ratio of O:Zn. In comparison the stack offered a 2% reduction in reflection, which would suggest that light is being absorbed. Optimization reduced the absorption of deposited zinc has been shown through higher oxidant ratios, which may prove beneficial in further refinements of this stack composition. The average transmission and reflection for this series are calculated in Table 43.

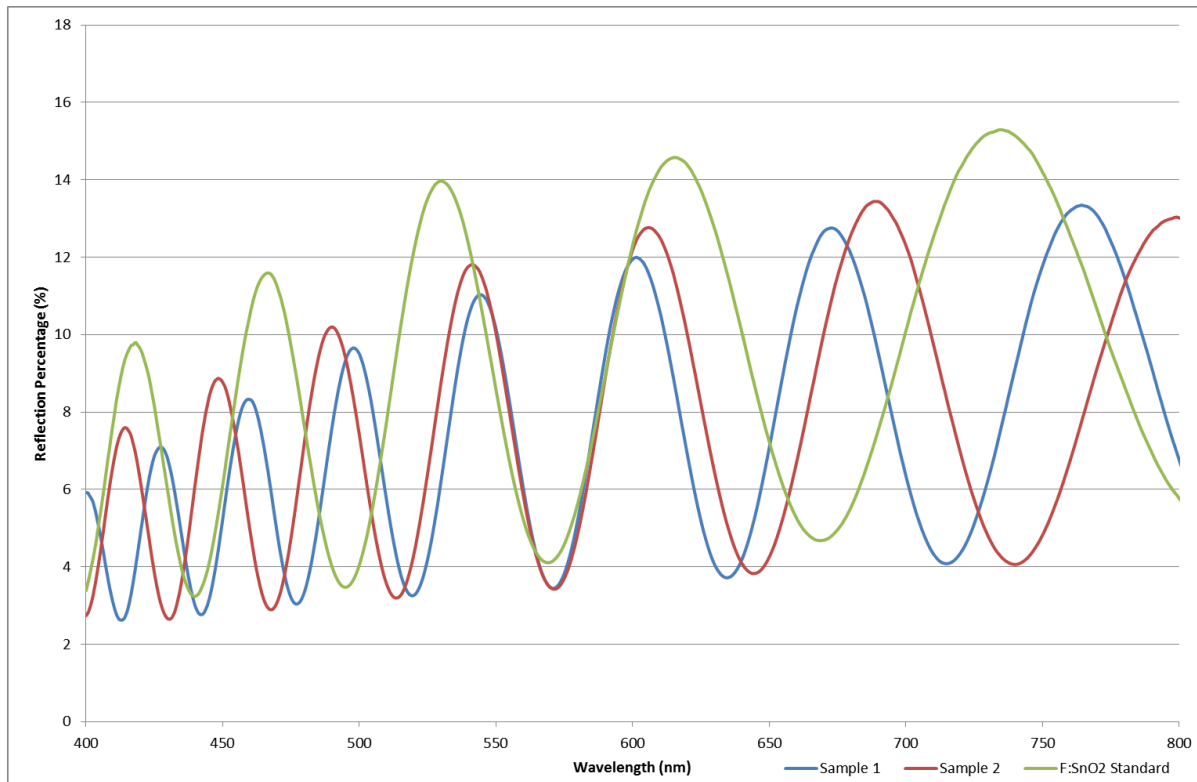


Figure 130 - Optical Reflection of F:SnO₂/F:ZnO Over coated

Sample	1	2	F:SnO ₂
Transmission %	80.1	80.62	82.89
Reflection %	7.61	7.74	9.24

Table 43 - Average Optical Performance across 400-800nm Wavelength

These samples offered encouraging results and exhibited the desired properties required of a TCO. The over coated samples were sent for photovoltaic testing to observe their

performance. Photovoltaic processing and testing was performed by EPFL, a contributing collaborator of the N2P European project. These samples were incorporated into amorphous silicon cells as the front TCO window layer. Processing and testing of the samples was performed at EPFL, a recognised group performing standardized characterization of photovoltaic modules. The results for the samples are given in Table 44 and transmittance data in Figure 131 (supplied by EPFL).

Sample	Surface (cm ²)	Voc (V)	Fill Factor (FF)	Rsc (Ohm.cm ²)	Roc (Ohm.cm ²)	Voc 0.4 (V)	Fill Factor 0.4 (FF)	Rsc 0.4 (Ohm.cm ²)	J EQE (mA/cm ²)	Efficiency EQE (%)
AGCU	0.25	0.907	0.59	1997.8	14.46	0.38	0.35	18072.3	14.49	7.75
F:SnO ₂	0.25	0.898	0.699	1948.4	4.88	0.3	0.35	11216.6	15.64	9.82
1	0.25	0.886	0.665	1000.5	4.51	0.05	0	1245.8	13	7.66
2	0.25	0.891	0.714	2197.1	4.86	0.25	0.29	6754.6	14.03	8.93

Table 44 - Performance Results of AGCU (standard), F:SnO₂ and Sample 1&2 (Data Supplied by EPFL)

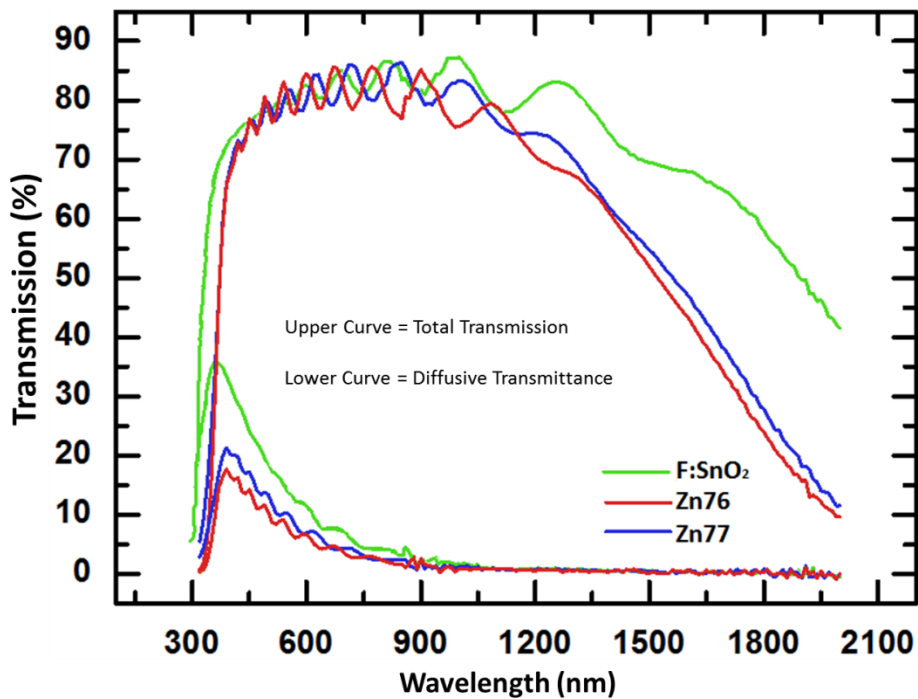


Figure 131 - Optical Performance of F:SnO₂ and Sample 1 (Zn76) & Sample 2 (Zn77) (Data Supplied by EPFL)

AGCU at present is a standard TCO product available in the marketplace, and used as a benchmark for comparative analysis in research. A comparable F:SnO₂ was analysed at the same time for a reference for the over-coated stack.

Critically what can be seen from the performance data is that the stack offers a better final efficiency compared to the reference AGCU. However a performance drop is noticed compared to a standard 900nm F:SnO₂ film without the F:ZnO cap. F:ZnO samples showed a low short circuit current due to the increased optical absorption of the TCO layer, which hindered their performance despite having an increased fill factor. ZnO deposited on F:SnO₂ smoothed the surface, corresponded by the AFM data. Optically the samples demonstrated reduced transparency in the Infra-red region, which has impacted on the cells efficiency. From the data of the cell performance, sample two had the best performance. This was reflected in the overall increase in optical transparency and haze. A reduction in carrier concentration would aid the transparency lost in the Infra-red region, having no impact on conductivity as shown by the low dopant series. Improving the cell performance would require the samples optical properties to be improved and low current capabilities. Table 45 – Properties of F:SnO₂/F:ZnO Stack Table 45 shows an overview of the TCO sample properties, with Figure 132 showing the development of a complete TCO stack.

Film Composition (F:SnO₂/F:ZnO)	Transmission (%)	Roughness R_{ms} (nm)	Sheet Resistance (Ohm/□) (FTO only)	Sheet Resistance (Ohm/□) (Stack)
900/0	82.4	39.2	11	-
900/100	80.6	33.7	11	9.5
900/200	80.1	36.6	11.8	8

Table 45 – Properties of F:SnO₂/F:ZnO Stack

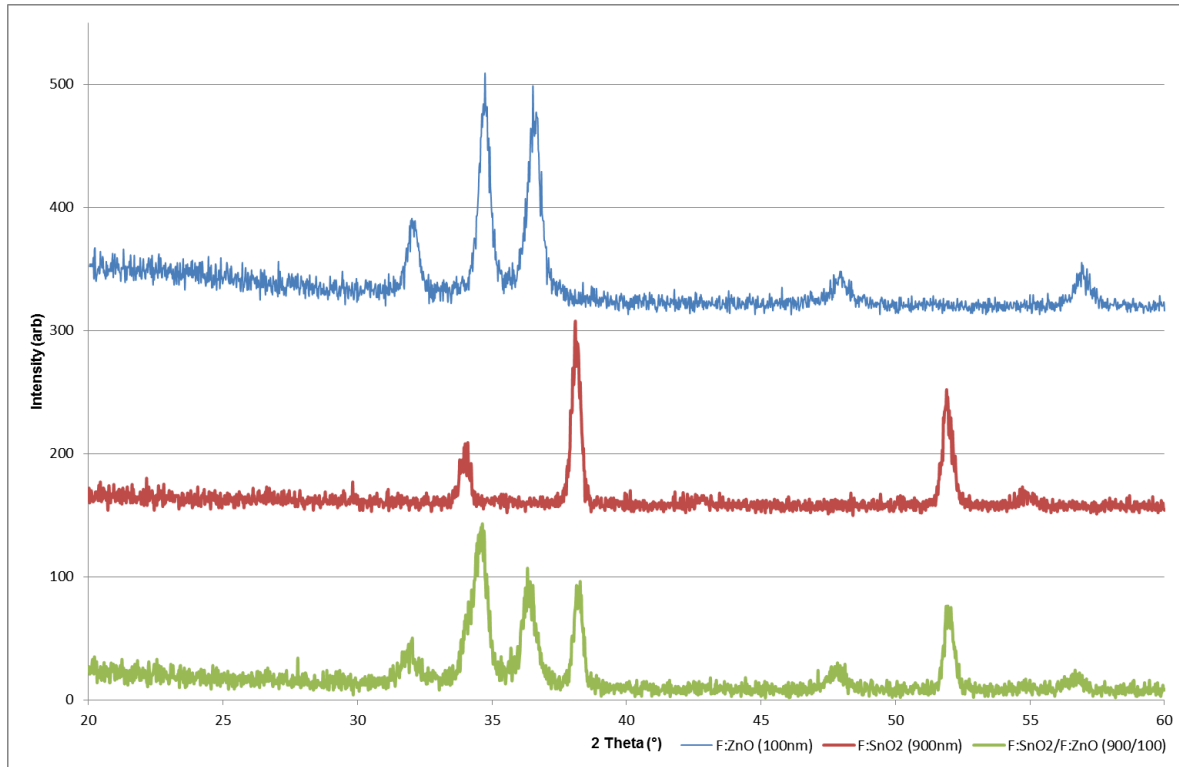


Figure 132 – XRD comparison of F:ZnO, F:SnO₂ and F:SnO₂ / F:ZnO Stack

For the second stage of photovoltaic testing greater optical properties were required. As determined from the previous growth investigation a greater Zn:O ratio improved the optical transparency. Variation of the seeding layer F:SnO₂ was investigated. Further investigation observed the deposition of thicker F:ZnO layer with the increased oxidant ratio for implementation into the second photovoltaic trial.

7.10.3 500/500 Series F:SnO₂/F:ZnO

Incorporation of F:SnO₂ as a seeding layer demonstrated the ability of a composite stack and posed some potential benefits. Further investigations observed the effects of increasing the F:ZnO layer thickness on the seeding layer. Testing developments utilizing the initial over coating conditions yielded a stable thickness of 500nm. This series investigated the conductive properties of the seeding layer upon the resultant stack. Observation of the resultant film would also show if the seeding layer doping affected the final structure.

Utilizing a lightly doped ZnO, combination of both developed material structures could lead to enhanced optical benefits. From the results of the previous oxidant series and the photovoltaic testing, a 20:1 oxidant to zinc ratio was chosen for enhanced transparency with a reduced fluorine doping ratio of 0.04:1. The conditions for this series are given in Table 46.

Sample	FTO Sample (Mol)	Passes	Speed	Substrate Temperature (°C)	Zinc Molar Flux (Mol/Min)	O:Zn Ratio	F:Zn Ratio	Stack Thickness (Nm)	Stack Roughness RMS (Nm)
1	2	4	1.45	410	4.84×10^{-4}	20:1	0.04:1	1000	62.5
2	1.5	4	1.45	410	4.84×10^{-4}	20:1	0.04:1	1000	60.8
3	1	4	1.45	410	4.84×10^{-4}	20:1	0.04:1	1000	56.47
4	0.17	4	1.45	410	4.84×10^{-4}	20:1	0.04:1	1000	61.45

Table 46 - F:ZnO Over-coating Conditions

In this series all the films exhibited a decrease in sheet resistance as the full stack was deposited, given in Table 47. This also corresponded with the increasing thickness developed.

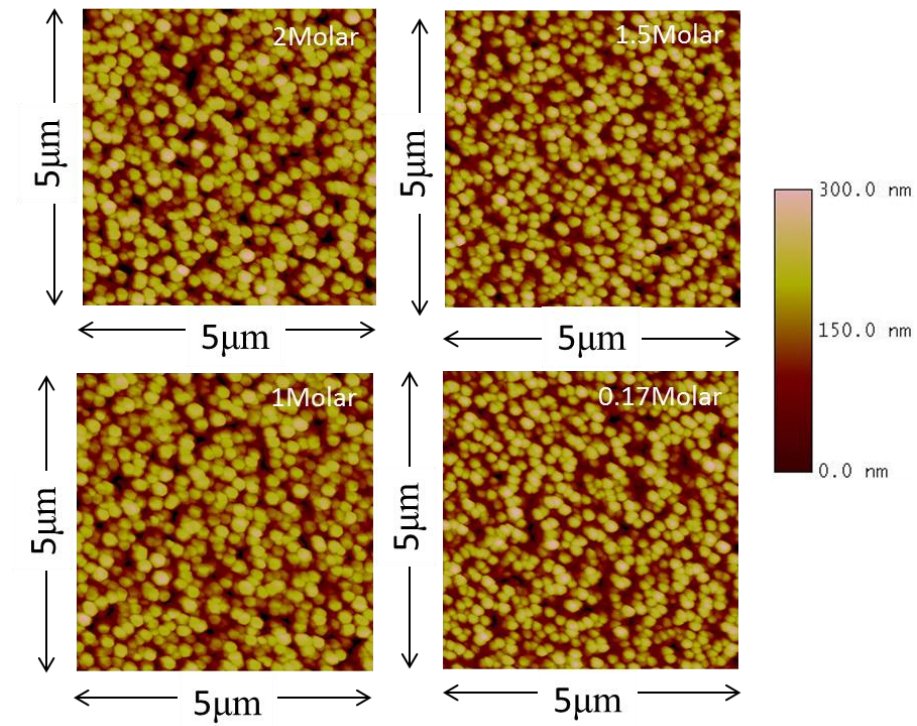


Figure 133 - AFM Images for 500/500 Series

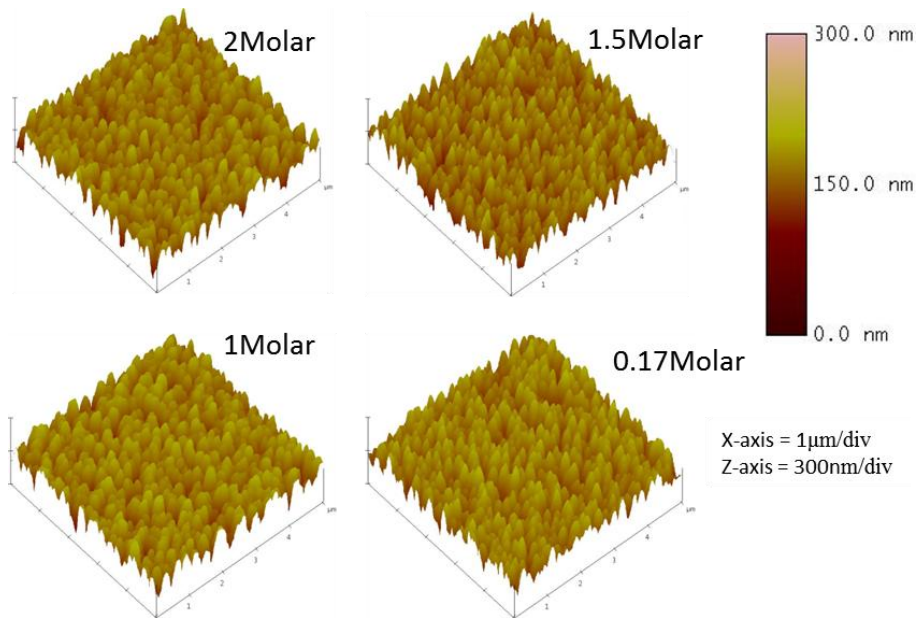


Figure 134 - 3D AFM Images of 500/500 Series

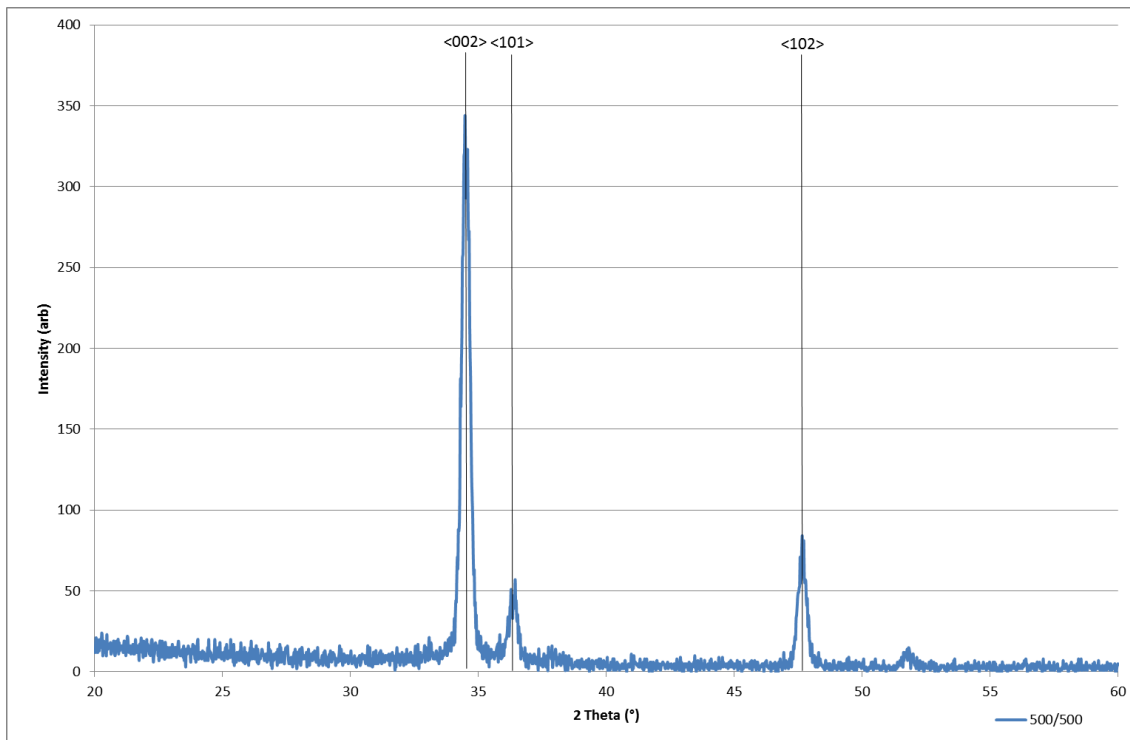


Figure 135 - XRD Data for 500/500 Series

Sample	1	2	3	4
Uncoated (ohm/□)	9.5	10	14	26
Over-coated (ohm/□)	9	8	11	16

Table 47 - Before/After Conductivity Values for 500/500 Series

AFM (Figure 133 & Figure 134) and XRD (Figure 135) data showed that the resultant morphology and crystal structure remained constant throughout the series. Minimal changes were noted for surface roughness, demonstrating a typically low doped F:ZnO structure. The higher doped F:SnO₂ resulted in sub 10 ohm/□ film, with a small reduction in conductivity within the additional top coat. The 0.17 molar samples was the adopted standard for F:SnO₂ growth, as developed through the N2P project. Current specifications as requested by EPFL for TCO parameters is a film of 1µm thick with conductivity sub 20 ohm/□. All of these samples were within the target specification. Continuing forward the lowest dopant samples will be of significant interest, as they exhibited greater transparency in the Infra-red region

with low carrier concentration. In the previous photovoltaic trials, the over-coated samples suffered from free carrier absorption in the infra-red region. Retaining higher mobility in conjunction with low carrier concentration led to improved result cell efficiency.

Specifically this series has demonstrated that thicker F:ZnO layer are able to be deposited and implement into a composite structure. Importantly these films retain their conductivity with increased F:ZnO thickness, reaching target requirements for photovoltaic implementation. Critically utilizing the higher oxidant ratio F:ZnO to increase transparency in conjunction with optical benefits of the F:SnO₂ layer will ultimately lead to an improved TCO layer through this composite structure. These newly developed structures were implemented into the second trial of photovoltaic testing.

7.11 Photovoltaic Testing Round Two

Two significant changes were implemented into the growth of F:ZnO, with an increase in the oxidant molar ratio to zinc and reduction in the fluorine quantity. For this second round of photovoltaic testing, samples were now deposited with a 20:1 oxidant to zinc ratio with a 0.04:1 of fluorine. F:SnO₂ base coatings were prepared to previous standard parameters, utilizing 0.17 molar of fluorine dopant. Included in this series were two plasma etched samples that utilized a 900/300nm F:SnO₂/F:ZnO stack, possessing adequate F:ZnO thickness for modification. “Heavy” and “light” were associated names based on the degree of etching activity administered to the samples from previous experimentation. Heavy and light etching was achieved through manipulation of the sample etching time, light (ES1) experienced 15 passes and heavy (ES2) 30 passes. Deposition conditions are given in Table 48 and the etching conditions in Table 49.

Sample	Substrate Temperature (°C)	Zinc Molar Flux (Mol/Min)	O:Zn Ratio	F:Zn Ratio	Stack Thickness (Nm)	Thickness F:SnO ₂ /F:ZnO (nm)	Sheet Resistance (Ω/□)
1	410	4.84×10^{-4}	20:1	0.04:1	1200	900/300	12
2	410	4.84×10^{-4}	20:1	0.04:1	1100	900/200	12.5
3	410	4.84×10^{-4}	20:1	0.04:1	1000	900/100	13
4	410	4.84×10^{-4}	20:1	0.04:1	1000	700/300	13.6
5	410	4.84×10^{-4}	20:1	0.04:1	1000	500/500	18

Table 48 - F:ZnO Top Layer Conditions

Sample	Voltage (kV)	Current (mA)	Frequency (kHz)	Plasma Power (W)	Nitrogen (L/min)	Oxygen (cc/min)	H2O (L/min)	Passes
“Light” - ES1	3.6	534	2.361	11.6	3	0.12	1	15
“Heavy” - ES2	3.6	545	2.418	11.8	3	0.12	1	30

Table 49 - Etching Conditions for Over Coated Samples

The AFM data for the grown films of this series are shown in Figure 136 and Figure 137, with the etched AFM data given in Figure 138. A summary all samples roughness data is given in Table 50.

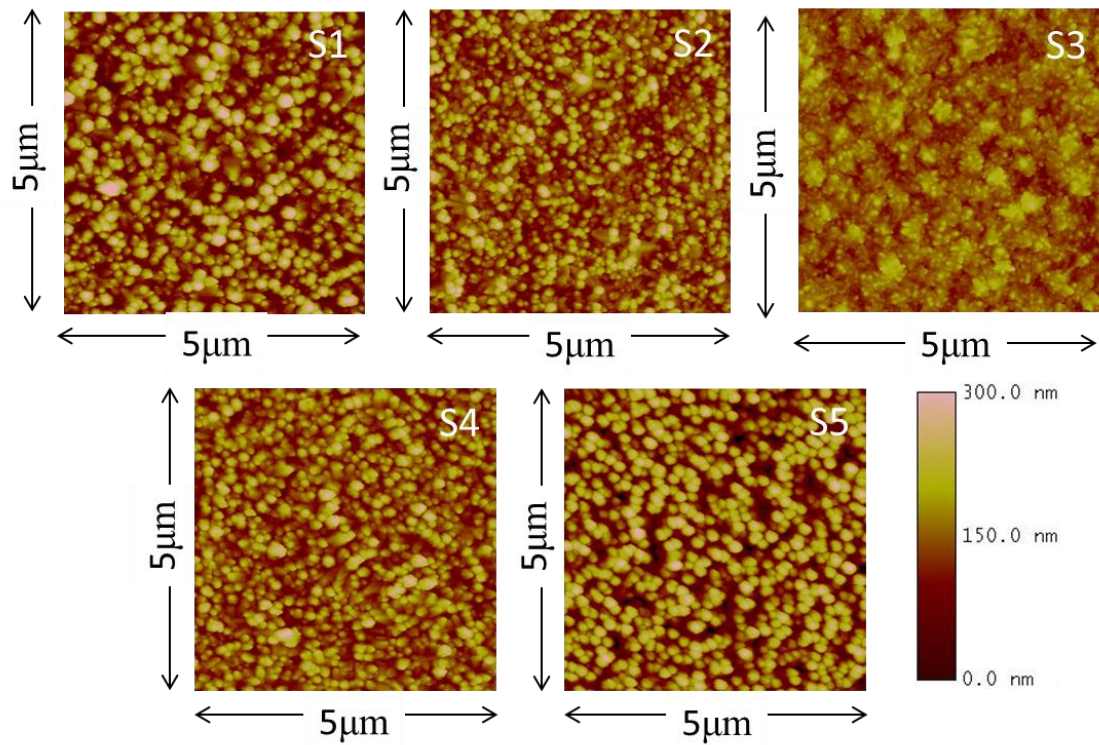


Figure 136 - AFM Data for Second Over-Coated PV Trials

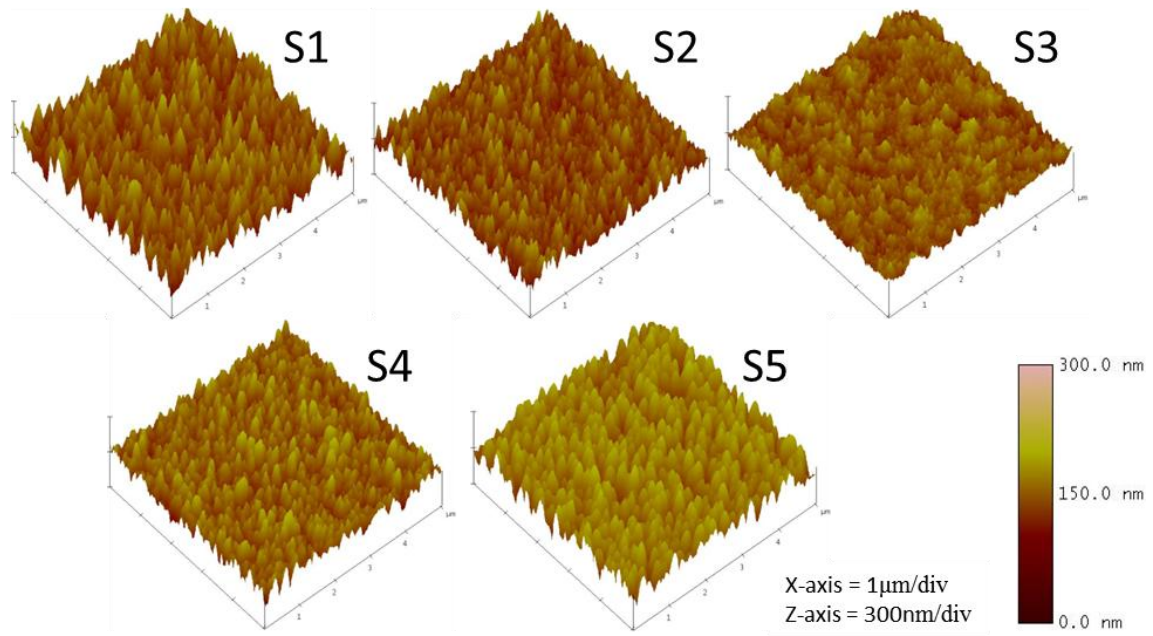


Figure 137 – 3D AFM Data for Second Over-Coated PV Trials

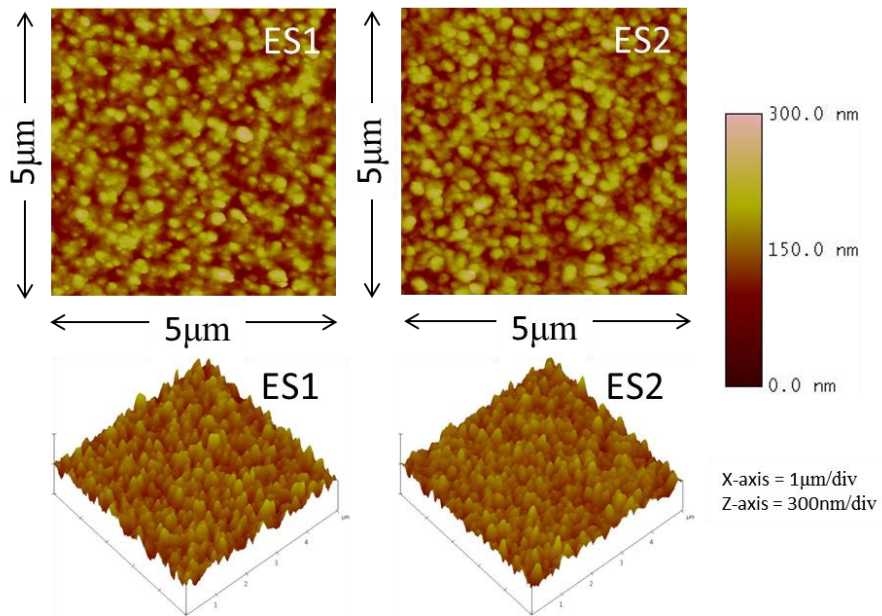


Figure 138 - AFM of Etched Over-coated Samples

Sample	S1	S2	S3	S4	S5	ES1	ES2
Roughness RMS (nm)	54.66	41.45	25.59	40.82	61.45	33.12	31.66

Table 50 - Roughness Data of AFM's

Prior to samples being processed in to photovoltaic modules, AFM analysis was conducted. Samples 1-5 showed the expected structure of the low dopant F:ZnO, with the development of the F:ZnO layer emanating from the F:SnO₂ facet surface. As the F:ZnO increased from 300nm it appeared to be typical of a fully developed F:ZnO structure. No samples showed signs of fracturing post deposition; this was confirmed by observation under the optical microscope. Previous experimentation had shown comparatively thick films deposit via multiple passes and speeds showed different structures. Samples 3-5 were deposited to a resultant stack of 1µm, however because of the varying ZnO thickness the roughness changed. Thicker ZnO tended towards a rougher surface structure development. This may have some drawbacks with subsequent processing despite the possible optical gains. ES1&ES2 showed a considerable decrease in roughness post etching (54.66 to 33/31). The etching cycle appears to have eliminated the smaller facets on the surface reducing the density of peaks.

Sample	S1	S2	S3	S4	S5	F:SnO₂ STD
Transmission %	81.35	81.72	81.98	82.93	80.01	82.82
Reflection %	9.87	10.02	9.72	8.52	5.35	9.24

Table 51 - Average Optical Performance over 400 - 800nm

From Table 51 sample 4 showed a slight increase in overall transmission compared to the standard F:SnO₂ and exhibited nearly a 1% drop in reflection. This would suggest that the non-reflected light was transmitted or absorbed by the film. Further tuning of the twin structure could refine this further, increasing transmission with a reduction in absorption. Samples 1 to 5 optical were assessed using the optical fibre system as shown in Figure 139 and Figure 140.

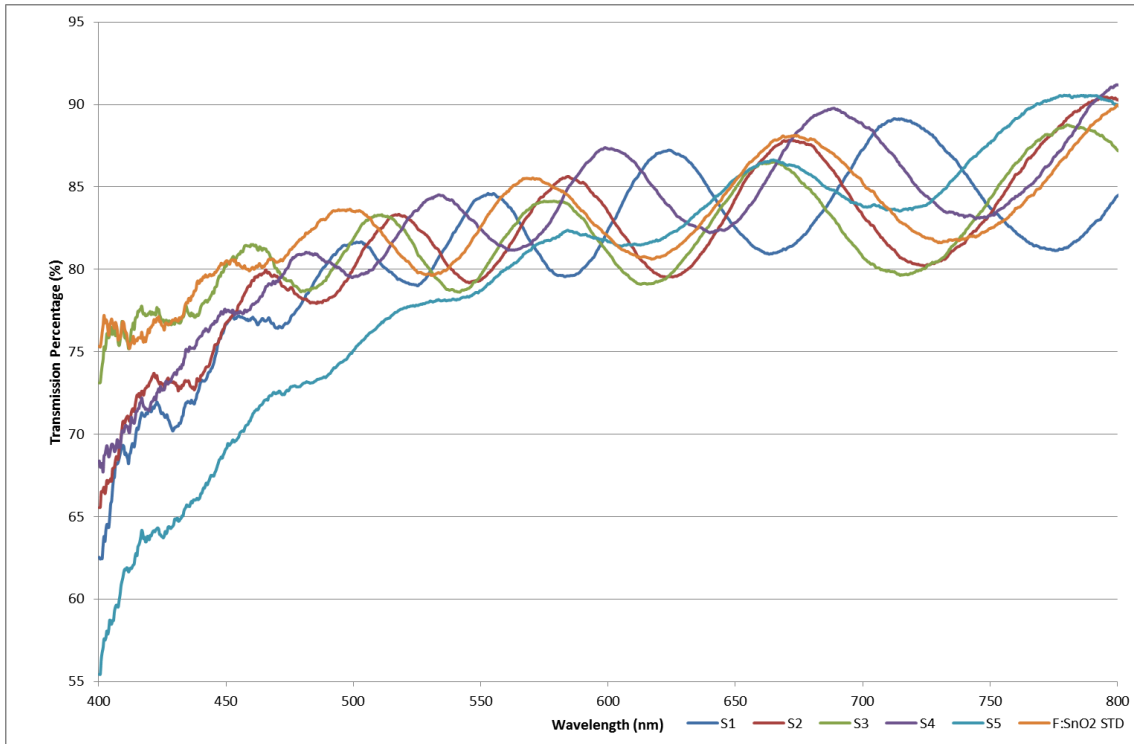


Figure 139 - Optical Transmission for Samples 1-5

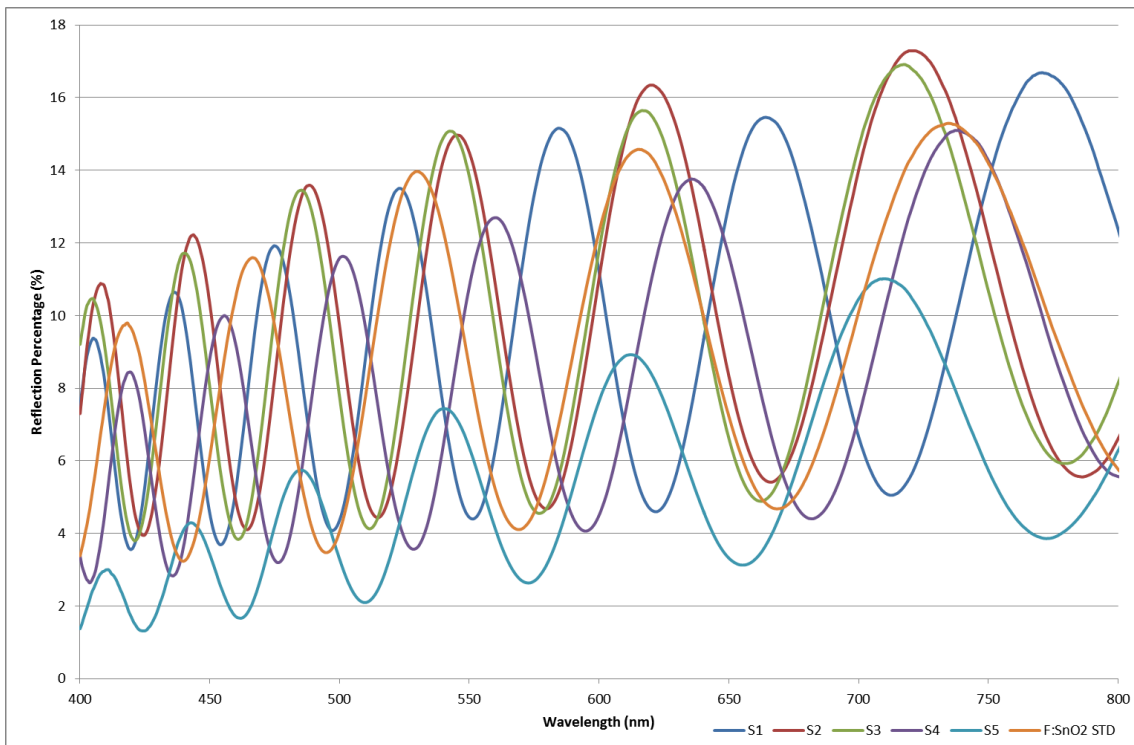


Figure 140 - Optical Reflection for Samples 1-5

In Table 52 the cell results are given for this series. The corresponding EQE data is shown in Figure 141, transmission/diffusive transmission in Figure 142 and haze/absorption in Figure 143.

Sample	Voc (V)	Fill Factor (FF)	Rsc (Ohm.cm ²)	Roc (Ohm.cm ²)	Imax (mA/cm ²)	Vmax (V)	Efficiency (%)	Isc 0.4	Voc 0.4	Fill Factor 0.4 (FF)	Rsc 0.4 (Ohm.cm ²)	Efficiency EQE (%)
F:SnO ₂	0.90	0.75	3200.81	5.05	14.26	0.74	10.59	0.04	0.52	0.36	35082.94	9.7
1	0.88	0.69	844.38	4.98	11.57	0.72	8.35	0.03	0.04	0.00	1023.78	8.1
2	0.89	0.68	783.41	5.09	12.21	0.72	8.80	0.04	0.04	0.00	1017.67	8
3	0.89	0.72	1454.24	4.52	12.44	0.73	9.13	0.04	0.09	0.27	2407.56	8.4
4	0.88	0.71	1832.27	4.65	13.08	0.72	9.38	0.04	0.08	0.26	2191.32	8.7
5	0.80	0.61	586.29	6.57	13.63	0.60	8.12	0.04	0.04	0.00	954.00	7
ES1	0.90	0.68	1175.23	6.01	12.10	0.72	8.71	0.03	0.07	0.33	2004.76	8.1
ES2	0.85	0.65	1517.58	7.13	11.94	0.65	7.77	0.04	0.12	0.27	3481.39	6.7

Table 52 - Photovoltaic Performance Results for Second Trial (Data Supplied by EPFL)

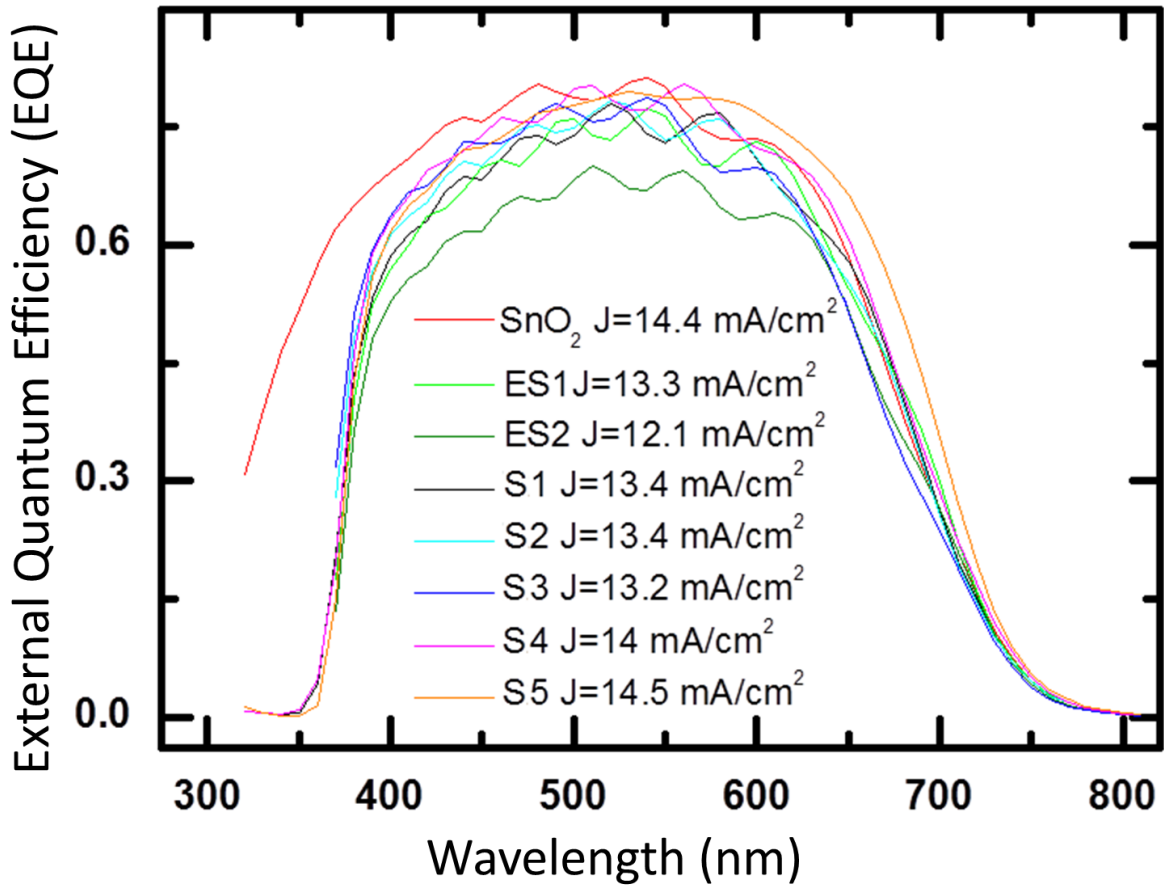


Figure 141 – External Quantum Efficiency of 2nd PV Trial (Data Supplied by EPFL)

Throughout this series none of the samples were able to compete with the standard F:SnO₂ TCO, with regards to stabilised PV efficiencies. F:SnO₂ TCO produced a cell with an efficiency of 9.7%, compared with the best of the composite F:ZnO/ F:SnO₂ TCO achieving 8.7%. Unfortunately due to errors with the samples, optical data was not assessed for the etched samples in number 5. Indicated by the results of the photovoltaic testing the samples were revisited, and it was noticed that sample 5 had signs of cracking. Despite the previous investigation, it appeared that the 500nm was not stable and subsequently failed.

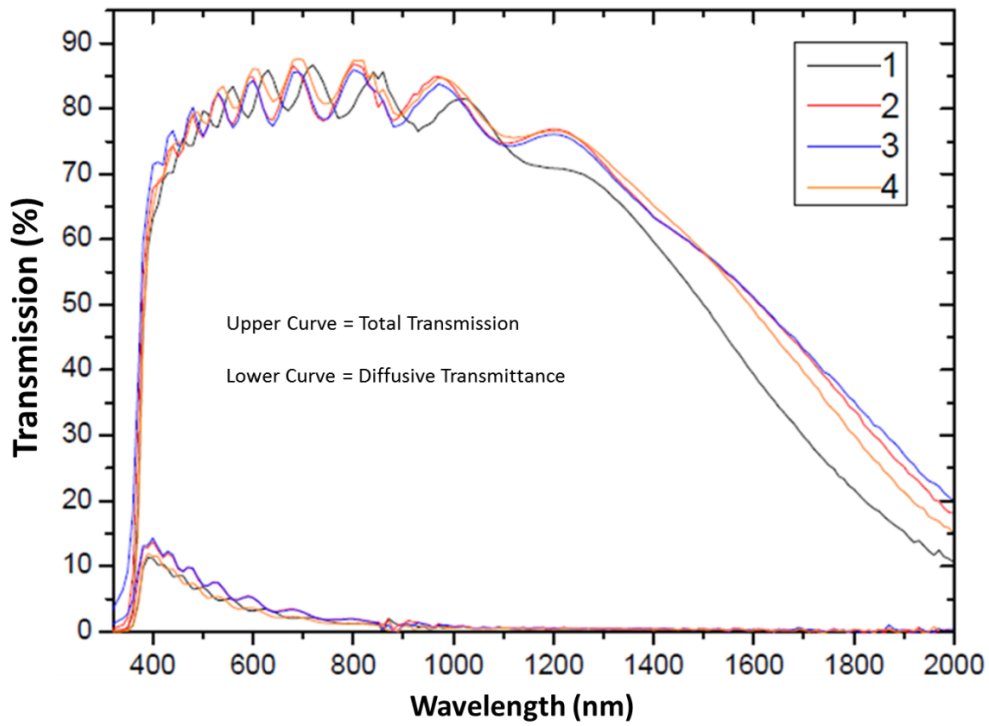


Figure 142 - Transmission and Diffusive Transmission for Samples 1-4 (Data Supplied by EPFL)

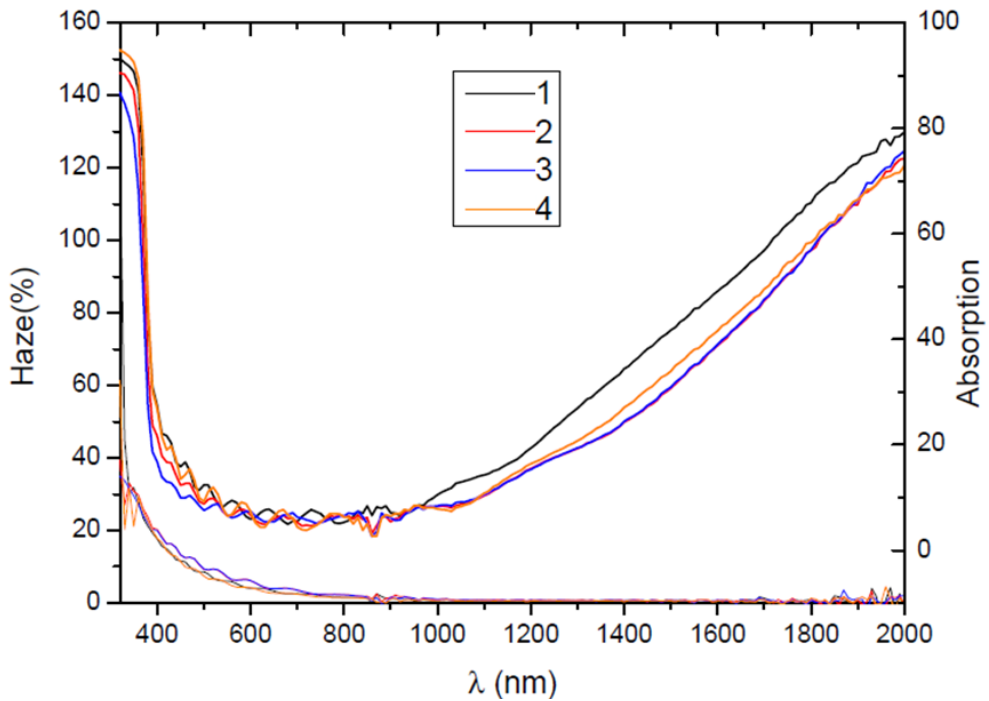


Figure 143 – Haze (Upper Curve) and Absorption (Lower Curve) Measurements for Samples 1-4 (Data Supplied by EPFL)

Figure 144 highlights SEM images of particular samples from these series. In an attempt to observe the initialization of the fracturing, side-on SEM's were performed. Clearly shown in the 900nm F:ZnO film is the initiation of fracturing that extended to the substrate. It is difficult to specifically ascertain what factors allow the fracture to permeate. As sample thickness increased one would expect an increase in feature width through preferred orientation growth and coalescence of islands. It is likely the increased crystal preference resulted in a stress point in the uppermost layer which then ruptures down through the film. The 300nm F:ZnO shows traces of fractures at the film/glass interface, which may be due to the typical growth mechanisms. These types of grain separations are common in the early stages of film growth. In the composite stack of 900/300nm F:SnO₂/F:ZnO the film grows with no defects, showing a conformal film that extended from the F:SnO₂ base layer. This indicated that the fractures in the standard 300nm F:ZnO are due to the initial stages of growth into a continuous film. The 500/500nm composite stack showed signs of cracking through the film that appeared to extend back through the F:SnO₂ layer. This sample was part of the photovoltaic testing which subsequently failed to meet expectations.

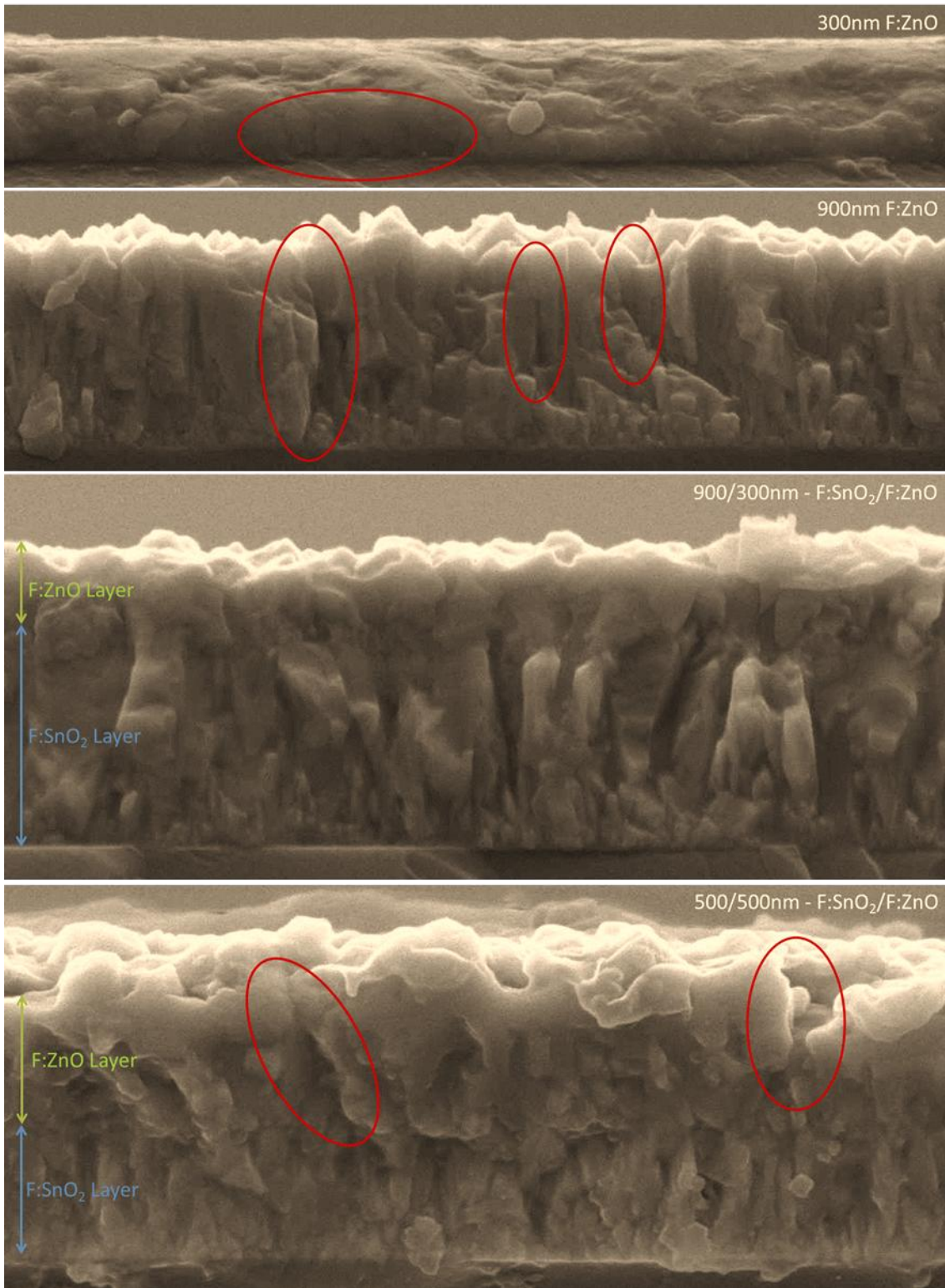


Figure 144 - SEM Monitoring of Film Cracking (Defects Highlighted in Red)

This series demonstrated that a composite F:SnO₂ / F:ZnO stack can be successfully incorporated into photovoltaic cells. Currently, efficiency of photovoltaic cells involving the composite material have not surpassed a single F:SnO₂ TCO. Continued optimization of the deposition conditions of the ZnO layer could potentially enable a higher performing layer, through further free carrier absorption reduction enhancing optical properties.

From this round of testing sample 3 & 4 proved the best samples of the series after full cell construction. Sample 4 demonstrated the best stabilized efficiency with a corresponding peak optical performance. A 0.11% increase in transmission is noted over 400-800nm with a 0.72% reduction in reflection compared to the F:SnO₂ standard. This reduction in reflection without a corresponding increase in transmission would indicate that the additional light was either absorbed or diffusively scattered. Investigation indicated that the infra-red region for sample 4 against sample 3 had a reduction in transmission. Equally sample 4 compared to sample 3 showed a reduction in absorption and increase in haze. Sample 3 shows a reduction in transmission (0.84%) and increase in reflection (0.48%) compared to the F:SnO₂ standard.

Sample 3 & 4 demonstrated good fill factors of 0.72/0.71 respectively compared to the F:SnO₂ standard of 0.75. Unity would be the ideal value for the fill factor of the IV curve, with these samples demonstrating very high values. The zinc over-coated samples show comparable open circuit voltages, but were hindered by the reduction in short circuit current density. As the short circuit current essentially defines the performance of the cell (collection of light induced carriers), these cells were fundamentally limited in performance despite any other layer benefits. Maximising the carrier collection through enhanced optical parameters (increased transmission/scatter and reduce absorption) would improve the overall cell performance. Observation of the external quantum efficiency of the samples showed that the standard F:SnO₂ had an increased spectral response in the lower wavelength of the blue region/UV. The literature describes that this defect stems from front surface recombination^{(214) (337)}. Effective capturing of these wavelengths would hopefully increase the current density and improve the cell performance. Comments from EPFL indicate that free carrier absorption is responsible for the low cell efficiencies.

Sample 3 had a much reduced current density of 13.2 mA/cm^3 compared to the F:SnO₂ of 14.4 mA/cm^3 . Despite the limitation of the current density it exhibited a high fill factor which results in a decent final efficiency of 8.4%. Sample 4 shows a comparable current density of 14 mA/cm^3 , which in-turn had a high fill factor and subsequent efficiency. Interestingly in this series sample 5 shows the highest current density of 14.5 mA/cm^3 but had the lowest fill factor and efficiency of the series. It exhibits a reduction in both transmission (2.81%) and reflection (3.89%), indicating that a possible increase in diffuse transmission or absorption was present. The increased thickness of F:ZnO improved the possible light conversion in the cell, and improvements in optical transmission could help this further. However the problems encountered with film cracking resulted in a loss of electrical performance, limiting the efficiency of the cell.

AFM data of the samples showed that sample 4 had a fully developed F:ZnO structure with fewer sharp features, exhibiting a large rounded surface. This would aid cell manufacturing, reducing the potential for voids in the subsequent layers limiting performance. Sample 3 shows sharp surface features on top on the F:SnO₂ structure, but demonstrated a low surface roughness. These structural differences had influenced a small change in the optical performance, but may have limited the current density for the films. The composite stack appeared to be optimized with the $1 \mu\text{m}$ thickness in sample 4. It would indicate that sample 3 had a comparatively high performance due to bulk F:SnO₂ but due to the interfacial properties of the zinc layer in the stack has reduced the TCO performance potential.

Plasma etched samples utilized the same 900/300nm stack as sample one. Exposure of the sample to the plasma had significantly reduced the roughness by approximately $\sim 20\text{nm}$. The AFM data showed that the surface had been smoothed with the reduction of smaller features. A consequence of this was a reduction in peak density which resulted in a lower roughness value. Increasing the plasma exposure had further reduced the roughness of the surface, but has reduced the final resultant cell efficiency. This is due likely to the affected optical performance by reducing scatter of the film and potentially affecting the absorption. Between ES1 and ES2 we note the cyclic progression of the plasma etching system through reduction to increase of sample roughness as more material is removed. An intermediate stage may be

identified that offers enhanced optical performance. Unfortunately due to equipment error, these samples were not optically assessed prior to cell construction so these properties cannot be confirmed.

ES1 critically demonstrated the same resultant efficiency as the standard un-etched film (Sample 1/S1). Open circuit voltage is increased from 0.88 to 0.9 suggesting a reduction in recombination. The current density exhibited a small reduction from 13.4 mA/cm^2 to 13.3 mA/cm^2 and corresponding reduction in fill factor from 0.69 to 0.68. Both films however exhibit a resultant cell efficiency of 8.1%. A reduction in recombination is beneficial as shown by the open circuit voltage. Due to the reduction in short circuit current density, the effective capturing of incident light for carrier generation is reduced. Maximizing the short circuit current density and fill factor whilst maintaining the reduced recombination effects, would improve cell performance surpassing the standard film. Indicated by the AFM's we would need to reduce the peak density whilst maintaining a degree of roughness for effective optical scattering. ES2 exhibits a decrease in the key parameters (V_{oc} J_{sc} FF) which resulted in a low efficiency. As the AFM data suggest that the film surface is smoother and reduction in small features is noted we would anticipate a comparable V_{oc} & FF despite a low J_{sc} . It is difficult to identify any defect in the sample that would result in a significant reduction in performance, and indicated a possible defective sample.

8 - Discussion

Initial growth experiments demonstrated the capability to produce a wide range of textures of ZnO. This was achieved through varying multiple process parameters, with temperature being critical for defining surface roughness. Oxidant purity was discovered to be vital, enabling high temperature depositions. Higher temperatures facilitated the incorporation of dopant materials during growth. Throughout the depositions, a reference set of conditions was established ultimately concluding ethanol as the preferred oxidant source. This produced a highly textured surface suitable for doping and plasma etching. Two dopant materials were selected and deposited, fluorine and aluminium. Fluorine doping had particular interest for its novelty value and proposed doping benefits. Progression of fluorine doping revealed a cracking defect for the given chemistry that could not be eliminated.

Through analysis it became evident that the $\langle 101 \rangle$ crystal orientation developing with thickness was indicative of cracking. An upper thickness limit of 300nm was discovered to be stable, and exhibited the preferential $\langle 002 \rangle$ orientation. Undoped ZnO grown in excess of 1 μ m without cracking, demonstrated fluorine to be the causal factor. The fluorine doping mechanism was to replace one of the Zn atoms. This mechanism may be responsible for inducing film stress resulting in cracking.

Cracking was visible by optical microscope and evident through conductivity measurements. Repeat measurements of films over several hours showed subsequent loss of conductive properties. Attempts to prevent cracking involved using a variety of coating systems, temperatures, mechanism, flow rates, precursor type and delivery. Aluminium doping in the initial stages was successful without apparent cracking. The doping mechanism for aluminium is different to fluorine, replacing oxygen atoms. The doping mechanism may have been the catalyst for film cracking, in conjunction with increasing thickness and a low saturation of fluorine.

Oxygen ingress was considered as a possible cause as the initial stable depositions were performed using a sealed nozzle coating arrangement. These films possessed the required thickness and conductivity however when revisited (after several months in storage) these

samples again demonstrated cracking. Deposition was performed in a controlled environment it may be deduced that oxygen ingress was not the issue Resonance time was investigated to observe the effects of reaction rate and cracking. Films deposited in a single pass were limited by the translational speed of the susceptor. Single pass films retained their properties however did not exceed the critical 300nm thickness. Limited to a film thickness of 300nm, these samples were not suitable for TCO applications. Furthermore, reducing the number of passes and translation speed did not prevent cracking.

Seeding layers were introduced to manipulate the developing structure. This process appeared to disrupt the incubation period before cracking developed. Conformal island growth was interrupted allowing increased thickness. Film growth of 500nm was established before cracking. Presently no viable route forward to deposit solo fluorine doped zinc oxide via thermal CVD seems available with the chemistries screened.

Investigation into various compositions of seeding layers demonstrated sufficient carrier diffusion. Combining an undoped top coat with a highly doped under coat, demonstrated ample conductivity. A problem of the homogeneous zinc structure, undoped and doped layer, was again cracking after a given period. Utilizing any form of zinc as the bulk material resulted in the defect. A composite stack of F:SnO₂ and F:ZnO was deposited as a viable solution. This offers multiple benefits as well as avoiding the potential to crack. Two rounds of photovoltaic testing were conducted on the composite TCO stack.

The first series combined the reference F:SnO₂ plus the standard condition F:ZnO. Samples were produced with a 900nm F:SnO₂ under coat and 100nm/200nm F:ZnO top coat. F:ZnO layer thickness was maintained under 300nm to ensure stability during further processing. Both samples were successfully implemented into a full amorphous silicon solar cell. Each cell performed reasonably well however neither surpassed the standard F:SnO₂. This was attributed to the optical performance losses due to the additional top coat. Optical assessment demonstrated a reduction in transmission primarily in the infra-red region. Low short circuit current indicated an increased absorption from an excessive carrier concentration.

The second series of investigation implemented two processes to improve optical performance. Increasing the oxidant to zinc ratio improved visible transmission by significantly reducing carbon incorporation. Fluorine doping was reduced to improve the transparency in the infra-red region. A combination of these growth parameters enabled a higher performing F:ZnO layer. These changes were performed without any significant reduction in conductivity. Carrier diffusion was still present from the bulk F:SnO₂ undercoat which exhibited a sheet resistance in the desired range.

Cells produced from this revised configuration did not surpass the standard F:SnO₂ efficiency despite improvements to the F:ZnO layer. Performance analysis of the cells indicated a smoother surface structure but free carrier absorption was still evident. Optimizations of the structure and properties showed an increase in performance from initial trial. Further optimization would need to study the resultant top coat structure/doping and involve trials of various F:SnO₂ compositions. This could be achieved with oxidant ratio zinc deposition or further reduction in dopant concentration. Alternatively as shown during ZnO growth trials, samples of comparable thickness deposited under different process conditions demonstrated alternative surface structures. To promote TCO performance it may be beneficial to specifically promote one of the alternative structures.

Overall what has been demonstrated throughout testing is the potential of a composite TCO material. Currently we are limited by the cracking of fluorine doping, this method offers a viable solution. Application of alternative dopants, precursors and interface layers may also prove beneficial for further progression. Resultant surface morphology has had an impact on optical performance limiting the resultant cell efficiency. Subsequent investigation will seek to reduce these defects by tailoring the deposition process, reducing absorption and increasing transmission.

Manipulating zinc oxide through the growth process is equally important as is the combination with the plasma etching system. Demonstrated through this body of work is effective ability to modify thin films using an atmospheric pressure dielectric barrier discharge. The proposed etching mechanism for atmospheric plasma etching has been drafted from the experimental results and existing low pressure techniques. As the pressure regime

significantly influences the available etching processes, the criteria for atmospheric pressure become limited. Study of the environment and processing conditions have isolated the key components essential for etching. Etching components are specifically required for a given material. ZnO and SnO exhibited different etching requirements as a consequence we will consider their mechanism separately.

Tin oxide required gaseous hydrochloric acid to be dissociated in the plasma for effective etching. Chlorine is a well-established etching medium in low pressure regime's, reflecting the chemical process of etching. Atmospheric conditions would not be conducive for a sputter type etching process, due to the high particle density. EPFL (collaborators of the N2P project) have conducted comparable plasma etching experiments under vacuum conditions, exposing F:SnO₂ to relatively high HCl concentrations with no effect. In this regime we would have expected a significant increase in ion bombardment from the high order of mean free path. Combination of high energy particle interaction in conjunction with an HCl saturated environment theoretically should etch F:SnO₂. Investigation into the chemical nature of chlorinated products and tin oxide showed no etching effects with the sample being submersed in concentrated liquid HCl (lab grade 37% purity).

The experiments indicated a specific component was produced under atmospheric conditions that enabled etching. Chlorinated products have an expressed chemical reactivity⁽²⁴⁴⁾, with particular pairing of atmospheric gases offering a volatile product that was easily accessible for etching. Chlorine as described by Liebermann⁽²⁴⁴⁾ exhibits crystallographic etching preference. This effect dominates at crystal boundaries for specific orientations of low energy densities. These weaker atomic bonds are broken by the chemically active chlorine.

Removal and lifetime of the operating etchant was shown to exist in the exhaust system on the initial HCl runs, the exhaust ducting being attacked by the waste products. This was strongly indicative of the chemical nature of the process. A water bath being introduced was sufficient to capture the etchant material which significantly reduced exhaust damage.

The etching environment largely determines the etching processes available. Sputtering requires the exchange of energy which is angle and energy dependant. A consequence of this

mechanism is that only one incident bombardment specie will release one sample atom, resulting in very low yields. Typically sputtering techniques may encapsulate incident ions, imbedding them into the surface. EDAX imaging of etched F:SnO₂ revealed no chlorinated products where impregnated into the film or deposited on the surface. Uniformity is another distinction of etching mechanism. Chemical process exhibits a high degree of uniformity. Sputtering is shown to be highly directional based on incident particles. Observations from several microscopy techniques confirmed the uniformity of the etching system, showing full sample treatment. A crystallographic preference was not demonstrated either during processing. In conclusion from the etching results, chemical etching dominates from a combination of dissociated chlorine and atmospheric gases.

Zinc oxide etching was enabled by O₂ and H₂O in the N₂ discharge. Zinc oxide is easily etched by wet chemical processing in HCl unlike F:SnO₂ (a common etching practice for ZnO TCO materials). Exposure of dissociated O₂ and H₂O readily etches ZnO, demonstrating the oxygen product volatility. Oxygen is also documented⁽²⁴⁴⁾ as an aggressive etchant source, chemically reacting and removing exposed material. Atmospheric conditions supplies sufficient oxidant through several sources, being dissociated in the plasma for etching. Optical emission spectrometry performed by University of Salford associates confirmed the high presence of oxygen in the discharge. Multiple oxygen species are recognised in the spectra, offering multiple components for etching. XRD analysis has shown no dependence on crystal orientation, modifying all variations of ZnO structures presented. Treatment uniformity is very high and only limited by the dimensions of the etching arrangement. Prolonged exposure annihilated the ZnO structure.

Classification of the plasma mechanism from the observed effects and analysis suggests the chemical nature of the process. Liebermann⁽²⁴⁴⁾ suggests four dominant etching processes available in the vacuum conditions for microelectronic etching; however for the atmospheric pressure conditions only one condition is feasible for the observed scenarios. The life time of the ions would not be sufficient to etch the sample surface nor would the energetic rate be favourable enough for it to break the bonds. Yield rates of the etching process could not be paralleled by sputtering techniques, even under vacuum conditions. Combinations of all of

the observed effects emphasize the chemical nature of the plasma etching mechanism. Conversely it may be found possible to implement the ion energy and enhanced effects. Incorporating these would require extremely high energy plasma, which would result in a power expensive process and the possibility of adverse resultant effects.

The etching process enabled the effective surface modification of tin oxide and zinc oxide. Tin oxide showed a capable process that preferentially removed the smaller facets of the surface structure. Of the two materials, zinc oxide was easier to etch, with severe conditions completely removing the film. Varying sample exposure to the plasma meant the surface structure could be tailored. Controlling the process gases, plasma power and resonance time we are able to define the resulting morphology. Photovoltaic testing of etched F:ZnO over coated F:SnO₂ demonstrated the potential of plasma etching. Aspects of the modified surface proved beneficial reducing recombination effects in the cell. However a reduction in short circuit current and fill factor resulted in no performance gain. Critically the etched film ES1 did not exhibit a reduction in cell performance compared to the un-etched sample. This identifies that the etching system with further refinement could enhance the TCO performance in solar cells.

9 - Conclusion

The overall main focus of this research was to produce an enhanced TCO film utilizing advancements in growth and post modification techniques. Investigations began with multiple aims and objectives to achieve, the majority of these were successfully accomplished.

Through the initial phases of ZnO growth objectives A1 to A4 were achieved. ZnO growth showed a dependency on the oxidant source purity, multiple oxidant sources, temperature range and development of multiple structures. Critically, these developments enabled dopant introduction to be considered as a result of ZnO being stably deposited at a higher temperatures. Deposition involving several oxidant and dopant sources revealed varying growth rates and structures. Fluorine and aluminium doping was successfully introduced into the ZnO deposition thus satisfying objectives A5 to A7. Initial investigations showed aluminium as a promising doping material, however fluorine was concentrated on due to the novel value of F:ZnO produced by APCVD.

Unfortunately, F:ZnO was found to crack beyond a critical thickness of 300 nm, prohibiting its implementation as a TCO layer. Despite all efforts this problem was not overcome, but an alternative solution was applied. A composite stack of F:SnO₂ and F:ZnO was deposited and successfully implemented as a TCO layer for photovoltaic testing. Scalability of the process was enabled through careful selection of the CVD system and head, allowing uniform deposition onto substrates of 100x100mm for PV testing. The F:ZnO cracking presented a hurdle which was overcome by the composite TCO structure. This permitted continued working into ZnO growth and plasma etching, satisfying objectives A8 to A10.

Further work with ZnO growth would involve investigation into alternative zinc precursors. Data published by Ye et al⁽³³⁸⁾ have shown a significant difference between dimethylzinc and diethylzinc. Diethylzinc exhibits an alternative growth structure of ZnO and subsequently possesses greater optical transparency. Application of alternative zinc precursor may stabilize the fluorine dopant growth, reducing the potential for cracking. Alternatively, introduction of

a non-adduct form of the zinc precursors may yield positive results, but would require further consideration to stabilize the reaction for thin film deposition.

Alongside the use of alternative precursors, investigation of the mechanisms associated with film cracking would be beneficial. Attempts by the author to reduce film stresses through temperature cycling and deposition conditions were unsuccessful. Understanding the failure mechanism would enable greater control over the resultant film structure. This could prevent possible failure in fully constructed PV cells, therefore improving expected lifetimes. Another avenue of investigation would be alternative glass substrates. As shown in this thesis, investigations utilizing a seeding layer proved beneficial, and further investigation into other glass types may help understand the cracking problem. Certain limitations are placed on substrates for solar cell construction, typically to 1mm rolled glass as required by EPFL.

Alternative fluorine sources for dopant inclusion should be investigated. This may help reduce the potential for cracking and aid the growth of various crystal structures. Continuation of aluminium doping from the initial stages would be useful for cracking investigations. Aluminium has a different dopant mechanism to fluorine, replacing an oxygen atom rather than a zinc atom during deposition. If the aluminium doping also cracked, it would suggest a possible problem with the use of dimethylzinc as a precursor. Equally, introduction of different oxidant sources may reduce the potential for cracking during growth.

Discussions with collaborators at EPFL have highlighted comparable experiences with the cracking of zinc oxide (doped & undoped). EPFL deposit ZnO via LPCVD, typically doped with boron. Oxygen ingress and ambient purity is not an issue for these systems due to the pressure regime and environment control. As both atmospheric and low pressure techniques exhibit cracking of zinc oxide, it would indicate cracking as an inherent property of film chemistry.

EPFL demonstrated that the $\langle 002 \rangle$ orientation was responsible for cracking, whilst alternative orientations were stable. Film properties were shown to be manipulated by the flow rates & temperature of the substrate⁽⁹⁶⁾⁽¹⁰⁹⁾. Contrary to the observed crystal orientation responsible for cracking at EPFL, APCVD growth observed a dominance of the $\langle 101 \rangle$ peak.

Initially as the films developed $\langle 002 \rangle$ was prominent, as the thickness increased the $\langle 101 \rangle$ became favourable. This transition coincided with the onset of cracking.

Continuing the success of the composite F:SnO₂ and F:ZnO structure, further work would intend to produce a TCO with improved performance. Analysis of the results indicated that optical losses were a problem, resulting in a lowered performance. Several processes could be adopted to improve these films with a tweaked F:SnO₂ film, F:ZnO from diethylzinc and alternative dopants. F:SnO₂ for the PV trials, was not optimized for the twin structure due to experimental limitations. Lower doping of this layer in conjunction with various oxidant ratios could prove beneficial. Trials including multiple F:SnO₂ conditions would be required to ascertain the best properties for the twin structure. Combination of an optimized F:SnO₂ and F:ZnO may potentially compete with the leading standards and prove a viable alternative TCO.

Reported in this thesis is the initial investigation of atmospheric pressure plasma etching. Utilizing this process, the modification of multiple TCO films was possible. F:SnO₂ and ZnO were successfully etched and published ⁽³³⁴⁾ ⁽³³⁵⁾ ⁽³³⁶⁾, satisfying objectives B1 to B3. Throughout the course of investigation, objectives B3 to B8 were successfully achieved. Each TCO material responded differently to the etching process conditions and feed gas mixture. F:SnO₂ required HCl to be present in the plasma for etching to occur, whereas ZnO required a mixture of O₂ and H₂O. Utilizing an etching medium of non-hazardous chemistry is very important for commercial processing for reducing the potential operational hazards. An investigation into the etching environment enabled the isolation of the working gasses to determine the most efficient gas mixtures and breakdown conditions for etching.

Combined with the advances in F:ZnO growth into the composite stack, plasma etching was applied to this TCO material. Photovoltaic cells demonstrated the viability of the etching process for performance enhancement. Despite this no direct efficiency improvements were evident at the time, for this reason objective B8 was met with partial success.

Characterisation of the plasma is critical for the next stage of development. Spectroscopy techniques could be used to observe the species present in the plasma at any given point. This

would help to identify the key etching species and resolve the etching mechanism. Spectroscopy measurements would be required for multiple gas compositions in order to identify the various species available and the effect of the applied plasma power. Analysis of this nature would be critical for applying the etching system to new materials, enabling insight into the potentially effective species required. Examination of the waste products in conjunction with this study would aid resolution of the specific etching interaction. As part of these developments, specific recipes may be deduced for a given materials. This may allow for specific etching regimes to be conducted, targeting structure, etch rate and preferential etching.

For the continuation of product development, a larger etching system would be required. Scaling of the equipment onto large area substrates would be essential for commercial adoption. This must be done with high uniformity, ease of use and the potential for high throughput. The next stage of development would be creating a larger etching head with a modular design. This would aid changes made to the electrodes and help introduce multiple baffle systems. Modular design would allow the etching system to be customised; this would be beneficial where materials have specific etching requirements. As part of these new developments, various power delivery techniques would be introduced. The current system used employed a sinusoidal power supply for plasma discharge. Further investigation would introduce a pulsed power supply system. This may achieve greater etching potential through the careful selection and isolation of etchant species available by pulsing. It could potentially lead to higher etching efficiency and selectivity of the etching regime, allowing for greater control over the resultant film. These developments, in conjunction with spectroscopic measurements and determination of the etching mechanism would lead to a fully capable etching system.

Overall, this research has led to multiple successes and has achieved the objectives initially proposed. Certain problems were encountered, these were either resolved by following alternative directions or by the proposal of additional investigation. Further refinement of the etching processes in conjunction with advanced growth techniques are required to improve and surpass the characteristics of current standard TCO materials. These advancements, in

conjunction with continued improvements of the plasma etching system, could lead to the development of improved photovoltaic device efficiencies.

10- Bibliography

1. **Toub, D.** *A Review of Photovoltaic Cells.* New York : Department of Electrical and Computer Engineering.
2. *Optimization methods applied to renewable and sustainable energy: A review.* **Banos, R, Manzano-Agugliaro, F , Montoya, F, Gil, C, Alcayde, A , Gómez, J.** Pages 1753–1766, s.l. : Renewable and Sustainable Energy Reviews, Vol. 15. 1364-0321.
3. *Accelerating the transition to sustainable energy systems.* **Jefferson, M.** Pages 4116–4125, s.l. : Energy Policy, 2008, Vol. 36. 0301-4215.
4. *Electric Vehicles and the Electric Grid : A Review of Modeling Approaches, Impacts and Renewable Energy Intergration.* **Richardson, D.** s.l. : Renewable and Sustainable Energy Reviews, 2013, Vol. 19. 1364-0321.
5. *Technologies for Electric, Hybrid and Hydrogen Vehicles : Electricity from Renewable Energy Sources in Transport.* **Jorgensen, K.** 2, s.l. : Utilities Policy, 2008, Vol. 16. 0957-1787.
6. **Bossert, R H, et al., et al.** *Thin-Film Solar Cells : Technology Evaluation and Perspectives.* s.l. : Netherlands Energy Research Foundation - ECN, 2000. DV 1.1.17.
7. *A Review of Solar Photovoltaic Technologies.* **Parida, B, Iniyar, S, Goic, R.** Pages 1625–1636, s.l. : Renewable and Sustainable Energy Reviews, Vol. 15. 1364-0321.
8. *A Review on Sustainable Design of Renewable Energy Systems.* **Shi, L, Chew, M, Y, L.** s.l. : Renewable and Sustainable Energy Reviews, 2012, Vol. 16. 1364-0321.
9. *Small Hydro Power : Technology and Current Status.* **Paish, O.** 6, s.l. : Renewable and Sustainable Energy Reviews, 2002, Vol. 6. 1364-0321.
10. *Techno-Economic Review of Existing and New Pumped Hydro Energy Storage Plant.* **Deane, J, P, Gallachoir, B, P, O, McKeogh, E, J.** 4, s.l. : Renewable and Sustainable Energy Reviews, 2010, Vol. 14. 1364-0321.
11. *Mobilising for Marine Wind Energy in the United Kingdom.* **Jay, S.** 7, s.l. : Energy Policy, 2011, Vol. 39. 0301-4215.
12. **Kaldellis, J, K.** *Wind Energy.* [book auth.] Sayigh. A. *Comprehensive Renewable Energy.* 978-0-08-087873-7 : Elsevier, 2012.

13. *A Review on Global Solar Energy Policy*. **Solangi, K, Islam, M, Saidur, R, Rahim, N, Fayaz, H**. Pages 2149–2163, s.l. : Renewable and Sustainable Energy Reviews, Vol. 15. 1364-0321.
14. *Recent Advances in Nuclear Power : A Review*. **Abu-Khader, M, M**. 2, s.l. : Progress in Nuclear Energy, 2009, Vol. 51. 0149-1970.
15. *Nuclear Energy for Transportation : Paths Through Electricity, Hydrogen and Liquid Fuels*. **Hori, M**. 2-6, s.l. : Progress in Nuclear Energy, 2008, Vol. 50. 0149-1970.
16. *Energy Models for Demand Forecasting—A review*. **Suganthi, L, Samuel, A**. Pages 1223– 1240, s.l. : Renewable and Sustainable Energy Reviews, Vol. 16. 1364-0321.
17. *A Review of Climate Change, Mitigation and Adaptation*. **VijayaVenkataRaman, S**. Pages 878– 897, s.l. : Renewable and Sustainable Energy Reviews, Vol. 16. 1364-0321.
18. *Role of Renewable Energy Sources in Environmental Protection : A Review*. **Panwar, N, L, Kaushik, S, C, Kothari, S**. 3, s.l. : Renewable and Sustainable Energy Reviews, 2011, Vol. 15. 1364-0321.
19. *The Oil Industry and Climate Change : Strategies and Ethical Dilemmas*. **Van Den Hove, S, Menestrel, M, Bettignies, H, C, de**. 1, s.l. : Climate Policy, 2002, Vol. 2. 1469-3062.
20. *Transparent Conductors as Solar Energy Materials : A Panoramic Review*. **Granqvist, C G**. 17, pp. 1529-1598, s.l. : Solar Energy Materials & Solar Cells, 2007, Vol. 91. 0927-0248.
21. **Nations, United**. *Population Ageing and Development 2012 - Wall Chart*. s.l. : United Nations, 2012. 978-92-1-151494-0.
22. **Waterlow, J, C, Armstrong, D, G, Fowden, L, Riley, R**. *Feeding a World Population of More Than Eight Billion People : A Challenge to Science*. s.l. : Oxford University Press, 1998. 978-0195113129.
23. *A Review on the Role of Materials Science in Solar Cells*. **Asim, N, Sopian, K, Ahmadi, S, Saeedfar, K, Alghoul, M, Saadatian, O, Zaidi, S**. Pages 5834–5847, s.l. : Renewable and Sustainable Energy Reviews, Vol. 16. 1364-0321.
24. *The Challenge to UK Energy Polic : An Ageing Population Perspective on Energy Saving Measures and Consumption*. **Hamza, N, Gilroy, R**. 2, s.l. : Energy Policy, 2011, Vol. 39. 0301-4215.

25. **British Government, Energy Saving Trust.** Energy Saving Trust - Lighting. *Energy Saving Trust*. [Online] [Cited: 3 October 2012.] <http://www.energysavingtrust.org.uk/Electricals/Lighting>.
26. *Accuracy of Home Energy Rating Systems.* **Stein, J, Meier, A.** Pages 339-354, s.l. : Energy, Vol. 25. 0360-5442.
27. *A Review of Benchmarking, Rating and Labelling Concepts within the Framework of Building Energy Certification Schemes.* **Perez-Lombard, L, Ortiz, J, Gonzalez, R, Maestre, I.** Pages 272-278, s.l. : Energy and Buildings, Vol. 41. 0378-7788.
28. *Development of an Energy Rating System for Existing Houses.* **Zmeureanu, R, Fazio, P, DePani, S, Calla, R.** Pages 107-119, s.l. : Energy and Buildings, Vol. 29. 0378-7788.
29. **British Government, Recycle Now.** Recycle Now. *Recycle Now*. [Online] 2010. [Cited: 25th July 2010.] <http://www.recyclenow.com/>.
30. **Agency, International Energy.** *Technology Roadmap - Fuel Economy of Road Vehicles.* s.l. : International Energy Agency, 2012.
31. *Fuel Economy Evaluation of Fuel Cell Hybrid Vehicles Based on Equivalent Fuel Consumption.* **Zheng, C, Oh, C, Park, Y, Cha, S.** Pages 1790-1796, s.l. : International Journal of Hydrogen Energy, Vol. 37. 0360-3199.
32. *Fuel Economy and Life-Cycle Cost Analysis of a Fuel Cell Hybrid Vehicle.* **Jeong, K, Oh, B.** Pages 58-65, s.l. : Journal of Power Sources, Vol. 105. 0378-7753.
33. **Greenhalgh, E.** Imperial College London - News and Events. *Imperial College London*. [Online] 5th February 2010. [Cited: 15th March 2010.] http://www3.imperial.ac.uk/newsandeventspggrp/imperialcollege/newssummary/news_5-2-2010-10-26-39.
34. *Solar Photovoltaic Electricity: Current Status and Future Prospects.* **Razykov, T, Ferekides, C, Morel, D, Stefanakos, E, Ullal, H, Upadhyaya, H.** Pages 1580-1608, s.l. : Solar Energy , Vol. 85. 0038-092X.
35. *Review of Photovoltaic Technologies.* **Chaar, L, Lamont, L, Zein, N.** Pages 2165–2175, s.l. : Renewable and Sustainable Energy Reviews, Vol. 15. 1364-0321.
36. *Transparent Conducting Oxides Films for Thin Film Silicon Photovoltaics.* **Beyer, W, Hüpkes, J and Stiebig, H.** 2-4, p.p. 147-154, s.l. : Thin Solid Films, 2007, Vol. 516. 0040-6090.

37. *Solar Photovoltaics R&D at the Tipping Point : A 2005 Technology Overview*. **Kazmerski, L.** 2-3, Pages: 105-135, s.l. : Journal of Electron Spectroscopy and Related Phenomena, 2006, Vol. 150. 03682048.
38. *Potential of Thin-Film Silicon Solar Cells by Using High Haze TCO Superstrates*. **Krc, J, et al., et al.** 11, Pages: 3054-3058, s.l. : Thin Solid Films - Transparent Oxides for Electronics and Optics (TOEO-6), 31 March 2010, Vol. 518. 0040-6090.
39. *High Mobility Transparent Conducting Oxides for Thin Film Solar Cells*. **Calnan, S and Tiwari, A N.** 7, Pages: 1839-1849, s.l. : Thin Solid Films, 2009, Vol. 518. 00406090.
40. *Thin-Film Solar Cells: An Overview*. **Chopra, K L, Paulson, P D and Dutta, V.** 2-3, Pages: 69-92, Delhi : Progress in Photovoltaics: Research and Applications, 2004, Vol. 12. 10627995.
41. *Chemical Vapour Deposition of Coatings*. **Choy, K L.** 2, Pages: 57-170, s.l. : Progress in Materials Science, 2003, Vol. 48. 0079-6425.
42. *Basic Material Physics of Transparent Conducting Oxides*. **Edwards, P P, et al., et al.** 19, p.p. 2995-3002, Cardiff : Dalton The Royal Society of Chemistry, 2004, Vol. 7. 1477-9226.
43. *The Surface and Material Science of Tin Oxide*. **Batzill, M and Diebold, U.** 2-4, Pages: 47-154, s.l. : Progress in Surface Science, 2005, Vol. 79. 00796816.
44. *Transparent Conducting Oxide Layers for Thin Film Silicon Solar Cells*. **Rath, J, Liu, Y, Jong, M, Wild, J, Schuttauf, J, Brinza, M, Schropp, R.** Pages e129–e135, s.l. : Thin Solid Films, Vol. 518. 0040-6090.
45. *Resistivity of Polycrystalline Zinc Oxide Films: Current Status and Physical Limit*. **Ellmer, K.** 21, Pages: 3097-3108, Berlin : Journal of Physics D: Applied Physics, 2001, Vol. 34. 00223727.
46. *TCO and Light Trapping in Silicon Thin Film Solar Cells*. **Müller, J, et al., et al.** 6, Pages: 917-930, s.l. : Solar Energy, 2004, Vol. 77. 0038-092X.
47. *Surface Studies of Crystalline and Amorphous Zn–In–Sn–O Transparent Conducting Oxides*. **Proffit, D, Harvey, S, Klein, A, Schafrank, R, Emery, J, Buchholz, D, Chang, R, Bedzyk, M, Mason, T.** Pages 5633–5639, s.l. : Thin Solid Films, Vol. 520. 0040-6090.
48. **Baumann, A, et al., et al.** *Photovoltaic Technology Review*. [Powerpoint Presentation] Berkeley : University of California, 2004.

49. *Micro/nanomechanical Properties of Aluminium Doped Zinc Oxide Films Prepared by Radio Frequency Magnetron Sputtering.* **Lin, L, Jeong, M, Kim, D, Myoung, J.** 6, s.l. : Surface and Coatings Technology, 2006, Vol. 201. 0257-8972.
50. *Synthesis of Fluorine Doped Zinc Oxide by Reactive Magnetron Sputtering.* **Noirfalise, X, Godfroid, T, Guisbiers, G, Snyders, R.** s.l. : Acta Materialia, 2011, Vol. 59. 1359-6454.
51. *Microstructure and Optical Properties of ZnO:Al Films Prepared by Radio Frequency Reactive Magnetron Sputtering.* **Chen, H, X, Ding, J, J, Zhao, X, G, Ma, S, Y.** 5, s.l. : Physica B, 2010, Vol. 405. 0921-4526.
52. *Chemical Spray Pyrolysis Deposited Fluorine Doped Zinc Oxide Thin Films : Effect of Acetic Acid Content in the Starting Solution on Physics Properties.* **Castañeda, L, Maldonado, A, Rodríguez-Baez, J, Cheang-Wong, J, C, López-Fuentes, M, Olvera, M.** 3, s.l. : Materials Science in Semiconductor Processing, 2012, Vol. 15. 1369-8001.
53. *Effect of Doping Concentration on the Optical Properties of Aluminium Doped Zinc Oxide Films Prepared by Spray Pyrolysis for Transparent Electrode Applications.* **Muiva, C, M, Sathiaraj, T, S, Maabong, K.** 2, s.l. : Ceramics International, 2011, Vol. 37. 0272-8842.
54. *Preparation of Aluminium Doped Zinc Oxide Films and the Study of Their Microstructure , Electrical and Optical Properties.* **Zhou, H, Yi, D, Yu, Z, Xiao, L, Li J.** s.l. : Thin Solid Thins, 2007, Vol. 515. 0040-6090.
55. *Synthesis, Diffused Reflectance and Electrical Properties of Nanocrystalline Fe-Doped ZnO via Sol-Gel Calcination Technique.* **Aydin, C, El-sadek, M, Zheng, K, Yahia, I, Yakuphanoglu, F.** s.l. : Optics & Laser Technology, 2013, Vol. 48. 0030-3992.
56. *Nitrogen Doping in Pulsed Laser Deposited ZnO Thin Films Using Dense Plasma Focus.* **Karamat, S, Rawat, R, Tan, T, Springham, S, Charehabani, E, Chen, R, Sun, H.** s.l. : Applied Surface Science, 2011, Vol. 257. 0169-4332.
57. *Structural and Optical Properties of Pulsed Laser Deposited ZnO Thin Films.* **Fazio, A, Patane, S, Scibilia, S, Mezzasalma, A, Mondio, G, Neri, F, Trusso, S.** 4, s.l. : Current Applied Physics, 2013, Vol. 13. 1567-1739.
58. *Study of the Effect of Plasma Power on ZnO Thin Films Growth Using Electron Cyclotron Resonance Plasma Assisted Molecular Beam Epitaxy.* **Yang, Z, Lim, J, Chu, S, Zuo, Z, Liu, J.** 5, s.l. : Applied Surface Science, 2008, Vol. 255. 0169-4332.
59. *Textured fluorine-doped ZnO films by atmospheric pressure chemical vapour deposition and their use in amorphous silicon solar cells.* **Gordon, R G.** 1-4, Pages: 437-450, s.l. : Solar Cells, 1991, Vol. 30. 03796787.

60. *Aerosol Assisted Chemical Vapor Deposition of Transparent Conductive Zinc Oxide Films*. **Bhachu, D, S, Sankar, G, Parkin, I**. s.l. : Chemistry of Materials, 2012, Vol. 24. 0897-4756.
61. *Polycrystalline ZnO:B Grown by LPCVD as TCO for Thin Film Silicon Solar Cells*. **Fay, S, Steinhäuser, J, Nicolay, S, Ballif, C**. Pages 2961–2966, s.l. : Thin Solid Films, 2010, Vol. 518. 0040-6090.
62. *Atmospheric Pressure CVD Coatings on Glass*. **Sheel, D**. s.l. : ICCG, 2002, Vol. 4.
63. *Modeling and Control of Transparent Conducting Oxide Layer Surface*. **Huang, J, Orkoulas, G, Christofides, P**. Pages 135–147, s.l. : Chemical Engineering Science, Vol. 74. 0009-2509.
64. *Optimal design of the light absorbing layer in thin film silicon solar cells*. **Soh, H, Yoo, J, Kim, D**. Pages 2095-2105, s.l. : Solar Energy, Vol. 86. 0038-092X.
65. *High Transmittance and Low Resistive ZnO:Al Films for Thin Film Solar Cells*. **Yoo, J, Lee, J, Kim, S, Yoon, K, Park, I, Dhungel, S, Karunakaran, B, Mangalaraj, D, Yi, J**. Pages 213-217, s.l. : Thin Solid Films, Vols. 480-481. 0040-6090.
66. *New Texture Etching for Zinc Oxide Tunable Light Trapping for Si Thin Film Solar Cells*. **Hüpkes, J, Owen, J, Bunte, E, Zhu, H, Pust, S, Worbs, J, Jost, G**. Valencia, Spain : 25th European Photovoltaic Solar Energy Conference and Exhibition / 5th World Conference on Photovoltaic Energy Conversion, 2010.
67. *Recent Developments on Surface-Textured ZnO:Al Films Prepared by Sputtering for Thin-Film Solar Cell Application*. **Berginski, M, Hupkes, J, Reetz, W, Rech, B, Wuttig, M**. Pages 5836-5841, s.l. : Thin Solid Films, Vol. 516. 0040-6090.
68. **Phillipps, P, Dimroth, F, Bett, A, W**. Chapter IC-6 - High Efficiency III–V Multijunction Solar Cells. [book auth.] A, Castaner, L, Markvart, T McEvoy. *Solar Cells : Materials, Manufacture and Operation*. 9780123869647 : Elsevier, 2013.
69. **EMPA**. *A New World Record for Solar Cell Efficiency*. Duebendorf : EMPA, 2013. http://www.empa.ch/plugin/template/empa/*/131441.
70. *Effective Passivation of Black Silicon Surfaces by Atomic Layer Deposition*. **Repo, P, Haarahiltunen, A, Sainiemi, L, Yli-Koski, M, Talvitie, H, Schubert, M, C, Savin, H**. 1, s.l. : IEEE Journal of Photovoltaics, 2013, Vol. 3. 2156-3381.

71. *Development Status of High Efficiency HIT Solar Cells*. **Mishima, T, Taguchi, M, Sakata, H, Maruyama, E.** 1, s.l. : Solar Energy Materials and Solar Cells, 2011, Vol. 95. 0927-0248.
72. **Osborne, M.** NREL Verifies First Solar's Big Leap in CdTe Cell Efficiency. *PVTECH*. [Online] 27 February 2013. [Cited: 19 April 2013.] http://www.pv-tech.org/news/nrel_verifies_first_solars_big_leap_in_cdte_cell_efficiency.
73. **Choudhury, N.** Spectrolab Breaks World Record with 37.8% Cell Efficiency. *PVTECH*. [Online] 15 April 2013. [Cited: 19 April 2013.] http://www.pv-tech.org/news/spectrolab_breaks_world_record_with_37.8_efficiency.
74. **Nkwocha, K.** Empa Achieves Record 20.4% Efficiency for Flexible Thin Film. *PVTECH*. [Online] 18 January 2013. [Cited: 2013 April 19.] http://www.pv-tech.org/news/empa_achieves_record_efficiency_for_converting_sunlight_into_electricity.
75. **Osborne, M.** Verified: Heliatek Organic Solar Cell Achieves Record 12% Efficiency. *PVTECH*. [Online] 16 January 2013. [Cited: 19 April 2013.] http://www.pv-tech.org/news/verified_heliatek_organic_solar_cell_achieves_record_12_conversion_efficiency.
76. **Scanlon, B.** Award Winning PV Cell Pushes Efficiency Higher. *NREL*. [Online] 28 December 2012. [Cited: 19 April 2013.] http://www.nrel.gov/news/features/feature_detail.cfm/feature_id=2055.
77. **Kaften, C.** The 2012 Solar Year in Review and What Lies Ahead. *PV Magazine*. [Online] 28 December 2012. [Cited: 19 April 2013.] http://www.pv-magazine.com/news/details/beitrag/the-2012-solar-year-in-review-and-what-lies-ahead-in-2013_100009692/#axzz2QAn6UeVG.
78. **Beetz, B.** Bankruptcy or Acquisition Facing Half of PV Manufacturers. *PV Magazine*. [Online] 30 May 2012. [Cited: 19 April 2013.] http://www.pv-magazine.com/news/details/beitrag/bankruptcy-or-acquisition-facing-half-of-pv-manufacturers-_100006977/#axzz2QtjOI500.
79. **Bohner, M.** Yingli Financial Report Shows Future of PV. *Renewables International : The Magazine*. [Online] 5 March 2013. [Cited: 19 April 2013.] <http://www.renewablesinternational.net/yingli-financial-report-shows-future-of-pv/150/537/61010/>.
80. *Analysis on the Development and Policy of Solar PV Power in China*. **Zhang, S, He, Y.** 393-401, s.l. : Renewable and Sustainable Energy Reviews, 2013, Vol. 21. 1364-0321.

81. *Lessons from Photovoltaic Policies in China for Future Development*. **Huo, M, Zhang, D.** 38-45, s.l. : Energy Policies, 2012, Vol. 51. 0301-4215.
82. **Choudhury, N.** China Calls for Diplomacy in EU Trade Case. *PVTECH*. [Online] 15 April 2013. [Cited: 19 April 2013.] http://www.pv-tech.org/news/china_calls_for_diplomacy_in_eu_trade_case.
83. *Progress in Solar PV Technology : Research and Achievement*. **Tyagi, V, Rahim, N, Rahim, N, Selvaraj, J.** 443-461, s.l. : Renewable and Sustainable Energy Reviews, 2013, Vol. 20. 1364-0321.
84. *Revised Feed-in Tariff for Solar Photovoltaic in the United Kingdom: A Cloudy Future Ahead?* **Muhammad-Sukki, F, Ramirez-Iniguez, R, Munir, A, Yasin, S, Abu-Bakar, S, McMeekin, S, Stewart, B.** 832-838, s.l. : Energy Policy, 2013, Vol. 52. 0301-4215.
85. *Analysis on the Development and Policy of Solar PV Power in China*. **Zhang, S, He, Y.** 393-401, s.l. : Renewable and Sustainable Energy Reviews, 2013, Vol. 21. 1364-0321.
86. **Bullis, K.** Why We Need More Solar Companies to Fail. *MIT Technology Review*. [Online] 18 March 2013. [Cited: 19 April 2013.] [why-we-need-more-solar-companies-to-fail](http://www.technologyreview.com/2013/03/18/why-we-need-more-solar-companies-to-fail/).
87. *Improving Solar Cell Efficiency with Optically Optimised TCO Layers*. **Fleischer, K, Arca, E, Shvets, I.** Pages 262-269, s.l. : Solar Energy Materials & Solar Cells, Vol. 101. 0927-0248.
88. *Geometric Light Trapping for High Efficiency Thin Film Silicon Solar Cells*. **Escarre, J, Soderstrom, K, Despeisse, M, Nicolay, Sylvain, Battaglia, C, Gugnon, G, Ding, L, Meillaud, F, Haug, F, Ballif, C.** pp 185-190, s.l. : Solar Energy Materials & Solar Cells, 2012, Vol. 98. 0927-0248.
89. *Tailoring the Absorption Properties of Black Silicon*. **Baumann, A, Guenther, K, Saring, P, Gimpel, T, Kontermann, S, Seibt, M, Schade, W.** 480-484, s.l. : Energy Procedia, 2012, Vol. 27. 1876-6102.
90. *A Novel Method to Produce Black Silicon for Solar Cells*. **Xia, Y, Liu, B, Liu, J, Shen, Z, Li, C.** 1574-1578, s.l. : Solar Energy, 2011, Vol. 85. 0038-092X.
91. *Influence of the Texture Structure on the Properties of Black Silicon Solar Cell*. **Zhong, S, Liu, B, Xia, Y, Liu, J, Liu J, Shen, Z, Li, C.** 200-204, s.l. : Solar Energy Materials and Solar Cells, 2013, Vol. 108. 0927-0248.

92. *Tandem Solar Cell Concept Using Black Silicon for Enhanced Infrared Absorption*. **Guenther, K, Baumann, A, Gimpel, T, Kontermann, S, Schade, W.** 555-560, s.l. : Energy Procedia, 2012, Vol. 27. 1876-6102.
93. *Nanoporous Black Multi-Crystalline Silicon Solar Cells: Realization of Low Reflectance and Explanation of High Recombination Loss*. **Shi, J, Xu, F, Ma, Z, Zhou, P, Zheng, L, Yang, J, Chen, D, Jiang, Z.** 441-448, s.l. : Material Science in Semiconductor Processing, 2013, Vol. 16. 1369-8001.
94. **Bullis, K.** Nanowires Suck Up Light from Around Them. *MIT Technology Review*. [Online] 26 March 2013. [Cited: 19 April 2013.] <http://www.technologyreview.com/news/512786/nanowires-suck-up-light-from-around-them/>.
95. **LaMonica, M.** A Startup's Nanowire Ink Lifts Solar Cell Efficiency. *MIT Technology Review*. [Online] 10 April 2013. [Cited: 19 April 2013.] <http://www.technologyreview.com/news/513396/a-startups-nanowire-ink-lifts-solar-cell-efficiency/>.
96. *Control of CVD-Deposited ZnO Film Properties Through Water/DEZ Ratio : Decoupling of Electrode Morphology and Electrical Characteristics*. **Nicolay, S, Benkhaira, M, Ding, L, Escarre, J, Bugnon, G, Meillaud, F, Ballif, C.** s.l. : Solar Energy Materials & Solar Cells, 2012, Vol. 105. 0927-0248.
97. *Chemical Etching of Zinc Oxide for Thin-Film Silicon Solar Cells*. **Hupkes, J, Owen, J, Pust, S, Bunte, E.** 66-73, s.l. : ChemPhysChem, 2012, Vol. 13. 1439-7641.
98. *Refractive Index Graded Anti-Reflection Coating for Solar Cells Based on Low Cost Reclaimed Silicon*. **Liu, Y, Guy, O, Patel, J, Ashraf, H, Knight, N.** s.l. : Microelectronic Engineering, 2013, Vol. In Press. 0167-9317.
99. *Optimal Design for Antireflective Si Nanowire Solar Cells*. **Jung, J, Um, H, Jee, S, Park, K, Bang, J, Lee, J.** 84-90, s.l. : Solar Energy Materials and Solar Cells, 2013, Vol. 112. 0927-0248.
100. *Broadband Anti-Reflective and Water-Repellent Coatings on Glass Substrates for Self-Cleaning Photovoltaic Cells*. **Li, X, He, J, Liu, W.** s.l. : Materials Research Bulletin, 2013, Vol. In Press. 0025-5408.
101. *Energy Storage for Mitigating the Variability of Renewable Electricity Sources: An Updated Review*. **Beaudin, M, Zareipour, H, Schellenberglabe, A, Rosehart, W.** 302-314, s.l. : Energy for Sustainable Development, 2010, Vol. 14. 0973-0826.

102. *The Dimensioning of PV-Battery Systems Depending on the Incentive and Selling Price Conditions*. **Mulder, G, Six, D, Claessens, B, Broes, T, Omar, N, Mierlo, J.** s.l. : Applied Energy, 2013, Vol. In Press. 0306-2619.
103. *Energy Management of Stand-Alone Hybrid PV System*. **Wang, C, Chen, W, Shao, S, Chen, Z, Zhu, B, Li, H.** 471-479, s.l. : Energy Procedia, 2011, Vol. 12. 1876-6102.
104. **Enkhardt, S.** Germany: PV Storage Subsidies Expected in May. *PV Magazine*. [Online] 08 February 2013. [Cited: 19 April 2013.] http://www.pv-magazine.com/news/details/beitrag/germany--pv-storage-subsidies-expected-in-may_100010135/#axzz2QtjOI500.
105. **Choudhury, N.** World's Largest Battery Storage System to be Installed in Japan. *PVTECH*. [Online] 19 April 2013. [Cited: 19 April 2013.] http://www.pv-tech.org/news/worlds_largest_battery_storage_system_to_be_installed_in_japan.
106. *Evaluating the Limits of Solar Photovoltaics in Electric Power Systems Utilizing Energy Storage and Other Enabling Technologies*. **Denholm, P, Margolis, R.** 4424-4433, s.l. : Energy Policy, 2007, Vol. 35. 0301-4215.
107. *The Future Prospect of PV and CSP Solar Technologies: An Expert Elicitation Survey*. **Bosetti, V, Catenacci, M, Fiorese, G, Verdolini, E.** 308-317, s.l. : Energy Policy, 2012, Vol. 49. 0301-4215.
108. *LPCVD ZnO-Based Intermediate Reflector for Micromorph Tandem Solar Cells*. **Bugnon, G, Soderstrom, T, Nicolay, S, Ding, L, Despeisse, M, Hedler, A, Eberhardt, J, Wachtendorf, C, Ballif, C.** 2161-2166, s.l. : Solar Energy Materials and Solar Cells, 2011, Vol. 95. 0927-0248.
109. *Control of LPCVD ZnO Growth Modes for Improved Light Trapping in Thin Film Silicon Solar Cells*. **Nicolay, S, Despeisse, M, Haug, F, Ballif, C.** s.l. : Solar Energy Materials & Solar Cells, 2011, Vol. 95. 0927-0248.
110. *Realization of High Efficiency Micromorph Tandem Silicon Solar Cells on Glass and Plastic Substrates : Issues and Potential*. **Meillaud, F, Feltrin, A, Despeisse, M, Haug, F, Domine, D, Python, M, Soderstrom, T, Cuony, P, Boccard, M, Nicolay, S, Ballif, C.** 127-130, s.l. : Solar Energy Materials and Solar Cells, 2011, Vol. 95. 0927-0248.
111. *Atmospheric Pressure Chemical Vapor Deposition of Gallium Doped Zinc Oxide Thin Films from Diethyl Zinc, Water, and Triethyl Gallium*. **Hu, J, Gordon, R.** 11, s.l. : Journal of Applied Physics, 1992, Vol. 72. 1089-7550.

112. *Influence of the Substrate Geometrical Parameters on Microcrystalline Silicon Growth for Thin-Film Solar Cells*. **Python, M, Madani, O, Domine, D, Meillaud, F, Vallat-Sauvain, E, Ballif, C.** s.l. : Solar Energy Materials & Solar Cells, 2009, Vol. 93. 0927-0248.
113. **NREL.** *Best Research Cell Efficiencies*. s.l. : NREL, 2012.
114. *Transparent Conducting Oxides Semiconductors for Transparent Electrodes*. **Minami, T.** 4, s.l. : Semiconductor Science and Technology (IOP), 2005, Vol. 20. 1088-0268.
115. **Perkins, J, et al., et al.** *A Combinatorial Approach to TCO Synthesis and Characterization*. s.l. : National Renewable Energy Laboratory, 2001.
116. *A Comparison of Composite Transparent Conductive Oxides Based on the Binary Compounds CdO and SnO₂*. **Li, Xiaonan.** Colorado : National Renewable Energy Laboratory, 2001. NREL/CP-520-31017.
117. *Transparent Conducting Oxides for Photovoltaics: Manipulation of Fermi Level, Work Function & Energy Band Alignment*. **Klein, A, Korber, C, Wachu, A, Sauberlich, F, Gassenbauer, Y, Harvey, S, Proffit, D, Masson, T.** Pages 4892-4914, s.l. : Materials, Vol. 3. 1996-1944.
118. *Microwave-Assisted Hydrothermal Synthesis of Nanocrystalline SnO Powders*. **Pires, F I, et al., et al.** 2, Pages: 239-242, s.l. : Materials Letters, 2007, Vol. 62. 0167577X.
119. *Transparent Conducting Oxides for Electrode Applications in Light Emitting and Absorbing Devices*. **Liu, H, Avrutin, V, Izyumskaya, N, Ozgur, U, Morkoc, H.** Pages 458-484, s.l. : Superlattices and Microstructures, 2010, Vol. 48. 0749-6036.
120. *Transparent Conducting Oxides : Status and Opportunities in Basic Research*. **Coutts, T, Perkins, J, Ginley, D, Mason, T.** 1999 : National Renewable Energy Laboratory. NREL/CP-520-26640.
121. *Detailed Balance Limit for Solar Cell Efficiency*. **Queisser, H.** Pages 322–328, s.l. : Materials Science and Engineering B, Vols. 159–160. 0921-5107.
122. **Ginley, S.** *Handbook of Transparent Conductors*. 2010 : Springer Science. 978-1-4419-1637-2.
123. *Tin Oxide Thin Films : Electronic Properties and Growth Mechanism Under Electrochemical Control*. **Diaz, R.** s.l. : The Electrochemical Society, 2002.
124. *In Situ Analysis of the Conductance of SnO₂ Crystalline Nanoparticles in the Presence of Oxidizing or Reducing Atmosphere by Scanning Tunneling Microscopy*. **Arbiol, J,**

Gorostiza, P, Cirera, A, Cornet, A, Morante, J. Pages 57-63, s.l. : Sensors and Actuators B, Vol. 78. 0925-4005/01.

125. **Hartnagel, H.** *Semiconducting Transparent Thin Films*. s.l. : Institute of Physics Publishing, 1995. 0750303220.

126. *Applications and Processing of Transparent Conducting Oxides*. **Lewis, B, Paine, D.** 8, s.l. : Materials Research Society 2000, Vol. 25. DOI: <http://dx.doi.org/10.1557/mrs2000.147>.

127. *Origins of coexistence of conductivity and transparency in SnO₂*. **Kilic, C, Zunger, A.** 9, s.l. : Physical Review Letters, Vol. 88. 095501.

128. *Defect Structure and Electronic Donor Levels in Stannic Oxide Crystals*. **Samson, S, Fonstad, C.** 10, 1973, Vol. 44. 1089-7550.

129. *Transparent Conductors - A Status Review*. **Chopra, K, Major, S, Pandya, D.** Pages 1-46, s.l. : Thin Solid Films, 1983, Vol. 102. 0040-6090.

130. *Characterization of rf-sputtered SnO_x Thin Films by Electron Microscopy, Hall-Effect Measurement and Mossbauer Spectrometry*. **Stjerna, B, Granqvist, C, Seidel, A, Haggstrom, L.** 12, s.l. : Journal of Applied Physics, 1990, Vol. 68. 1089-7550.

131. *Sb-Doped SnO₂ Transparent Conducting Oxide from the Sol-Gel Dip-Coating Technique*. **Terrier, C, Chatelon, J, Berjoan, R, Roger, J.** Pages 37-41, s.l. : Thin Solid Films, Vol. 263. 0040-6090.

132. *Control of Tin Oxide Film Morphology by Addition of Hydrocarbons to the Chemical Vapour Deposition Process*. **Yates, H, Evans, P, Sheel, D, Remes, Z, Vanecek, M.** Pages 1334-1340, s.l. : Thin Solid Films, 2010, Vol. 519. 0040-6090.

133. *Atmospheric Pressure Chemical Vapor Deposition of Fluorine Doped Tin Oxide Thin Films*. **Suh, S, Zhang, Z, Chu, W, Hoffman, D.** Pages 240-243, s.l. : Thin Solid Films, 1999, Vol. 345. 0040-6090.

134. *Effect of Substrate Temperature on Structural, Electrical and Optical Properties of Sprayed Tin Oxide Thin Films*. **Patil, P, Kawar, R, Seth, T, Amalnerkar, D, Chigare, P.** Pages 725-734, s.l. : Ceramics International, 2003, Vol. 29. 0272-8842.

135. **Jagadish, C, Pearnton, S.** *Zinc Oxide Bulk, Thin Films and Nanostructures : Processing, Properties and Applications*. s.l. : Elsevier, 2006. 978-0-08-044722-3.

136. *Characterization of Homoepitaxial p-type ZnO Grown by Molecular Beam Epitaxy*. **Look, D, Reynolds, D, Litton, C, Jones, R, Eason, D, Cantwell, G.** 10, s.l. : Applied Physics Letters, 2002, Vol. 81. 0003-6951.

137. *Fundamentals of Zinc Oxide as a Semiconductor*. **Janotti, A, Van de Walle, Chris, G.** s.l. : Reports on Progress in Physics, 2009, Vol. 72. 0034-4885.
138. *Structural, Transport and Optical Properties of Boron-doped Zinc Oxide Nanocrystalline*. **Kumar, V, Singh, R, Purohit, L, Mehra, R.** Pages 481-488, s.l. : Journal of Materials Science & Technology, 2011, Vol. 27. 1005-0302.
139. *Sol-Gel Deposited ZnO Thin Films : A Review*. **Znadi, L.** Pages 18-30, s.l. : Materials Science and Engineering B, 2010, Vol. 174. 0921-5107.
140. *Transparent and Conductive ZnO:Al Films Deposited by Large Area Reactive Magnetron Sputtering*. **Szyska, B, Sittinger, V, Jiang, X, Hong, R, Werner, W, Pflug, A, Ruske, M, Lopp, A.** s.l. : Thin Solid Films, 2003, Vol. 442. 0040-6090.
141. *High Deposition Rate Aluminium-Doped Zinc Oxide Films with High Efficient Light Trapping for Silicon Thin Film Solar Cells*. **Calnan, S, Hupkes, J, Rech, B, Siekmann, H, Tiwari, A.** Pages 1242-1248, s.l. : Thin Solid Films, Vol. 516. 0040-6090.
142. *Indium Doped Zinc Oxide Films as Transparent Electrodes for Solar Cells*. **Major, S, Chopra, K, L.** s.l. : Solar Energy Materials, 1988, Vol. 17. 0165-1633.
143. *The Effects of Fluorine on the Structural, Surface Morphology and Optical Properties of ZnO Thin Films*. **Yakuphanoglu, F, et al., et al.** 1, Pages: 86-92, s.l. : Physica B: Physics of Condensed Matter, 2007, Vol. 394. 0921-4526.
144. *Nanowire Ultraviolet Photodetectors and Optical Switches*. **Kind, H, Yan, Messer, B, Law, M, Yang, Peidong.** 2, s.l. : Advanced Materials, 2002, Vol. 14. 0935-9648.
145. *Indium Phosphide Nanowires as Building Blocks for Nanoscale Electronic and Optoelectronic Devices*. **Duan, X, Huang, Y, Cui, Y, Wang, J, Lieber, C.** Pages 66-69, s.l. : Nature, 2001, Vol. 409. 0028-0836.
146. *Functionalised Zinc Oxide Nanowire Gas Sensors : Enhanced NO₂ Gas Sensors Response by Chemical Modification of Nanowires Surfaces*. **Waclawik, E, Chang, J, Ponzoni, A, Concina, I, Zappa, D, Comini, E, Motta, N, Fagila, G, Sberveglieri, G.** Pages 368–377, s.l. : Beilstein Journal of Nanotechnology, 2012, Vol. 3. 2190-4286.
147. *Nanowire Nanosensors for Highly Sensitive and Selective Detection of Biological and Chemical Species*. **Cui, Y, Wei, Q, Park, H, Lieber.** s.l. : Science, 2001, Vol. 293. 1095-9203.

148. *Electronic Memory Effects in Diodes of Zinc Oxides Nanoparticles in a Matrix of Polystyrene or Poly (3-hexylthiophene)*. **Verbakel, F, Meskers, S, Janssen, R.** s.l. : Journal of Applied Physics, 2007, Vol. 102. 1089-7550.
149. *Defects in ZnO*. **McCluskey, M, Jokela, S.** s.l. : Journal of Applied Physics, 2009, Vol. 106. 0021-8979.
150. *High Transmittance and Low Resistive ZnO:Al Films for Thin Film Solar Cells*. **Yoo, J, Lee, J, Kim, S, Yoon, K, Park, I, Dhungel, S, Karunagaran, B, Mangalaraj, D, Yi, J.** Pages 213-217, s.l. : Thin Solid Films, 2005, Vols. 480-481. 0040-6090.
151. *Ti-Doped ZnO Thin Films Prepared at Different Ambient Conditions : Electronic Structure and Magnetic Properties*. **Yong, Z, et al., et al.** 6, Pages 3642-3653, Singapore : Materials, 2010, Vol. 3. 1996-1944.
152. *New n-type Transparent Conducting Oxides*. **Minami, T.** 8, s.l. : Materials Research Society (Bulletin), 2000, Vol. 25. 0883-7694.
153. *Control of Preferred Orientation of ZnOx Films: Control of Self-Texture*. **Fujimura, N, Nishihara, T, Goto, S, Xu, J, Ito, T.** Pages 269-279, s.l. : Journal of Crystal Growth, 1993, Vol. 130. 0022-024.
154. *Zinc Oxide as a Model Transparent Conducting Oxide : A Theoretical and Experimental Study of the Impact of Hydroxylation, Vacancies, Interstitials, and Extrinsic Doping on the Electronic Properties of the Polar ZnO (0002) Surface*. **Li, H, Schira, L, Shim, J, Cheun, H, Kippelen, B, Monti, O, Bredas, J.** Pages 3044-3055, s.l. : Chemistry of Materials, 2012, Vol. 24. 0897-4756.
155. *Initial Preferred Growth in Zinc Oxide Thin Films on Si and Amorphous Substrates by a Pulsed Laser Deposition*. **Choi, J, Tabata, H, Kawai, T.** Pages 493-500, s.l. : Journal of Crystal Growth, 2001, Vol. 226. 0022-0248.
156. *Group III Impurity Doped ZnO Films Prepared by Atmospheric Pressure Chemical Vapor Deposition Using Zinc Acetylacetonate and Oxygen*. **Haga, K, Wijesena, P, Watanabe, H.** s.l. : Applied Surface Science, 2001, Vols. 169-170. 0169-4332.
157. *Low-Resistivity ZnO:F:Al Transparent Thin Films*. **Altamirano-Juraez, D, Torres-Delgado, G, Jimenez-Sandoval, S, Jimenez-Sandoval, O, Catanedo-Perez, R.** s.l. : Solar Energy Materials and Solar Cells, 2004, Vol. 82. 0927-0248.
158. *High-Efficiency P-I-N Microcrystalline and Micromorph Thin Film Silicon Solar Cells Deposited on LPCVD ZnO Coated Glass Substrates*. **Bailat, J, Domine, D, Schluchter, R, Steinhauser, J, Fay, S, Freitas, F, Bucher, C, Feitknecht, L, Niquille, X, Tschärner, T.**

pp 1533-1536 : Proceedings of the IEEE 4th World Conference on Photovoltaic Energy Conversion Vol 1-2, 2006. 1-4244-0016-3.

159. *Electrical, structural and Optical Properties of Fluorine-Doped Zinc Oxide Thin Films: Effect of the Solution Aging Time.* **Rozati, S, Moradi, S, Golshahi, S, Martins, R, Fortunato, E.** 1279-1282, s.l. : Thin Solid Films, 2009, Vol. 518. 0040-6090.

160. *TCO/metal/TCO Structures for Energy and Flexible Electronics.* **Guillen, C, Herrero, J.** 1, s.l. : Thin Solid Films, 2011, Vol. 520. 0040-6090.

161. *Effect of Fluorine Doping on Structural, Electrical and Optical Properties of ZnO Thin Films.* **Kumar, P M, et al., et al.** 3, Pages: 307-312, s.l. : Thin Solid Films - Material Science and Engineering B, 2005, Vol. 117. 00406090.

162. *Electronic properties of ZnO/CdS/Cu(In,Ga),Se₂ solar cells - Aspects of Heterojunction Formation.* **Rau, U and Schmidt, M.** 1-2, Pages: 141-146, Stuttgart : Thin Solid Films, 2001, Vol. 387. 00406090.

163. *Transparent Conducting Oxides - An Up-to Date Overview.* **Stadler, A.** Pages 661-683, s.l. : Materials, 2012, Vol. 5. 1996-1944.

164. *Fluorine Doped Zinc Oxide Transparent & Conducting Electrode by Chemical Spray Synthesis.* **Pawar, B, Ham, D, Mane, R, Ganesh, T, Cho, Byung, Han, S.** Pages 6294-6297, s.l. : Applied Surface Science, Vol. 254. 0169-4332.

165. *Recent Developments in the Emerging Field of Crystalline p-type Transparent Conducitng Oxide Thin Films.* **Banerjee, A, Chattopadhyay, K.** Pages 52-105, s.l. : Progress in Crystal Growth and Characterization of Materials, Vol. 50. 0960-8974.

166. *Studies On Growth of ZnO Thin Films by a Novel Chemical Method.* **Shinde, V R, Gujar, T P and Lokhande, C D.** 12, Pages: 1055-1061, Kolhapur : Solar Energy Materials & Solar Cells, 2007, Vol. 91.

167. *Optical and Structural Investigation of ZnO Thin Films Prepared by Chemical Vapour Deposition (CVD).* **Purica, M, et al., et al.** Pages 485-488, Bucharest : Thin Solid Films, 2002, Vols. 403-404. 0040-6090.

168. *Discovery Based Design of Transparent Conducting Oxide Films.* **Exarhos, G, J, Zhou, Z, D.** 18, s.l. : Thin Solid Films, 2007, Vol. 515. 0040-6090.

169. *Present Status of Transparent Conducting Oxide Thin-Films Development for Indium-Tin-Oxide (ITO) Substitutes.* **Minami, T.** Pages 5822-5828, s.l. : Thin Solid Films, Vol. 516. 0040-6090.

170. *Thin Film Solar Cells*. **Aberle, A.** Pages 4706–4710, s.l. : Thin Solid Films, Vol. 517. 0040-6090.
171. *The Effect of the Transparent Conductive Oxide on the Performance of Thin Film CdS/CdTe Solar Cells*. **Alamri, S, Brinkman, A.** s.l. : Journal of Physics D: Applied Physics, Vol. 33. 0022-3727.
172. *Hall Effect*. **Lindberg, O.** s.l. : Institute of Radio Engineers (I.R.E), 1952. R282.12.
173. *Present Status of the Development and Application of Transparent Conductors Oxide Thin Solid Films*. **Castañeda, L.** s.l. : Materials Sciences and Applications, 2011, Vol. 2. 2153-1188.
174. *Electronic Structure Studies of Main Group Oxides Possessing Edge-Sharing Octahedra: Implications for the Design of Transparent Conducting Oxides*. **Mizoguchi, H, Woodward, P, M.** 25, s.l. : Chemistry of Materials, 2004, Vol. 16. 0897-4756.
175. **Look, D, C, Claflin, B.** *Progress in Compound Semiconductor Materials IV Electronic and Optoelectronic Applications*. s.l. : Materials Research Society Symposium Proceedings (Vol 829), 2005. 9781558997776.
176. *Hydrogen as a Cause of Doping in Zinc Oxide*. **Van de Walle, C, G.** 5, s.l. : Physical Review Letters, 2000, Vol. 85. 0031-9007.
177. *Intrinsic Performance Limits in Transparent Conducting Oxides*. **Bellingham, J, Phillips, W, Adkins, C.** 5, Journal of Material Science Letters : s.n., 1992, Vol. 11. 0261-8028.
178. *Intrinsic Limit of Electrical Properties of Transparent Conductive Oxide Films*. **Chen, M, Pei, Z, L, Wang, X, Yu, Y, h, Liu, X, H, Sun, C, Wen, L, S.** s.l. : Journal of Applied Physics D, 2000, Vol. 33. 0022-3727.
179. *Estimation and Verification of the Optical Properties of Indium Tin Oxide Based on the Energy Band Diagram*. **Knickerbocker, S, A, Kulkarni, A, K.** 3, s.l. : Journal of Vacuum Science & Technology, 1996, Vol. 14. 0734-2101.
180. *Carrier Transport in Polycrystalline Transparent Conductive Oxides : A Comparative Study of Zinc Oxide and Indium Oxide*. **Ellmer, K, Mientus, R.** s.l. : Thin Solid Films, 2007, Vol. 516. 0040-6090.
181. **Li, X, et al., et al.** *A Comparison of Composite Transparent Conducting Oxide Based on the Binary Compounds CdO and SnO₂*. s.l. : National Renewable Energy Laboratory.

182. *Magnetron Sputtering of Transparent Conductive Zinc Oxide : Relation Between the Sputtering Parameters and the Electronic Properties.* **Ellmer, K.** Pages 17-32, s.l. : Journal of Physics D: Applied Physics, Vol. 33. 0022-3727.
183. *Modeling of Carrier Mobility Against Carrier Concentration in Arsenic, Phosphorus and Boron Doped Silicon.* **Masetti, G, Severi, M, Solmi, S.** 7, 1983 : IEEE Transactions on Electron Devices, Vol. 30. 0018-9383.
184. *Electron Scattering by Ionized Impurities in Semiconductors.* **Chattopadhyay, D, Queisser, H.** 4, s.l. : Reviews of Modern Physics, 1981, Vol. 53. 0034-6861 .
185. *Importance of Many-Body Effects in the Clustering of Charged Zn Dopant Atoms in GaAs.* **Ebert, P, Zhang, T, Kluge, F, Simon, M, Zhang, Z, Urban , K.** 4, s.l. : Physical Review Letters, 1999, Vol. 83. 0031-9007.
186. *Scattering of Charge Carriers in Transparent and Conducting Thin Oxide Films with a Non-Parabolic Conduction Band.* **Pisarkiewicz, T, Zakrzewska, K, Leja, E.** Pages 217-223, s.l. : Thin Solid Films, 1989, Vol. 174. 0040-6090.
187. *Industrial High-Rate(~14 nm/s) Deposition of Low Resistive and Transparent ZnOx:Al on Glass.* **Illberi, A, Kniknie, B, Deelen, J, Streijvers, H., Habets, D, Simons, P.** s.l. : Solar Energy Materials & Solar Cells, 2011, Vol. 95. 0927-0248.
188. **Freund, L, Suresh, S.** *Thin Film Materials : Stress, Defect Formation and Surface Evolution.* s.l. : Cambridge University Press, 2003. 0-521-82281-5.
189. *Studies of Band Structure and Free-Carrier Scattering in Transparent Conducting Oxides Based on Combined Measurements of Electron Transport Phenomena.* **Kaydanov, V, Coutts, T, Young, D.** Denver : National Renewable Energy Laboratory, 2000. Vol. Material Research Society Workshop. NREL/CP-520-29064.
190. *Effect of Substrate Temperature on Physical Properties of In₂O₃:Sn Films Deposited by e-beam Technique.* **Mohamed, H.** 13, s.l. : International Journal of Physical Sciences, 2012, Vol. 7. 1992-1950.
191. *The Optical Energy Gap Dependence on Both Carrier Concentration and Intrinsic Energy Gap in n-type Semiconductors.* **Omar, M, Gorges, F.** Pages 164-167, s.l. : Materials Science in Semiconductor Processing, 2006, Vol. 9. 1369-8001.
192. *Effect of Carrier Concentration on Optical Bandgap Shifts in ZnO:Ga Thin Films.* **Kim, C, Moon, P, Kim, S, Myoung, J, Jang, H, Bang, J, Yun, I.** Pages 6304-6307, s.l. : Thin Solid Films, 2010, Vol. 518. 0040-6090.

193. *Hall, R. Cells, Silicon Photovoltaic*. Pages 595-616, s.l. : Solid State Electronics, 1981, Vol. 24. 0038-1101.
194. *Optical Characterization of Dielectric and Semiconductor Thin Films by Use of Transmission Data*. **Cisneros, J, I.** 22, s.l. : Applied Optics, 1998, Vol. 37. 0003-6935.
195. *Progress and Outlook for High Efficiency Crystalline Silicon Solar Cells*. **Green, M, A, Zhao, J, Wang, A, Wenham, S, R.** Pages 9-16, s.l. : Solar Energy Materials & Solar Cells, 2001, Vol. 65. 0927-0248.
196. **Ebil, O, Aparicio, R, Birkmire, R.** In-Situ Aluminum-Induced Crystallization of Si Thin-Films on Glass Substrates above the Eutectic Temperature using HW-CVD. [book auth.] MRS Proceedings (808). *Symposium A – Amorphous and Nanocrystalline Silicon Science and Technology*. s.l. : Materials Research Society, 2004.
197. *Recent Advances of Thin Film Solar Cells and Their Technologies*. **Hamakawa, Y.** Hawaii : WCPEC, 1994. CH3365-4.
198. **Guha, S.** *Amorphous Silicon Alloy Technology for Photovoltaics*. pp. 55–60 : 6th International Photovoltaic Science and Engineering Conference, 1992. 978-8120406797.
199. *Amorphous Silicon Solar Cell*. **Carlson, D, E, Wronski, C, R.** 11, s.l. : Applied Physics Letters, 1976, Vol. 28. 0003-6951 .
200. *Intrinsic Microcrystalline Silicon: A New Material for Photovoltaics*. **Vetterl, O, Finger, F, Carius, R, Hapke, P, Houben, L, Kluth, O, Lambertz, A, Mück, A, Rech, B, Wagner, H.** 1-2, s.l. : Solar Energy Materials and Solar Cells, 2000, Vol. 62. 0927-0248.
201. *Preparation of Highly Photosensitive Hydrogenerated Amorphous Si-C Alloys from a Glow-Discharge Plasma*. **Matsuda, A, Yamaoka, T, Wolff, S, Koyama, M, Imanishi, Y, Kataoka, H, Matsuura, H, Tanaka, K.** 11, s.l. : Journal of Applied Physics, 1986, Vol. 60. 1089-7550.
202. *Enhancement of Open Circuit Voltage in High Efficiency Amorphous Silicon Alloy Solar Cells*. **Guha, S, Yang, J, Nath, P, Hack, M.** 4, s.l. : Journal of Applied Physics, 1986, Vol. 49. 1089-7550.
203. *On Light-Induced Effect in Amorphous Hydrogenated Silicon*. **Guha, S, Narasimhan, K, L, Pietruszko, S, M.** 2, s.l. : Journal of Applied Physics, 1981, Vol. 52. 1089-7550.
204. *Reversible Conductivity Changes in Discharge Produced Amorphous Si*. **Staebler, D, L, Wronski, C, R.** 4, s.l. : Applied Physics Letters, 1977, Vol. 31. 1077-3118.

205. *Potential of Amorphous Silicon for Solar Cells*. **Rech, B, Wagner, H.** 2, s.l. : Applied Physics A, 1999, Vol. 69. 1432-0630.
206. *Thin Film Silicon Solar Cells Grown Near the Edge of Amorphous to Microcrystalline Transition*. **Guha, S.** 6, s.l. : Solar Energy, 2004, Vol. 77. 0038-092X.
207. **Diefenbach, K, H.** *Wiped away*. Pages 48-67 : Photon International, 2005.
208. *Thin-Film Silicon Solar Cell Technology*. **Shah, A, V, Schade, H, Vanecek, M, Meier, J, Vallat-Sauvain, E, Wyrsh, N, Kroll, U, Droz, C, Bailat, J.** 2-3, s.l. : Progress in Photovoltaics : Research and Applications, 2004, Vol. 12. 1099-159X.
209. *A High Efficiency Thin Film Silicon Solar Cell and Module*. **Yamamoto, K, Nakajima, A, Yoshimi, M, Sawada, T, Fukuda, S, Suezaki, T, Ichikawa, M, Koi, Y, Goto, M, Meguro, T, Matsuda, T, Kondo, M, Sasaki, T, Tawada, Y.** 6, s.l. : Solar Energy, 2004, Vol. 77. 0038-092X.
210. *Detailed Balance Limit for Solar Cell Efficiency*. **Queisser, H.** pp 322-328, s.l. : Materials Science and Engineering B, 2009, Vols. 159-160. 0921-5107.
211. **Green, M.** *Third Generation Photovoltaics : Advanced Solar Energy Conversion*. s.l. : Springer, 2003. 9783540401377.
212. **Luque, A, Hegedus, S.** *Handbook of Photovoltaic Science and Engineering*. s.l. : John Wiley & Sons, 2011. 9780470976128.
213. **Mukerjee, A, Thakur, N.** *Photovoltaic Systems: Analysis and Design*. s.l. : PHI Learning Pvt. Ltd, 2011. 9788120344174.
214. **McEvoy, A, Markvart, T, Castaner, L.** *Practical Handbook of Photovoltaics : Fundamentals and Applications*. s.l. : Academic Press, 2011. 9780123859358.
215. *Frontier of Transparent Oxide Semiconductors*. **Ohta, H, Monura, K, Hiramatsu, H, Ueda, K, Kamiya, T, Hirano, M, Hosono, H.** pp 2261-2267, s.l. : Solid-State Electronic, 2003, Vol. 47. 0038-1101.
216. **Roth, J.** *Industrial Plasma Engineering*. Knoxville : Insitute of Physics Publishing Bristol and Philadelphia, 2001. 0750305444 / 0750305452.
217. *Recent Progress in Processing and Properties of ZnO*. **Pearton, S, Norton, D, Ip, K, Heo, Y, Steiner, T.** pp 3-32, s.l. : Superlattices and Microstructure, 2003, Vol. 34. 0749-6036.

218. **Seshan, K.** *Handbook of Thin Film Deposition Processes and Techniques (2nd Edition)*. s.l. : Noyes Publication, 2002. 0-8155-1442-5.
219. **Pierson, H O.** *Handbook of Chemical Vapour Deposition (CVD)*. New York : Noyes Publications / William Andrew Publishing,, 1999. 0-8155-1432-8.
220. **Chopra, K.** *Thin Film Phenomena*. 1969 : McGraw-Hill. 9780882757469.
221. **Martin, P.** *Handbook of Deposition Technologies for Films and Coatings : Science, Applications and Technology*. s.l. : Elsevier, 2010. 978-0-8155-2031-3.
222. **Bunshah, R.** *Handbook of Deposition Technologies for Films and Coatings*. Los Angeles : William Andrew Publishing/Noyes, 1994. 0-8155-1337-2.
223. **Kodas, T, Hampden-Smith, M.** *The Chemistry of Metal CVD*. s.l. : VCH Verlagsgesellschaft, 1994. 3-527-29071-0.
224. **Vasicek, A.** *Optics of Thin Films*. s.l. : North Holland Publishing, 1960. 978-1124142012.
225. **Heavens, O.** *Optical Properties of Thin Solid Films*. 1955 : Butterworths Scientific Publications. 9780486669243.
226. **Ohring, M.** *Materials Science of Thin Films : Deposition & Structure 2nd Edition*. s.l. : Academic Press, 2002. 0-12-524975-6.
227. **Jones, Anthony.** *Chemical Vapour Deposition: Precursors, Processes and Applications*. s.l. : Royal Society of Chemistry, 2008. 978-0854044658.
228. **Xiu-Tian, Y, Yongdon, X.** *Chemical Vapour Deposition : An Integrated Engineering Design for Advanced Materials*. s.l. : Springer, 2010. 9781848828940.
229. **Bach, H, Krause, D.** *Thin Films on Glass*. s.l. : Springer, 1997. 978-3-540-58597-8.
230. *Widely Transparent Electrodes Based on Ultrathin Metals*. **Ghosh, G, Matinez, L, Giurgola, S, Vergani, P, Pruneri, V.** 3, s.l. : Optics Letters - Optical Society of America, 2009, Vol. 34. 0146-9592.
231. *Equipment Modelling of CVD and Etching*. **Ulacia, F, Werner, C.** Pages 217-232, s.l. : Microelectronic Engineering, 1991, Vol. 10. 0167-9317.
232. **Timberlake, Ian.** Intel opens biggest ever chip plant in Vietnam. *PhysOrg.com*. [Online] 29 10 2010. [Cited: 04 11 2010.] <http://www.physorg.com/news/2010-10-intel-vietnam-biggest-chip.html>.

233. **Hitchman, M, Jensen, K.** *Chemical Vapor Deposition - Principles and Applications.* s.l. : Academic Press LTD, 1993. 0-12-349670-5.
234. *Growth Mode During Initial Stages of Chemical Vapour Deposition.* **Kajikawa, Y and Noda, S.** 1-4, Pages 281-289, s.l. : Applied Surface Science, 2005, Vol. 245. 0169-4332.
235. **Matacotta, F, Ottaviani, G.** *Science and Technology of Thin Films.* s.l. : World Scientific, 1995. 9810221932.
236. **Grundy, B, Hargreaves, E.** *Process for Coating Glass (Pilkington plc).* 5041150 / C03C 2502 United States of America, 20 August 1991. Engineering.
237. *Some Properties of Boundary Layer Flow During the Transition from Laminar to Turbulent Motion.* **Dhawan, S, Narasimha, R.** 4, s.l. : Journal of Fluid Mechanics, 1957, Vol. 3. 0022-1120.
238. **Spurk, J, Aksel, N.** *Fluid Mechanics.* s.l. : Springer, 2008. 978-3540735366.
239. **Lewis, B, Anderson, J.** *Nucleation and Growth of Thin Films.* s.l. : Academic Press Inc , 1978. 0-12-446680-X.
240. **Maruimumi, T, Ushio, J, Takemura, Y, Kobayashi, N.** Sticking Coefficients in Film Profile Prediction For Chemical Vapor Deposition. [book auth.] M, Bernard, C Allendorf. *Chemical Vapor Deposition: Proceedings of the Fourteenth International Conference and EuroCVD 11.* 9781566771788 : Electrochemical Society Proceedings Volume 97-25, 1997.
241. *Nucleation and Growth of Thin Films.* **Venables, J, A, Spiller, G, D, T, Hanbucken, M.** 4, s.l. : Reports on Progress in Physics, 1984, Vol. 47. 1361-6633.
242. **Park, J, Sudarshan, T.** *Chemical Vapor Deposition.* s.l. : ASM International, 2001. 9780871707314.
243. **Fridman, A.** *Plasma Chemistry.* s.l. : Cambridge University Press, 2008. 9781139471732.
244. **Lieberman, M A and Lichtenberg, A J.** *Principle of Plasma Discharges and Materials Processing.* New Jersey : John Wiley & Sons, 2005. 0-471-72001-1.
245. *Atmospheric Pressure Plasmas: A Review.* **Tendero, C, et al., et al.** 1, p.p. 2-30, s.l. : Spectrochimica Acta Part B Atomic Spectroscopy, 2006, Spectrochimica ACT A Part B, Vol. 61, pp. 2-30. 05848547.
246. **Hitchon, W.** *Plasma Processes for Semiconductor Fabrication.* Cambridge : Cambridge University Press, 1999. 13 978-0-521-59175-1.

247. **Fridman, A and Kennedy, L A.** *Plasma Physics and Engineering*. s.l. : Taylor & Francis Routledge, 2004. 1560328487.
248. *Plasma Processes at Atmospheric and Low Pressures.* **Bárdos, L and Baránková, H.** 3, Pages: 522-527, s.l. : Vacuum - Elsevier, 2009, Vol. 83. 0042-207X.
249. **Smirnov, B.** *Plasma Processes and Plasma Kinetics*. s.l. : Wiley & Co, 2007. 978-3-527-40681-4.
250. *Atmospheric Non-Thermal Plasma Sources.* **Nehra, V, Kumar, A, Dwivedi, H.** 1, s.l. : International Journal of Engineering, 2008, Vol. 2. 1025-2495.
251. *Validity of Local Thermal Equilibrium in Plasma Spectroscopy.* **Griem, H.** 3, s.l. : Physical Review, 1963, Vol. 131. 10.1103/PhysRev.131.1170.
252. *Excitation Kinetic in an Argon Plasma Column Produced by a Surface Wave at Atmospheric Pressure.* **Calzada, M, Rodero, A, Sola, A, Gamero, A.** 4, s.l. : Journal of the Physical Society of Japan, 1995, Vol. 65. 1347-4073.
253. *Gomes, A.* **Pressure, Criteria for Partial LTE in an Argon Thermal Discharge at Atmospheric and Temperature, Validity of the Spectroscopically Measured Electronic.** Pages 357-378, s.l. : Journal of Applied Physics D, 1982, Vol. 16. 1361-6463.
254. *Non-thermal Atmospheric Pressure Discharges.* **Fridman, A, Chirokov, A, Gutso, A.** Pages R1 - R24, s.l. : Journal of Applied Physics D, 2004, Vol. 38. 0022-3727.
255. *Modelling of Dielectric Barrier Discharge Chemistry.* **Eliasson, B, Egli, W, Kogelschatz, U.** 6, s.l. : Pure & Applied Chemistry, 1994, Vol. 66. 1365-3075.
256. *Atmospheric Pressure Plasma of Dielectric Barrier Discharges.* **Chirokov, A, Gutsol, A, Fridman, A.** 2, s.l. : Pure & Applied Chemistry, 2005, Vol. 77. 1365-3075.
257. *Dielectric Barrier Discharge: Their History, Discharge Physics and Industrial Applications.* **Kogelschatz, U.** 1, s.l. : Plasma Chemistry and Plasma Processing, 2003, Vol. 23. 0272-4324.
258. *Fundamentals and Applications of Dielectric Barrier Discharges.* **Kogelschatz, U.** Greifswald : HAKONE VII Int. Symp. On High Pressure Low Temperature Plasma Chemistry, 2000.
259. *Electrical Characterization of Microdischarges Produced by Dielectric Barrier Discharge in Dry Air at Atmospheric Pressure.* **Jidenko, N, Petit, M, Borra, J.** Pages 281-293, s.l. : Journal of Applied Physics D, 2006, Vol. 39. 0022-3727.

260. *Plasma Generation and Plasma Sources*. **Conrads, H, Schmidt, M.** 4, s.l. : Plasma Sources Science and Technology, 2000, Vol. 9. 0963-0252.
261. *Dielectric Barrier Discharge - Properties and Applications*. **Xu, X.** Pages 237-242, s.l. : Thin Solid Films, 2001, Vol. 390. 0040-6090.
262. *Atmospheric Pressure Dielectric Barrier Discharge Chemical and Biological Applications*. **Morgan, N.** 13, s.l. : International Journal of Physical Sciences, 2009, Vol. 4. 1992 - 1950.
263. *Dielectric Barrier Discharges. Principles and Applications*. **Kogelschatz, U, Eliasson, B, Egli, W.** C4, s.l. : Journal de Physique IV, 1997, Vol. 7. 1155-4339.
264. *Physics and Chemistry in a Glow Dielectric Barrier Discharge at Atmospheric Pressure : Diagnostics and Modelling*. **Massines, F, Segur, P, Gherardi, N, Khamphan, C, Ricard, A.** Pages 8-14, s.l. : Surface and Coatings Technology, 2003, Vols. 174-175. 0257-8972.
265. *The Barrier Discharge: Basic Properties and Applications to Surface Treatment*. **Wagner, H, Brandenburg, R, Kozlov, K, Sonnenfeld, A, Michel, P, Behnke, J.** Pages 417-436, s.l. : Vacuum, 2003, Vol. 71. 0042-207X.
266. **Donohoe, K.** *PhD thesis*. Pasadena : California Institute of Technology, 1976.
267. *Stable Glow Plasma at Atmospheric Pressure*. **Kanazawa, S, Kogoma, M, Moriwaki, T, Okazaki, S.** Pages 838-840, s.l. : Journal of Applied Physics D, 1988, Vol. 21. 0022-3727.
268. *Appearance of Stable Glow Discharge in Air, Argon, Oxygen and Nitrogen at Atmospheric Pressure using a 50Hz Source*. **Okazaki, S, Kogoma, M, Uehara, M, Kimura, Y.** Pages 889, s.l. : Journal of Applied Physics D, 1993, Vol. 26. 0022-3727.
269. *Transition from Glow Silent Discharge to Micro-discharge in Nitrogen Gas*. **Gherardi, N, Gouda, G, Gat, E, Ricard, A, Massines, F.** Pages 340-346, s.l. : Plasma Sources Science and Technology, 2000, Vol. 9. 0963-0252.
270. *Glow and Townsend Dielectric Barrier Discharge in Various Atmosphere*. **Massines, F, Gherardi, N, Naude, N, Segur, P.** Pages B577 - B588, s.l. : Plasma Physics and Controlled Fusion, 2005, Vol. 47. 0741-3335.
271. **Nonogaki, S, Ueno, T, Ito T.** *Microlithography Fundamentals in Semiconductor Devices and Fabrication Technology*. s.l. : Dekker, 1998. 0-8247-9951-8.
272. **Yoo, C.** *Semiconductor Manufacturing Technology*. s.l. : World Scientific, 2008. 981-256-823-9.

273. **Mack, C.** *Fundamental Principles of Optical Lithography : The Science of Microfabrication.* s.l. : Wiley, 2007. 978-0-470-01893-4.
274. **Pouch, J, Alterovitz, S.** *Plasma Properties, Deposition and Etching.* s.l. : Trans Tech Publications, 1993. 0-87849-670-x.
275. **Rossnagel, S, Cuomo, J, Westwood, W.** *Handbook of Plasma Processing Technology : Fundamentals, Etching, Deposition, Surface Interactions.* s.l. : Noyes Publications, 1993. 0-8155-1220-1.
276. **Rai-Choudhury, P.** *Handbook of Microlithography, Micromachining and Microfabrication.* s.l. : SPIE Press, 1999. 978-0819423788.
277. **Chapman, B.** *Glow Discharge Processes.* 1980 : John Wiley & Sons. 0-471-07828-X.
278. **Abhulimen, I.** *Characterization of Deep Reactive Ion Etching (DRIE) for Via Formation in Chip Stacking Applications.* s.l. : ProQuest, 2011. 978-1243516701.
279. *Advanced Etching of Silicon Based on Deep Reactive Ion Etching for Silicon High Aspect Ratio Microstructures and Three-Dimensional Micro and Nano Structures.* **Marty, F, Rousseau, L, Saadany, B, Mercier, B, Francais, O, Mita, Y, Bourouina, T.** Pages 673-677, s.l. : Microelectronics Journal, 2005, Vol. 36. 0026-2692.
280. *High-Aspect-Ratio Micromachining Via Deep X-Ray Lithography.* **Guckel, H.** 8, s.l. : Proceedings of the IEEE, 1998, Vol. 86. 0018-9219.
281. *An Advanced Reactive Ion Etching Process for Very High Aspect Ratio Sub Micron Wide Trenches in Silicon.* **Abdolvand, R, Ayazi, F.** Pages 109-116, s.l. : Sensors and Actuators A, 2008, Vol. 144. 0924-4247.
282. *Microelectromechanical Systems (MEMS) : Fabrication, Design and Applications.* **Judy, J.** Pages 1115-1134, s.l. : Smart Materials and Structures, 2001, Vol. 10. 0964-1726.
283. *Comparison of Bosch and Cryogenic Processes for Patterning High Aspect Ratio Features in Silicon.* **Walker, M.** Pages 89-99, s.l. : Proceedings of SPIE, 2001, Vol. 4407. 0277-786X.
284. **Hunsperger, R.** *Integrated Optics : Theory and Technology.* s.l. : Springer, 2009. 0387897747.
285. *Low Temperature Reactive Ion Etching and Microwave Plasma Etching of Silicon.* 8, s.l. : Applied Physics Letters, 1988, Vol. 52. 1077-3118.

286. *Guidelines for Etching Silicon MEMS Structures Using Fluorine High-Density Plasmas at Cryogenic Temperatures*. **Boer, M, Gardeniers, J, Jansen, H, Smulders, E, Gilde, M, Roelofs, G, Sasserath, J, Elwenspoek, M.** 4, s.l. : Journal of Microelectromechanical Systems, 2002, Vol. 11. 1057-7157.
287. *SiO_xF_y Passivation Layer in Silicon Cryoetching*. **Mellhaoui, X, Dussart, R, Tiloche, T, Lefaucheu, P, Ranson, P.** s.l. : Journal of Applied Physics, 2005, Vol. 98. 0021-8979.
288. *Bosch Deep Silicon Etching : Improving Uniformity and Etching Rate for Advanced MEMS Applications*. **Laermer, F.** s.l. : Micro Electro Mechanical Systems 12th International Conference IEEE, 17-21 Jan 1999. 0-7803-5194-0.
289. *Balancing the Etching and Passivation in Time-Multiplexed Deep Dry Etching of Silicon*. **Blauw, M, Zijlstra, T, Drift, E.** 6, s.l. : Journal of Vacuum Science & Technology B: Microelectronics and Nanometer Structures, 2001, Vol. 19. 1071-1023.
290. **Mahan, J.** *Physical Vapor Deposition of Thin Films*. s.l. : John Wiley & Sons, 2000. 0-471-33001-9.
291. *Surface Treatment of Aramid Fiber by Air Dielectric Barrier Discharge Plasma At Atmospheric Pressure*. **Jia, C, Chen, P, Liu, W, Li, B, Wan, Q.** Pages 4165-4170, s.l. : Applied Surface Science, 2011, Vol. 257. 0169-4332.
292. *Atmospheric Pressure Gas Discharges for Surface Treatment*. **Pochner, K, Neff, W, Lebert, R.** Pages 394-398, s.l. : Surface Coatings and Technology, 1995, Vols. 74-75. 0257-8972.
293. *The Dry Etching Properties of ZnO Thin Film in Cl₂/Cl₃/Ar Plasma*. **Woo, J, Kim, C.** 3, s.l. : Transaction on Electrical and Electronic Materials, 2010, Vol. 11. 1229-7607.
294. *Inductively Coupled Plasma Dry Etching of a ZnO Thin Film by Ar Diluted CF₄ Gas*. **Kim, D, Hwang, I, Son, J, Kim, H.** 5, s.l. : Journal of the Korean Physical Society, 2011, Vol. 58. 1976-8524.
295. **Shul, R, Pearton, S.** *Handbook of Advanced Plasma Processing Techniques*. s.l. : Springer, 2000. 3540667725.
296. **Manos, D, Flamm, D.** *Plasma Etching : An Introduction*. s.l. : Academic Press Inc, 1989. 0124693709.
297. **Kaupp, G.** *Atomic Force Microscopy, Scanning Nearfield Optical Microscopy and Nanoscratching*. s.l. : Springer, 2006. 3-540-28405-2.

298. **Haugstad, G.** *Atomic Force Microscopy : Understanding Basic Modes and Advanced Applications*. s.l. : John Wiley, 2012. 978-0-470-63882-8.
299. *Atomic Force Microscope*. **Binnig, G, Quate, C, Gerber, C.** 9, s.l. : Physical Review Letters, 1986, Vol. 56. 1079-7114.
300. **Wilson, R and Bullen, H.** Introduction to Scanning Probe Microscopy - Basic Theory AFM. *Analytical Sciences Digital Library*. [Online] University of Kentucky, 2010. [Cited: 15th June 2010.] http://asdl.org/onlineArticles/ecourseware/Bullen/SPMModule_BasicTheoryAFM.pdf.
301. *Atomic Force Microscopy*. **Blanchard, C.** 5, New York : The Chemical Educator, 1996, Vol. 1. 1430-4170.
302. **Botello, Eric.** *Atomic Force Microscopy - A Guide to Understanding and Using the AFM*. Texas : Galloway Group, 2004.
303. **Morita, S, Giessibl, F, Wiesendanger, R.** *Noncontact Atomic Force Microscopy*. s.l. : Springer, 2009. 978-3-642-01494-9.
304. **De Oliveira, R, Albuquerque, D, Cruz, T, Yamaji, F, Leite, F.** *Measurement of the Nanoscale Roughness by Atomic Force Microscopy: Basic Principles and Applications, Atomic Force Microscopy - Imaging, Measureing and Manipulating Surfaces at the Atomic Scale*. s.l. : InTech, 2012. 978-953-51-0414-8.
305. *Roughness Parameters*. **Gadelmawla, E, Koura, M, Maksoud, T, Elewa, I, Soliman, H.** 1, s.l. : Journal of Materials Processing Technology, 2002, Vol. 123. 0924-0136.
306. **Reimer, L.** *Scanning Electron Microscopy : Physics of Image Formation and Microanalysis (Second Edition)*. s.l. : Springer, 1998. 3-540-63976-4.
307. **Khursheed, A.** *Scanning Electron Microscope Optics and Spectrometers*. s.l. : World Scientific Publishing Co. , 2011. 981-283-667-5.
308. **Egerton, R.** *Physical Principles of Electron Microscopy : An Introduction to TEM, SEM and AEM*. s.l. : Springer, 2005. 0-387-25800-0.
309. *Scanning Electron Microscopy for Material Characterization*. **Joy, D C.** 4, Pages: 465-468, University of Tennessee, Knoxville : Current Opinion in Solid State and Materials Science, 1997, Vol. 2. 13590286.
310. **Eisberg, R, Resnick, R.** *Quantum Physics of Atoms, Molecules, Solids, Nuclei and Particles*. s.l. : Wiley, 1985. 047187373X.

311. **Hawkes, P, Kasper, E.** *Principles of Electron Optics : Basic Geometric Optics Vol 1.* s.l. : Academic Press, 1996. 978-0123333414.
312. **Ekspång, Gösta.** Nobel Prize in Physics 1986. *Nobelprize.org.* [Online] Nobel Media. [Cited: 2012 11 29.] http://www.nobelprize.org/nobel_prizes/physics/laureates/1986/ruska-autobio.html.
313. **Williams, D, Carter, C.** *Transmission Electron Microscopy (Second Edition).* s.l. : Springer, 2009. 978-0-387-76500-6.
314. **Goodhew, P, Humphreys, F, Beanland, R.** *Electron Microscopy and Analysis (Third Edition).* s.l. : Taylor & Francis, 2000. 978-0748409686.
315. **Ramsden, E.** *Hall Effect Sensors : Theory & Application.* s.l. : Newnes, 2006. 978-0750679343.
316. **Popovic, R.** *Hall Effect Devices : Magnetic Sensors and Charactization of Semiconductors.* s.l. : Taylor & Francis, 2004. 978-0750308557.
317. **Czichos, H.** *Springer Handbook of Metrology and Testing.* s.l. : Springer, 2011. 978-3642166402.
318. *A Method of Measuring the Resistivity and Hall Coefficient on Lamellae of Arbitrary Shapes.* **Pauw, L.J Van Der.** 8, Pages: 220-224, s.l. : Philips Technical Review, 1958, Vol. 20.
319. **Nalwa, H, S.** *Handbook of Thin Films.* s.l. : Academic Press Inc, 2001. 978-0125129084.
320. **Schroder, D, K.** *Semiconductor Material and Device Characterization.* s.l. : John Wiley & Sons, 2006. 978-0-471-74908-0.
321. National Institute of Standards and Technology (NIST) - Semiconductors & Hall Effect. *National Institute of Standards and Technology (NIST).* [Online] U.S. Commerce Department, 17 March 2010. [Cited: 18 October 2010.] <http://www.nist.gov/pml/semiconductor/hall.cfm>.
322. **Saniee, Nessa Fereshteh.** Warwick Univeristy - Hall Effect. *Warwick Univeristy.* [Online] 3 December 2009. [Cited: 2010 October 18.] <http://www2.warwick.ac.uk/fac/sci/physics/postgraduate/current/regs/mpags/ex5/techniques/electronic/hall-effect/>.
323. **Lake Shore Cryotronics, Inc.** Hall Effect Measurements - Appendix A. [book auth.] Lake Shore. *Lake Shore 7500/9500 Series Hall System User's Manual.* 2002.

324. *Hall Effect Measurement Techniques in Metallic Thin Films*. **Palevski, A.** 12, Pages: 1155-1156, Tel Aviv : Journal of Physics E Scientific Instruments, 1983, Vol. 16.
325. **Stenzel, O.** *The Physics of Thin Film Optical Spectra: An Introduction*. s.l. : Springer, 2005. 978-3540231479 .
326. **Cao, G.** *Nanostructures and Nanomaterials : Synthesis, Properties & Applications*. s.l. : Imperial College Press, 2004. 978-1860944802.
327. **Birkholz, M.** *Thin Film Analysis by X-ray Scattering*. s.l. : Wiley, 2005. 978-3-527-31052-4.
328. **Freund, L, B, Suresh, S.** *Thin Film Materials: Stress, Defect, Formation and Surface Evolution*. s.l. : Cambridge University Press, 2004. 978-0521822817.
329. **Tilley, R, J, D.** *Understanding Solid : The Science of Materials*. s.l. : John Wiley & Sons, 2005. 9780470026465.
330. **Aslanov, L, A, Fetisov, G, V, Howard, J, A, K.** *Crystallographic Instrumentation*. s.l. : Oxford Scientific Publication, 1998. 978-0198559276.
331. **Hosokawa, M, Nogi, K, Naito, M, Yokoyama, T.** *Nanoparticle Technology Handbook*. s.l. : Elsevier, 2007. 9780444531223.
332. **Aslanov, L, A, Fetisov, G, V, Howard, J, A, K.** *Crystallographic Instrumentation*. s.l. : Oxford University Press, 1998. 9780198559276.
333. *A Scalable Approach to Provide Diffuse Nitrogen Discharge Atmospheric Pressure for Large Area Processing*. **Hodgkinson, J, L, Murray, J, G, Sheel, D, W.** s.l. : PENDING PUBLICATION, 2013.
334. *Non-Thermal Atmospheric Pressure Plasma Etching of F:SnO₂ for Thin Film Photovoltaics*. **Hodgkinson, J, Thomson, M, Cook, I, Sheel D.** s.l. : Journal of Nanoscience and Nanotechnology, 2011, Vol. 11. 8403–8407.
335. *Surface Nanostructuring Via Combined All Atmospheric Pressure Processing, COating, Patterning and Etching*. **Cook, I, Sheel, D, Hodgkinson, J.** 2, s.l. : Surface and Coating Technology, 2011, Vol. 205. 0257-8972.
336. *Control of Zinc Oxide Surface Structure Using Combined Atmospheric Pressure Based CVD Growth and Plasma Etching*. **Thomson, M, Hodgkinson, J, Sheel, D.** s.l. : Surface Coating and Technology, 2013, Vol. Pending Publication. 0257-8972.

337. *Surface Recombination, Surface States and Fermi Level Pinning*. **Moison, J, M, Bensoussan, M.** 5, s.l. : Revue de Physique, 1987, Vol. 22. 0035-1687.
338. *Comparative Study of Diethylzinc and Dimethylzinc for the Growth of ZnO*. **Ye, J, Gu, S, Zhu, S, Liu, S, Liu, W, Zhou, X, Hu, L, Zhang, R, Shi, Y, Zheng, Y.** s.l. : Journal of Crystal Growth, 2005, Vol. 274. 0022-0248.
339. *Abundant Non-Toxic Materials for Thin Film Solar Cells : Alternative to Conventional Materials*. **Alharbi, F, Bass, J, Salhi, A, Alyamani, A, Kim, H, Miller, R.** s.l. : Renewable Energy, 2011, Vol. 36. 0960-1481.
340. *Recent Developments of Silicon Thin Film Solar Cells on Glass Substrates*. **Beneking, C, Rech, B, Wieder, S, Kluth, O, Wagner, H, Frammelsberger, W, Geyer, R, Lechner, P, Rubel, H, Schade, H.** s.l. : Thin Solid Films, 1999, Vol. 351. 0040-6090.
341. *Introduction to Gas Discharges*. **Braithwaite, N.** s.l. : Plasma Sources Science and Technology, 2000, Vol. 9. 0963-0252.
342. *Optical Properties of Silicon-Based Thin-Film Solar Cells in Substrate and Superstrate Configuration*. **Brammer, T, Reetz, W, Senoussaoui, O, Vetterl, O, Kluth, O, Rech, B, Stiebig, H, Wagner, H.** s.l. : Solar Energy Materials and Solar Cells, 2002, Vol. 74. 0927-0248.
343. *A Review of Solar Photovoltaic Levelized Cost of Electricity*. **Branker, K, Pathak, M, Pearce, J.** s.l. : Renewable and Sustainable Energy Reviews, 2011, Vol. 15. 1364-0321.
344. *Widely Transparent Electrodes Based on Ultrathin Metals*. **Ghosh, D, Martinez, L, Giurgola, S, Vergani, P, Pruneri, V.** 3, s.l. : Optics Letters, 2009, Vol. 34. 0146-9592.
345. *Solar Cell Efficiency Measurements*. **Emery, K, Osterwald, C.** s.l. : Solar Cells, 1986, Vol. 17. 0379-6787.
346. *Etching Materials With an Atmospheric-Pressure Plasma Jet*. **Jeong, J, Babayan, S, Tu, V, Park, J, Henins, I, Hicks, R, Selwyn, G.** s.l. : Plasma Sources Science and Technology, 1998, Vol. 7. 0963-0252.
347. *Annealing Effect for Structural Morphology of ZnO Film on SiO₂ Substrates*. **Kim, H, Kim, N.** s.l. : Materials Science in Semiconductor Processing, 2004, Vol. 7. 1369-8001.
348. *Dry Etching of ZnO Using an Inductively Coupled Plasma*. **Lee, J, Chang, K, Kim, K, Choi, W, Park, S.** s.l. : Journal of The Electrochemical Society, 2001, Vol. 148. 0013-4651.
349. *Recent Advances in ZnO Materials and Devices*. **Look, D.** s.l. : Materials Science and Engineering, 2001, Vol. 80. 0921-5107.

350. *Electrical and Optical Properties of Defects and Impurities in ZnO*. **Look, D, Coskun, C, Claflin, B, Farlow, G.** s.l. : Physica B, 2003, Vols. 340-342. 0921-4526.
351. *A Simple and Effective Light Trapping Technique for Polycrystalline Silicon Solar Cells*. **Willeke, G, Nussbaumer, H, Bender, H, Bucher, E.** s.l. : Solar Energy Materials and Solar Cells, 1992, Vol. 26. 0927-0248.
352. *Nucleation Theory and the Early Stages of Thin Film Growth*. **Ratsch, C, Venables, J.,** 5, s.l. : Journal of Vacuum Science and Technology, 2003, Vol. 21. 0734-2101.
353. *Study of (100) Orientated ZnO Films by APCVD Systems*. **Pacio, M, Juarez, H, Escalante, G, Garcia, G, Diaz, T, Rosendo, E.** s.l. : Materials Science and Engineering B, 2010, Vols. 1-3. 0921-5107.
354. *Impact of Transparent Conductive Oxide on the Admittance of Thin Solar Cells*. **Principato, F, Cannella, G, Lombardo, S, Foti, M.** s.l. : Solid-State Electronics, 2010, Vol. 54. 0038-1101.
355. *Transparent Electrode Requirements for Thin Film Solar Cell Modules*. **Rowell, M, McGehee, M.** pp. 131-134, s.l. : Energy & Environmental Science, 2011, Vol. 4. 1754-5706.
356. *ZnO Transparent Conductive Oxide for Thin Film Silicon Solar Cells*. **Soderstrom, T, Domine, D, Feltrin, A, Despeisse, M, Meillaud, F, Bugnon, G, Boccard, M, Cuony, P, Haug, F, Nicolay, S, Ballif, C.** s.l. : Proceedings of SPIE, 2010, Vol. 7603. 1996-756X.
357. *Atmospheric Pressure Chemical Vapour Deposition of F Doped SnO₂ for Optimum Performance Solar Cells*. **Sheel, D, Yates, H, Evans, P, Dagkaldiran, U, Gordijn, A, Finger, F, Remes, Z, Vanecek, M.,** s.l. : Thin Solid Films, 2009, Vol. 517. 0040-6090.
358. *The Transition from a Filamentary Dielectric Barrier Discharge to a Diffuse Barrier Discharge in Air at Atmospheric Pressure*. **Rahel, J, Sherman, D.** s.l. : Journal of Applied Physics D, 2005, Vol. 38. 0022-3727.
359. *The Effect of Air Plasma on Barrier Dielectric Surface in Dielectric Barrier Discharge*. **Wang, C, Zhang, G, Wang, X, He, X.** s.l. : Applied Surface Science, 2010, Vol. 257. 0169-4332.
360. *Comparison of Photovoltaic Module Performance Measurements*. **Fanney, A, Davis, M, Dougherty, B, Kinig, D, Boyson, W, Kratochvil, J.** 2, s.l. : Journal of Solar Energy Engineering, 2006, Vol. 128. 01996231.
361. *Resistivity of Polycrystalline Zinc Oxide Films : Current Status and Physical Limit*. **Ellmer, K.** s.l. : Institute of Physics Publishing D: Applied Physics, 2001, Vol. 34.

362. **Lin, R.** Distributed Energy Production and The DIY Movement. *altenergymag.com*. [Online] LJB Management Inc. [Cited: 12 16 2010.] http://www.altenergymag.com/emagazine.php?art_id=1473.
363. **Cave, A.** Nuclear Industry Demands Green Subsidies Too. *The Sunday Telegraph*. [Online] 10 July 2010. [Cited: 2010 12 16.] <http://www.telegraph.co.uk/finance/newsbysector/energy/7883357/Nuclear-targets-at-risk.html>.
364. **British Government, Energy Saving Trust.** Energy Saving Trust. *Energy Saving Trust*. [Online] 2010. [Cited: 25th July 2010.] <http://www.energysavingtrust.org.uk/>.
365. *Amorphous Silicon Solar Cells Made with SnO₂:F TCO Films deposited by Atmospheric Pressure CVD.* **Dagkaldiran, Ü, et al., et al.** Pages 6-9, Salford : Material Science and Engineering B, 2009, Vols. 159-160. 0921-5107.
366. **Electric Power Research Institute, EPRI.** *Solar Photovoltaics : Expanding Electric Generation Options*. California : Electric Power Research Institute (EPRI), Inc., 2007. 1016279.
367. **Landsberg, P.** *Theoretical Limits of Solar Energy Conversion*. Southampton : World Climate & Energy Event, 2002.
368. **Elshabini-Riad, A and Barlow, F D.** *Thin Film Technology Handbook*. s.l. : McGraw-Hill Professional, 1997. 0-07-019025-9.
369. *Multiscale Modeling of CVD Film Growth - A Review of Recent Works.* **Dollet, A.** Pages 245-251, s.l. : Surface and Coatings Technology, 2004, Vols. 177-178. 0257-8972.
370. **Surface Engineering Coating Association.** Physical Vapour Deposition of Thin Film Hard Wear Resistant Coatings. *SECA - Surface Engineering Coating Association*. [Online] [Cited: 15 August 2010.] <http://www.surfaceengineering.org/pdf/pvd.pdf>.
371. **AZo Journal of Materials Online.** Physical Vapour Deposition (PVD) – An Introduction. *AZo Journal of Materials Online*. [Online] AZoM™, 2002 August 2002. [Cited: 15 July 2010.] <http://www.azom.com/details.asp?ArticleID=1558>.
372. *Magnetron Sputtering.* **Swann, S.** 2, Pages: 67-75, s.l. : Physics in Technology, 1988, Vol. 19. 03054624.
373. **Tarrant, R.** The Scanning Electron Microscope. *University of Sydney*. [Online] University of Sydney, 2010. [Cited: 15th June 2010.] http://www.physics.usyd.edu.au/pdfs/current/sphys/3yr_lab/Expt_31.pdf.

374. **Smits, F.** Measurements of Sheet Resistivity with the Four Point Probe. *Four Point Probes*. [Online] Bridge Technology, 1957. <http://www.fourpointprobes.com/smits.pdf>.
375. *Resistivity Measurements on Germanium for Transistors*. **Valdes, L. B.** 2, Pages: 420-427, s.l. : Proceedings of the IRE, February 1954, Vol. 42. 0096-8390.
376. **Lark-Horowitz, K and Johnson, V A.** *Solid state physics: Electrical, magnetic and optical properties*. New York : Methods in Experimental Physics, 1959. Vol. 6. 0124759467, 9780124759466.
377. **O'Hanlon, J F.** *A User's Guide to Vacuum Technology - Third Edition*. s.l. : Wiley-Blackwell; 3rd Edition edition, 2003. 0471270520.
378. **Steiner, T D.** *Semiconductor nanostructures for optoelectronic applications*. s.l. : Artech House, 2004. 1-58053-751-0.
379. **Ledentsov, N N.** *Growth Processes and Surface Phase Equilibria in Molecular Beam Epitaxy*. s.l. : Springer, 1999. 3-540-65794-0.
380. **International Conference on Metallurgical Coatings, and Thin Films.** Review of TCO Thin Films. Singapore : International Conference on Metallurgical Coatings and Thin Films, 2008.
381. **Robertson, J, Falabretti.** *Handbook of Transparent Conductors*.
382. **Sakka, S.** *Sol-Gel Science and Technology : Processing Characterization and Applications*. s.l. : Springer, 2005. 1402079699.
383. *Plasma Processes at Atmospheric and Low Pressures*. **Bárdos, L, Baránková, H.** 3, Pages: 522-527, s.l. : Vacuum - Elsevier, 2009, Vol. 83. 0042-207X.
384. *The Development of Dielectric Barrier Discharges in Gas Gaps and on Surfaces*. **Gibalov, V, Pietsch, G.** Pages 2618-2636, s.l. : Journal of Applied Physics D, 2000, Vol. 33. 0022-3727.
385. **Bhushan, B.** *Springer Handbook of Nanotechnology*. s.l. : Springer, 2007. 9783540012184.
386. **Beneq.** Aerosol Coating. *Beneq*. [Online] 2010. [Cited: 2011 06 28.] <http://www.beneq.com/aerosol-coating.html>.
387. **Wasa, K, Kitabatake, M, Adachi, H.** *Thin Film Materials Technology : Sputtering of Compound Materials*. s.l. : William Andrew, 2004. 9780080946986.

388. **Mattox, D.** *Handbook of Physical Vapor Deposition (PVD) Processing*. s.l. : William Andrew, 2010. 9780080951959.
389. **Farrow, R.** *Molecular Beam Epitaxy : Applications to Key Materials*. s.l. : William Andrew, 2012. 9780080946115.
390. **Guo, Z, Tan, L.** *Fundamentals and Applications of Nanomaterials*. s.l. : Artech House, 2009. 9781596932630.
391. **Davis, J.** *Handbook of Thermal Spray Technology*. s.l. : ASM International, 2004. 9780871707956.
392. **Brinker, C, Scherer, G.** *Sol-Gel Science: The Physics and Chemistry of Sol-Gel Processing*. s.l. : Gulf Professional Publishing, 1990. 9780121349707.

11 – Appendix

11.1 Published Papers



Control of zinc oxide surface structure using combined atmospheric pressure-based CVD growth and plasma etching

M. Thomson ^{*}, J.L. Hodgkinson, D.W. Sheel

Materials and Physics Research Center, University of Salford, Computing Science and Engineering, Salford, UK

ARTICLE INFO

Available online 14 June 2013

Keywords:

Atmospheric plasma etching
Zinc oxide (ZnO)
CVD
Low temperature
Surface texture control

ABSTRACT

In photovoltaic thin film cells, a transparent conducting oxide (TCO) layer is required to transport current. The most common TCOs used are F:SnO₂ (fluorine doped tin oxide), ZnO (zinc oxide) and ITO (indium doped tin oxide). ZnO is normally deposited in a vacuum-based process, sputtering or low pressure chemical vapour deposition (LPCVD). Atmospheric pressure chemical vapour deposition (APCVD) is an attractive alternative for ZnO deposition. A critical parameter for TCOs in photovoltaic thin films is the surface morphology, which defines the optical scattering properties. The ability to control the spectral sensitivity and the degree of scattering are both important process parameters for high performance cells.

In this work, we employ APCVD for film growth and study the effects of atmospheric pressure plasma etching of ZnO. The ZnO films were deposited onto glass, with the surface morphology analyzed by AFM. Optical assessment was conducted using custom built equipment. Modification of the surface morphology was achieved by atmospheric pressure plasma, based on a dielectric barrier discharge configuration. In this study, we explored the effects of etching conditions, particularly the variation of feed gas composition (N₂, O₂ and H₂O).

By controlling the treatment environment, we were able to establish a relationship between the feed gas mixture and the etchant rate. Careful selection and control of processing parameters demonstrated the ability to modify the morphology with a high degree of uniformity and enhance the optical scatter properties. Atmospheric pressure-based processes are attractive for scalable production development, and future work will explore the potential of this process for large scale application.

© 2013 Elsevier B.V. All rights reserved.

1. Introduction

ZnO has received considerable interest in recent years for the next generation of transparent conducting oxide (TCO) film implementation for solar cell fabrication. ZnO is natively a semiconducting material possessing a wide energy band gap of 3.3 eV, exhibiting transparency in the visible spectrum with low reflectance in the infra-red and low conductivity [1–3]. Implementation as a TCO requires extrinsic dopants to be introduced which are typically fluorine, aluminium, boron and gallium resulting in a highly conductive non-stoichiometric material [1,4]. Critically, it is important to select the dopant material carefully for the intended application to ensure high levels of conductivity while maintaining optical performance [5–7].

In most thin film solar cell configurations, a TCO layer is required, and the surface structure of this layer may radically influence the ultimate cell performance. Amorphous silicon cells can benefit between 10% to 20% difference in final cell efficiency depending on TCO properties [3,8]. One way to enhance efficiency is to maximize light trapping by increasing optical scatter across the wavelength range by using a textured TCO, with pyramidal structures proposed to give high scatter

[6,9,10]. A drawback of this topography is that sharp features in the peaks and troughs can cause defects in subsequent layers of the fabrication process. This may lead to voltage (Voc) loss across the cell, which is often indicated by reduced shunt resistance [11,12]. Currently, a shift for desired morphology has changed from a rough and rounded pyramidal structure towards large crater like structures [13]. This is essentially broadening of the pyramidal structure to obtain the desired optical properties [14]. Typically this structure is achieved through post-wet etching the smooth deposited material in HCl [9,15].

Post-growth treatments have been widely adopted to optimize the surface structure of deposited films, typically involving vacuum processing or additional process steps (off-line) of wet chemistry [15–17]. Production methods involving these systems impose additional costs and process steps. The utilization of a low-cost manufacturing process is vital to reduce cost of ownership. In this work, we report a dry post-growth process treatment using the afterglow from low temperature atmospheric pressure plasma produced from a dielectric barrier discharge.

Plasma etching systems have been traditionally employed in microelectronic manufacturing [16,18]. These systems typically operate under vacuum conditions to maintain the high degree purity during the process, avoiding the possibilities of contamination that would destroy component characteristics. Vacuum-based plasma etching

^{*} Corresponding author. Tel.: +44 161 295 4800.

E-mail address: m.thomson@edu.salford.ac.uk (M. Thomson).

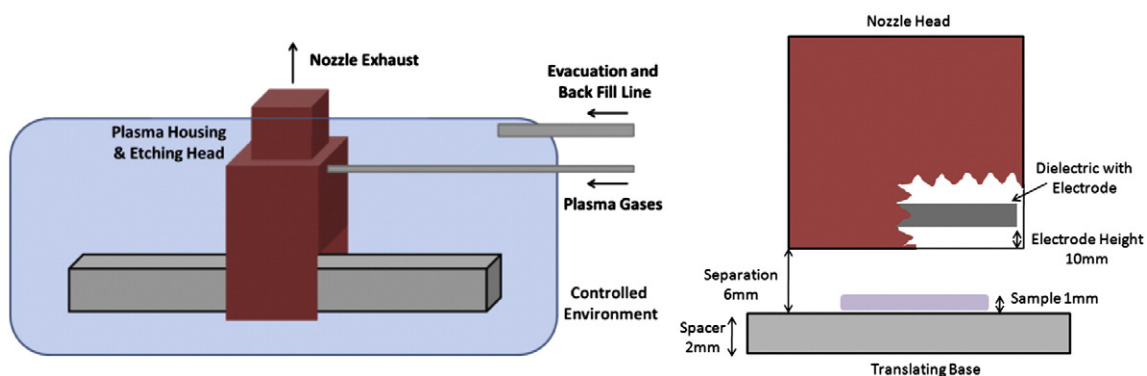


Fig. 1. Plasma nozzle housed in nitrogen environment and schematic.

processes have seen significant research due to the industries reliance on the technique to manufacture smaller components. In this application, plasma processes have rendered traditional wet chemical processing as less attractive, as it can often no longer satisfy the criteria for reduced components sizes and contamination free production [18,19].

Atmospheric pressure chemical vapour deposition (APCVD) is highly suited to the cost effective, continuous production of TCOs on large area substrates such as glass [7,20,21]. An analogous atmospheric pressure etching system employing an in-line head would be highly complementary, further optimizing the carefully controlled film growth with post-growth modification. In this paper, we report the first studies of atmospheric pressure plasma etching of ZnO for TCO implementation, demonstrating the dry chemical process that both removes the need for vacuum equipment and also requires no hazardous wet chemistry to effectively manipulate the surface topology of the films.

2. Experimentation

A parallel plate arrangement driven by an audio frequency power supply was used to produce a visually diffuse discharge in nitrogen. The discharge cell was mounted perpendicular to the sample surface to provide remote activation of the process gases and surface treatment via the active species carried convectively in the “afterglow” region. The diffuse discharge is intended to provide consistent, uniform generation of species with baffles to provide uniform gas flow and hence consistent flux of active species across the 80-mm treatment width. Area coverage and uniformity in the “X” direction is provided by translation of the sample below the head to simulate in-line operation.

The delivery system allows for various combinations of process gases; however, a key advantage of the described process is the ability to etch ZnO using only non-hazardous commodity gases.

In particular, for this series of experiments, the entire etching system was contained within a nitrogen environment as shown in Fig. 1. Essentially, this comprised of a vacuum PVC case, which was evacuated and backfilled for each experiment, in order to test or exclude the influence of ambient air entrained within the active zone.

ZnO was deposited using thermally activated chemical vapour deposition at atmospheric pressure, dimethylzinc triethylamine $[\text{Zn}(\text{C}_2\text{H}_5)_2 \cdot \text{N}(\text{C}_2\text{H}_5)_3]$ and ethanol (anhydrous) mixture to produce the films. The temperature of deposition was 430 °C at the substrate surface, resulting in natively rough films. The film thickness was approximately 500 nm and demonstrated peaks facets typical of enhancing light scattering. These films were subjected to the plasma etching system under the nitrogen environment to observe the topological effects. Investigation was conducted for the plasma etching using various discharge parameters and chemistry mixtures delivering nitrogen, oxygen, air and H₂O. Three distinct sets of experiments were performed;

1. Open atmospheric etching vs. nitrogen atmosphere.
2. Nitrogen atmosphere with plasma feed gas of nitrogen and oxygen.
3. Nitrogen atmosphere with plasma feed gas of nitrogen, oxygen and H₂O.

Subsequent investigation involved the regulation of H₂O pick up by variance of the quantity of water supplied to the bubbler. This secondary investigation seeks to resolve a working mixture to balance the effects of the plasma towards an advanced etching control.

Table 1
Etching Conditions—I.

Series	Sample	Total flow (L/min)	O ₂ Percentage	Voltage (kV)	Frequency (kHz)	Primary current (mA)	Plasma power (W)	Passes	H ₂ O (L/min)	H ₂ O (ml)
Open vs. N ₂ atmosphere	S1	10	–	4.95	3.177	515	14.68	50	–	–
	S2	10	–	4.91	3.264	552	15.62	50	–	–
Etching with oxygen	S1	7	14.3	4.98	3.098	554	15.9	20	–	–
	S2	7	12.5	4.98	3.094	552	15.84	20	–	–
	S3	7	20	4.93	3.104	530	15.05	20	–	–
N ₂ , O ₂ and H ₂ O	S1	7	0	4.98	2.948	519	14.9	50	–	50
	S2	7	20	4.93	3.018	514	14.6	50	–	50
Regulated H ₂ O	S1	7	14	4.6	3.125	480	13.25	100	0.2	5
	S2	7	14	4.6	3.109	486	13.35	100	0.4	5
	S3	7	14	4.5	3.113	501	13.63	100	0.6	5
	S4	7	14	4.5	3.102	519	14.12	100	0.8	5
	S5	7	14	4.6	3.102	520	14.04	100	1	5
	S6	7	14	4.5	3.108	489	13.25	100	1.2	5
	S7	7	14	4.5	3.102	496	13.54	100	1.4	5
	S8	7	14	4.6	3.125	493	13.51	100	1.6	5
	S9	7	14	4.5	3.109	500	13.6	100	1.8	5

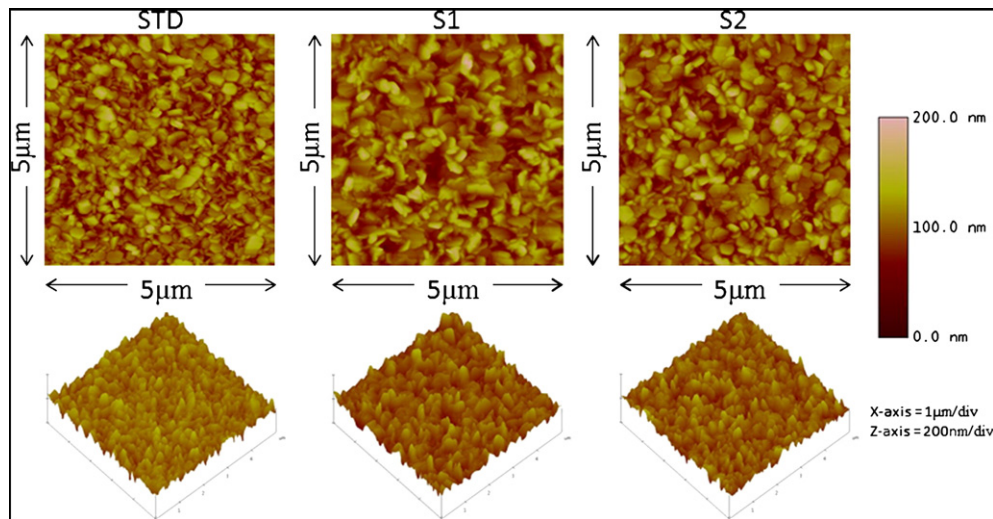


Fig. 2. Two-dimensional AFM Images of ZnO Grown and etched in various environments.

3. Results

3.1. Open atmospheric etching vs. nitrogen atmosphere

The etching system comprises of the controlled environment, sample translation unit and the dielectric barrier discharge etching head. Environment exchange is achieved by a gas extraction and backfilling the environment with the required gas. Fig. 1 shows a schematic of the system.

The first investigation was to observe the effect of etching with a standard atmospheric environment and with a controlled nitrogen environment. Comparatively, the plasma discharge was configured identically, as was the feed gas flow rate, composition (nitrogen only discharge) and exposure time. The controlled environment was nitrogen reducing the possible oxygen exposure to a minimum. Each pass has a residence time of 4.2 s for the given translation speed. The etching conditions for this series are expressed in Table 1.

To compare the effects of the process, AFM images (Fig. 2) were taken of an as-grown zinc oxide film, standard open atmosphere etched and nitrogen environment etched. It was evident from the AFM images that the use of the nitrogen environment significantly reduced the etching effects.

Table 2 shows the respective roughness values associated to the AFM data. Minimal visual difference was noted between the as grown zinc oxide and the sample etched in the nitrogen environment, which showed a nominal difference in measured roughness. However the open atmosphere etching shows a visual different topology and subsequently produces a rougher surface exhibiting a higher RMS.

3.2. Nitrogen atmosphere with plasma feed gas of nitrogen and oxygen

Investigation has shown that additional gases are required for ZnO etching. Oxygen is known to be a reactive gas and would be the significant part of our etching medium in the atmospheric environment [11]. This series of experiments involved the introduction of oxygen into the feedstock in a ratio mixture comparable to ambient air.

In Fig. 3, the relevant AFM images of each sample are shown. There are visibly subtle changes in this series, which may be due to the sample growth. It is difficult to attribute any significant changes made by oxygen exposure, with the variance in appearance and roughness values (Table 2). Oxygen delivered in the feed gas demonstrates a subtle change in etching performance; however, another component maybe required for the effective etching, gas type, ratio of gases, etc.

3.3. Nitrogen atmosphere with plasma feed gas of nitrogen, oxygen and H₂O

Open atmospheric pressure conditions show enhanced etching performance. Oxygen was demonstrated to be a significant component for etching; therefore, H₂O was added as an additional oxygen source. Implementation of an in-line bubbler configuration permits the regulation of H₂O introduction. Blending this design into the original etching configuration enabled control over the three components for required etching.

This series demonstrates the effective etching of the zinc oxide material utilizing a combination of nitrogen, oxygen and H₂O for the plasma feed gases. Neither oxygen nor water alone is able to drastically etch the sample, illustrated by the AFM images in Fig. 4. This series reveals the critical components of oxygen and water is required for etching for ZnO.

3.4. Regulated H₂O Etching

A series of experiments involving flow rate adjustment was performed to observe the etching effects with H₂O delivery. Each sample was exposed to 100 passes under the plasma discharge as

Table 2
Roughness values—II.

Series	Sample	Roughness
Open vs. N ₂ atmosphere	STD	20.41
	S1	21.97
	S2	20.44
Etching with oxygen	STD	19.26
	S1	17
	S2	17.32
N ₂ , O ₂ and H ₂ O	S3	18.72
	STD	17.42
	S1	17.95
Regulated H ₂ O	S2	47.34
	STD	21.26
	S1	19.58
	S2	16.94
	S3	27.77
	S4	28.24
	S5	26.49
	S6	32.06
	S7	38.3
S8	22.55	
S9	32.04	

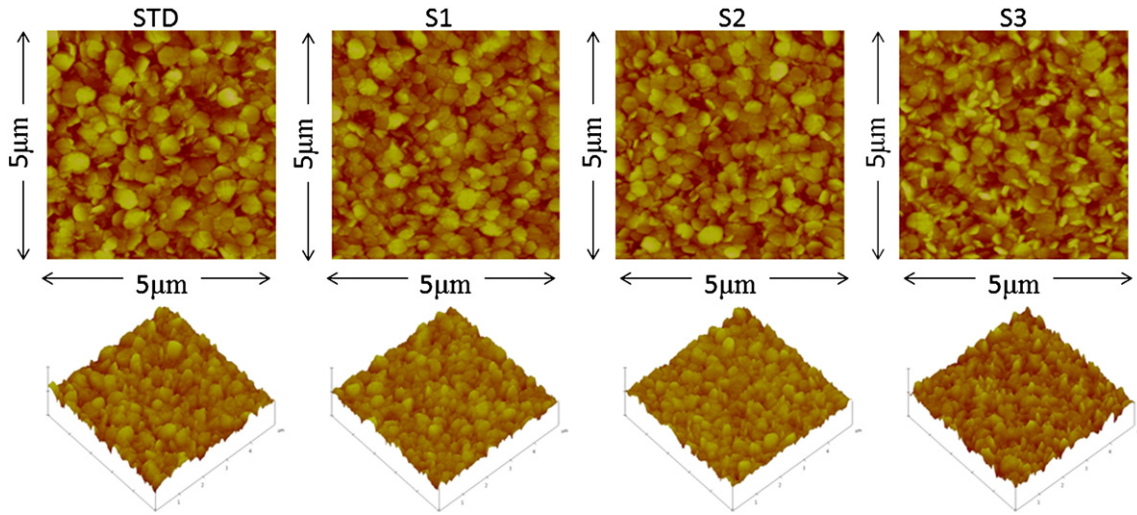


Fig. 3. Two-dimensional AFMs of nitrogen and oxygen etching.

described in Table 1. The oxygen/nitrogen ratio for the bulk for the discharge remained constant through the series.

Illustrated by AFM data (Fig. 5) is the effectiveness of the etching cycle upon the ZnO surface. With varying H₂O content in the feedstock gases, various stages of etching are noted. We observed a smoothing of the surface features for a given gas composition and increased roughness. These samples indicate a scale of control available for tailoring the surface structure. Roughness data show a decline for the sample one and two, with the rest of the samples increasing roughness. Highest-order roughness is shown in sample seven, where it appears most of the smaller facets had been removed, leaving the larger more dominant structure behind. Sample 7 optical assessment indicates a comparative drop in performance with respect to the series. This may be due to the manipulation towards larger sparse surface features increasing absorption, which also do not effectively scatter across the measured wavelengths.

Optical analysis of the series shows that sample 5 has a trending increase in transmission across the multiple wavelengths compared to the standard sample, while also exhibiting peak scattering properties (increased forward/reverse haze). A corresponding reduction in specular reflection further indicates the enhanced scattering property. Observation of the AFM data shows an approximate increase in roughness by

25%, with a morphology exhibiting a more conformal surface. Surface analysis identified a reduction in smaller features while retaining larger crystals that are smoothed through processing. This indicates an etching preference towards the smoothing the film surface. Enhancement of both these elements simultaneously is a key advantage for TCOs, and the primary focus of the post-treatment.

4. Conclusion and discussion

Atmospheric pressure plasma etching has been demonstrated as effective as a new approach to achieve surface profile control for ZnO thin films. We have shown (Fig. 6) that an increase in transmission is established in conjunction with an increase in forward/reverse haze, across the target wavelength range. A corresponding reduction in specular reflection further indicates the enhanced scattering property. Surface analysis identifies a reduction in smaller features while retaining larger crystals that are smoothed through processing. This indicates an etching preference towards the smaller facets on the film surface. Resulting from this process are larger features that resemble the desired pyramidal structure.

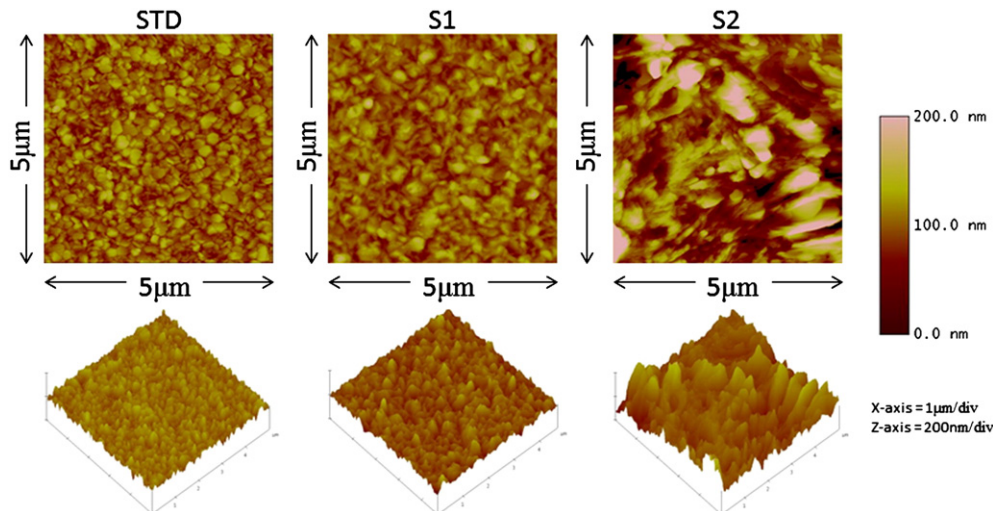


Fig. 4. AFM of H₂O bubbler etching.

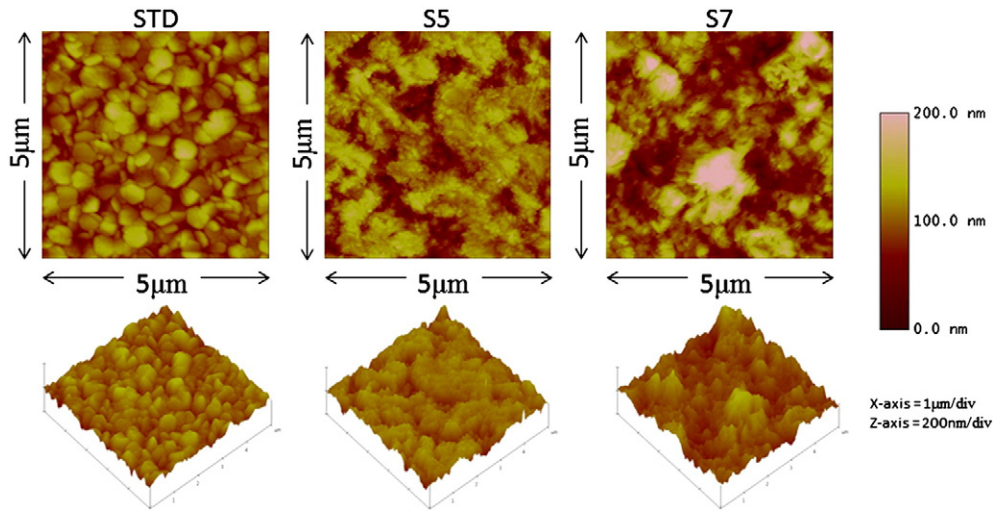


Fig. 5. AFM of regulated H₂O etched samples (standard, S5 and S7).

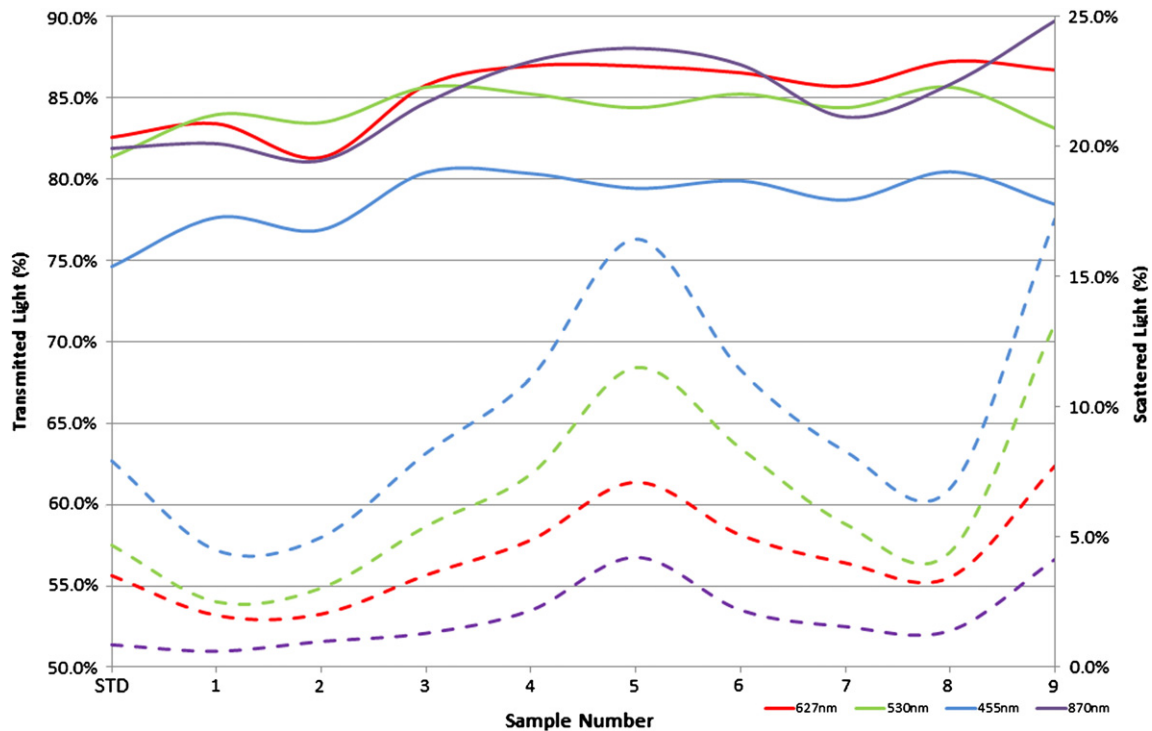


Fig. 6. Transmission and scatter for regulated etching (455 nm, 530 nm, 627 nm and 870 nm).

Plasma feedstock gases have been shown to have a significant effect on etching cycle. Water introduction into the standard nitrogen and oxygen mixture has been shown to be important for efficient ZnO etching. Separately, water and oxygen do not offer the same degree of etching activity until combined. We postulate that a two-stage reaction process is occurring with intermediate (e.g. a hydrate or partial hydrate) reacting faster with oxygen. Varying the contribution of H₂O concentration into the plasma led to an evolution of surface structures that demonstrated the flexibility of the etching system. Several aspects may be involved during the surface evolution. Etching activity increases with a corresponding increase in H₂O delivery. Equally with increasing H₂O delivery, a saturation point may develop, reducing etching activity. If the plasma becomes quenched with “contaminates,” effective breakdown will reduce and therefore the active specie production will diminish [22].

Testing involving increased oxygen introduction developed filamentary spikes visibly in the discharge and observed on the oscilloscope.

Acknowledgements

This work was funded by the FP7-NMP-N2P no. CP-IP 214134-2 *Flexible Production Technologies and Equipment Based on Atmospheric Pressure Plasma Processing for 3D Nano Structured Surfaces*.

References

- [1] J. Hu, R. Gordon, *Sol. Cells* 30 (1991) 437–450.
- [2] M. Purica, E. Budianu, E. Rusu, M. Danila, R. Gavrilă, *Thin Solid Films* 403–404 (2002) 485–488.
- [3] J. Muller, B. Rech, J. Springer, M. Vanecek, *Sol. Energy* 77 (2004) 917–930.

- [4] P.M. Ratheesh Kumar, C. Sudha Kartha, K.P. Vijayakumar, F. Singh, D.K. Avasthi, *Mater. Sci. Eng. B* 117 (2005) 307–312.
- [5] S. Nicolay, M. Despeisse, F.-J. Haug, C. Ballif, *Sol. Energy Mater. Sol. Cells* 95 (2011) 1031–1034.
- [6] J. Escarre, K. Soderstrom, M. Despeisse, S. Nicolay, C. Battalia, G. Bugnon, L. Ding, F. Meillaud, F.-J. Haug, C. Ballif, *Sol. Energy Mater. Sol. Cells* 98 (2012).
- [7] D.S. Bhachu, G. Sankar, I.P. Parkin, *Chem. Mater.* 24 (2012) 4704–4710.
- [8] D.E. Proffit, S.P. Harvey, A. Klein, R. Schafranek, J.D. Emery, B. Bucholz, R.P.H. Chang, M.J. Bedzyk, T.O. Mason, *Thin Solid Films* 520 (2012) 5633–5639.
- [9] M. Python, O. Madani, D. Dominé, F. Meillaud, E. Vallat-Sauvain, C. Ballif, *Sol. Energy Mater. Sol. Cells* 93 (2009) 1714–1720.
- [10] H. Soh, J. Yoo, D. Kim *Sol. Energy* 86 (2012) 2095–2105.
- [11] M. Python, E. Vallat-Sauvain, J. Bailat, D. Domine, L. Fesquet, A. Shah, C. Ballif, *J. Non-Cryst. Solids* 254 (2008) 0022–3093.
- [12] In: A. Luque, S. Hegedus (Eds.), *Front Matter*, in *Handbook of Photovoltaic Science and Engineering*, Second ed., John Wiley & Sons, Ltd, Chichester, UK, 2011.
- [13] S. Nicolay, M. Benkhaira, L. Ding, J. Escarre, G. Bugnon, F. Meillaud, C. Ballif, *Sol. Energy Mater. Sol. Cells* 105 (2012) 46–52.
- [14] J. Ye, S. Gu, S. Zhu, S. Liu, W. Liu, X. Zhou, L. Hu, R. Zhang, Y. Shi, Y. Zheng, *J. Cryst. Growth* 274 (2005) 489–494.
- [15] J. Hüpkkes, J.I. Owen, E. Bunte, H. Zhu, S.E. Pust, J. Worbs, G. Jost, *Proceedings of the 25th EU Photovoltaic Solar Energy Conference*, 2010, pp. 3224–3227, <http://dx.doi.org/10.4229/25thEUPVSEC2010-3AV.2.25> (ISBN 3-936338-26-4) (Valencia, Spain).
- [16] M.A. Lieberman, A.J. Lichtenberg, *Principle of Plasma Discharges and Materials Processing*, Second ed. John Wiley & Sons, New Jersey, 2005.
- [17] J. Hüpkkes, J.I. Owen, S.E. Pust, E. Bunte, *Chemphyschem* 13 (2012) 66–73.
- [18] C. Tendero, C. Tixier, P. Tristant, J. Desmaison, P. Leprince, *Spectrochim. Acta B* 61 (2006) 2–30.
- [19] R.J. Roth, Institute of Physics Publication, 2002.
- [20] X.-T. Yan, Y. Xu, *Chemical Vapour Deposition: An Integrated Engineering Design for Advanced Materials*, Springer, 2010.
- [21] D. Sheel, M. Pemble, *International Conference on Coatings on Glass*, 4, 2002.
- [22] F. Massines, P. Ségur, N. Gherardi, C. Khamphan, A. Ricard, *Surf. Coat. Technol.* 174–175 (2003) 8–14.

Non-Thermal Atmospheric Pressure Plasma Etching of F:SnO₂ for Thin Film Photovoltaics

J. L. Hodgkinson*, M. Thomson, I. Cook, and D. W. Sheel

*Physics and Materials Research Centre, CVD Research Group, Cockcroft Building,
Peel Park Campus, The University of Salford, M5 4WT, UK*

Thin film based photovoltaic systems offer significant advantage over wafer based technologies enabling the use of low cost, large area substrates such as glass, greatly facilitating the construction and integration of large modules. The viability of such systems has advanced in recent years, with researchers striving to optimise performance through the development of materials and cell design. One way to improve efficiency is to texture the interface between the TCO and the absorber layer to maximise scattering over the appropriate wavelength range, with nanometre scale features such as pyramids being reported as giving high scatter. These textures may be achieved by advanced growth processes, such as CVD, post growth etching or a combination of both. In this work, textured F:SnO₂ films produced by APCVD were favourably modified using a remote, non thermal, atmospheric plasma to activate a selective dry etch process resulting in significantly enhanced topography. Uniform treatment of the samples was achieved by translation of the samples below the plasma head. Advantages of this approach, compared to competitive technologies such as wet chemical processes, are the relatively low power consumption and ease of scalability and retro-process integration. The modified structures were studied using AFM, SEM and EDAX, with the observed topography controlled by process variables. Optical properties were assessed along with Hall measurements.

Keywords: Atmospheric Pressure, Plasma, Etch, Photovoltaic, Thin Film.

1. INTRODUCTION

F:SnO₂ is a well documented transmitting conductive oxide (TCO) material, employed as the front contact layer for thin film microcrystalline Si ($\mu\text{c-Si:H}$) based single junction or tandem amorphous Si/microcrystalline Si ($\alpha\text{-Si:H}/\mu\text{c-Si:H}$) solar cells. Typically cell structures aim to maximise light trapping to increase optical path length through the absorber layers and hence improve conversion efficiency. This may be achieved via structuring of the TCO surface to maximise light scattering or haze, with large angles being desirable.^{1,2} Such structuring may be achieved via control of growth parameters, typically producing pyramidal features, or post growth etching often applied to sputtered films to produce a crater-like structure. Previous work has shown atmospheric pressure (AP) CVD to be highly suited for online deposition of F:SnO₂ to provide high volume, large area substrates,^{3,4} with this approach demonstrating a high degree of control to achieve the desired topography.⁵ Critically, whilst

a defined pyramidal structure can enhance light trapping, sharp vertices and V-shaped troughs may lead to cracks or voids within the subsequently deposited $\mu\text{c-Si:H}$ and even $\alpha\text{-Si:H}$, offsetting any advantage with reduced electrical performance.⁶ Post growth etching of LPCVD ZnO to convert the V-shaped troughs to U-shaped whilst removing smaller pyramids has been reported to provide a notable improvement in efficiency.⁷ In this case, a low pressure plasma treatment was applied following deposition.

Now we present a complementary atmospheric pressure plasma activated etch process to provide similar modification to the APCVD films. This additional process, designed for large scale online integration may further build on the significant advantages offered by an all atmospheric pressure process.

2. EXPERIMENTAL DETAILS

Highly structured F:SnO₂ films were produced via thermal CVD and modified by exposure to the ‘afterglow’ of a remote plasma torch as depicted in figure one below. The non-equilibrium or ‘cold’ plasma is established using

*Author to whom correspondence should be addressed.

Table I. Etch conditions with varying flow rates and discharge power.

Sample	A1	A2	A3	A4	B1	B2	B3	B4
Voltage (kV)	6.8	6.6	6.6	6.6	5.1	5.1	8.3	8.1
Primary Current (mA)	755	783	762	732	551	541	735	698
Frequency (kHz)	2.979	3.027	3.019	3.027	3.338	3.314	2.882	2.879
HCl Flow Rate (cc/min)	0.3	0.2	0.3	0.3	0.3	0.2	0.3	0.2
Nitrogen (L/min)	6	6	8	8	6	6	6	6
Passes	20	20	20	20	20	20	20	20
Working distance (mm)	15	15	15	15	15	15	15	15

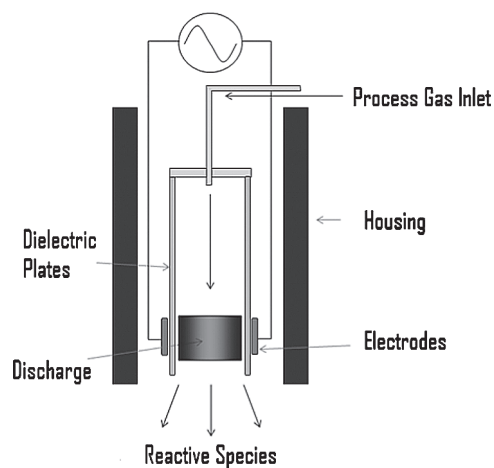
Table II. Etch conditions with varying working distance.

Sample	C1	C2	C3	C4	D1	D2	D3	D4
Voltage (kV)	7.0	6.9	5.2	5.2	7.2	7.1	4.9	5.0
Primary Current (mA)	717	708	501	495	867	832	582	572
Frequency (kHz)	3.03	3.016	3.24	3.245	3.067	3.056	3.356	3.369
HCl Flow Rate (cc/min)	0.3	0.2	0.3	0.2	0.3	0.2	0.3	0.2
Nitrogen (L/min)	6	6	6	6	6	6	6	6
Passes	20	20	20	20	20	20	20	20
Working distance (mm)	14	14	14	14	16	16	16	16

Table III. Optical measurements for the as deposited F:SnO₂ film.

Wavelength	Transmission	Hf (Io) (%)	Hf (T) (%)	Hr (Io) (%)	Hr (Sp) (%)	Sp (%)	Abs (%)
870	86.8	1.9	2.2	3.0	47.5	3.7	6.6
627	80.7	5.3	6.6	3.5	33.6	6.9	8.9
530	78.3	9.1	11.6	2.6	30.9	10.3	8.8
455	73.4	14.2	19.4	4.1	55.9	6.4	16.1

a dielectric barrier discharge (DBD) arrangement with a nitrogen discharge gas. The electrodes are driven by a sinusoidal ac signal in the order of 5–8 kV via a bespoke audio frequency supply designed to facilitate a visually diffuse ‘glow type’ discharge at atmospheric pressure. This diffuse mode is preferred to the more conventional filamentary discharge condition for deposition processes^{8–11} and it is expected that the diffuse discharge will provide more complete activation of the process gasses, to provide a more uniform and controlled surface treatment. The remote configuration decouples the plasma electrical parameters from the substrate/transport mechanism, greatly facilitating process integration. Small quantities of hydrogen chloride (HCl) are introduced into the nitrogen flow, which becomes activated in the plasma and helps provide the etching effect on F:SnO₂. It was noted that in the absence of the discharge, the HCl had no perceivable effect. Area treatment was achieved by translation of the substrate.

**Fig. 1.** Schematic showing the remote DBD torch used for the activated etch process.**Table IV.** Optical measurements for etched sample A1.

Wavelength	Transmission	Hf (Io) (%)	Hf (T) (%)	Hr (Io) (%)	Hr (Sp) (%)	Sp (%)	Abs (%)
870	85.4	2.8	3.3	0.9	13.9	5.8	7.9
627	80.6	5.3	6.6	2.4	27.4	6.2	10.8
530	78.4	9.3	11.8	3.2	41.8	8.7	9.7
455	72.3	12.8	17.6	3.4	37.8	8.6	15.7

The films were etched using the conditions outlined in Tables I and II with a view to correlating the process parameters with the observed effect, with key parameters being, flow rates, discharge power and sample-electrode working distance. Each series involved a variation in the introduced HCl flow rate with intended series conditions. The modified surfaces were observed using AFM and SEM. The enhanced topography was evaluated in terms of optical scatter.

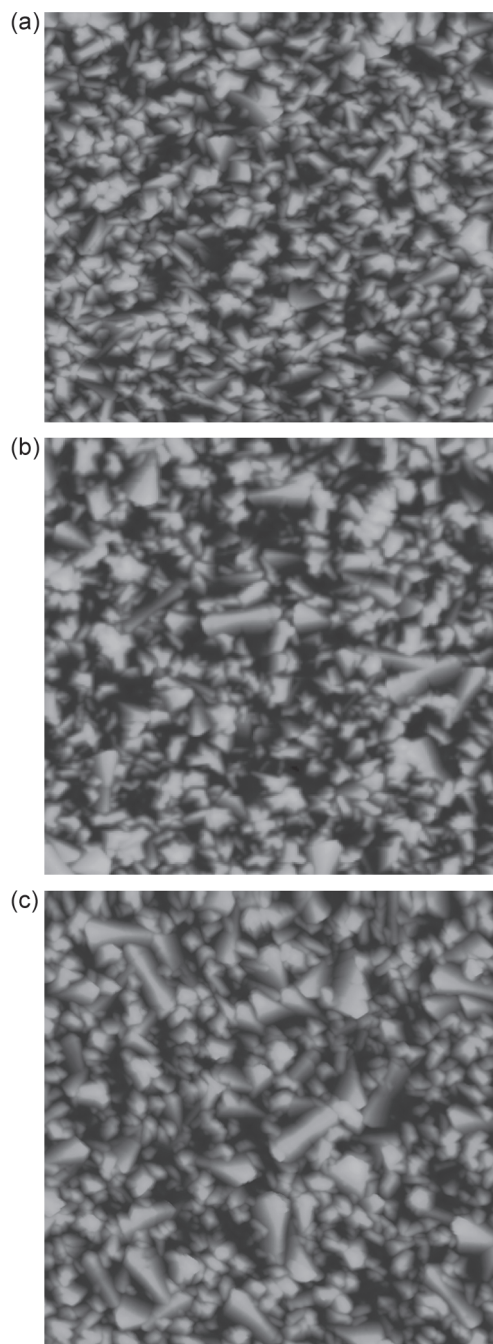


Fig. 2. 5 μm AFM images showing (a) the as deposited F:SnO₂ film, (b) etched sample A1 and (c) etched sample B3.

3. RESULTS AND DISCUSSION

The surfaces of the etched films were studied using atomic force microscopy (AFM) to identify any changes in topography compared to the as deposited films. It was found that the whilst the variation in HCl addition and working distance had minimal discernable effect over the experimental range, the power applied to the discharge had a distinct effect on the feature size. Figure 2 shows the AFM images (5 μm scan) of the as deposited surface alongside etched samples A1 and B3. It can be seen that the etch process provides a change in the size and distribution of the surface features, apparently preferentially removing the smaller peaks. This results in larger surface structures which may be expected to increase light scattering,

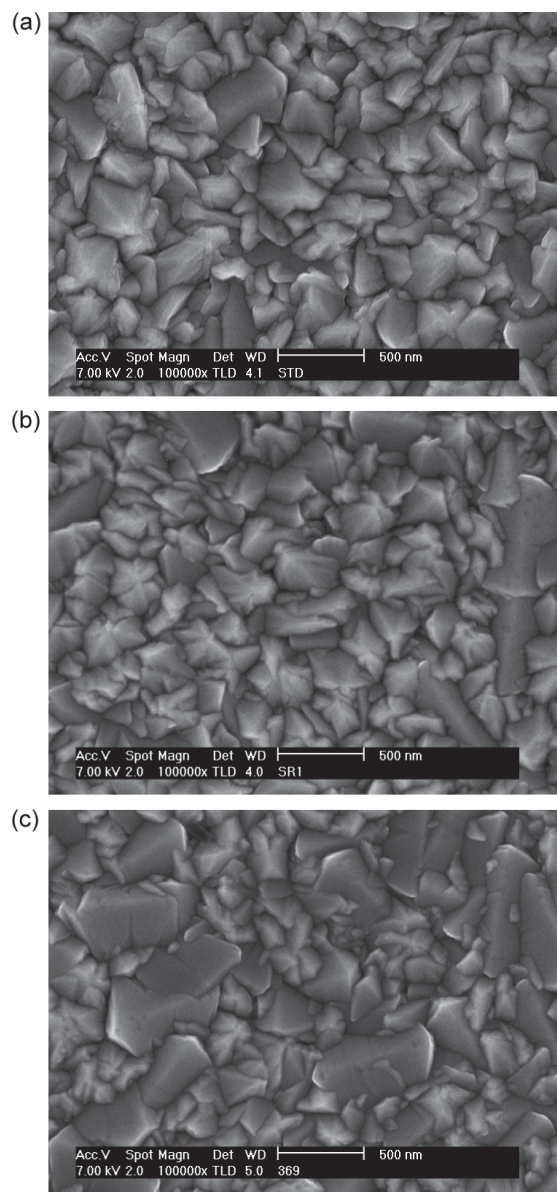


Fig. 3. The SEM images showing (a) the as deposited F:SnO₂, (b) etched sample A1 and (c) etched sample B3.

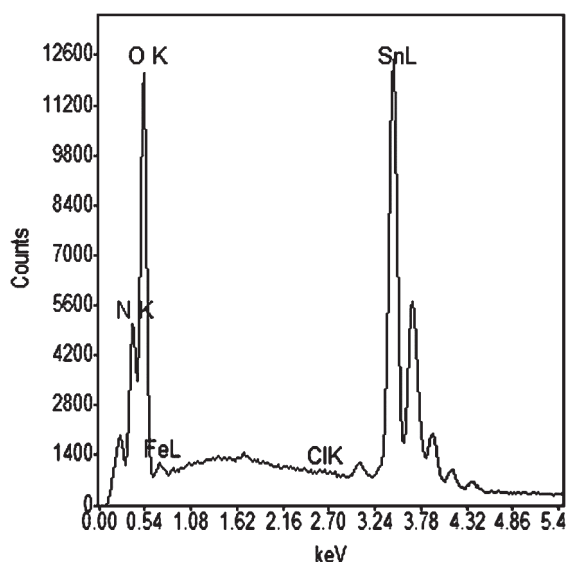


Fig. 4. EDAX analysis showing the lack of chlorine contamination on the modified films (ClK emission expected ~ 2.7 KeV).

with the possibility of reducing interface related defects in the subsequently deposited $\mu\text{c-Si:H}$. The changes are more clearly shown by the complementary SEM images (Fig. 3) which show close agreement with the AFM analysis. The results compare favourably to those reported for a HF/H₂O₃/CH₃COOH based etch process applied to a pyramidal textured wafer, which provided notable improvements in performance attributed to improved $\mu\text{c-Si:H}$.⁶ Furthermore, similar structural changes had shown advantage when applied via a low pressure treatment to LPCVD

ZnO,^{6,12} supporting the suggestion that this approach could offer an analogous atmospheric pressure process to further optimise APCVD F:SnO₂.

The nature of the features presented in the SEM images suggest a genuine etching process as opposed to the effects of deposited reaction products produced from the HCl and F:SnO₂ film. EDAX analysis (Fig. 4) confirmed the chemical composition of the film to be approximately stoichiometric without the presence of any chlorinated by products. The nitrogen was assumed to be adsorbed on the surface and was seen to increase with increasing exposure time.

The effect of the surface modification on optical properties was assessed using an integrating sphere and four LEDs to provide scatter and transmission measurements at a range of fixed wavelengths. The results given in Tables III–V show a minimal reduction in forward haze and a general decrease in reverse haze along with an increase in specular reflection, particularly at longer wavelengths. It is anticipated that the apparent reduction in optical performance can be off set by enhanced $\mu\text{c-Si:H}$ growth, with considerable scope for optimisation. AP Plasma etched APCVD F:SnO₂ films are currently under evaluation in solar cells to test this hypothesis and we hope to publish these results in due course.

Hall measurements were taken to monitor any influence of the etch process on TCO electrical properties. The data given in Tables VI–VIII shows a reduction in sheet resistance for the etched films, due to an increase in carrier concentration which more than compensates for the slight reduction in mobility. Critically, this did not seem to

Table V. Optical measurements for etched sample B3.

Wavelength	Transmission	Hf (Io) (%)	Hf (T) (%)	Hr (Io) (%)	Hr (Sp) (%)	Sp (%)	Abs (%)
870	82.9	1.8	2.2	2.1	24.5	6.9	8.1
627	82.5	5.3	6.4	2.5	27.5	6.6	8.4
530	78.4	8.1	10.4	2.3	26.8	10.5	8.8
455	74.9	13.1	17.4	4.1	51.3	7.0	13.9

Table VI. Hall properties for the as deposited film.

Film thickness (nm) = 1000 Magnetic field (T) = 0.79			Hall volt rms (V) = 9.688E-03 Hall current rms (A) = 2.389E-01	
Rs (Ohm sq)	Rho (Ohm · m)	Ns (cm ⁻²)	Mobility (cm ² /Vs)	N = Ns/d (cm ⁻³)
1.713E+01	1.713E-05	1.218E+16	2.997E+01	1.218E+20

Table VII. Hall properties for etched sample A1.

Film thickness (nm) = 1000 Magnetic field (T) = 0.79			Hall volt rms (V) = 8.660E-03 Hall current rms (A) = 2.577E-01	
Rs (Ohm sq)	Rho (Ohm · m)	Ns (cm ⁻²)	Mobility (cm ² /Vs)	N = Ns/d (cm ⁻³)
1.423E+01	1.423E-05	1.469E+16	2.989E+01	1.469E+20

Table VIII. Hall properties for etched sample B3.

Film thickness (nm) = 1000 Magnetic field (T) = 0.79			Hall volt rms (V) = 8.613E-03 Hall current rms (A) = 2.495E-01	
Rs (Ohm sq)	Rho (Ohm · m)	Ns (cm ⁻²)	Mobility (cm ² /Vs)	N = Ns/d (cm ⁻³)
1.582E+01	1.582E-05	1.431E+16	2.762E+01	1.431E+20

adversely affect the optical transmission of the films over the measured range.

4. CONCLUSION

APCVD has significant advantages over LPCVD or sputter based processes for the large scale manufacture of TCO substrates for thin film photovoltaic systems. Post growth treatment to further optimise the surface textures has shown clear benefits in terms of cell efficiency; although to date such processes typically involve reduced pressures or wet chemical processing. We have demonstrated a low cost and highly scalable plasma activated etch process operating at atmospheric pressure, compatible with continuous in line operation downstream of the APCVD head. Initial results suggest significant potential and work is ongoing to evaluate the effect of modification when incorporated into thin film solar cells.

Acknowledgments: This work was funded FP7-NMP-N2P No. CP-IP 214134-2 *Flexible Production Technologies and Equipment Based on Atmospheric Pressure Plasma Processing for 3D Nano Structured Surfaces*. The authors would also like to thank Geoff Parr of Salford Analytical Services for the SEM images and Vladimir Vishnyakov of Manchester Metropolitan University for the EDAX analysis.

References and Notes

1. J. Krc, B. Lipovsek, M. Bokalic, A. Campa, T. Oyama, M. Kambe, T. Matsui, H. Sai, M. Kondo, and M. Topic, *Thin Solid Films* 518, 3054 (2010).
2. S. Fay, L. Feitknecht, R. Schlüchter, U. Kroll, E. Vallat-Sauvain, and A. Shah, *Sol. Energy Mater. Sol. Cells* 90, 2960 (2006).
3. D. W. Sheel, H. M. Yates, P. Evans, U. Dagkaldiran, A. Gordijn, F. Finger, Z. Remes, and M. Vanecek, *Thin Solid Films* 517, 3061 (2009).
4. Ü. Dagkaldiran, A. Gordijn, F. Finger, H. M. Yates, P. Evans, D. W. Sheel, Z. Remes, and M. Vanecek, *Mater. Sci. Eng. B* 159–160, 6 (2009).
5. H. M. Yates, P. Evans, D. W. Sheel, Z. Remes, and M. Vanecek, *Thin Solid Films* 519, 1334 (2010).
6. M. Python, O. Madani, D. Dominé, F. Meillaud, E. Vallat-Sauvain, and C. Ballif, *Sol. Energy Mater. Sol. Cells* 93, 1714 (2009).
7. J. Bailat, D. Dominé, R. Schlüchter, J. Steinhauser, S. Fay, F. Freitas, C. Bücher, L. Feitknecht, X. Niquille, T. Tschärner, A. Shah, and C. Ballif, High-efficiency p–i–n microcrystalline and micromorph thin film silicon solar cells deposited on LPCVD ZnO coated glass substrates, *Proceedings of the Fourth WCPEC Conference*, Hawaii (2006).
8. S. Martin, F. Massines, N. Gherardi, and C. Jimenez, *Surf. Coat. Technol.* 177–178, 693 (2004).
9. R. Foest, F. Adler, F. Sigeneger, and M. Schmidt, *Surf. Coat. Technol.* 163, 323 (2003).
10. J. L. Hodgkinson, H. M. Yates, and D. W. Sheel, *Plasma Processes and Polymers* 6, 575 (2009).
11. D. W. Sheel and J. L. Hodgkinson, *Plasma Processes and Polymers* 4, 537 (2007).
12. M. Python, E. Vallat-Sauvain, J. Bailat, D. Domine, L. Fesquet, A. Shah, and C. Ballif, *J. Non-Cryst. Solids* 354, 2258 (2008).

Received: 28 April 2011. Accepted: 24 June 2011.

Control of Zinc Oxide Surface Structure Using Combined Atmospheric Pressure based CVD Growth and Plasma Etching

M. Thomson*, J.L. Hodgkinson, D.W. Sheel

Materials and Physics Research Center, University of Salford, Computing Science and Engineering, Salford, UK
m.thomson@edu.salford.ac.uk

ABSTRACT

In photovoltaic thin film cells, a transparent conducting oxide (TCO) layer is required to transport current. The most common TCOs used are F:SnO₂ (fluorine doped tin oxide), ZnO (zinc oxide) and ITO (indium doped tin oxide). ZnO is normally deposited in a vacuum based process, sputtering or low pressure chemical vapour deposition (LPCVD). Atmospheric pressure chemical vapour deposition (APCVD) is an attractive alternative for ZnO deposition. A critical parameter for TCOs in photovoltaic thin films is the surface morphology which defines the optical scattering properties. The ability to control the spectral sensitivity and degree of scattering are both important process parameters for high performance cells.

In this work we employ APCVD for film growth and study the effects of atmospheric pressure plasma etching of ZnO. The ZnO films were deposited onto glass, with the surface morphology analysed by AFM. Modification of the surface morphology was achieved by atmospheric pressure plasma, based on a dielectric barrier discharge configuration. In this study we explored the effects of etching conditions, particularly the variation of feedgas composition (N₂, O₂, H₂O).

By controlling the treatment environment, we were able to establish a relationship between the feedgas mixture and etchant rate. Careful selection and control of processing parameters demonstrated the ability to modify the morphology with a high degree of uniformity. Atmospheric pressure based processes are attractive for scalable production development and future work will explore the potential of this process for large scale application.

1.1. Introduction

ZnO has received considerable interest in recent years for the next generation of transparent conducting oxide (TCO) film implementation for solar cell fabrication. ZnO is natively a semiconducting material

possessing a wide energy band gap of 3.3eV, exhibiting transparency in the visible spectrum with low reflectance in the infra-red and low conductivity [1][2][3]. Implementation as a TCO requires extrinsic dopants to be introduced which are typically fluorine or aluminium, resulting in a highly conductive non-stoichiometric material [1][4]. Critically it is important to select the dopant material carefully for the intended application, to ensure high levels of conductivity whilst maintaining optical performance.

In most thin film solar cell configurations, a TCO layer is required, and the surface structure of this layer may radically influence the ultimate cell performance. Amorphous silicon cells can benefit between 10% to 20% difference in final cell efficiency depending on TCO properties [3][5]. One way to enhance efficiency is to maximise light trapping by increasing optical scatter across the wavelength range by using a textured TCO, with pyramidal structures proposed to give high scatter [6][7]. A drawback of this topography is that sharp features in the peaks and troughs can cause defects in subsequent layers of the fabrication process. This may lead to voltage (Voc) loss across the cell, which is often indicated by reduced shunt resistance [8][9]. Currently a shift for desired morphology has changed from a rough and rounded pyramidal structure towards large crater like structures. This is essentially broadening of the pyramidal structure to obtain the desired optical properties. Typically this structure is achieved through post wet etching the smooth deposited material in HCl [6][10].

Atmospheric pressure chemical vapour deposition (APCVD) is highly suited to the cost effective, continuous production of TCOs on large area substrates such as glass. An analogous atmospheric pressure etching system employing an in-line head would be highly complementary, further optimising the carefully controlled film growth with post growth modification. In this paper we report the first studies of atmospheric pressure plasma etching of ZnO for TCO implementation,

*Authors contact details : m.thomson@salford.edu.ac.uk 01612954800

demonstrating the dry chemical process that both removes the need for vacuum equipment and also requires no hazardous wet chemistry to effectively manipulate the surface topology of the films.

1.2. Plasma Etching System

A parallel plate arrangement driven by an audio frequency power supply was used to produce a visually diffuse discharge in nitrogen. The discharge cell was mounted perpendicular to the sample surface to provide remote activation of the process gasses and surface treatment via the active species carried convectively in the 'afterglow' region. The diffuse discharge is intended to provide consistent, uniform generation of species with baffles to provide uniform gas flow and hence consistent flux of active species across the 80mm treatment width. Area coverage and uniformity in the 'X' direction is provided by translation of the sample below the head to simulate in-line operation. The delivery system allows for various combinations of process gasses, however a key advantage of the described process is the ability to etch ZnO using only non-hazardous commodity gasses.

In particular, for this series of experiments, the entire etching system was contained within a nitrogen environment as show in Figure 1. Essentially this comprised of a vacuum PVC case, which was evacuated and back filled for each experiment, in order to test or exclude the influence of ambient air entrained within the active zone.

2. Experimentation

ZnO was deposited using thermally activated chemical vapour deposition at atmospheric pressure, employing a dimethylzinc adduct and pure ethanol mixture to produce the films. The temperature of deposition was 430°C at the substrate surface, resulting in natively rough films demonstrating peaks facets typical of the form advantageous for light scattering enhancement. Deposited film thickness was approximately 500nm. These films were subjected to the plasma etching system under the nitrogen environment, to observe the topological effects.

3. Results

3.1. Open Atmospheric Etching vs. Nitrogen Atmosphere

The etching system comprises of the controlled environment, sample translation unit

and the dielectric barrier discharge etching head. Environment exchange is achieved by a gas extraction and back filling the environment with the required gas. Figure 1 shows a schematic of system.

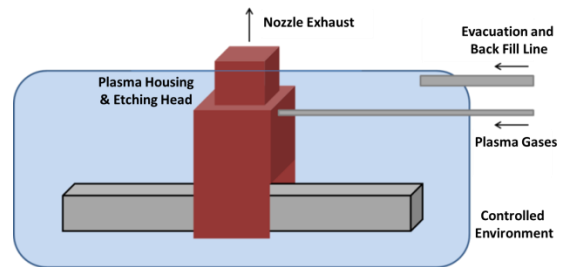


Figure 1 – Plasma Etching system Schematic

The first investigation was to observe the effect of etching with a standard atmospheric environment and with a controlled nitrogen environment. Comparatively the plasma discharge was configured identically, as was the feedgas flow rate and exposure time. The controlled environment was nitrogen reducing the possible oxygen exposure to a minimum. Each pass has a resonance time of 4.2 seconds for the given translation speed. Table 1 expresses the etching conditions for this series;

Sample	N ₂ (L/Min)	Voltage (kV)	Frequency (kHz)	Primary Current (mA)	Plasma Power (W)	Passes	N ₂ Environment
S1	10	4.95	3.18	515	14.68	50	N/A
S2	10	4.91	3.26	552	15.62	50	Yes

Table 1 - Open Atmosphere vs Nitrogen Atmosphere etching Conditions.

To compare the effects of the process, AFM images (Figure 2) were taken of an as grown zinc oxide film, standard open atmosphere etched and nitrogen environment etched. It was evident from the AFM images that the nitrogen environment significantly reduced the etching effects.

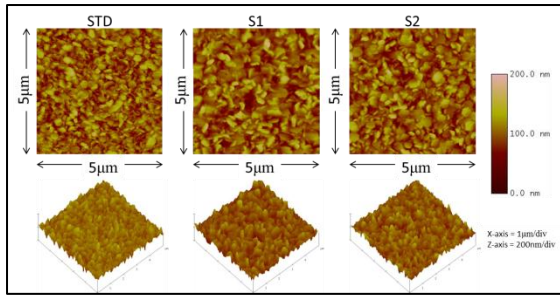


Figure 2 – AFM's Open Atmosphere vs Nitrogen Atmosphere etching.

Sample	STD	S1	S2
RMS (nm)	20.41	21.97	20.44

Table 2 – Roughness Data for Open Atmosphere vs Nitrogen Atmosphere etching.

Minimal visual difference was noted between the as grown zinc oxide and the sample etched in the nitrogen environment, which showed a nominal difference in measured roughness. However the open atmosphere etching shows a visual different topology and subsequently produces a rougher surface exhibiting a higher RMS.

3.2. Nitrogen Atmosphere with Plasma Feedgas of Nitrogen, Oxygen and H₂O

Open atmospheric pressure conditions show enhanced etching performance. Oxygen & H₂O showed to be a significant component for etching. The etching conditions are shown in Table 3.

Sample	Total Flow (L/Min)	O ₂ Percentage (%)	Voltage (kV)	Frequency (kHz)	Primary Current (mA)	Plasma Power (W)	Passes	H ₂ O (ml)
S1	7	0	4.98	2.95	519	14.9	50	50
S2	7	20	4.93	3.02	514	14.6	50	50

Table 3 – Etching Conditions for N₂, O₂ & H₂O Plasma Feedstock

This series demonstrates the effective etching of the zinc oxide material utilizing a combination of nitrogen, oxygen and H₂O for the plasma feedstock gases.

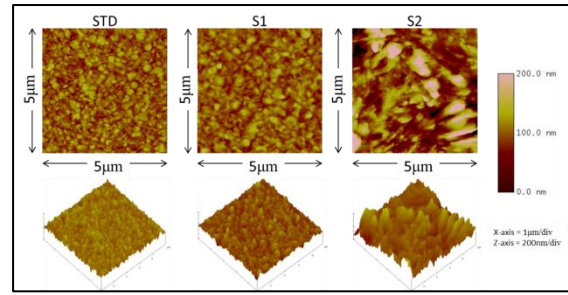


Figure 3 – AFM analysis of N₂, O₂ & H₂O Plasma Etching

Sample	STD	S1	S2
RMS (nm)	17.42	17.95	47.34

Table 4 – Roughness Data for N₂, O₂ & H₂O Plasma Etching

A large change in AFM roughness is observed, with a complete alteration of the surface structure. This series reveals the critical components of oxygen and water is required for etching for ZnO.

4. Conclusion and Discussion

Atmospheric pressure plasma etching has been demonstrated as effective as a new approach to achieve surface profile control for ZnO thin films. AFM analysis shows a minimal etching effect in the nitrogen environment. Introduction of additional feed gases to plasma discharge readily etched the ZnO films. Surface analysis identifies a reduction in smaller features whilst retaining larger crystals that are smoothed through processing. This indicates an etching preference towards the smaller facets on the film surface. Resulting from this process are larger features that resemble the desired pyramidal structure.

Plasma feedstock gases have shown a significant effect on the etching cycle. Controlling the process environment has revealed that oxygen & H₂O are critical for etching ZnO.

Acknowledgements

This work was funded FP7-NMP-N2P No. CP-IP 214134-2 *Flexible Production Technologies and Equipment Based on Atmospheric Pressure Plasma Processing for 3D Nano Structured Surfaces*.

References

[1] J.Hu, R.Gordon, Sol. Cells, 30 (1991) 437-450

- [2] M. Purica, E. Budianu, E. Rusu, M. Danila, R. Gavrila, *Thin Solid Films*, 403-404 (2002) 485-488
- [3] J.Muller, B.Rech, J.Springer, M.Vanecek, *Sol. Energy*, 77 (2004) 917-930
- [4] P.M. Ratheesh Kumar, C. Sudha Kartha, K.P. Vijayakumar, F. Singh, D.K. Avasthi, *Mater. Sci. Eng:B*, 117 (2005) 307-312
- [5] D.E.Proffit, S.P.Harvey, A.Klein, R.Schafranek, J.D.Emery, B.Bucholz, R.P.H Chang, M.J.Bedzyk, T.O.Mason, *Thin Solid Films*, 520 (2012) 5633-5639
- [6] M. Python, O. Madani, D. Dominé, F. Meillaud, E. Vallat-Sauvain, C. Ballif, *Sol. Energy Mater. Sol. Cells*, 93 (2009) 1714-1720
- [7] H.Soh, J.Yoo, D.Kim *Sol. Energy*, 86 (2012) 2095-2105
- [8] M.Python, E.Vallat-Sauvain, J.Bailat, D.Domine, L,Fesquet, A.Shah, C.Ballif, *J. Non-Cryst. Solids*, 254 (2008) 0022-3093
- [9] A.Luque, S.Hegedus (eds) (2011) *Front Matter*, in *Handbook of Photovoltaic Science and Engineering*, Second Edition, John Wiley & Sons, Ltd, Chichester, UK.
- [10] J. Hüpkes, J.I. Owen, E. Bunte, H. Zhu, S.E. Pust, J. Worbs, G. Jost, *Proceedings of the 25th EU Photovoltaic Solar Energy Conference*, 2010, p. 3224-3227, Valencia, Spain



Surface nanostructuring via combined all atmospheric pressure processing, coating, patterning and etching

Ian Cook ^{*}, David W. Sheel, John L. Hodgkinson

University of Salford, Chemical Vapour Deposition Group, Cockcroft Building, University of Salford M5 4WT, UK

ARTICLE INFO

Available online 24 March 2011

Keywords:

Nanostructures
Surface energy
Atmospheric pressure barrier glow discharge

ABSTRACT

Manipulation of surface nanostructure is reported by a sequential multi stage novel combination of all atmospheric pressure based processing. Firstly a thermal chemical vapour deposition (CVD) process is used to deposit a thin zinc oxide film. A flame assisted CVD process is then used to produce the patterning layer. Subsequently an atmospheric pressure dielectric barrier discharge plasma is used to etch the surface to further nanostructure it. We report that this approach can be used to generate a low surface energy organic surface treatment using atmospheric pressure plasma enhanced chemical vapour deposition. The films were characterised by means of atomic force microscopy, transmission spectroscopy, scanning electron microscopy and contact angle.

© 2011 Elsevier B.V. All rights reserved.

1. Introduction

Surface energy control is important in defining many properties including contamination resistance, adhesion, misting, wettability, clean-ability and run off angle. Surface structure plays a crucial role in defining and controlling surface energy. Structuring may be achieved by a variety of both 'bottom up' and 'top down' methods including vacuum evaporation [1], sputtering [2], thermal forming and electro- and mechanical liquid phase chemical processes. Surface patterning and etching are particular methods of manipulating surface structure and involve the controlled deposition and/or removal of material of interest at specific sites on the surface (as opposed to growth of particular structures, via manipulation of process parameters, over an area). Both are commercially established techniques notably applied in the semiconductor industry. A wide range of approaches have been reported including electron beam etching [3], photolithography [4], soft lithography [5] and laser machining [6]. Of the above, electron beam etching is often favoured for patterning at the nanoscale, but can result in a high thermal load and is relatively slow leading to small area restrictions. Lithographic methods typically operate around the micro- and sub micron scale rather than nano level (although nanolithography is a continuing area of research [7]) and involve multiple process stages. Laser based processes have the advantage of fast material processing speed, large area treatment capability and single stage processing, and have been used to pattern the surface of silicon wafers [8]. Other laser methods include the use of microlens arrays [6] and photochemical deposition [9].

Chemical etching applications include optimised light scattering [10], hydrophobic surface synthesis [11] and microelectromechanical systems and integrated circuits [12,13]. For the processing of temperature sensitive substrates, where low thermal loads are required, plasma etching and reactive ion etching are preferable, with the latter used extensively in silicon microstructuring [14,15].

Dry plasma etching of zinc oxide at reduced pressure has been reported by numerous groups [16–19], along with other transparent conducting oxides [20,21]. Virtually all of the techniques described above operate at reduced pressure. While thin zinc oxide films have been deposited by plasma systems at atmospheric pressure [22], surface modification of zinc oxide by atmospheric pressure plasma etching has received little attention, although similar techniques have been used to treat polymers, including polyamides [23], fluorocarbons [24], hydrophilic polytetrafluoroethylene [25] and polypropylene [26], amongst other materials. Here we report the application of a multi stage, combinatorial approach to surface nanostructuring of zinc oxide employing a combination of atmospheric pressure (AP) plasma processes, which offer significant advantages for large scale in-line, continuous processing, removing the necessity for complex and costly vacuum systems. A key objective of this work was to explore how these processes may be combined to achieve enhanced, nanostructured surfaces, and as a specific example to explore the effect this has on wettability. Each process stage influences and can enhance surface properties, such as roughness. The importance of surface roughness at the nano- to microscale is well established as an important feature of hydrophobic surfaces in nature, with two models, Wenzel and Carrière-Baxter, used to describe wetting behaviour on rough substrates, an important consideration for self cleaning surfaces. Carrière-Baxter wetting characterises contact with air filled voids in a rough surface, and is often associated with the rolling action of water droplets. The

^{*} Corresponding author.

E-mail address: i.cook@edu.salford.ac.uk (I. Cook).

results presented here however more closely fit the Wenzel model of homogeneous contact, with high roll off angles due to water infiltration of water into surface voids; it may be possible to further combine the described techniques as a means of producing controllable hydrophobic surfaces.

In this work, we report for the first time a combination of atmospheric pressure based techniques. Firstly, thermal chemical vapour deposition (CVD) was used to grow a zinc oxide film. A flame assisted CVD (FACVD) process was then used to produce the patterning layer, before etching via a remote atmospheric pressure dielectric barrier discharge (DBD) based plasma torch to produce the desired topography. Non equilibrium or cold plasmas as used, which maintain bulk gas temperatures at or near to ambient while creating reactive and charged species, more usually operate (for nanostructure etching) at reduced pressure. The described AP system offers reduced costs in comparison to vacuum based processing. In addition, AP plasma enhanced (PE)CVD has been explored to apply an organic surface coating to alter surface energy, a practise more usually performed at low pressure [27,28], although AP operation has been reported [29].

2. Materials and methods

Zinc oxide films were deposited on borosilicate glass by conventional thermally induced metal organic (MO)CVD using nitrogen as the carrier gas. The precursor was diethylzinc: triethylamine adduct (flow rate 320 sccm), with ethanol as the oxygen source (flow rate 500 sccm); the process gas was carried to the substrate (heated to 400 °C) with a nitrogen flow rate of 1900 sccm. A deposition time of 3 min gave a ZnO film thickness of approximately 1000 nm. Pre grown films were then exposed (initially without patterning) to the remote afterglow of a DBD nitrogen (flow rate 6 l/min) plasma at AP; processing was performed without supplementary substrate heating. The system is shown in Fig. 1. An alternating current (695 mA; 40 V) with a frequency of 2.8 kHz was applied to the dielectric plates. The distance from plates to substrate was 10 mm.

An enhanced (in terms of surface topography) and controllable etching effect was achieved by applying an intermediate step. MOCVD ZnO films were overcoated with a discontinuous metallic silver nanolayer via FACVD, prior to structural enhancements being applied

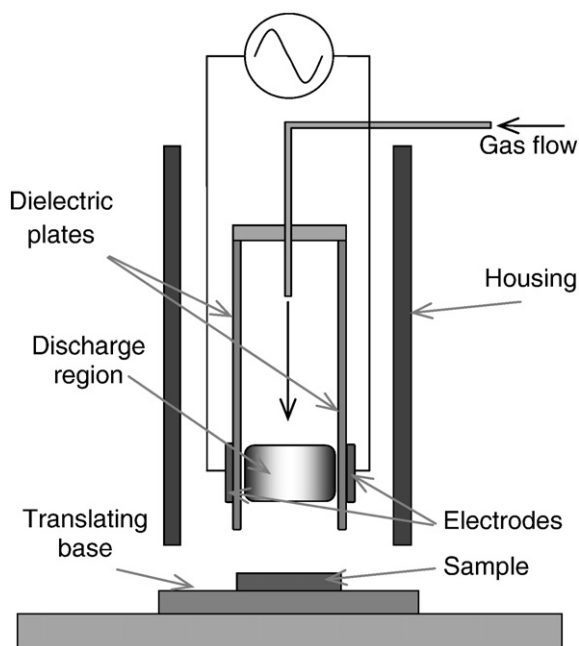


Fig. 1. DBD plasma etching system.

via plasma etching as described above. This technique uses the energy provided by a flame to breakdown chemical precursors, in this case (and typically) simple aqueous metal salts, at atmospheric pressure. As a process FACVD is relatively easy and inexpensive to instal and maintain, having no requirement for complex and costly vacuum and/or reaction chambers. It is suitable for high volume continuous growth and may be retro fitted to existing coating systems and/or production lines. The system has been described in detail elsewhere, being used to deposit oxides of molybdenum and tungsten [30], antibacterial silver/silver titania films [31] and copper oxides [32]. The experimental apparatus is shown schematically in Fig. 2.

In this work, the metallic nanolayer (arising from nucleation and subsequent controlled growth) was used as a plasma etch resistant 'mask'. The nature (thickness, density and size of the metallic 'islands') of the mask may be widely manipulated by varying operational parameters; typical values for this work were as follows: silver nitrate precursor concentration: 0.5 M; burner head height: 10 mm; propane flow rate: 1 l min⁻¹; air flow rate 20 l min⁻¹; nitrogen (precursor carrier) flow rate: 3 l min⁻¹; and substrate speed: 36 mm s⁻¹. Again, no supplementary heating was applied to the substrate, but due to direct heating from the flame the surface temperature rose to 100 °C after 10 passes.

Furthermore, as an additional approach, PECVD was used to explore the possibility of applying a low surface energy organic treatment, again at atmospheric pressure. The power supply (from a Vetaphone CP1 system) applied a frequency of 30 kHz between electrodes in a helium atmosphere, producing a uniform glow discharge. A set power delivery of 200 W is achieved by balancing current and voltage via generator design. The system, shown schematically in Fig. 3, has been used in previous work within the group to deposit titania [33], composite metal/metal oxides [34] and alumina [35]. Ethylene (C₂H₄) was the organic precursor used to apply low surface energy coatings/surface treatment to enable a further mechanism for surface property control, supplied to the reactor at a flow rate of 100 cm³ min⁻¹. Helium was used as the process gas to form the plasma, at 9 l min⁻¹. Nitrogen was used as a baffle in a quartz tube around the reactor to reduce the possibility of streamer formation and arcing, at ~3 l min⁻¹. Additionally, 2,2,2 trifluoroethanol was used in some examples as a fluorine source. As with the plasma etching and FACVD stages, PECVD was performed at atmospheric pressure and ambient substrate temperature.

3. Analysis

Surface topography was investigated by atomic force microscopy (AFM) (Veeco nanoscope D3000).

Surfaces were examined under a Carl Zeiss Supra 40VP variable pressure Field Emission Gun (FEG) scanning electron microscope (SEM).

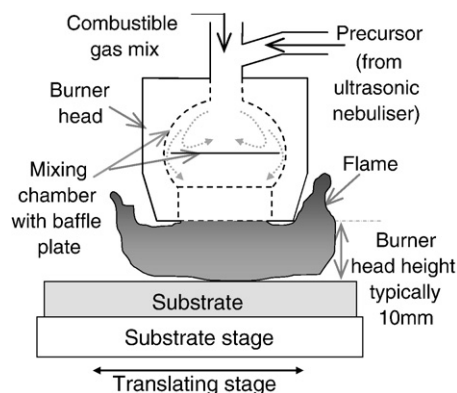


Fig. 2. FACVD setup.

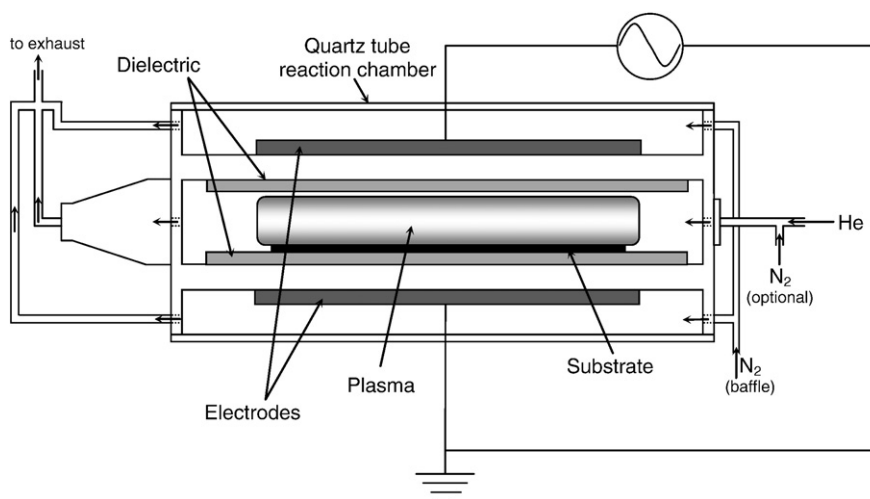


Fig. 3. Atmospheric pressure PECVD system.

A Bruker Optics Vector 22 Fourier Transform Infrared (FTIR) spectrometer, with a frequency range of $4000\text{--}400\text{ cm}^{-1}$ was used to analyse low surface energy coatings.

Contact angles were measured via a variant of the static sessile drop method. A $10\text{ }\mu\text{l}$ droplet of deionised water is deposited on the surface via a needle and microsyringe and observed under an optical microscope; the spread (that is, the diameter of the surface covered by the drop) is then measured. Data is inputted into a computer programme which calculates the contact angle based on the set volume forming a hemisphere on the surface.

4. Results

ZnO films in the as-grown condition show a uniform, smooth structure. At the deposition temperatures employed ($390\text{--}410\text{ }^{\circ}\text{C}$), hexagonal plate like structures, around $200\text{--}600\text{ nm}$ in diameter and tens of nanometres in depth, were apparent under SEM examination (see Fig. 4).

Exposure to the plasma etching system described above resulted in the removal of material from the surface with mean RMS value increasing from 12.2 nm to 18.4 nm . This is revealed by atomic force microscopy as shown in Fig. 5 which shows a) as-grown ZnO surface; b) ZnO after DBD plasma etching. Fig. 5a also confirms the plate like morphology observed under SEM. The plasma etching was sufficiently effective to remove the full 1000 nm film in as little as 60 s . Increased control of the etch rate and selectivity will be achieved with further calibration and careful adjustment of process parameters.

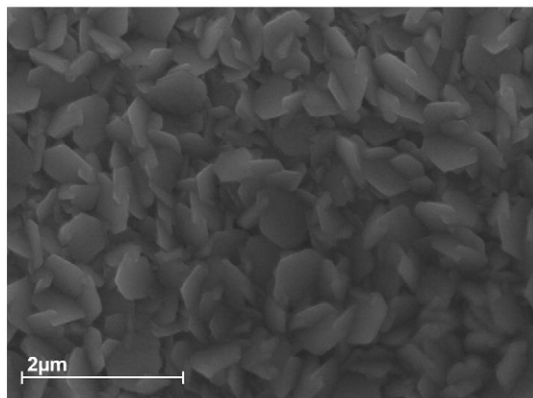


Fig. 4. SEM of ZnO by MOCVD, as deposited.

FACVD of a plasma resistant discontinuous metallic silver nanolayer was an effective means of enhancing the etching effect. Fig. 6 shows SEMs of as-deposited silver films with varied thickness; the deposition rate was approximately 10 nm per pass under the FACVD head, with a residence time of approximately 1.5 s per pass in

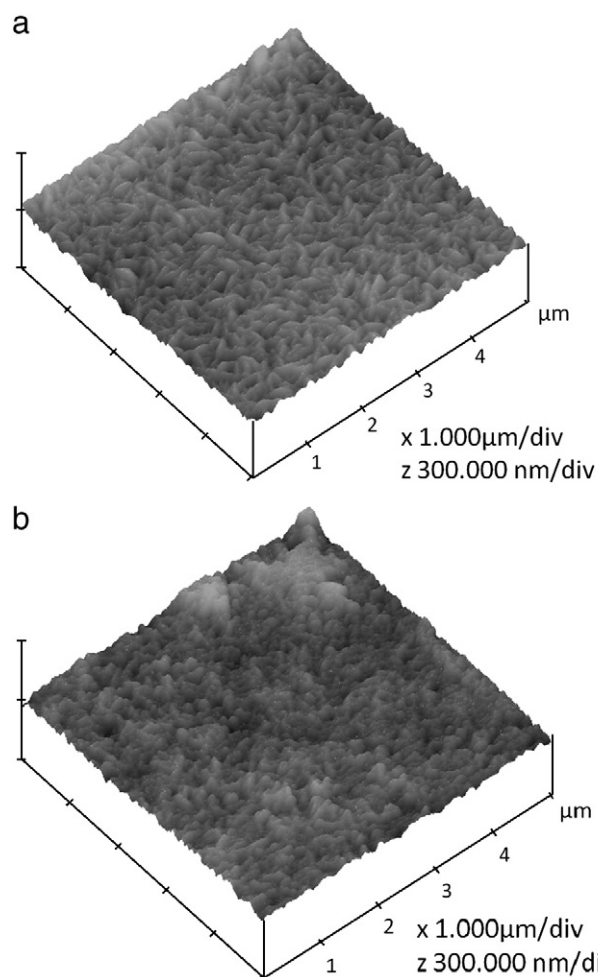


Fig. 5. AFM images of MOCVD ZnO. a) (top) before plasma etching; b) (bottom) after plasma etching.

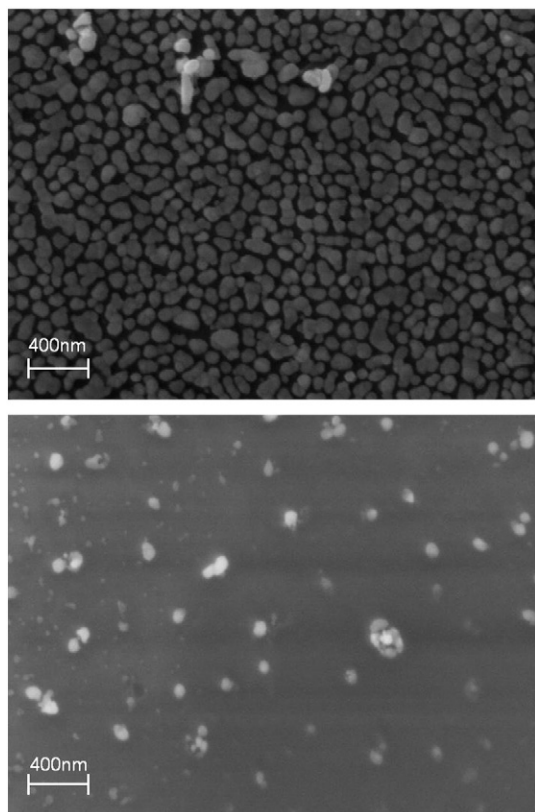


Fig. 6. FACVD silver. Top: 100 nm film showing closely spaced islands; bottom: 40 nm film showing adhered particulates. Longer deposition times/film thickness promotes island-like films while thinner layers are more particulate in nature.

the flame. Apparent is the discontinuous, island-like nature of the film.

Again, AFM images reveal the surface structure modification, presented in Fig. 7.

Clearly apparent is the significantly increased roughness, with high aspect ratio sharp peaks exhibited. Table 1 shows typical RMS and Z-plane tip deflection values for various materials/processes. A 100 nm thick film of silver (10 passes or ~15 s residence time in the flame) showed the greatest surface modification, with a 2–3 fold increase in roughness.

Static contact angles for sequential process stages are shown in Table 2.

MOCVD ZnO as deposited here is a mildly hydrophilic material, although this effect is greatly enhanced with silver masked plasma etching; the increased roughness results in a significant increase in hydrophilicity as demonstrated in the reduction in contact angle to below that observed on uncoated, smooth (less than 1 nm RMS [36]) glass.

In addition to nanostructuring by plasma etching and to explore further mechanisms for tuning of surface energy properties, the described atmospheric pressure PECVD system has been used at room temperature to apply low surface energy coatings. Ethylene was used as a precursor gas and resulted in a soft, polymeric deposit (on clean glass) that was smooth and uniform. The films showed an increase in hydrophobicity compared with plain glass (see Table 3).

To characterise the deposit, films were analysed by FTIR. Due to the highly absorbing nature of the usual glass substrate, deposition was performed on NaCl flats fixed in a perspex mount (to maintain laminar gas flow in the reactor), designed in-house, prior to analysis.

Fig. 8 shows the main absorption bands of a typical FTIR spectra obtained under standard conditions. The complete spectra are simple with few characteristic bands, suggesting a simple lower molecular

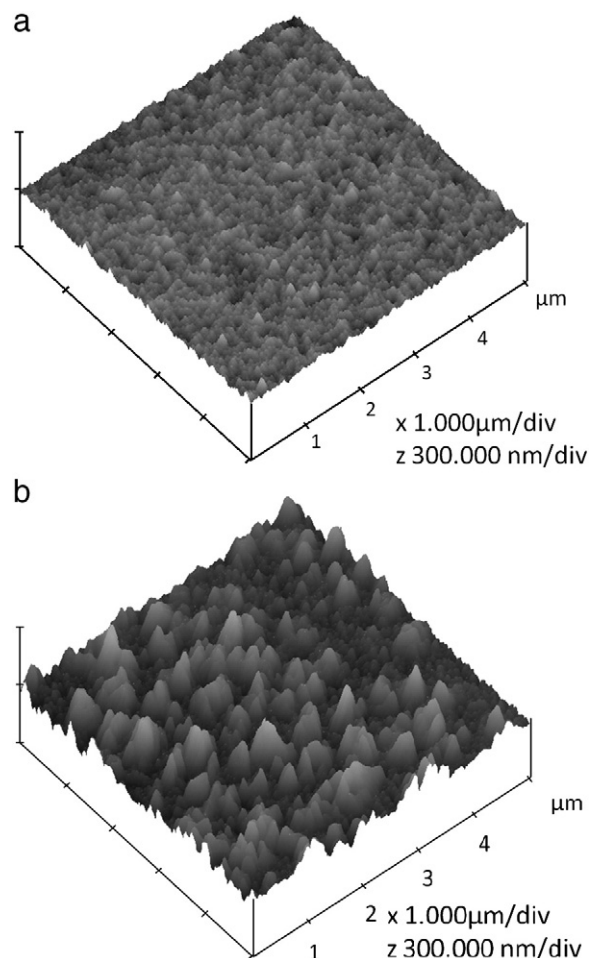


Fig. 7. AFM images of silver masked (100 nm silver) ZnO. a) (top) before plasma etching; b) (bottom) after plasma etching.

weight organic compound forming the thin film. Further, the main absorption is below 3000 cm^{-1} suggesting an aliphatic compound. The band at 2875 cm^{-1} is assigned to C–H stretching [37].

5. Discussion

Fig. 9 shows schematically the surface modification process by silver masking. The silver nanolayer etches at a far lower rate than the underlying ZnO film, resulting in deep troughs separated by high aspect ratio peaks with the silver nanolayer remaining on top. This is apparent from Fig. 7b, showing a highly rough surface at the nanoscale.

The key to this process is the discontinuous nature of the silver masking layer. Surface modification (i.e. roughness) increases with film thickness as a decreasing area of ZnO is exposed, forcing the etching of deep valleys in between the silver. As the silver film becomes thicker, the distribution and degree of agglomeration of nanoparticles increases, forcing the plasma afterglow products into a narrower gap, which creates an increasingly rough surface. As the

Table 1
ZnO roughness.

Material	RMS, nm	Z, nm
ZnO	14	130
Etched ZnO	15	130
Ag on ZnO	10	90
Ag on ZnO, etched	35	250

Table 2
ZnO contact angles.

Material	Static contact angle range
Uncoated glass	30–38°
ZnO	74–83°
Etched ZnO	70–80°
Ag on ZnO	42–49°
Ag on ZnO, etched	17–26°

silver film becomes more continuous, spatial saturation is approached. When this occurs, the effect virtually ceases due to the ZnO being completely protected by silver and thus escapes exposure to the plasma and surface modification. In this study, saturation appears to be almost reached after 15 s residence time in the depositing flame, constituting a film of silver around 100 nm thick (see Fig. 6, which shows a dense, thick film after 15 s residence time in the flame (left) and a relatively thin film of lesser density and continuity after 6 s residence time (right)). This thickness gives the greatest degree of modification, due to the limited space between the silver islands. Further silver deposition simply results in a greater build up on an already saturated film.

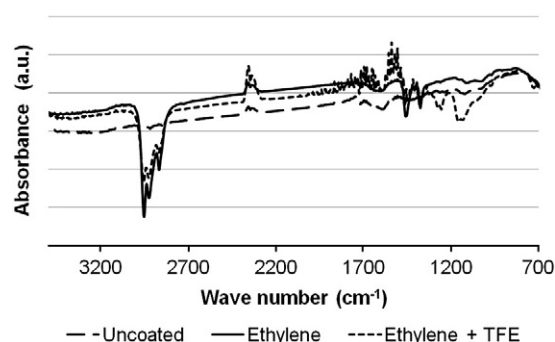
The mechanism of the etching effect itself is not fully understood and further work in this area is necessary and underway. It is not thought to be a physical, sputtering, effect as this is unlikely to be a significant effect at AP. Additionally, the apparent differential etching rate between the two materials is thought to be too great to be attributed to mechanical removal alone (particularly at AP), supporting a reactive chemical driven effect.

The wettability results of the masked etching process are interesting and warrant further discussion. The interaction of water on a surface is related to the relative surface energies of the materials involved. The static contact angle at the three phase interface of a water droplet on a surface is a measure of this and defines whether a surface is hydrophilic or hydrophobic. Thus, a completely hydrophilic surface has a contact angle approaching zero degrees and the surface wets out. A surface is said to be hydrophobic if the contact angle is greater than 90°, and superhydrophobic if it exceeds 150°. As stated above, two models are typically used to characterise the wetting behaviour of hydrophobic surfaces: Wenzel and Cassie-Baxter. In simple terms, Wenzel wetting describes a full contact with the surface, with complete infiltration of any voids at the micro to nanoscale. Cassie-Baxter behaviour by contrast is characterised by water droplets resting on the tips of surface protrusions, with, significantly, air trapped beneath. This promotes high static contact angles and, more importantly, a 'slippery' surface, where water droplets roll off at very low angles, carrying dirt and debris with them. This is in contrast to the 'sticky' hydrophobicity more commonly associated with Wenzel-type wetting. Hence, roughness at the nano to micro scale is vital for the creation of a superhydrophobic surface. Further work optimising the enhanced etching by silver surface patterning as described above will hopefully result in greater surface roughness.

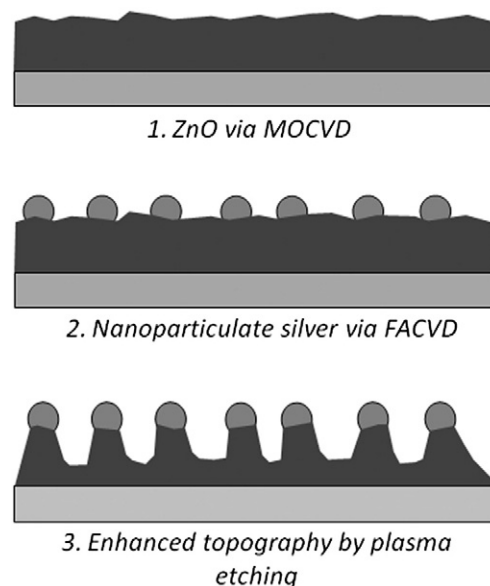
However, roughness alone is insufficient to achieve this hydrophobicity as often the surface structure results in the infiltration of water into the voids. This effect explains the increased hydrophilicity

Table 3
Contact angles of low surface energy coating.

Material	Static contact angle range
Uncoated glass	30–38°
Ethylene, 5 min	85–92°
Ethylene, 10 min	91–96°
TFE alone	66–70°
TFE plus ethylene	80–85°

**Fig. 8.** FTIR spectra of AP DBD plasma polymerised ethylene, ethylene with TFE and uncoated salt flat for comparison.

exhibited by silver masked and plasma etched zinc oxide (see Table 2: contact angle 17–26°) with its enhanced surface roughness (see Table 3 and compare Figs. 5a and 7b: 2–3 fold increase in roughness over unmodified ZnO); the material has a relatively high surface energy resulting in a significant wetting of the surface. As a surface's energy is reduced, the adhesive forces between droplet and surface become relatively less thermodynamically favourable compared with the cohesive forces within the droplet. Hence, a surface with low surface energy, such as those produced with the PECVD system described above, becomes increasingly hydrophobic; if this can be combined with roughness, a surface with high static contact angle and low roll-off angle (the two defining characteristics of superhydrophobic surfaces), may be achieved. Numerous examples of such surfaces exist in nature, such as the leaves of certain plants and the wings and limbs of certain insects. Collectively such surfaces are said to exhibit the 'lotus effect' following initial studies on lotus flower leaves [38]. Scanning electron microscopy images revealed two contributory features: papillose epidermal cells and epicuticular wax crystals. These are roughly analogous to the surface roughness and lowered surface energy described above and indeed provide both inspiration and motivation for the creation of artificial superhydrophobic surfaces. An example of such a fabrication is presented by Lau et al. [39], who report the creation of a superhydrophobic surface consisting of a forest of vertically aligned carbon nanotubes over coated with a non wetting polytetrafluoroethane (PTFE) layer. A nickel catalyst layer was formed by sintering on an oxidised silicon

**Fig. 9.** Silver masked plasma etching for enhanced nanotopography.

substrate; carbon nanotubes, around 2 μm in height, were then grown over this layer via a DC plasma discharge of acetylene and ammonia. Such a surface alone exhibits contact angles of 84–86°; water droplets penetrate the forest due to its high surface energy. Hence, the PTFE layer is added, via a hot filament chemical vapour deposition (HFCVD) process, to reduce this. Contact angles of 160–170° were then demonstrated on the stable surface. In this work, the use of TFE did not result in fluorine incorporation at the surface (fluorine based films being an established means of lowering surface energy [18,40,41]) however the polymeric coating did result in an increase in hydrophobicity (see Table 3: ethylene films were slightly hydrophobic with contact angles of up to 96°). Future work will explore the use of alternative fluorine precursors in the AP PECVD system, with the aim of increasing hydrophobicity.

6. Concluding remarks

We have described a new combination of atmospheric pressure techniques to produce a degree of controlled surface nanostructure. In addition we have shown examples of such surface structure, in ZnO, and their potential for manipulating surface energy. The processing techniques reported here (post thermal CVD) have the significant advantage of being performed at low (i.e. <100 °C) temperature and atmospheric pressure. Future planned work will include introducing masking/patterning and also exploring nucleation approaches to further enhance surface structure control.

References

- [1] K. Cai, M. Müller, J. Bossert, A. Rechtenbach, K.D. Jandt, *Appl. Surf. Sci.* 250 (2005) 252.
- [2] Z.F. Wu, X.M. Wu, L.J. Zhuge, B. Hong, X.M. Yang, T. Yu, J.J. He, Q. Chen, *Appl. Surf. Sci.* 256 (2010) 2259.
- [3] M.N. Kozicki, J. Allgair, A. Jenkins-Gray, D.K. Ferry, T.K. Whidden, *Phys. B* 227 (1996) 318.
- [4] G. Yuan, P. Wang, Y. Lu, Y. Cao, D. Zhang, H. Ming, W. Xu, *Opt. Commun.* 281 (9) (2008) 2680.
- [5] J.A. Rogers, R.G. Nuzzo, *Mater. Today* 8 (2) (2005) 50.
- [6] C.S. Lim, M.H. Hong, Y. Lin, G.X. Chen, A. Senthil Kumar, M. Rahman, L.S. Tan, J.Y.H. Fuh, G.C. Lim, *J. Mater. Process. Technol.* 192–193 (2007) 328.
- [7] X.N. Xie, H.J. Chung, C.H. Sow, A.T.S. Wee, *Mater. Sci. Eng. R* 54 (2006) 1.
- [8] A. Dalili, B. Tan, K. Venkatakrishnan, *Opt. Lasers Eng.* 48 (2010) 346.
- [9] E. Hugonnot, J.P. Delville, *Appl. Surf. Sci.* 248 (2005) 185.
- [10] J.M. Müller, B. Rech, J. Springer, M. Vanecek, *Sol. Energy* 77 (2004) 917.
- [11] I.P. Parkin, C.R. Crick, *Eur. J. Chem.* 16 (2010) 3568.
- [12] K.R. Williams, R.S. Muller, *J. Microelectromech. Syst.* 5 (4) (1996) 256.
- [13] K.R. Williams, K. Gupta, M. Wasilik, *J. Microelectromech. Syst.* 12 (6) (2003) 761.
- [14] W. Lang, *Mater. Sci. Eng. R17* (1996) 1.
- [15] H. Jansen, H. Gardeniers, M.D. Boer, M. Elwenspoek, J. Fluitman, *J. Micromech. Microeng.* 6 (1996) 14.
- [16] R. Groenen, M. Creatore, M.C.M. van de Sanden, *Appl. Surf. Sci.* 241 (2005) 321.
- [17] D.Y. Lee, C.W. Chung, *Thin Solid Films* 517 (2009) 4047.
- [18] J.C. Woo, D.S. Um, C.I. Kim, *Thin Solid Films* 518 (2010) 2905.
- [19] W.T. Lim, L. Stafford, J.I. Song, J.S. Park, Y.W. Heo, J.H. Lee, J.J. Kim, S.J. Pearton, *Appl. Surf. Sci.* 253 (8) (2007) 3773.
- [20] Y.J. Lee, J.W. Bae, H.R. Han, J.S. Kim, G.Y. Yeom, *Thin Solid Films* 383 (1–2) (2001) 281.
- [21] S.M. Kong, Y. Xiao, K.H. Kim, W.I. Lee and C.W. Chung, *Thin Solid Films* 519 10 (2011) 3173.
- [22] M.D. Barankin, E. Gonzalez, A.M. Ladwig, R.F. Hicks, *Sol. Energy Mater. Sol. Cells* 91 (10) (2007) 924.
- [23] Z. Gao, S. Peng, J. Sun, L. Yao, Y. Qiu, *Appl. Surf. Sci.* 255 (17) (2009) 7683.
- [24] F. Fanelli, F. Fracassi, R. d'Agostino, *Surf. Coat. Technol.* 204 (2010) 1779.
- [25] J.H. Noh, H.K. Baik, I. Noh, J.C. Park, I.S. Lee, *Surf. Coat. Technol.* 201 (9–11) (2007) 5097.
- [26] H.S. Choi, V.V. Rybkin, V.A. Titov, T.G. Shikova, T.A. Ageeva, *Surf. Coat. Technol.* 200 (14–15) (2006) 4479.
- [27] S.H. Yang, C.H. Liu, W.T. Hsu, H. Chen, *Surf. Coat. Technol.* 203 (2009) 1379.
- [28] D. Liu, W. Li, A. Feng, X. Tan, B. Chen, J. Niu, Y. Liu, *Surf. Coat. Technol.* 203 (2009) 1231.
- [29] I.P. Vinogradov, A. Dinkelmann, A. Lunk, *Surf. Coat. Technol.* 174–175 (2003) 509.
- [30] M.J. Davis, G. Benito, D.W. Sheel, M.E. Pemble, *Chem. Vapour Deposition* 10 (1) (2004) 29.
- [31] L.A. Brook, P. Evans, H.A. Foster, M.E. Pemble, A. Steele, D.W. Sheel, H.M. Yates, *J. Photochem. Photobiol., A* 187 (2007) 53.
- [32] H.M. Yates, L.A. Brook, D.W. Sheel, I.B. Ditta, A. Steele, H.A. Foster, *Thin Solid Films* 517 (2008) 517.
- [33] J.L. Hodgkinson, H.M. Yates, D.W. Sheel, *Plasma Processes Polym.* 6 (2009) 575.
- [34] D.W. Sheel, J.L. Hodgkinson, *Plasma Processes Polym.* 4 (2007) 537.
- [35] J.L. Hodgkinson, H.M. Yates, D.W. Sheel, M.E. Pemble, *Plasma Processes Polym.* 3 (2006) 597.
- [36] H.K. Jang, Y.D. Chung, S.W. Whangbo, I.W. Lyo, and C.N. Whang, *J. Vac. Sci. Technol., A* 18 (5) (2000) 2563.
- [37] L. Sharma, T. Kimura, *Polym. Adv. Technol.* 14 (2003) 392.
- [38] C. Neinhuis, W. Barthlott, *Ann. Bot.* 79 (1997) 667.
- [39] K.K.S. Lau, J. Bico, K.B.K. Teo, M. Chhowalla, G.A.J. Amaratunga, W.I. Milne, G.H. McKinley, K.K. Gleason, *Nano Lett.* 3 (12) (2003) 1701.
- [40] Y. Ohtsu, Y. Masuda, S. Yazaki, T. Misawa, H. Fujita, *Surf. Coat. Technol.* 202 (2008) 5367.
- [41] D. Liu, W. Li, Z. Feng, X. Tan, B. Chen, J. Niu, Y. Liu, *Surf. Coat. Technol.* 203 (2009) 1231.